



HAL
open science

Numerical Homogenization and Model Reduction for Transient Heat, Diffusion and coupled Mechanics Problems

Abdullah Waseem

► **To cite this version:**

Abdullah Waseem. Numerical Homogenization and Model Reduction for Transient Heat, Diffusion and coupled Mechanics Problems. Mechanics of materials [physics.class-ph]. École centrale de Nantes; Technische hogeschool (Eindhoven, Pays-Bas), 2020. English. NNT : 2020ECDN0028 . tel-03178405

HAL Id: tel-03178405

<https://theses.hal.science/tel-03178405>

Submitted on 23 Mar 2021

HAL is a multi-disciplinary open access archive for the deposit and dissemination of scientific research documents, whether they are published or not. The documents may come from teaching and research institutions in France or abroad, or from public or private research centers.

L'archive ouverte pluridisciplinaire **HAL**, est destinée au dépôt et à la diffusion de documents scientifiques de niveau recherche, publiés ou non, émanant des établissements d'enseignement et de recherche français ou étrangers, des laboratoires publics ou privés.

THESE DE DOCTORAT DE

L'ÉCOLE CENTRALE DE NANTES
Et l'UNIVERSITÉ TECHNIQUE D'EINDHOVEN

ÉCOLE DOCTORALE N° 602
Sciences pour l'Ingénieur
Spécialité : Mécanique des solides, des matériaux des structures et des surfaces

Par

Abdullah WASEEM

Numerical homogenization and model reduction for transient heat, diffusion and coupled mechanics problems

Thèse présentée et soutenue à Eindhoven, le 17 novembre 2020

Unité de recherche : UMR 6183, Institut de recherche en Génie Civil et Mécanique (GeM)

Rapporteurs avant soutenance :

Fredrik LARSSON Professeur, Chalmers University of Technology (Suède)
Eduardo DE SOUZA NETO Professeur, Swansea University (Royaume-Uni)

Composition du Jury :

Président :	Phillip DE GOEY	Professeur, Université Technique d'Eindhoven (Pays-Bas)
Examineurs :	Varvara KOUZNETSOVA Herald VAN BRUMMELEN	Associate professeur, Université Technique d'Eindhoven (Pays-Bas) Professeur, Université Technique d'Eindhoven (Pays-Bas)
Dir. de thèse:	Marc GEERS	Professeur, Université Technique d'Eindhoven (Pays-Bas)
Dir. de thèse :	Laurent STAINIER	Professeur des universités, École Centrale de Nantes
Co-encadrant:	Thomas HEUZÉ	Maître de conférences, École Centrale de Nantes

Numerical Homogenization and Model Reduction
for Transient Heat, Diffusion and Coupled
Mechanics Problems

Abdullah Waseem

Numerical Homogenization and Model Reduction for Transient Heat, Diffusion and Coupled Mechanics Problems

Abdullah Waseem

A catalogue record is available from the Eindhoven University of Technology Library.

ISBN: 978-90-386-5134-7

Cover design: ProefschriftMaken

Printed by: ProefschriftMaken || www.proefschriftmaken.nl

Support for this research was provided by European Commission through an Erasmus Mundus grant in the framework of the Simulation in Engineering and Entrepreneurship Development (SEED) program. SEED program is an initiative of 8 universities Partners, managed by EACEA and financed by the European Commission with grant Ref. 2013-0043.

© Copyright, 2020, Abdullah Waseem. All rights reserved.

Numerical Homogenization and Model Reduction for Transient Heat, Diffusion and Coupled Mechanics Problems

PROEFSCHRIFT

ter verkrijging van de graad van doctor aan de Technische
Universiteit Eindhoven, op gezag van de rector magnificus
prof.dr.ir. F.P.T. Baaijens, voor een commissie aangewezen
door het College voor Promoties, in het openbaar te
verdedigen op
dinsdag 17 November 2020 om 13:30 uur

door

Abdullah Waseem

geboren te Jhelum, Pakistan

Dit proefschrift is goedgekeurd door de promotoren en de samenstelling van de promotiecommissie is als volgt:

voorzitter: prof.dr. L.P.H. de Goey
1^e promotor: prof.dr.ir. M.G.D. Geers
2^e promotor: prof.dr.ir. L. Stainier (Ecole Centrale de Nantes)
1^e copromotor(en): dr.ir. V.G. Kouznetsova
2^e copromotor(en): dr. T. Heuzé (Ecole Centrale de Nantes)
leden: prof.dr.ir. E.H.V. Brummelen
prof.dr. F.I. Larsson (Chalmers University of Technology)
prof. E.A. de Souza Neto (Swansea University)

Het onderzoek of ontwerp dat in dit proefschrift wordt beschreven is uitgevoerd in overeenstemming met de TU/e Gedragscode Wetenschapsbeoefening.

To planet Earth, its wilderness and lifeforms.

Summary

Numerical Homogenization and Model Reduction for Transient Heat, Diffusion and Coupled Mechanics Problems

This dissertation presents computationally efficient numerical homogenization techniques for transient diffusion phenomena in heterogeneous materials. The transient behavior arises due to the material properties, the characteristic length scales and the time varying loading conditions. Homogenization of such materials generally requires computationally expensive solution schemes for the transient diffusion equations at the macro- and the micro-scale. Concepts from numerical techniques like *computational homogenization*, *component mode synthesis* and *data-driven mechanics* are used to efficiently homogenize problems for heat diffusion, mass diffusion and mass diffusion coupled to mechanics. The background and motivation is presented in **Chapter 1**.

In **Chapter 2**, as a preliminary step, a model reduction for the transient heat diffusion equation is performed at the micro-scale using component mode synthesis, which provides an emergent enriched-continuum description of the homogenized level at the macro-scale. Assuming linear material behavior and relaxed separation of scales, the microscopic response is decomposed into a steady-state and a transient part. For the steady-state response static-condensation is used, whereas for the model reduction of the transient response an eigenvalue problem is solved and the system of equations is projected onto a reduced number of eigenbases. As a consequence, the microscopic problem is replaced by a set of decoupled ordinary differential equations which are computationally inexpensive to solve. The numerical examples solved at the micro-scale confirm the accuracy and computational efficiency of the method.

Chapter 3 deals with different solution methods for the macro-scale enriched-continuum for transient mass diffusion problems. Two spatial discretization schemes are discussed for the enrichment-variables. The primary macroscopic field is interpolated with finite element shape functions, while the enrichment-variables can either be interpolated using finite elements, leading to a multi-field solution method,

or evaluated at the Gauss quadrature points, leading to an internal-variable solution method. Different time integration methods are also presented for the internal-variable solution method. Enriched-continuum results are compared with those obtained from classical transient homogenization and direct numerical simulations for evaluating the accuracy and computational gains.

The proposed model reduction method is extended to the transient mass diffusion coupled to the mechanics, in **Chapter 4**, with application to lithium-ion batteries operating in a linear regime. Using the Legendre transformation, the primary variables of the coupled model are converted to the chemical potential and strain fields, which allows the use of standard C^0 -continuous finite elements. A model reduction using component mode synthesis is performed and an enriched-continuum for mass diffusion coupled to mechanics is obtained. The micro-scale problem, which usually involves an expensive solution of the coupled mass diffusion-mechanics problem, is now replaced by a set of ordinary differential equations.

Chapter 5 constitutes a novel model reduction and homogenization procedure for history dependent diffusion at the macro-scale using data-driven mechanics. It replaces the solution of the microscopic problems with a direct search in a data-set. The data-set is generated efficiently using the enriched-continuum formulation in an offline stage. The enrichment-variables serve as a pointer in time for keeping track of the history dependent diffusion. It also provides a route to extend the proposed model reduction method to the non-linear regime. Finally, conclusions and future research directions are discussed in **Chapter 6**.

Contents

Summary	iv
1 Introduction	1
1.1 Background and Motivation	1
1.1.1 Examples	1
1.1.2 Analysis Techniques	2
1.2 Objective and Research Questions	3
1.3 Outline of the thesis	4
2 Model Reduction in Computational Homogenization for Transient Heat Diffusion	7
2.1 Introduction	8
2.1.1 Outline	11
2.1.2 Symbols and Notations	11
2.2 Homogenization Framework	12
2.2.1 Separation of Scales	12
2.2.2 Energy Balance Equation at the Macro- and Micro-scales . .	14
2.2.3 Downscaling	15
2.2.4 Upscaling	17
2.3 Model Order Reduction	19
2.3.1 Micro-scale Discrete Problem	19
2.3.2 Micro-scale Model Reduction	21
2.3.3 Macroscopic Quantities	26
2.3.4 Thermal Enriched-Continuum at Macro-scale	28
2.3.5 Identification of Transient Reduced Basis	28
2.4 Numerical Examples	29
2.4.1 Problem Settings	29
2.4.2 Reduced Basis Identification	30
2.4.3 Homogenization Results	35

2.4.4	Applicability Limits of RTH	40
2.5	Conclusions and Perspectives	42
3	Two-scale Analysis of Transient Diffusion Problems Through a Homogenized Enriched-Continuum	45
3.1	Introduction	46
3.1.1	Outline	49
3.1.2	Symbols and Notations	50
3.2	Enriched-Continuum Formulation	51
3.2.1	Direct Numerical Simulation	51
3.2.2	Computational Homogenization	51
3.2.3	Enriched-Continuum	54
3.3	Solution Methods	55
3.3.1	Time Integration Schemes	55
3.3.2	Multi-Field Method	56
3.3.3	Internal-Variable method	59
3.4	Numerical Examples	61
3.4.1	Accuracy of the Time Integration Schemes for the Internal-Variable Method	64
3.4.2	Homogenized Solution	65
3.4.3	Macroscopic Discretization Effect	66
3.4.4	Computational Efficiency	67
3.5	Conclusions	69
4	Enriched-Continuum for Multi-scale Transient Diffusion Coupled to Mechanics	71
4.1	Introduction	72
4.1.1	Outline	75
4.1.2	Symbols and Notation	76
4.2	Coupled Diffusion-Mechanics Formulation:	76
4.2.1	Conservation Laws	77
4.2.2	(c, ε) Formulation	78
4.2.3	(μ, ε) Formulation	80
4.2.4	Linear Isotropic Constitutive Model	81
4.3	Computational Homogenization	82
4.3.1	Separation of Scales	82
4.3.2	Conservation Laws at Micro and Macro-scales	84

4.3.3	Downscaling	85
4.3.4	Upscaling	87
4.4	Model Reduction Leading to an Enriched-Continuum	89
4.4.1	Finite Element Discretization	90
4.4.2	Microscopic Fields Decomposition	91
4.4.3	Steady-State Response	92
4.4.4	Transient Response	93
4.4.5	Linear Superposition	95
4.4.6	Evolution Equation	96
4.4.7	Reaction Fluxes and Forces	97
4.4.8	Macroscopic Quantities	99
4.4.9	Mode Selection Criteria	101
4.4.10	Macro-scale Enriched-Continuum	103
4.5	Numerical Examples	104
4.5.1	Problem Setting	104
4.5.2	Reduced Basis Identification	106
4.5.3	Micro-scale Simulations	109
4.5.4	Effective Macroscopic Quantities	110
4.5.5	Diffusion-Mechanics Coupling Effect	112
4.5.6	Size Effect	113
4.6	Conclusions	114
5	Data-driven Reduced Homogenization for Transient Diffusion	
	Problems with Emergent History Effects	117
5.1	Introduction	118
5.1.1	Outline	122
5.1.2	Symbols and Notation	122
5.2	Enriched Continuum for Diffusion Problems	123
5.3	Data-Driven Reduced Homogenization	125
5.3.1	Data-Set and Phase-Space	126
5.3.2	Distance Minimizing Data-Driven Problem	128
5.3.3	Solution Procedure	129
5.3.4	Algorithm	133
5.4	Numerical Examples	134
5.4.1	Problem Settings: Micro-scale and Macro-scale	135
5.4.2	Data-Generation from Micro-Scale Simulations	138
5.4.3	Homogenized and Microscopic Fields	142

5.4.4	Numerical Values of the Coefficients ${}^J\bar{\mathcal{C}}_m$	144
5.4.5	Noisy Data-Set	145
5.4.6	Different Data-Sets	146
5.4.7	Convergence Analysis	148
5.5	Future Perspectives	149
5.6	Conclusions	151
6	Conclusions and Recommendations	153
6.1	Summary and Results	154
6.2	Recommendations for Future Research	157
A	Appendix	161
A.1	Coupling Terms for Mass Diffusion Problem	161
A.2	Relative L_2 -Error for Different Coefficient Values Using Data-Set $D_{(R+S)}$	163
A.3	Relative L_2 -Error for Different Coefficient Values Using Data-Set with Noise $\tilde{D}_{(R+S)}$	164
	Bibliography	167
	Publications	181
	Acknowledgments	183
	Curriculum Vitae	185

Introduction

1.1 Background and Motivation

All physical phenomena in materials tend towards an equilibrium state. A non-equilibrium state can be caused by a difference in the concentration of a quantity across a region. For example, a gradient in temperature causes heat diffusion, and the spatial difference in the mass concentration of species causes mass diffusion. To achieve an equilibrium state, heat or mass irreversibly flows from a region of higher concentration to a lower one. During the diffusion process, the material also stores some part of the heat or species energy. The speed of diffusion of a quantity and the storage capacity are the physical properties of the material. If the net flow of a quantity across a region is constant, the diffusion is said to be in a steady-state, otherwise it is transient. Heterogeneous materials are formed when two or more materials with different physical properties are combined. The effective diffusion and effective storage capacity of a heterogeneous material are obviously different from those of its constituents. In this dissertation, the transient diffusion phenomenon in heterogeneous materials will be analyzed.

1.1.1 Examples

Transient diffusion in heterogeneous materials occurs in numerous natural phenomena and engineering applications. For example, in modern-day computers, the increasing demand for computational power requires to pack as many transistors in a small processor (CPU) packaging as possible. During operation of a CPU, a large amount of heat energy is generated which should be evacuated to keep the system running. It involves a complex thermal management system from the component level to the system level. Specifically tailored heterogeneous materials with overall excellent diffusivity and low storage capacity are required.

Figure 1.1(a) shows a heterogeneous material, made of 40% silicon-carbide (SiC) inclusions embedded in the copper (Cu) matrix, used for the CPU heat sink [1]. The percentage of SiC in Cu is modified according to the application and desired mechanical and thermal properties.



Figure 1.1: Engineering applications of transient diffusion phenomena using heterogeneous materials. (a) The heat sink material for the processor of a computer, the irregularly shaped silicon-carbide particles are embedded in a copper matrix [1, 2]. (b) The electrolyte-electrode system of a lithium-cobalt-oxide battery, the large circular active particles are embedded in the matrix [3, 4].

For mass diffusion problems, in poly-crystalline materials [5], the diffusion in grain boundaries happens faster than in the grains i.e. , the grain boundaries reach a steady-state while the grains remain in a transient-state. In the electrolyte-electrode system of a lithium-ion battery, shown in Figure 1.1(b) [4], the diffusion of lithium ions follows a similar trend. The lithium-ions diffuse orders of magnitude faster in the electrolyte, while coupled to the diffusion of lithium in the active particles.

1.1.2 Analysis Techniques

To analyze such engineering problems, the governing equation describing the transient balance law needs to be solved in each constituent. The energy balance equation allows to determine the heat diffusion, whereas the mass balance equation enables to determine the mass diffusion. Due to the complexity of the procedure, numerical methods have to be used for analyzing diffusion in heterogeneous materials with complicated morphologies and random distribution of the phases. One of the commonly used numerical techniques is the finite element method (FEM) [6]. It divides the region under consideration into sub-regions (elements) and solves

the transient balance laws in the discretized domain. To approximate the phenomena accurately enough, a large number of elements are typically required, which renders the method prohibitively time consuming for transient diffusion problems in heterogeneous materials.

To circumvent this pitfall, homogenization techniques [7–9] are used, which substitute the heterogeneous material domain by an equivalent homogeneous macro-scale domain and a small but representative heterogeneous micro-scale volume element. The homogeneous material response is obtained by averaging the properties of the constituents at the micro-scale. At the macro-scale, due to the adopted homogeneous (smooth) description, usually, only a few finite elements are required to accurately capture the diffusion response. If the diffusion through the micro-scale is instantaneous, i.e., the material properties and the boundary conditions are such that micro-scale reaches a steady-state instantly, then a full separation of scales holds. Otherwise, if the micro-scale constituents show transient behavior, the micro- and macro-scales can no longer be assumed to be completely separable. In this regime, the micro-scale transient diffusion equation needs to be solved at every macroscopic material point in time, which also becomes computationally expensive.

Devising an efficient numerical solution technique enables a faster decision making process during the design phase of a component. For example, if the simulations are not time-consuming, one can analyze a large number of parameters: shape, size, or percentage of inclusion material, to identify an application-specific heat sink material. Model reduction techniques can be used to reduce computational costs. There exists a large body of related literature, see [10] and the references therein, in the field of homogenization and model reduction. However, the literature is mostly limited to elasticity problems or diffusion problems with a full separation of scales. Hence, there is a clear need to develop numerical methods that efficiently solve diffusion problems in heterogeneous materials when the assumption of full separation of scales does not apply.

1.2 Objective and Research Questions

The main objective of this dissertation is to develop reduced-order numerical homogenization techniques for capturing the transient diffusion in heterogeneous materials with transient micro-scale phenomena. To this end, this thesis addresses the following research questions:

- How to properly define the (non) separation of scales regimes for the homogenization of transient diffusion problem? In which regime is model reduction applicable?
- What kind of homogenized macroscopic description is obtained when homogenization is performed by model reduction at the micro-scale? Is it as accurate as the expensive homogenization methods?
- Which spatial and temporal discretization methods can be used to solve the new, enriched, macroscopic description? Does it accurately capture the expensive FEM solution and how efficient is it compared to the expensive homogenization method?
- Is it possible to extend the newly developed reduced-order homogenization technique to coupled multi-physics problems?
- What are the options to relax the assumptions on linear material properties? Is there a different methodology available for the homogenization of transient diffusion problems with nonlinear material properties?

1.3 Outline of the thesis

This thesis addresses the above-mentioned research questions in detail and is arranged as follows: In **Chapter 2**, first, the separation of scales is defined in the context of heat diffusion problems in heterogeneous materials. Next, model reduction is performed for a specific separation of scales regime and linear material behavior. The homogenization is performed by the equivalence of power between the micro- and macro-scales. Numerical examples demonstrate the accuracy, computational efficiency and limitations of the proposed framework. The macroscopic enriched homogenized description is implemented using different spatial and temporal discretization schemes in **Chapter 3**. The solution procedures are discussed and numerical examples are solved for transient mass diffusion problems. The developed reduced-order homogenization method is demonstrated to capture the fully resolved FEM solution accurately with large computational time gains. **Chapter 4** extends the developed homogenization method to multi-physics problem. To this end, the model reduction is performed at the micro-scale to replace the coupled mass diffusion-mechanics problem with a reduced model. The

accuracy and computational efficiency are compared with expensive homogenization methods. **Chapter 5** presents the basis for extending the framework towards nonlinear material behavior by using a data-driven approach. It uses the developed reduced-order homogenization method to generate large data-sets in an efficient manner. The emergent macroscopic behavior is well captured by the data-driven approach and it presents a straightforward extension toward nonlinear regimes. Finally, in **Chapter 6**, conclusions based on the present work and recommendations for future research are provided.

Model Reduction in Computational Homogenization for Transient Heat Diffusion

Reproduced from:

A. Waseem, T. Heuzé, L. Stainier, M.G.D. Geers, and V.G. Kouznetsova

Computational Mechanics, (65), 249-266, 2020

<https://doi.org/10.1007/s00466-019-01767-3>

Abstract

This chapter presents a computationally efficient homogenization method for transient heat conduction problems. The notion of relaxed separation of scales is introduced and the homogenization framework is derived. Under the assumptions of linearity and relaxed separation of scales, the microscopic solution is decomposed into a steady-state and a transient part. Static condensation is performed to obtain the global basis for the steady-state response and an eigenvalue problem is solved to obtain a global basis for the transient response. The macroscopic quantities are then extracted by averaging and expressed in terms of the coefficients of the reduced basis. Proof-of-principle simulations are conducted with materials exhibiting high contrast material properties. The proposed homogenization method is compared with the conventional steady-state homogenization and transient computational homogenization methods. Within its applicability limits, the proposed homogenization method is able to accurately capture the microscopic thermal inertial effects with significant computational efficiency.

2.1 Introduction

With the advent of micro-fabrication technologies [11], the demand for miniature devices utilizing heterogeneous materials is steadily increasing. These devices encompass a variety of applications, ranging from electronic machinery [12, 13] to a special class of engineered materials called thermal meta-materials [14] which can be used to harvest thermal energy [15–17], manipulate heat flux [18, 19], as well as to perform thermal cloaking [20–22]. In order to design these components, it is important to correctly simulate and capture the underlying physics. Usually, an energy balance equation is solved to capture the heat transfer using a numerical method such as finite elements [6]. However, a high contrast in material properties, a complex topology and time varying thermal loads render the coefficients in the energy balance equation highly oscillatory, which requires an excessively a very fine discretization in both space and time. Consequently, simulations become computationally intractable.

The homogenization of heterogeneous medium [23–27] introduces the concept of an equivalent homogeneous macroscopic medium, representing an effective behavior of the microscopic medium with highly variable coefficients. Homogenization enables reduction of the computational cost, since an approximate response can

be captured with a coarser discretization. It is achieved by solving a two-scale problem in a coupled manner, which requires the solution of the energy balance equation at the micro-scale, usually using a representative volume element (RVE), associated to each macroscopic material point, followed by an averaging procedure to extract homogenized effective macroscopic quantities that are used in the energy balance equation at the macro-scale. To include transient terms in the energy balance equation, certain conditions on the material properties and loading should hold [7, 28–30], which requires a proper definition of the separation of scales. For heat conduction problems, separation of scales is defined based on the characteristic diffusion times t_k associated to each k -th material constituent and the characteristic loading time T .

For the homogenization of transient diffusion problems, the ratios between the different characteristic diffusion times and the loading time determines if the micro-scale and the macro-scale are separated or not. A full separation of scales indicates that the characteristic macroscopic loading time scale is much larger than all the microscopic characteristic diffusion times, independently of the ratios between the characteristic diffusion times of the different microstructural constituents. In such regimes, transient effects are negligible at the micro-scale and it is appropriate to use a steady-state energy balance equation at the micro-scale. This assumption has been widely used in the literature, see for example [28, 30–35]. The macroscopic thermal gradient is then the only conjugate quantity for the macroscopic heat flux and the macroscopic heat capacity can be calculated using the rule of mixtures. For a linear material model, in the regime of full separation of scales, the microscopic analysis and averaging performed only once to recover the (constant) effective macroscopic quantities.

However, when the microscopic characteristic diffusion times are of the same order of magnitude as the characteristic macroscopic loading time scale, the assumption of full separation of scales is no longer valid and the macro and micro-scale phenomena are coupled. In such regimes, significant transient effects are present at the micro-scale, in some or all microstructural constituents, which must be taken into account when homogenization is performed. If steady-state is assumed in such regimes, the microscopic transient effects, due to so-called *micro-scale thermal inertia* [9], will not be captured in the homogenized macroscopic description. Taking into account the transient micro-scale effects, the energy balance equation with the transient term should be solved at both scales. Homogenization in such transient regimes for thermal diffusional [8, 9, 36, 37] and mechanical vibration [38–41]

problems have already been developed. Since, the microscopic problem has to be solved at each macroscopic material point in time, the homogenization in transient regimes comes with a substantially higher computational cost. The present work aims at reducing the computational cost for homogenization in such transient regimes.

A reduced order model based on sub-structuring technique such as Craig-Bampton mode synthesis [42] was proposed for the homogenization of mechanical acoustic meta-materials [43]. It makes use of material linearity and the relaxed separation of scales. Substructuring of a mechanical system involves the division of the whole structure into smaller sub-structures with connected boundaries. Each substructure boundary is assumed to experience a rigid body motion and the dynamic effects only exist internally. If the boundary of the substructure is also dynamic then the substructuring provides a stiffer approximation [43]. For the homogenization of transient mechanical problems, the relaxed separation of scales implies that the matrix remains quasi-static under transient loading conditions and only the inclusions experience dynamic effects [38]. In the context of computational homogenization, when relaxed separation of scales is satisfied, each microscopic domain attached to a macroscopic material point is assumed to be a substructure attached to the macroscopic domain.

Similarly, in transient heat conduction problems, the relaxed separation of scales constitutes a thermal diffusion phenomenon in which the matrix remains in steady-state under transient thermal loads and only the inclusions exhibit transient heat diffusion. Assuming linear material properties and relaxed separation of scales, an additive decomposition is performed to compute the microscopic steady-state and transient response, separately. The reduced basis is obtained using a static condensation for the steady-state part and an eigenvalue problem is solved for the transient part. To benefit from the model reduction, the microscopic problem is projected on the reduced basis subspace, which yields an evolution equation for the micro-scale thermal inertia in terms of the coefficients of the reduced basis. These evolution equations for the amplitudes of the reduced variables, together with the macroscopic energy balance and the effective homogenized constitutive equations give rise to an enriched-continuum description at the macro-scale. This chapter deals with the model reduction at the micro-scale and compares the proposed formulation with a conventional transient computational homogenization scheme [8, 9]. The solution of the macro-scale enriched-continuum, emerging from the model reduction at the micro-scale, and the comparison to direct numerical

simulations are beyond the scope of this contribution and will be addressed in the future work.

A related work has been published recently [44], which focuses primarily on the error analysis for the model reduction in transient computational homogenization. However, in that work no discussion is made on the separation of scales and the limitations it imposes on reduced order computational homogenization. To the best of authors' knowledge the novel aspects of the current work, in the context of computational homogenization for transient heat conduction problems, are:

- introduction of the relaxed separation of scales.
- a model reduction technique for the micro-scale which leads to an enriched-continuum formulation at the macro-scale.

2.1.1 Outline

In this chapter, the homogenization framework is derived in section 2.2; the notion of the separation of scales is here defined, the generalized Hill-Mandel condition, upscaling, and downscaling relations are presented. In section 2.3, a computational method combined with model reduction is developed. Section 2.4 presents the proof-of-principle numerical examples. The chapter ends with concluding remarks and future perspectives.

2.1.2 Symbols and Notations

Macroscopic quantities are represented with a bar on top: for example a scalar, a vector and a second-order tensorial macroscopic quantity are written as \bar{a} , $\bar{\mathbf{a}}$, and $\bar{\mathbf{A}}$, respectively. Microscopic quantities are represented without a bar on top, a microscopic scalar, vector and second-order tensorial quantity are written as a , \mathbf{a} and \mathbf{A} . The same Cartesian basis is adopted at the macro and micro scales. The dot product between two vectors and between a second-order tensor and a vector is represented as $\mathbf{a} \cdot \mathbf{b} := a_i b_i$ and $\mathbf{A} \cdot \mathbf{a} := A_{ij} a_j \mathbf{e}_i$, respectively. A tensorial dyadic product is denoted with $\mathbf{a} \otimes \mathbf{b} := a_i b_j \mathbf{e}_i \otimes \mathbf{e}_j$ and $\mathbf{A} \otimes \mathbf{a} := A_{ij} a_k \mathbf{e}_i \otimes \mathbf{e}_j \otimes \mathbf{e}_k$. The gradient of a scalar and a vector is defined as $\nabla a := \partial a / \partial x_i \mathbf{e}_i$ and $\nabla \mathbf{a} := \partial a_i / \partial x_j \mathbf{e}_i \otimes \mathbf{e}_j$. Similarly, the divergence operates as $\nabla \cdot \mathbf{a} := \partial a_i / \partial x_i$ and $\nabla \cdot \mathbf{A} := \partial A_{ij} / \partial x_i \mathbf{e}_j$. For linear algebra operations, columns are represented with a tilde underneath a lowercase letter e.g., \underline{a} and matrices are represented with a bar underneath an uppercase letter e.g., $\underline{\mathbf{A}}$. A tensorial product between two column arrays of vectors

is defined as $\underline{\underline{\mathbf{a}}}^T \underline{\underline{\otimes}} \underline{\underline{\mathbf{b}}}$, where

$$\underline{\underline{\otimes}} := \begin{bmatrix} \otimes & 0 & \dots & 0 \\ 0 & \otimes & & \vdots \\ \vdots & & \ddots & \\ 0 & 0 & \dots & \otimes \end{bmatrix}. \quad (2.1)$$

The microscopic domain and its boundary are represented by Ω_{\square} and $\partial\Omega_{\square}$, respectively. The volume average of a microscopic quantity \bullet is defined as

$$\langle \bullet \rangle := \frac{1}{V} \int_{\Omega_{\square}} \bullet \, d\Omega_{\square}, \quad (2.2)$$

where, $V = \int_{\Omega_{\square}} d\Omega_{\square}$ is the volume of the microscopic domain Ω_{\square} . Acronyms RTH, CTH and SSH are used for *reduced transient computational homogenization* (present contribution), *conventional transient homogenization* (i.e., without model reduction) and *steady-state computational homogenization*, respectively. The material with the lowest characteristic diffusion time is called “*fast*” and the material with large characteristic diffusion time is called “*slow*”.

2.2 Homogenization Framework

In this section, the relaxed separation of scales is defined for heat conduction problems. The energy balance equations at the micro and macro-scales are presented and finally, the downscaling and upscaling relations are derived.

2.2.1 Separation of Scales

The separation of scales in homogenization of transient diffusion problems is defined in terms of the characteristic diffusion times that are linked to the loading conditions, material properties and characteristic length scales. In this work, a two-phase periodic medium is considered in which the connected phase is the matrix and the embedded particulates are the inclusions. The characteristic diffusion times for the matrix t_m and inclusions t_i are defined as

$$t_m := \frac{\ell_m^2}{\mathcal{D}_m}, \quad \text{and} \quad t_i := \frac{d^2}{\mathcal{D}_i}, \quad (2.3)$$

where ℓ_m and d are the characteristic lengths, e.g., the spacing between the inclusions and the inclusion diameter, respectively, and \mathcal{D}_m and \mathcal{D}_i are the thermal diffusivity coefficients of the matrix and inclusions, respectively. The characteristic loading time T is the inverse of the ratio of the rate of change of the macroscopic temperature field $\dot{\bar{\theta}}$ with respect to the macroscopic temperature $\bar{\theta}$

$$T \sim \frac{1}{\omega} := \left(\frac{\dot{\bar{\theta}}}{\bar{\theta}} \right)^{-1}, \quad (2.4)$$

where ω is the (angular) loading frequency. Different relations between t_m , t_i and T define different separation of scales regimes. For the development of the reduced computational homogenization and comparison to conventional methods a few separation of scales regimes are defined here.

Full Separation of Scales: In a full separation of scales regime the characteristic diffusion times at the micro-scale are much smaller than the characteristic loading time T , i.e., the material constituents reach steady-state instantly

$$T \gg (t_m \sim t_i), \text{ or } T \gg (t_m < t_i), \text{ or } T \gg (t_m > t_i). \quad (2.5)$$

The ratio between the characteristic diffusion times of different constituents does not matter in this case. Under these conditions, the classical steady-state homogenization is sufficient to capture the heat diffusion phenomena in a heterogeneous medium. For example, the homogenization procedure adopted in [32] assumes a steady-state micro-scale model for the simulation of refractory bricks used in a furnace lining. The macroscopic heat flux is obtained through the computational homogenization and the heat storage capacity is obtained by using the rule of mixtures.

Non-separating Scales: In these regimes, the microscopic diffusion times of the matrix, the inclusions or both are of the same order of magnitude as the macroscopic loading time. As a consequence, transient phenomena are active at the micro-scale. Some of these regimes can be represented as

$$T \sim t_m \sim t_i, \quad (2.6a)$$

$$(T \sim t_m) > t_i, \quad (2.6b)$$

$$(T \sim t_i) > t_m. \quad (2.6c)$$

In (2.6)(a) both the matrix and the inclusions are transient, in (2.6)(b) the matrix

is more transient than the inclusion and (2.6)(c) shows the regime in which the inclusions experience more transient effects than the matrix. The energy balance equation with the transient terms has to be used at the micro-scale to capture thermal inertia accurately. For example in [9], a sintering problem is solved using transient computational homogenization, the material properties and the loading conditions were such that they are adequately represented by the separation of scales regime of equation (2.6)(c). Therefore, both the macroscopic heat flux and the rate of change of the macroscopic internal energy are calculated by computational homogenization; if the rule of mixture would have been used instead, it would entail significant errors.

Relaxed Separation of Scales: This intermediate regime is characterized by specific material properties: a fast matrix, i.e., it attains the steady state almost instantaneously, and slow inclusions. It can be defined as

$$(T \sim t_i) \gg t_m. \quad (2.7)$$

This is a limiting case of the regime given by equation (2.6)(c) and represents no or negligible transient effects in the matrix. Heterogeneous materials operating in this regime are characterized by a high conductivity and low heat storage capacity in the matrix and low conductivity and high heat storage capacity in the inclusions. Since the evolution of the temperature field in the matrix is different from that in the inclusions, the microscopic temperature field can be decomposed into steady-state and transient parts. To capture the micro inertia effects, the transient balance of energy has to be solved at the micro-scale and both, the macroscopic heat flux and rate of change of macroscopic internal energy, must be computed/upscaled using computational homogenization.

2.2.2 Energy Balance Equation at the Macro- and Micro-scales

To model the transient heat conduction at the macro-scale, the energy balance equation with the transient term is used

$$\overline{\nabla} \cdot \bar{\mathbf{q}} + \dot{\bar{\epsilon}} = 0, \quad (2.8)$$

where $\bar{\mathbf{q}}$ and $\dot{\bar{\epsilon}}$ are the macroscopic heat flux and the rate of change of macroscopic internal energy. The constitutive forms for $\bar{\mathbf{q}}$ and $\dot{\bar{\epsilon}}$ are yet unknown, and in the

computational homogenization are obtained through an upscaling procedure. The macro-scale problem is complemented by boundary and initial conditions as given by the particular problem at hand. To capture the thermal inertia effects, the transient energy balance equation is considered at the micro-scale as well

$$\nabla \cdot \mathbf{q} + \dot{\epsilon} = 0, \quad (2.9)$$

where \mathbf{q} and $\dot{\epsilon}$ are the microscopic heat flux and the rate of change of the microscopic internal energy. The constitutive relations, for each micro-scale constituent, are assumed to be known and may in general be nonlinear. In the present work only linear micro-constituent materials will be considered to facilitate the application of the model reduction. For the microscopic heat flux, Fourier's law $\mathbf{q} = -\lambda \nabla \theta$ is used and for the internal energy ϵ the constitutive relation $\epsilon = \rho c \theta$ applied. In this work, an isotropic material behavior is assumed for simplicity, even though the methodology would be directly applicable to general anisotropic materials as well. To ensure consistent scale transition in computational homogenization, specific types of boundary conditions are required at the micro-scale, which will be defined through the downscaling procedure.

2.2.3 Downscaling

The microscopic temperature field is defined as a first order Taylor's approximation around a macroscopic point $\bar{\mathbf{x}}$

$$\theta(\bar{\mathbf{x}}, \mathbf{x}, t) := \bar{\theta}(\bar{\mathbf{x}}, t) + \bar{\nabla} \bar{\theta}(\bar{\mathbf{x}}, t) \cdot (\mathbf{x} - \bar{\mathbf{x}}) + \tilde{\theta}(\bar{\mathbf{x}}, \mathbf{x}, t), \quad (2.10)$$

where \mathbf{x} denotes the position vector at the micro-scale and $\tilde{\theta}$ represents the higher order term in the expansion which are the fluctuations in the temperature field at the micro-scale. These fluctuations arise due to the difference in material properties between the constituents subjected to transient loading conditions. The micro-scale is positioned relative to the macroscopic point such that $\langle \mathbf{x} - \bar{\mathbf{x}} \rangle = \mathbf{0}$.

Downscaling is a procedure to transfer information from the macro-scale to the micro-scale. In the first-order computational homogenization, both the macroscopic temperature and its gradient are transferred to the micro-scale and assumed to be constant over the considered microstructure domain. The downscaling relations in transient computational homogenization provide two constraints to be satisfied:

1. The average of the microscopic temperature field should be equal to the macroscopic temperature field at the macroscopic point $\bar{\mathbf{x}}$

$$\bar{\theta}(\bar{\mathbf{x}}, t) = \langle \theta(\bar{\mathbf{x}}, \mathbf{x}, t) \rangle, \quad (2.11)$$

which by using equation (2.10) and $\langle \mathbf{x} - \bar{\mathbf{x}} \rangle = 0$, requires the average of the fluctuation field at the micro-scale vanish

$$\langle \tilde{\theta} \rangle = 0 \quad (2.12)$$

2. The average of the microscopic temperature gradient field should be equal to the macroscopic temperature field

$$\overline{\nabla \theta}(\bar{\mathbf{x}}, t) = \langle \nabla \theta(\bar{\mathbf{x}}, \mathbf{x}, t) \rangle. \quad (2.13)$$

It is obtained by taking the gradient of the microscopic temperature field, in equation (2.10), and averaging it over the microscopic domain

$$\langle \nabla \theta \rangle = \overline{\nabla \theta} + \langle \nabla \tilde{\theta} \rangle, \quad (2.14)$$

where the identity $\nabla(\mathbf{x} - \bar{\mathbf{x}}) = \mathbf{I}$ is used. To fulfill the condition in equation (2.14), the average of the gradient of the fluctuation field has to be zero $\langle \nabla \tilde{\theta} \rangle = \mathbf{0}$, which after applying Gauss's divergence theorem, is written as

$$\int_{\partial\Omega_{\square}} \tilde{\theta} \mathbf{n} \, da = \mathbf{0}. \quad (2.15)$$

where \mathbf{n} is the unit-normal outward vector on the microscopic boundary $\partial\Omega_{\square}$ with infinitesimal surface area da .

Constraint (2.12) enforces the macroscopic temperature $\bar{\theta}(\bar{\mathbf{x}}, t)$ to be the reference temperature in the microscopic domain and constraint (2.15) requires specific types of boundary conditions to be used at the micro-scale. Typical choices for these boundary conditions adopted in the literature are (i) zero fluctuation boundary conditions or (ii) periodic fluctuation boundary conditions. Now that, the microscopic temperature field and the downscaling relations are defined, the upscaling relations are established next.

2.2.4 Upscaling

Upscaling is performed to transfer information from the micro-scale to the macro-scale through an averaging procedure. For transient computational homogenization, a generalized Hill-Mandel condition is used [8, 9], which states that the volume average of the virtual power at the micro-scale is equal to the virtual power (per unit of volume) at the associated macroscopic point $\bar{\mathbf{x}}$

$$-\bar{\nabla}\delta\bar{\theta} \cdot \bar{\mathbf{q}} + \delta\bar{\theta}\dot{\epsilon} = \left\langle -\nabla\delta\theta \cdot \mathbf{q} + \delta\theta\dot{\epsilon} \right\rangle. \quad (2.16)$$

Substitution of the perturbation of the microscopic temperature field (2.10) and its gradient in the right hand side of equation (2.16) provides

$$-\bar{\nabla}\delta\bar{\theta} \cdot \bar{\mathbf{q}} + \delta\bar{\theta}\dot{\epsilon} = \left\langle -\left(\bar{\nabla}\delta\bar{\theta} + \nabla\delta\tilde{\theta}\right) \cdot \mathbf{q} + \left(\delta\bar{\theta} + \bar{\nabla}\delta\bar{\theta} \cdot (\mathbf{x} - \bar{\mathbf{x}}) + \delta\tilde{\theta}\right) \dot{\epsilon} \right\rangle. \quad (2.17)$$

Expanding and rearranging the above expression for $\delta\bar{\theta}$ and $\delta\tilde{\theta}$ gives

$$-\bar{\nabla}\delta\bar{\theta} \cdot \bar{\mathbf{q}} - \delta\bar{\theta}\dot{\epsilon} = \left\langle \left[-\bar{\nabla}\delta\bar{\theta} \cdot (\mathbf{q} + (\mathbf{x} - \bar{\mathbf{x}})\dot{\epsilon}) + \delta\bar{\theta}\dot{\epsilon}\right] + \left[-\nabla\delta\tilde{\theta} \cdot \mathbf{q} + \delta\tilde{\theta}\dot{\epsilon}\right] \right\rangle. \quad (2.18)$$

The last term in equation (2.18) is the weak form of the microscopic balance of energy with admissible temperature fluctuation field $\delta\tilde{\theta}$, which by using integration by parts and the divergence theorem can be written as

$$\left\langle -\nabla\delta\tilde{\theta} \cdot \mathbf{q} + \delta\tilde{\theta}\dot{\epsilon} \right\rangle = \left\langle \delta\tilde{\theta} (\nabla \cdot \mathbf{q} + \dot{\epsilon}) \right\rangle - \int_{\partial\Omega_{\square}} \delta\tilde{\theta} \mathbf{q} \cdot \mathbf{n} \, da. \quad (2.19)$$

The first term in the right hand side of the above equation is the balance of energy at the micro-scale (2.9) which is satisfied by the micro-scale solution and therefore equals zero. The second term is also zero when appropriate boundary conditions are used, as discussed at the end of the previous section, for more details see [32]. Finally, equation (2.18) reduces to

$$-\bar{\nabla}\delta\bar{\theta} \cdot \bar{\mathbf{q}} + \delta\bar{\theta}\dot{\epsilon} = -\bar{\nabla}\delta\bar{\theta} \cdot \left\langle \mathbf{q} - (\mathbf{x} - \bar{\mathbf{x}})\dot{\epsilon} \right\rangle + \delta\bar{\theta} \left\langle \dot{\epsilon} \right\rangle, \quad (2.20)$$

from where the macroscopic heat flux is recognized as

$$\bar{\mathbf{q}} = \left\langle \mathbf{q} - (\mathbf{x} - \bar{\mathbf{x}})\dot{\epsilon} \right\rangle, \quad (2.21)$$

and the rate of change of the macroscopic internal energy as

$$\dot{\bar{\epsilon}} = \langle \dot{\epsilon} \rangle. \quad (2.22)$$

The second term in equation (2.21) is the moment of the rate of change of the microscopic internal energy, which is responsible for transferring the micro-scale thermal inertia to the macro-scale. It also carries the information about the size of the micro-scale, which makes transient computational homogenization sensitive to the micro-scale size. In the limit, when the RVE size is vanishingly small, the transient effects disappear and a classical SSH result $\bar{\mathbf{q}} = \langle \mathbf{q} \rangle$ is obtained.

Substituting the definition of the microscopic temperature field (2.10) into the constitutive equation (2.22) reveals that it is also a function of the macroscopic temperature gradient i.e., $\bar{\epsilon} = \bar{\epsilon}(\bar{\theta}, \bar{\nabla}\bar{\theta})$. This non-local dependence is not present in classical irreversible thermodynamics and requires a non-local thermodynamic description at the macro-scale. In the gradient enriched thermodynamics, an additional dissipation term is added in the entropy inequality at the macro-scale, upon averaging the (classical) dissipation at the micro-scale and applying proper boundary conditions, which can be recognized as the second term in the expression of macroscopic flux in equation (2.21). For a more detailed analysis of the emerging macroscopic thermodynamics in computational homogenization of transient dissipative phenomena the reader is directed to the recent articles on the topic [45, 46]. Also in [47], a thermodynamical model including temperature gradients is developed and rationalized using homogenization of heterogeneous media. However a steady-state assumption was made in that case. For a general analysis of extended thermodynamic theories the reader is directed to the review article [48].

Converting the volume integrals of equation (2.21) and (2.22) into boundary integrals using the divergence theorem and the microscopic energy balance (2.9), allows to write the macroscopic heat flux as

$$\bar{\mathbf{q}} = \frac{1}{V} \int_{\partial\Omega_{\square}} q_n(\mathbf{x} - \bar{\mathbf{x}}) da, \quad (2.23)$$

and the rate of change of macroscopic internal energy as

$$\dot{\bar{\epsilon}} = -\frac{1}{V} \int_{\partial\Omega_{\square}} q_n da, \quad (2.24)$$

where $q_n = \mathbf{q} \cdot \mathbf{n}$ is the normal outward heat flux at the boundary of the microscopic domain. Once q_n is known, the macroscopic quantities are obtained. Next, the

solution procedure will be discussed, along with the model reduction to obtain q_n .

2.3 Model Order Reduction

In this section, first the balance of energy at the micro-scale, equation (2.9), is written in a discrete form using the finite element formulation. Next, the reduced basis is obtained for the steady-state and transient parts of the microscopic response. The macroscopic constitutive equations and the microscopic balance of energy are then written in terms of the coefficients of the reduced variables leading to a thermal enriched-continuum resulting from the model reduction. Finally, the guidelines to identify the transient reduced basis are discussed.

2.3.1 Micro-scale Discrete Problem

The semi-discrete form of the balance of energy at the micro-scale reads

$$\underline{K}\underline{\theta} + \underline{C}\dot{\underline{\theta}} = -q_n, \quad (2.25)$$

where \underline{K} and \underline{C} are thermal conductivity and capacity matrices, respectively, $\underline{\theta}$ is the column of nodal temperature values and $-q_n$ is the incoming heat flux. The constraints following from equations (2.12) and (2.15) are applied using the master-slave approach [49]. The periodic boundary conditions are applied by setting the fluctuation fields on opposite sides of the microscopic domain to be equal i.e., $\tilde{\theta}^R = \tilde{\theta}^L$ and $\tilde{\theta}^T = \tilde{\theta}^B$, where R denotes right, L – left, T – top and B – bottom boundary of the unit cell as shown in Figure 2.1. Inserting $\tilde{\theta}^R = \tilde{\theta}^L$ and $\tilde{\theta}^T = \tilde{\theta}^B$ in equation (2.10) provides the constraint equations

$$\begin{aligned} \theta^L - \theta^R &= \overline{\nabla\bar{\theta}} \cdot (\mathbf{x}^L - \mathbf{x}^R), \\ \theta^B - \theta^T &= \overline{\nabla\bar{\theta}} \cdot (\mathbf{x}^B - \mathbf{x}^T). \end{aligned} \quad (2.26)$$

For temperature independent material properties, constraint (2.12) can be applied by prescribing the microscopic temperature $\theta(\bar{\mathbf{x}}, \mathbf{x}, t)$ at a point in the microscopic domain to be equal to the macroscopic temperature $\bar{\theta}(\bar{\mathbf{x}}, t)$. It is allowed to fix one point to apply the constraint (2.12) under the following assumptions:

- the material properties are linear;
- the relaxed separation of scales hold true i.e., classical homogenization, $\bar{\mathbf{q}} = \langle \mathbf{q} \rangle$ and $\dot{\bar{\epsilon}} = \langle \rho c \rangle \dot{\bar{\theta}}$, is sufficient to represent the matrix behavior;

- a symmetric shaped RVE, as shown in Figure 2.1, is used and it is attached to the macroscopic point at the center i.e., $\bar{\mathbf{x}} = \mathbf{x}^c$, where \mathbf{x}^c is the center coordinates of the RVE, providing $\langle \mathbf{x} - \bar{\mathbf{x}} \rangle = \mathbf{0}$;
- the prescribed point should be in the matrix.

However, if there are transient effects in the matrix then this constraint may not be applied in this manner. In that case, (2.12) can be enforced through Lagrange multipliers, as implemented in [132, 133] for elastodynamics problem. Here, this point is chosen to be node 1 at position \mathbf{x}^1 . Then by applying (2.26) to the corner nodes 1,2,3 and 4, the temperature at these nodes is fully prescribed and given by

$$\underline{\theta}^p = \underline{I}^p \bar{\theta} + \bar{\nabla} \bar{\theta} \cdot (\underline{\mathbf{x}}^p - \underline{I}^p \mathbf{x}^1), \quad (2.27)$$

where $p = \{1, 2, 3, 4\}$ and \underline{I}^p is a column of ones with dimension $(p \times 1)$. The set of the corner nodes thus will be called ‘‘prescribed’’. The constraint equations (2.26) can then also be written in a discrete setting in terms of the prescribed corner nodes as

$$\begin{aligned} \underline{\theta}^R &= \underline{\theta}^L + \underline{I} \theta^2 - \underline{I} \theta^1, \\ \underline{\theta}^T &= \underline{\theta}^B + \underline{I} \theta^4 - \underline{I} \theta^1, \end{aligned} \quad (2.28)$$

where \underline{I} is a column of ones. In equation (2.28), the temperature fields on the left hand side are dependent on the temperature fields on the right hand side. To apply these boundary conditions, the microscopic degrees of freedom (DOF) are first split into tied (dependent) ‘ t ’ and retained (independent) ‘ r ’ DOFs. The retained DOFs are then further subdivided into prescribed ‘ p ’ (nodes 1,2,3,4) and free ‘ f ’ parts as shown in Figure 2.1. Following the master-slave implementation procedure, a matrix of tying relations \underline{M} is created from the constraint equations (2.28), which eliminates the tied DOFs by mapping the complete set of DOFs to the retained DOFs only

$$\underline{\theta} = \begin{bmatrix} \underline{\theta}^t \\ \underline{\theta}^r \end{bmatrix} = \underline{M} \underline{\theta}^r, \quad (2.29)$$

where $\underline{\theta}^t$ are the temperature values of the tied DOFs and $\underline{\theta}^r$ are the temperature values of the retained DOFs. The constraints are applied by substituting the expression of $\underline{\theta}$ from (2.29) into (2.25), and pre-multiplying it with \underline{M}^T , giving

$$\underline{M}^T \underline{K} \underline{M} \underline{\theta}^r + \underline{M}^T \underline{C} \underline{M} \dot{\underline{\theta}}^r = -\underline{M}^T \underline{q}_n, \quad (2.30)$$

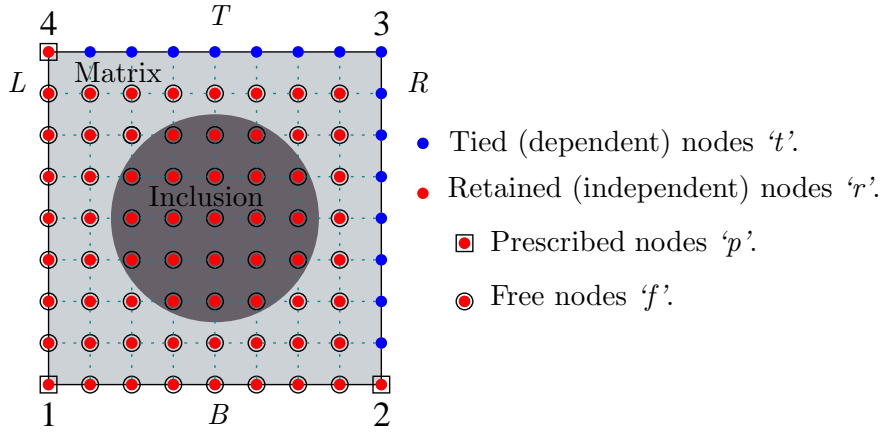


Figure 2.1: Discretized microscopic domain. The total set of DOFs are first divided into *tied* (dependent) and *retained* (independent) parts and then the retained DOFs are further subdivided into the *prescribed* and *free* parts. (This figure is for illustrative purpose only; calculations were performed on a material and geometry conforming mesh).

which reduces the dimensionality of the problem to the retained DOFs only

$$\underline{\underline{K}}^* \underline{\underline{\theta}}^r + \underline{\underline{C}}^* \dot{\underline{\underline{\theta}}}^r = -\underline{\underline{q}}_n^r, \quad (2.31)$$

where $\underline{\underline{K}}^*$, and $\underline{\underline{C}}^*$ are the reduced thermal conductivity and capacity matrices, respectively, and $\underline{\underline{q}}_n^r$ is the column of the incoming reaction heat fluxes at the retained DOFs. In the subsequent text the superscript '*r*' will be dropped from $\underline{\underline{\theta}}^r$ and $\underline{\underline{q}}_n^r$ for brevity.

2.3.2 Micro-scale Model Reduction

To calculate the macroscopic quantities $\bar{\mathbf{q}}$ and $\dot{\bar{\epsilon}}$, the expressions given in (2.23) and (2.24) are used. These expressions contain the incoming heat flux q_n . In a discrete setting, the incoming (reaction) heat flux at the prescribed nodes can be post-processed once the solution of the micro-scale problem is available. After further partitioning the system of equations (2.31) into the prescribed and free parts, it reads as

$$\begin{bmatrix} \underline{\underline{K}}^{pp*} & \underline{\underline{K}}^{pf*} \\ \underline{\underline{K}}^{fp*} & \underline{\underline{K}}^{ff*} \end{bmatrix} \begin{bmatrix} \underline{\underline{\theta}}^p \\ \underline{\underline{\theta}}^f \end{bmatrix} + \begin{bmatrix} \underline{\underline{C}}^{pp*} & \underline{\underline{C}}^{pf*} \\ \underline{\underline{C}}^{fp*} & \underline{\underline{C}}^{ff*} \end{bmatrix} \begin{bmatrix} \dot{\underline{\underline{\theta}}}^p \\ \dot{\underline{\underline{\theta}}}^f \end{bmatrix} = \begin{bmatrix} -\underline{\underline{q}}_n^p \\ \underline{\underline{q}}_n^f \end{bmatrix}. \quad (2.32)$$

Solving this system for each macroscopic point $\bar{\mathbf{x}}$ in time is a computationally expensive task, especially for a large macroscopic problem with a complex microstructural topology that usually requires a fine discretization in space and time. Therefore, a reduced model is sought which approximates the solution with a fewer DOFs only. The incoming heat flux q_n^p can then be written in terms of the coefficients of the reduced basis, making the homogenization process computationally efficient. To perform the model reduction at the micro-scale, the microscopic temperature field θ is decomposed into its steady-state θ_{ss} and transient θ_{tr} parts

$$\theta = \theta_{ss} + \theta_{tr}. \quad (2.33)$$

This additive split is always warranted for linear problems in the relaxed separation of scales regime, where the transient temperature field in the inclusions evolves independently of the temperature field in the matrix. This decomposition is also advantageous because the reduced global bases for the steady-state and transient parts are calculated separately, and later a linear superposition is performed to reconstruct the total microscopic temperature field.

2.3.2.1 Steady-State Contribution

The steady-state part of the micro-scale solution θ_{ss} represents very slow time variations, where the micro-scale still follows the macro-scale instantaneously. In the physical sense, this is a micro-scale that reaches steady-state very quickly. To obtain the steady-state response, the discrete system (2.32) is written in terms of θ_{ss} only

$$\underline{\underline{K}}^{pp} \underline{\underline{\theta}}^p + \underline{\underline{K}}^{pf} \underline{\underline{\theta}}_{ss}^f + \underline{\underline{C}}^{pp} \dot{\underline{\underline{\theta}}}^p + \underline{\underline{C}}^{pf} \dot{\underline{\underline{\theta}}}_{ss}^f = -\underline{\underline{q}}_{ss}^p, \quad (2.34)$$

$$\underline{\underline{K}}^{fp} \underline{\underline{\theta}}^p + \underline{\underline{K}}^{ff} \underline{\underline{\theta}}_{ss}^f + \underline{\underline{C}}^{fp} \dot{\underline{\underline{\theta}}}^p + \underline{\underline{C}}^{ff} \dot{\underline{\underline{\theta}}}_{ss}^f = \underline{\underline{0}}^f. \quad (2.35)$$

Equation (2.34) provides the steady-state reaction fluxes q_{ss}^p at the prescribed DOFs and (2.35) is the evolution equation for the steady-state part of the microscopic temperature field at the free DOFs. Imposing the steady-state assumption on (2.35) requires to fulfill the following constraint

$$\underline{\underline{C}}^{fp} \dot{\underline{\underline{\theta}}}^p + \underline{\underline{C}}^{ff} \dot{\underline{\underline{\theta}}}_{ss}^f = \underline{\underline{0}}^f, \quad (2.36)$$

which provides the steady-state response θ_{ss} in terms of the prescribed temperature field $\underline{\theta}^p$ as

$$\begin{bmatrix} \underline{\theta}^p \\ \underline{\theta}_{ss}^f \end{bmatrix} = \begin{bmatrix} \underline{I}^{pp} \\ \underline{S} \end{bmatrix} \underline{\theta}^p, \quad (2.37)$$

where $\underline{S} = -(\underline{K}^{*ff})^{-1} \underline{K}^{*fp}$ and \underline{I}^{pp} is the unit diagonal matrix with dimension $(p \times p)$. The columns of \underline{S} can be interpreted as the steady-state reduced basis for each θ in $\underline{\theta}^p$. To obtain the steady-state reaction fluxes in terms of the temperature at the prescribed DOFs, the constraint (2.36) is projected on the prescribed DOFs by premultiplying it with \underline{S}^T and the taking transpose of the expression i.e. ,

$$\underline{C}^{*pf} \underline{S} \dot{\underline{\theta}}^p + \underline{S}^T \underline{C}^{*ff} \underline{S} \dot{\underline{\theta}}^p = \underline{Q}^p, \quad (2.38)$$

and then added to equation (2.34) which yields

$$\underline{q}_{ss}^p = -\underline{K}_{ss} \underline{\theta}^p - \underline{C}_{ss} \dot{\underline{\theta}}^p, \quad (2.39)$$

where the steady-state conductivity \underline{K}_{ss} and capacity \underline{C}_{ss} matrices are defined as

$$\begin{aligned} \underline{K}_{ss} &:= \underline{K}^{*pp} + \underline{K}^{*pf} \underline{S}, \\ \underline{C}_{ss} &:= \underline{C}^{*pp} + 2\underline{C}^{*pf} \underline{S} + \underline{S}^T \underline{C}^{*ff} \underline{S}. \end{aligned} \quad (2.40)$$

The steady-state contribution does not capture the thermal inertia and micro-scale size effects. The transient contribution will therefore be added next.

2.3.2.2 Transient Contribution

The transient part of the microscopic solution is described through the reduced basis vector $\underline{\Phi}^{(k)}$ and the corresponding reduced degrees of freedom $\eta^{(k)}$, where $k = 1, 2, \dots, \mathcal{N}_q$ and $\mathcal{N}_q \ll \mathcal{N}$, with \mathcal{N}_q as the number of the reduced degrees of freedom and \mathcal{N} the total number of the degrees of freedom of the original problem. The transient part of the microscopic solution can then be written as

$$\begin{bmatrix} \underline{\theta}^p \\ \underline{\theta}_{tr}^f \end{bmatrix} = \begin{bmatrix} \underline{0}^{pq} \\ \underline{\Phi}^* \end{bmatrix} \underline{\eta}, \quad (2.41)$$

where $\underline{0}^{pq}$ is a $(\mathcal{N}_p \times \mathcal{N}_q)$ matrix of zeros, $\underline{\Phi}^*$ is the matrix combining all the reduced basis vectors and $\underline{\eta}$ is the column of the coefficients of the reduced basis. The

energy balance equation (2.9) is a parabolic partial differential equation, which has a natural solution that decays exponentially in time i.e., $\underline{\varrho} = \underline{\Phi}^{(k)} \exp[-\alpha^{(k)}t]$, substituting this expression in the free part of (2.32)

$$\underline{K}^{*ff} \underline{\varrho}^f + \underline{C}^{*ff} \dot{\underline{\varrho}}^f = \underline{Q}^f, \quad (2.42)$$

provides

$$(\underline{K}^{*ff} - \alpha^{(k)} \underline{C}^{*ff}) \underline{\Phi}^{(k)} = \underline{Q}. \quad (2.43)$$

Since the transient heat problem at the micro-scale is linear, equation (2.43) can be solved as a classical eigenvalue problem leading to the eigenvalues $\alpha^{(k)}$ and eigenvectors $\underline{\Phi}^{(k)}$. It is a standard procedure used in model reduction and stability analyses of time integration schemes for transient diffusion problems see [6, 50, 51]. Provided that \underline{K}^{*ff} is semi-positive definite and \underline{C}^{*ff} is positive definite, the eigenvectors $\underline{\Phi}^{(k)}$ are orthogonal and the corresponding eigenvalues $\alpha^{(k)}$ are real and can be arranged in a diagonal matrix $\underline{\alpha}$

$$\underline{\alpha} = \begin{bmatrix} \alpha^{(1)} & 0 & 0 \\ 0 & \ddots & 0 \\ 0 & 0 & \alpha^{(N_q)} \end{bmatrix}. \quad (2.44)$$

When the eigenvalue problem (2.43) is solved, the number of eigenvectors is the same as the number of DOFs in the original discrete system of equations and at this point no reduction has been performed. The reduction from the full transient basis $\underline{\Phi}$ to the reduced basis $\underline{\Phi}^*$ is performed by selecting a limited set of eigenvectors, based on criteria proposed at the end of this section. In heat conduction problems, the eigenvectors are the temperature distributions inside the domain and the corresponding eigenvalues are the inverse of decay/rise times i.e., $\tau^{(k)} = 2\pi/\alpha^{(k)}$ [50]. Normalizing the eigenvectors $\underline{\Phi}^{(k)}$ with respect to the capacity matrix,

$$(\underline{\Phi}^{(k)})^T \underline{C}^{*ff} \underline{\Phi}^{(k)} = 1, \quad (2.45)$$

yields the eigenvalues as

$$(\underline{\Phi}^{(k)})^T \underline{K}^{*ff} \underline{\Phi}^{(k)} = \alpha^{(k)}. \quad (2.46)$$

Now that the the transient reduced basis $\underline{\Phi}^*$ is identified through the eigenproblem analysis, it can be used for model reduction of the free part of the discrete system

of equation (2.32). Substituting equation (2.41) in (2.32) yields

$$\underline{\underline{K}}^{*ff} \underline{\underline{\Phi}}^* \underline{\underline{\eta}} + \underline{\underline{C}}^{*ff} \underline{\underline{\Phi}}^* \underline{\underline{\dot{\eta}}} = \underline{\underline{Q}}^f, \quad (2.47)$$

providing a set of decoupled ordinary differential equations (ODE). Using the normalization conditions (2.45) and (2.46) equation (2.47) takes the form

$$\underline{\underline{\alpha}} \underline{\underline{\eta}} + \underline{\underline{\dot{\eta}}} = \underline{\underline{0}}. \quad (2.48)$$

Equation (2.48) represents the transient evolution of the microscopic solution in terms of the variables $\underline{\underline{\eta}}$, which in this form it is not influenced by the macro-scale excitation. Next, the micro-scale steady-state and transient responses will be coupled through linear superposition.

2.3.2.3 Linear Superposition

The microscopic steady-state and transient temperature fields, given by equations (2.37) and (2.41) are superposed to obtain the total response

$$\begin{bmatrix} \underline{\underline{\theta}}^p \\ \underline{\underline{\theta}}^f \end{bmatrix} = \begin{bmatrix} \underline{\underline{\theta}}^p \\ \underline{\underline{\theta}}_{ss}^f + \underline{\underline{\theta}}_{tr}^f \end{bmatrix} = \begin{bmatrix} \underline{\underline{I}}^{pp} & \underline{\underline{0}}^{pq} \\ \underline{\underline{S}} & \underline{\underline{\Phi}}^* \end{bmatrix} \begin{bmatrix} \underline{\underline{\theta}}^p \\ \underline{\underline{\eta}} \end{bmatrix}. \quad (2.49)$$

The right-hand side of this expression resembles the Craig-Bampton reduction matrix as originally proposed in [42] in the context of structural dynamics. Substituting (2.49) into (2.32) yields a set of coupled equations

$$\underline{\underline{K}}^{*pf} \underline{\underline{\Phi}}^* \underline{\underline{\eta}} + \underline{\underline{C}}^{*pf} \underline{\underline{\Phi}}^* \underline{\underline{\dot{\eta}}} + \underline{\underline{K}}^{*pp} \underline{\underline{\theta}}^p + \underline{\underline{K}}^{*pf} \underline{\underline{S}} \underline{\underline{\theta}}^p + \underline{\underline{C}}^{*pp} \underline{\underline{\dot{\theta}}}^p + \underline{\underline{C}}^{*pf} \underline{\underline{S}} \underline{\underline{\dot{\theta}}}^p = -\underline{\underline{q}}_n^p, \quad (2.50)$$

$$\underline{\underline{K}}^{*ff} \underline{\underline{\Phi}}^* \underline{\underline{\eta}} + \underline{\underline{C}}^{*ff} \underline{\underline{\Phi}}^* \underline{\underline{\dot{\eta}}} + \underline{\underline{K}}^{*fp} \underline{\underline{\theta}}^p + \underline{\underline{K}}^{*ff} \underline{\underline{S}} \underline{\underline{\theta}}^p + \underline{\underline{C}}^{*fp} \underline{\underline{\dot{\theta}}}^p + \underline{\underline{C}}^{*ff} \underline{\underline{S}} \underline{\underline{\dot{\theta}}}^p = \underline{\underline{Q}}^f. \quad (2.51)$$

Equation (2.50) relates the incoming heat flux at the prescribed nodes to the temperature at the prescribed nodes $\underline{\underline{\theta}}^p$ and the coefficients $\underline{\underline{\eta}}$ (i.e., macro-scale variables) of the transient reduced basis. Equation (2.51) is the micro-scale evolution equation for $\underline{\underline{\eta}}$ in terms of $\underline{\underline{\theta}}^p$. Premultiplying equation (2.47) with $\underline{\underline{S}}^T$ and using the expression for the steady-state reduced basis $\underline{\underline{S}} = -(\underline{\underline{K}}^{*ff})^{-1} \underline{\underline{K}}^{*fp}$ provides the expression for the first term in equation (2.50) as $\underline{\underline{K}}^{*pf} \underline{\underline{\Phi}}^* \underline{\underline{\eta}} = \underline{\underline{S}}^T \underline{\underline{C}}^{*ff} \underline{\underline{\Phi}}^* \underline{\underline{\dot{\eta}}}$. Adding the constraint (2.38) to (2.50) and then rearranging for $\underline{\underline{\dot{\eta}}}$, $\underline{\underline{\theta}}^p$ and $\underline{\underline{\dot{\theta}}}^p$, allows to

write the heat fluxes at the prescribed nodes as

$$\underline{q}_n^p = -\underline{\varrho}\dot{\underline{\eta}} - \underline{K}_{ss}\underline{\vartheta}^p - \underline{C}_{ss}\dot{\underline{\vartheta}}^p, \quad (2.52)$$

where the matrix $\underline{\varrho}$ is defined as

$$\underline{\varrho} := \underline{S}^T \underline{C}^{*ff} \underline{\Phi}^* + \underline{C}^{*pf} \underline{\Phi}^*. \quad (2.53)$$

$\underline{\varrho}$ provides the coupling between microscopic transient effects and the macroscopic quantities through $\underline{\eta}$. Equation (2.51) is projected onto the orthogonal basis by premultiplying it with $\underline{\Phi}^T$

$$\begin{aligned} \underline{\Phi}^{*T} \underline{K}^{*ff} \underline{\Phi}^* \underline{\eta} + \underline{\Phi}^{*T} \underline{C}^{*ff} \underline{\Phi}^* \dot{\underline{\eta}} + \underline{\Phi}^{*T} \underline{K}^{*fp} \underline{\vartheta}^p + \\ \underline{\Phi}^{*T} \underline{K}^{*ff} \underline{S} \underline{\vartheta}^p + \underline{\Phi}^{*T} \underline{C}^{*fp} \dot{\underline{\vartheta}}^p + \underline{\Phi}^{*T} \underline{C}^{*ff} \underline{S} \dot{\underline{\vartheta}}^p = \underline{\Phi}^{*T} \underline{Q}^f. \end{aligned} \quad (2.54)$$

Using $\underline{K}^{*fp} = -\underline{K}^{*ff} \underline{S}$ cancels out the third and the fourth terms in the above equation and finally using the normalization conditions (2.45) and (2.46) leads to

$$\underline{\alpha} \underline{\eta} + \dot{\underline{\eta}} = -\underline{\varrho}^T \dot{\underline{\vartheta}}^p. \quad (2.55)$$

Unlike equation (2.48), the above equation is coupled to the macro-scale through $\underline{\varrho}^T \dot{\underline{\vartheta}}^p$, which is the forcing term for this ordinary differential equation and that serves as the input from the macro-scale in terms of the prescribed temperature field $\underline{\vartheta}^p$. Next, the expression for \underline{q}^p given by equation (2.52) is used to express the homogenized macroscopic constitutive equations (2.23) and (2.24) in terms of the coefficients of the steady state and transient reduced bases i.e., $\underline{\vartheta}^p$ and $\underline{\eta}$.

2.3.3 Macroscopic Quantities

In the discrete form, the boundary integral of the macroscopic heat flux (2.23) reads,

$$\bar{\underline{q}} = \frac{1}{V} (\Delta \underline{\mathbf{x}}^p)^T \underline{q}_n^p, \quad (2.56)$$

where $\Delta \underline{\mathbf{x}}^p = (\underline{\mathbf{x}}^p - \underline{I}^p \bar{\underline{\mathbf{x}}})$, and the discrete form of the rate of change of the macroscopic internal energy (2.24) is written as

$$\dot{\bar{\underline{\epsilon}}} = -\frac{1}{V} (\underline{I}^p)^T \underline{q}_n^p. \quad (2.57)$$

Substituting the expression for the reaction heat flux at the prescribed part of the boundary q_n^p from equation (2.52) in equation (2.56) and using the discrete form of the prescribed temperature field, given by equation (2.27), the macroscopic heat flux $\bar{\mathbf{q}}$ is written as

$$\bar{\mathbf{q}} = -\underline{\mathbf{a}}^T \underline{\dot{\eta}} - \mathbf{b}\bar{\theta} - \mathbf{B} \cdot \bar{\nabla}\bar{\theta} - \mathbf{c}\dot{\bar{\theta}} - \mathbf{C} \cdot \bar{\nabla}\dot{\bar{\theta}}, \quad (2.58)$$

where,

$$\begin{aligned} \underline{\mathbf{a}} &= \frac{1}{V} (\Delta \underline{\mathbf{x}}^p)^T \underline{\varrho}, && \text{(Column of } \mathcal{N}_q \text{ 1st-order tensors)} \\ \mathbf{b} &= \frac{1}{V} (\Delta \underline{\mathbf{x}}^p)^T [\underline{\mathbf{K}}_{ss} \underline{\mathcal{I}}^p], && \text{(1st-order tensor)} \\ \mathbf{B} &= \frac{1}{V} [(\Delta \underline{\mathbf{x}}^p)^T \underline{\mathbf{K}}_{ss}] \otimes \Delta \underline{\mathbf{x}}^p, && \text{(2nd-order tensor)} \\ \mathbf{c} &= \frac{1}{V} (\Delta \underline{\mathbf{x}}^p)^T [\underline{\mathbf{C}}_{ss} \underline{\mathcal{I}}^p], && \text{(1st-order tensor)} \\ \mathbf{C} &= \frac{1}{V} [(\Delta \underline{\mathbf{x}}^p)^T \underline{\mathbf{C}}_{ss}] \otimes \Delta \underline{\mathbf{x}}^p. && \text{(2nd-order tensor)} \end{aligned} \quad (2.59)$$

Similarly, substituting the expression for the reaction heat flux from equation (2.52) in (2.57) and using the discrete form of the prescribed temperature field, given by equation (2.27), leads to the expression for the rate of change of the macroscopic internal energy

$$\dot{\bar{\epsilon}} = \underline{\mathbf{d}}^T \underline{\dot{\eta}} + e\bar{\theta} + \mathbf{e} \cdot \bar{\nabla}\bar{\theta} + f\dot{\bar{\theta}} + \mathbf{f} \cdot \bar{\nabla}\dot{\bar{\theta}}, \quad (2.60)$$

where,

$$\begin{aligned} \underline{\mathbf{d}} &= \frac{1}{V} (\underline{\mathcal{I}}^p)^T \underline{\varrho}, && \text{(Column of } \mathcal{N}_q \text{ scalars)} \\ e &= \frac{1}{V} (\underline{\mathcal{I}}^p)^T [\underline{\mathbf{K}}_{ss} \underline{\mathcal{I}}^p], && \text{(Scalar)} \\ \mathbf{e} &= \frac{1}{V} (\underline{\mathcal{I}}^p)^T [(\Delta \underline{\mathbf{x}}^p)^T \underline{\mathbf{K}}_{ss}], && \text{(1st-order tensor)} \\ f &= \frac{1}{V} (\underline{\mathcal{I}}^p)^T [\underline{\mathbf{C}}_{ss} \underline{\mathcal{I}}^p], && \text{(Scalar)} \\ \mathbf{f} &= \frac{1}{V} (\underline{\mathcal{I}}^p)^T [(\Delta \underline{\mathbf{x}}^p)^T \underline{\mathbf{C}}_{ss}]. && \text{(1st-order tensor)} \end{aligned} \quad (2.61)$$

The evolution of the microscopic (modal) DOFs $\underline{\eta}$ can also be expressed in terms of $\bar{\theta}$ and $\bar{\nabla}\bar{\theta}$ using equation (2.55) in conjunction with equation (2.27)

$$\underline{\alpha} \underline{\eta} + \underline{\dot{\eta}} = -V \left(\underline{\mathbf{d}}^T \dot{\bar{\theta}} + \underline{\mathbf{a}}^T \cdot \bar{\nabla}\dot{\bar{\theta}} \right). \quad (2.62)$$

For the selected microscopic RVE, with known (constant) material properties, the calculation of, the steady-state basis, the eigenvectors $\underline{\Phi}^{(k)}$, decay times $\tau^{(k)}$ and the coefficients in equations (2.59) and (2.61) are performed in an off-line stage once and for all. The online stage consists of the solution of only the macroscopic enriched-continuum equations which are specialized in the following subsection.

2.3.4 Thermal Enriched-Continuum at Macro-scale

Together, the energy balance equation at the macro-scale (2.8), the constitutive equation for the macroscopic heat flux (2.58), the constitutive equation for the rate of change of macroscopic internal energy (2.60) and the evolution equation for $\underline{\eta}$ (2.62) constitute an enriched-continuum model at the macro-scale

$$\begin{aligned}
 \overline{\nabla} \cdot \underline{\bar{q}} + \dot{\underline{\epsilon}} &= 0 \\
 \underline{\bar{q}} &= - \underline{\alpha}^T \dot{\underline{\eta}} - \underline{b}\bar{\theta} - \underline{B} \cdot \overline{\nabla}\bar{\theta} - \underline{c}\dot{\bar{\theta}} - \underline{C} \cdot \overline{\nabla}\dot{\bar{\theta}} \\
 \dot{\underline{\epsilon}} &= \underline{d}^T \dot{\underline{\eta}} + \underline{e}\bar{\theta} + \underline{e} \cdot \overline{\nabla}\bar{\theta} + \underline{f}\dot{\bar{\theta}} + \underline{f} \cdot \overline{\nabla}\dot{\bar{\theta}} \\
 \dot{\underline{\eta}} &= - \underline{\alpha}\underline{\eta} - V \left(\underline{d}^T \dot{\bar{\theta}} + \underline{\alpha}^T \cdot \overline{\nabla}\dot{\bar{\theta}} \right)
 \end{aligned} \tag{2.63}$$

The modal amplitudes $\underline{\eta}$, can be considered at the macroscopic description as internal variables which are responsible for the representation of the lagging behavior due to thermal inertia. To solve the system of equations (2.63) different solution schemes can be adopted. For example, $\underline{\eta}$ can be condensed out at the macroscopic integration points leading to a single field (macroscopic temperature $\bar{\theta}$) solution scheme, or both $\underline{\eta}$ and $\bar{\theta}$ can be solved as macroscopic degrees of freedom, which leads to a multi-field solution scheme. The solution of the enriched macro-scale continuum is not the scope of the present work, but will be provided in future work instead.

2.3.5 Identification of Transient Reduced Basis

Here, we discuss the selection of the transient reduced basis $\underline{\Phi}^*$ from the complete basis $\underline{\Phi}$ obtained by solving the eigenvalue problem (2.43). Since the right-hand side of equation (2.62) acts as the forcing term for each k -th equation, the variable $\eta^{(k)}$ corresponding to a higher value of the coupling term $d^{(k)}$ or $a_i^{(k)}$ will have a higher amplitude. This information is exploited to identify the eigenvectors with a significant contribution to the thermal inertia at the macro-scale, whereas the other eigenvectors can be neglected in the analysis. The eigenvectors associated

to $d^{(k)}$ with relatively high contribution are identified using

$$E_{d^{(k)}} = \frac{|d^{(k)}|}{\max |d^{(k)}|}, \quad (2.64)$$

and the eigenvectors associated to $a_i^{(k)}$ with relatively high contribution are identified by,

$$E_{a_i^{(k)}} = \frac{\|\mathbf{a}^{(k)}\|}{\max |a_i^{(k)}|}, \quad (2.65)$$

Then, a reduced transient eigenbasis $\underline{\Phi}^*$ can be obtained by requiring a minimum threshold ε

$$\underline{\Phi}_{\underline{d}}^* = \{\underline{\Phi}^{(k)} \in \underline{\Phi} : E_{d^{(k)}} \geq \varepsilon\}, \quad (2.66a)$$

$$\underline{\Phi}_{a_i}^* = \{\underline{\Phi}^{(k)} \in \underline{\Phi} : E_{a_i^{(k)}} \geq \varepsilon\}, \quad (2.66b)$$

$$\underline{\Phi}^* = \underline{\Phi}_{\underline{d}}^* \cup \underline{\Phi}_{a_i}^*. \quad (2.66c)$$

2.4 Numerical Examples

In this section, numerical examples are presented for a microstructure with randomly distributed circular inclusions. First, the steady-state and the transient reduced basis are identified, then the identification criteria for the transient reduced basis are assessed by analyzing the $\eta^{(k)}$ evolution and the error norms. The temperature profile and the macroscopic quantities computed with the proposed reduced order homogenization method are compared with the conventional steady-state and transient computational homogenization. Finally, an analysis is performed for different separation of scales regimes and micro-scale domain sizes, which explores the range of validity of the proposed reduced order homogenization.

2.4.1 Problem Settings

A microscopic domain, shown in Figure 2.2, with mono-dispersed circular inclusions is generated using a level set based random sequential adsorption method [52]. The inclusions are allowed to cross the RVE boundary under the applied periodicity constraint. The RVE is discretized with a periodic finite element mesh, which ensures that opposite sides of the domain have corresponding nodes to match periodicity. The default parameters used in the numerical examples are provided in Table 2.1. A high contrast two phase material is considered in the simula-

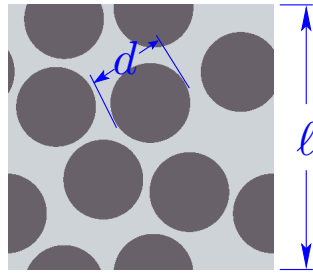


Figure 2.2: A microscopic domain (RVE) with mono-dispersed circular inclusions; ‘ ℓ ’ is the characteristic size of the RVE and ‘ d ’ the diameter of the inclusion.

tions, such that the ratio between the diffusivity of the matrix and the inclusion is $\mathcal{D}_m/\mathcal{D}_i = 10^5$. The microscopic domain is excited by the macroscopic temperature $\bar{\theta}$ and its gradient $\bar{\nabla}\bar{\theta}$ oscillating in time as

$$\begin{aligned}\bar{\theta}(\bar{\mathbf{x}}, t) &= \bar{\theta}_{\max} \sin(\omega t) \\ \bar{\nabla}\bar{\theta}(\bar{\mathbf{x}}, t) &= (\bar{\nabla}\bar{\theta})_{\max} \sin(\omega t)\end{aligned}\tag{2.67}$$

where $\omega = 2\pi/T$ is the angular frequency and T is the total loading time. In the simulations, one period of the loading cycle has been considered. Note, that the default material parameters, microscopic length scales and the characteristic loading time satisfy the relaxed separation of scales as presented in section 2.2. The RVE is discretized with three-node linear triangular finite elements with a finer mesh inside the inclusion. The time integration is performed using a backward-Euler scheme with a time step size of $\Delta t = 10^{-3}T$. Finally, a non-dimensional problem is solved, in which the total time is normalized with respect to the characteristic diffusion time of the inclusion i.e., $\hat{t} = t/t_i$, the lengths are normalized with respect to the characteristic length of the RVE i.e., $\hat{\ell} = x/\ell$, and the temperature is normalized with the maximum attainable temperature in the microscopic domain i.e., $\hat{\theta} = \theta/\theta_{\max}$, where $\theta_{\max} = \bar{\theta}_{\max} + \bar{\nabla}\bar{\theta}_{\max} \cdot \mathbf{x}_{\max}$ and $\mathbf{x}_{\max} = [\ell, \ell]$. Next, we identify the steady-state and transient reduced basis.

2.4.2 Reduced Basis Identification

The reduced bases are computed during an off-line stage, which consists in performing the static condensation, solving an eigenvalue problem and computing the coefficients given in equation (2.59) and (2.61).

Table 2.1: Default parameters used in the simulation.

Parameter	Symbol	Value	Units
RVE length	ℓ	1.0	[mm]
Inclusion diameter	d	0.3	[mm]
Matrix volume fraction	V_{f_m}	0.4349	
Inclusion volume fraction	V_{f_i}	0.5651	
Matrix Diffusivity	\mathcal{D}_m	1×10^5	[m ² /s]
Inclusion Diffusivity	\mathcal{D}_i	1	[m ² /s]
Matrix characteristic time	$t_m = \ell^2 / \mathcal{D}_m$	1×10^{-5}	[s]
Inclusion characteristic time	$t_i = d^2 / \mathcal{D}_i$	0.09	[s]
Number of elements		20620	TR13
Number of nodes		10484	
Total loading time	T	$0.1t_i$	[s]
Loading frequency	ω	1	
Maximum macroscopic temperature (normalized)	$\bar{\theta}_{\max}$	30	[K]
Maximum macroscopic temperature gradient (normalized)	$\bar{\nabla}\bar{\theta}_{\max}$	[3, 3]	[K/m]

2.4.2.1 Steady-State Basis

The steady-state part of the microscopic temperature field θ_{ss} is given by equation (2.37), where each column $\underline{\mathcal{S}}^{(k)}$ of $\underline{\mathcal{S}}$ is a load case constituting the steady-state global basis. The corresponding prescribed temperature degrees of freedom in $\underline{\theta}^p$ are the coefficients. The size of the steady-state reduced basis is dependent on the type of boundary conditions used at the micro-scale. If, for example, zero fluctuations boundary condition is applied to all nodes on the boundary to fulfill the scale transition relations then the size of the steady-state reduced basis will be equal to the number of nodes on the RVE boundary and the corresponding coefficients will be the prescribed temperature degrees of freedom at all the nodes of the RVE boundary. For the periodic boundary conditions, as used in this work, $\underline{\theta}^p$ includes the temperature values of the three prescribed nodes, i.e., which are defined at nodes 1, 2 and 4 and the size of the steady state reduced basis consequently equals three corresponding to the three load cases to be solved. For the considered microstructural model, the steady-state response is decomposed into its reduced basis and corresponding coefficients as shown in Figure 2.3.

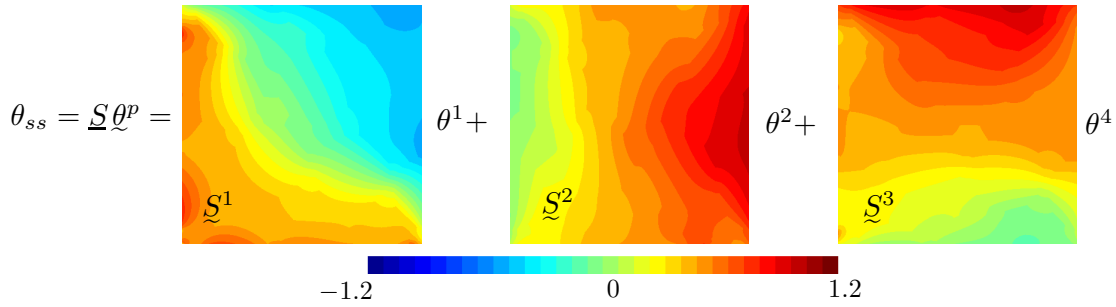


Figure 2.3: The steady-state part of the temperature field θ_{ss} decomposed into its reduced basis $\underline{\mathcal{S}}$ and corresponding coefficients θ^p .

2.4.2.2 Transient Basis

To identify the transient basis, an eigenvalue problem is solved for the first 200 eigenvectors $\underline{\Phi}$, through which the transient reduced basis $\underline{\Phi}^*$ is identified. The size of the transient reduced basis depends on the micro-structure topology and material contrast between the matrix and the inclusions. It is selected by the criteria provided in equation (2.66) based on the relative contribution of the coupling terms \underline{d} and \underline{a} . The transient response θ_{tr} is decomposed into its reduced basis, $\underline{\Phi}^* = \{\underline{\Phi}^{(1)}, \underline{\Phi}^{(5)}, \underline{\Phi}^{(41)}, \underline{\Phi}^{(42)}, \underline{\Phi}^{(47)}, \underline{\Phi}^{(113)}, \underline{\Phi}^{(119)}\} \in \underline{\Phi}$ and corresponding coefficients, as shown in Figure 2.4. Since the relaxed separation of scales is satisfied, the eigenvectors have non-negligible contributions only inside the inclusions. In general, when using a reduced basis description for the transient analysis of a heat conduction problem, only the first or first few consecutive eigenvectors with the lowest eigenvalues are commonly used [6]. This is different in the current analysis, where based on the coupling terms \underline{d} and \underline{a} , eigenvectors $\{\underline{\Phi}^{(41)}, \underline{\Phi}^{(42)}, \underline{\Phi}^{(47)}, \underline{\Phi}^{(113)}, \underline{\Phi}^{(119)}\}$, with high eigenvalues have also been selected, which are significantly important for capturing the effect of the micro-scale thermal inertia at the macro-scale. This will be verified in the following by assessing the evolution of the $\eta^{(k)}$ fields, and comparing the error norms with respect to the reference CTH solution.

The evolution of $\underline{\eta}$ is obtained by time integration of equation (2.55) for the given $\bar{\theta}$ and $\bar{\nabla}\bar{\theta}$. Seven $\eta^{(k)}$ with the highest amplitude are shown in Figure 2.5. These $\eta^{(k)}$ values correspond to the reduced transient basis shown in Figure 2.4, selected by the criteria (2.66). The selected eigenvectors, even these with higher eigenvalues, are important for an adequate approximation of the macroscopic quantities \bar{q} and $\dot{\bar{e}}$. Next, we perform an error analysis to verify this assertion.

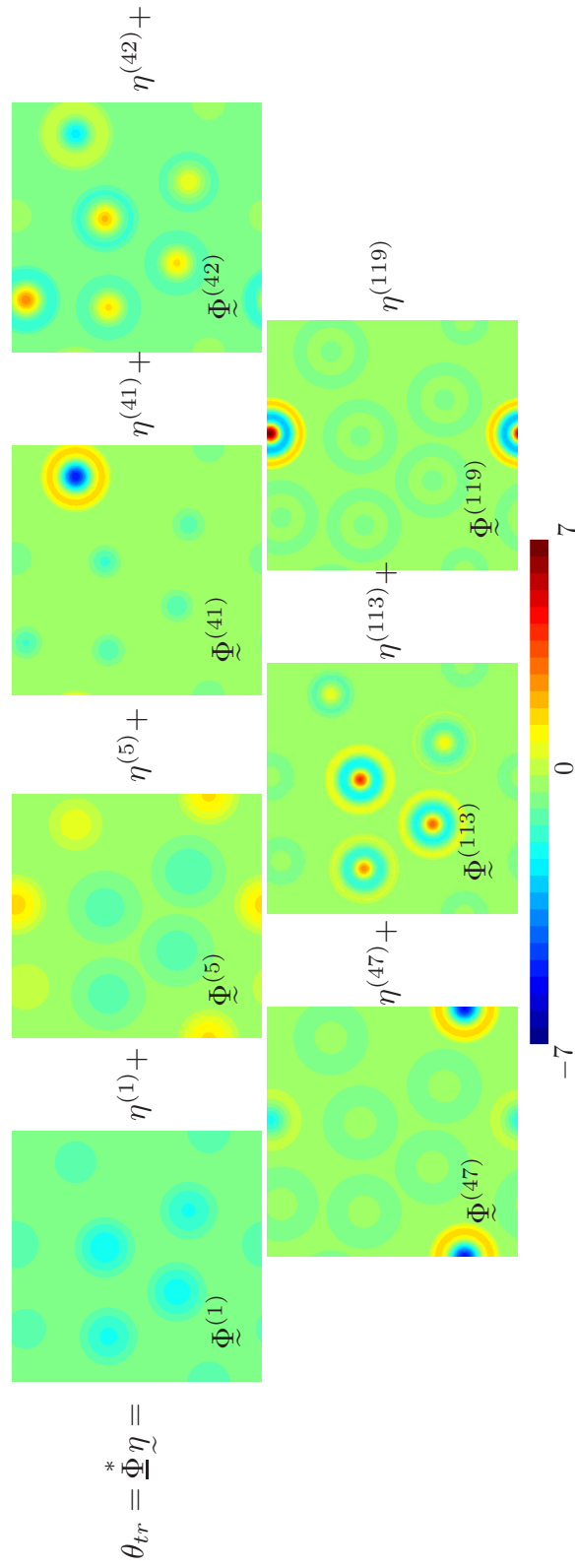


Figure 2.4: The transient part of the temperature field θ_{tr} decomposed into its reduced basis $\underline{\Phi}$ and corresponding coefficients η .

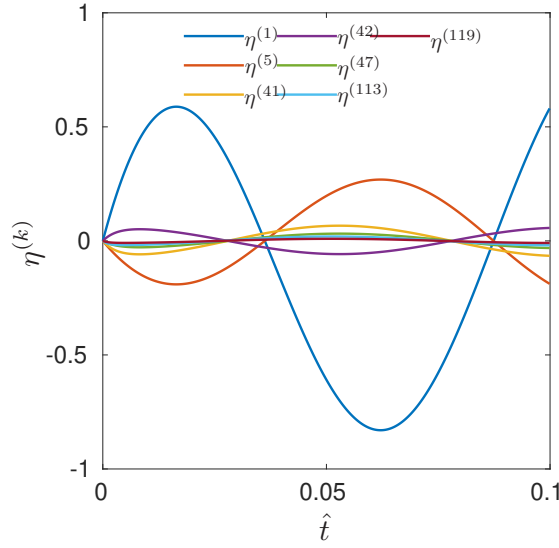


Figure 2.5: The time evolution of the $\eta^{(k)}$ coefficients acting on the transient reduced basis $\underline{\Phi}^*$.

Considering the computational transient homogenization (CTH) solution as the reference one, the selection criteria for the reduced transient basis $\underline{\Phi}^*$ can be verified using a-posteriori error measures. To evaluate the effect of the addition of each new eigenvector on the accuracy of the microscopic temperature field θ^{RTH} calculated with the reduced transient homogenization (RTH), it is enriched sequentially with \mathcal{N}_q eigenvectors i.e. ,

$$\underline{\theta}_{\mathcal{N}_q}^{\text{RTH}} = \underline{\theta}_{ss} + \underline{\theta}_{tr} = \underline{S}\underline{\theta}^p + \sum_{k=1}^{\mathcal{N}_q} \underline{\Phi}^{(k)} \eta^{(k)}, \quad \mathcal{N}_q = 1, 2, 3, \dots, 200. \quad (2.68)$$

A time averaged relative- L_2 error norm with respect to the reference CTH solution can be written as

$$\varepsilon_{\mathcal{N}_q}^\theta = \frac{1}{T} \int_T \frac{\|\underline{\theta}^{\text{CTH}}(t) - \underline{\theta}_{\mathcal{N}_q}^{\text{RTH}}(t)\|_{L_2}}{\|\underline{\theta}^{\text{CTH}}(t)\|_{L_2}} \Delta t, \quad \mathcal{N}_q = 1, 2, 3, \dots, 200. \quad (2.69)$$

Figure 2.6(a) shows that the decrease in the error $\varepsilon_{\mathcal{N}_q}^\theta$ only occurs with the addition of particular eigenvectors, which are exactly the ones identified by criterion (2.66) and shown in Figure 2.4. Similarly, an error measure is formulated for the macroscopic quantities, in this case for the rate of change of macroscopic internal energy as

$$\varepsilon_{\mathcal{N}_q}^{\dot{\epsilon}} = \frac{|\dot{\epsilon}^{\text{CTH}} - \dot{\epsilon}_{\mathcal{N}_q}^{\text{RTH}}|}{|\dot{\epsilon}^{\text{CTH}}|}, \quad \mathcal{N}_q = 1, 2, 3, \dots, 200. \quad (2.70)$$

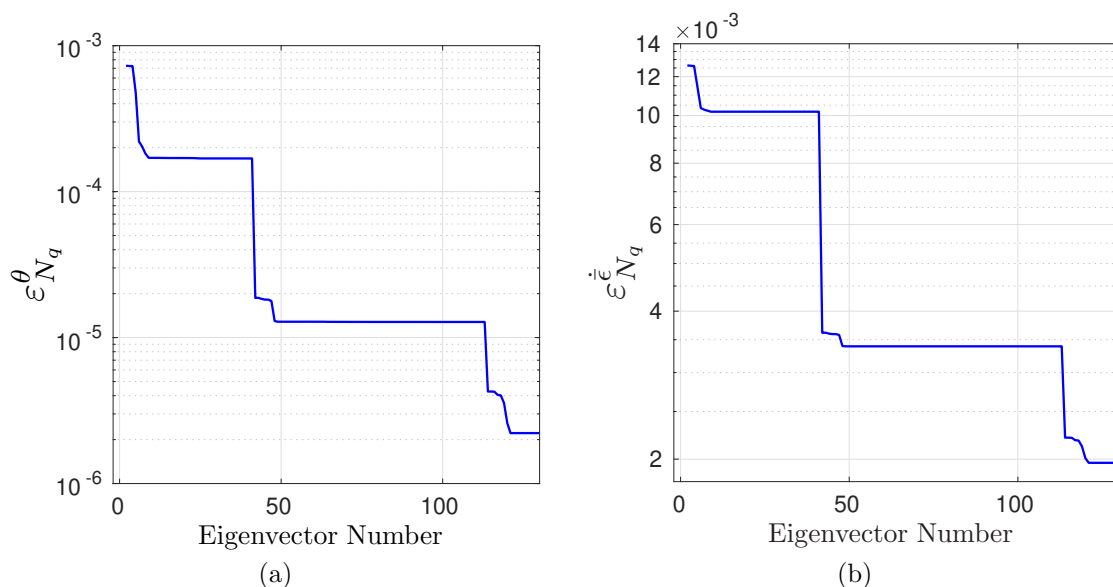


Figure 2.6: (a) Time averaged relative- L_2 error norm for the microscopic temperature field. (b) relative error norm for the rate of change of macroscopic internal energy $\dot{\epsilon}$. The error is computed relative to the reference CTH solution for the sequential enrichment of the microscopic transient basis by addition of extra eigenvectors.

The accuracy of the macroscopic quantity $\dot{\epsilon}$ also increases only with the addition the dominant eigenvectors indicated by the criteria in equation (2.66). This a-posteriori analysis is carried out for validation purposes only. Because of its associated computational costs, it is not recommended to be used in an actual multi-scale analysis.

2.4.3 Homogenization Results

Next, we compare the microscopic temperature field and the macroscopic quantities computed with the proposed reduced transient homogenization (RTH), method the conventional steady-state (SSH) and the transient computational homogenization (CTH) methods.

2.4.3.1 Microscopic Temperature Field

In this work, conventional transient homogenization (CTH) is considered as the reference solution, which is proven against DNS in the literature, for example see [8, 9]. Therefore, we chose not to repeat the validation of CTH against DNS.

In general, homogenization methods require the solution of the primary variable at the micro-scale and then averaging is performed to obtain macroscopic quantities. To calculate the temperature fields in SSH and CTH standard finite element computations (with periodic boundary conditions) on the microstructural domain (RVE) are performed. For computing the temperature field in RTH, first the $\underline{\eta}$ variables are solved using equation (2.62), then the total microscopic response is obtained by substituting $\underline{\eta}$ and $\underline{\theta}^p$ into equation (2.49). Figure 2.7 shows the temperature profiles at time step $t = 156 \times \Delta t[\text{s}]$ for RTH in the center, SSH on the left and CTH on the right. The RTH response is further decomposed into its steady-state θ_{ss} and transient θ_{tr} parts. The steady-state RTH part is equal to the SSH full microscopic response θ^{SSH} (i.e., computed using steady-state assumption at the micro-scale). The steady-state approximation is not able to capture the transient effects and be used in the transient regimes represented by equations (2.6) and (2.7). The RTH properly accounts for the transient and inertial effects and the resulting solution field is approximately equal to the reference, but computationally expensive, CTH response. Next, we compare the effective macroscopic quantities calculated with the different homogenization methods.

2.4.3.2 Effective Macroscopic Quantities

The effective macroscopic quantities are post-processed from the microscopic temperature field. The procedure for the evaluation of the effective quantities differ for the different homogenization schemes. In the SSH and CTH schemes, the computation of $\underline{\theta}^f$ and post-processing to obtain \underline{q}_n^p follows from the solution of the finite element system of equations and (2.32), respectively. For calculating the macroscopic heat flux $\bar{\mathbf{q}}$, in both SSH and CTH, equation (2.56) is used. For calculating the rate of change of the macroscopic energy $\dot{\bar{\epsilon}}$ for CTH, expression (2.57) is utilized. Since in SSH transient inertia effects are disregarded, following the work of [32], the rule of mixtures for the effective thermal capacity is used. In RTH, once the coefficients terms in (2.59) and (2.61) are calculated, the macroscopic heat flux $\bar{\mathbf{q}}$ and the rate of change of the macroscopic internal energy $\dot{\bar{\epsilon}}$ are computed directly using (2.58) and (2.60), respectively. The expressions for the macroscopic quantities used in different homogenization schemes are summarized in Table 2.2. As shown in Figure 2.8, the effective macroscopic quantities calculated with the proposed RTH method approximate very well the reference solution calculated with the CTH method. This indicates that the RTH method adequately captures the macroscopic phenomena. The macroscopic heat flux calculated with

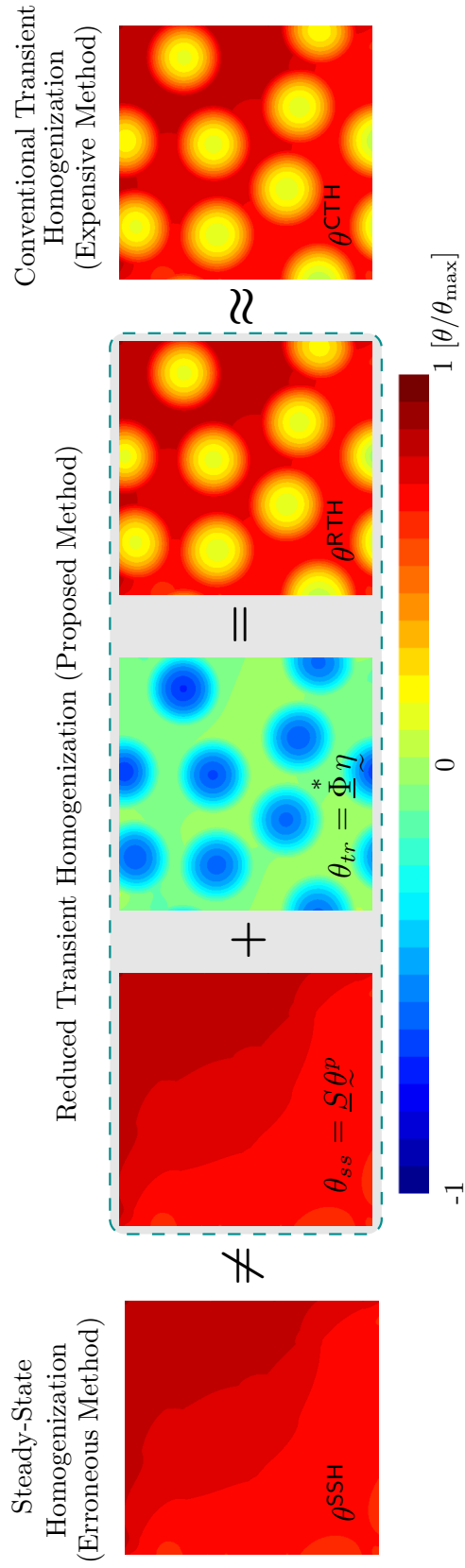


Figure 2.7: Non-dimensional temperature fields computed with the SSH (left), RTH (center) and CTH (right) at time step $t = 156\Delta t$.

Table 2.2: Expressions for the effective macroscopic quantities in different homogenization schemes.

Quantity	RTH	CTH	SSH
$\bar{\mathbf{q}}$	$-\underline{\mathbf{a}}\dot{\eta} - \mathbf{b}\bar{\theta} - \mathbf{B} \cdot \nabla \bar{\theta} - \mathbf{c}\dot{\theta} - \mathbf{C} \cdot \nabla \dot{\theta}$	$\langle \mathbf{q} - \dot{\epsilon}(\mathbf{x} - \bar{\mathbf{x}}) \rangle$	$\langle \mathbf{q} \rangle$
$\dot{\bar{\epsilon}}$	$\underline{\mathbf{d}}\dot{\eta} + \mathbf{e}\bar{\theta} + \mathbf{e} \cdot \nabla \bar{\theta} + \mathbf{f}\dot{\theta} + \mathbf{f} \cdot \nabla \dot{\theta}$	$\langle \dot{\epsilon} \rangle$	$\dot{\theta} \langle \rho c \rangle$

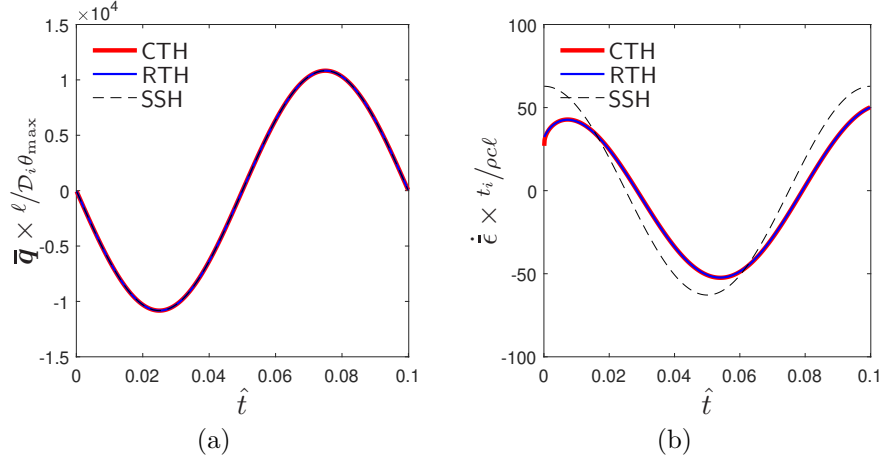


Figure 2.8: Comparison of (a) effective macroscopic heat flux $\bar{\mathbf{q}}$ and (b) effective rate of change of macroscopic internal energy $\dot{\bar{\epsilon}}$ computed with the CTH, RTH and SSH method.

SSH is nearly equal to the one calculated with the transient homogenization methods, which implies that for the considered example, the difference $\langle \dot{\epsilon}(\mathbf{x} - \bar{\mathbf{x}}) \rangle$ is negligible compared to $\langle \mathbf{q} \rangle$. Indeed, due to the “fast” connected matrix, the heat flux reaches a steady-state almost instantaneously when the temperature changes at the prescribed part of the boundary. When some transient phenomena in the matrix are not negligible, for example in the regime given by equation (2.6) (c), the difference $\langle \dot{\epsilon}(\mathbf{x} - \bar{\mathbf{x}}) \rangle$ becomes significant. However, such regimes are outside the limits of applicability of RTH; this limitation is further examined in section 2.4.4. In SSH, the rate of change of the macroscopic internal energy $\dot{\bar{\epsilon}}$ is overestimated due to the use of the rule of mixtures. The thermal inertia, due to the slow transient inclusions, results in a lagging behavior which is well captured by CTH and the proposed RTH method.

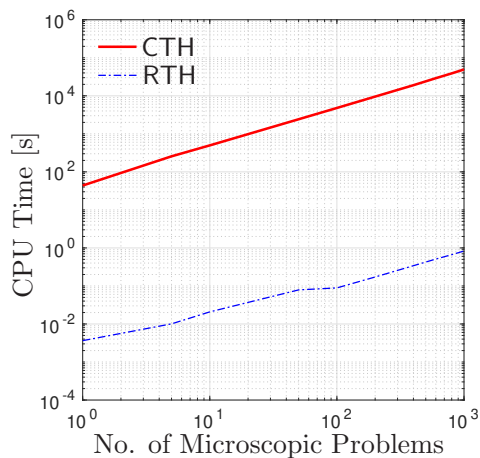


Figure 2.9: CPU time as a function of the number of microscopic problems solved with with computational expensive CTH and the proposed reduced order RTH method.

2.4.3.3 Computational Costs

In RTH, the solution of the micro-scale problem is obtained in two steps; an off-line step and an on-line step. In the off-line step, the eigenvalue problem is solved and the coefficients (2.59) and (2.61) are calculated and stored. In the on-line step, evolution of the modal coefficients is obtained by solving (2.62) and subsequently used to extract the effective quantities. In CTH, the solution to the micro-scale problem is obtained by an on-line step, only involving the solution of the system of equations (2.32). Comparison between the computational times for CTH and RTH, should be made only for the on-line solution stage corresponding to the costs of computing the effective quantities for a macroscopic point, since the RTH off-line stage and storage of the coefficients is done once and for all on beforehand. Figure 2.9 shows the computational times, as a function of the number of the underlying microscopic problems (in a two-scale macroscopic simulation this corresponds to an increasing number of elements at the macro-scale). The simulations were performed on a computer with a core-i7@4.4GHz processor and 16Gb RAM using Matlab 2018b. The computational gain with RTH is significant. The ratio between the simulation times using CTH and RTH was of the order of 10^4 in all cases. Considering the resulting high accuracy, as shown in Figure 2.6, and the computational gain observed here, RTH is qualified for replacing CTH in the regimes where it is applicable. To properly assess the limits of applicability of RTH the separation of scales due to changes in material properties and the size of microscopic domain are scrutinized next.

Table 2.3: Material properties used to achieve different scale separation regimes.

Scale separation regime	\mathcal{D}_i [m ² /s]	\mathcal{D}_m [m ² /s]
$T \sim t_m \sim t_i$ (2.6a)	1	5
$(T \sim t_m) > t_i$ (2.6b)	1×10^{-3}	1
$(T \sim t_i) > t_m$ (2.6c)	1	1×10^2

2.4.4 Applicability Limits of RTH

Performing RTH for mechanical problems [43] is equivalent to substructuring in structural dynamics systems [42], in which the boundary of each substructure is assumed to accommodate a rigid body motion with respect to the loading conditions, for which neglecting the dynamic effects of the boundary may lead to a too stiff mechanical response. Similar phenomena are observed here for heat conduction problems, i.e., when the combination of material properties of the micro-scale constituents and the loading conditions do not satisfy the relaxed separation of scale, pushing RTH outside its applicability limits, as illustrated in the following.

2.4.4.1 Scale Separation Regimes

To perform this analysis, only the material properties are varied to achieve different scale separation regimes in equation (2.6). These material properties are given in the Table 2.3.

When significant transient phenomena exist in the matrix, represented by equation (2.6a) and (2.6b), the results are shown in Figure 2.10 (a and b). In this case, the proposed RTH method over- or underestimates the macroscopic quantities as compared to CTH. However, when the matrix is comparatively less transient, as in equation (2.6c), RTH approximation becomes better again.

2.4.4.2 Size Effect

To obtain non-zero time averaged macroscopic quantities, the normalized loading frequency is changed to $\omega = 0.25$. The effect of the non-dimensional microscopic length $\hat{\ell}$ on the time-averaged macroscopic quantities can be seen in Figure 2.11. As discussed earlier, the SSH method relies on the steady-state assumption at the micro-scale and is therefore unable to capture the size effects; the SSH response remains constant as the RVE size increases. Both CTH and RTH methods capture the size effect, however as the RVE size increases the characteristic diffusion time

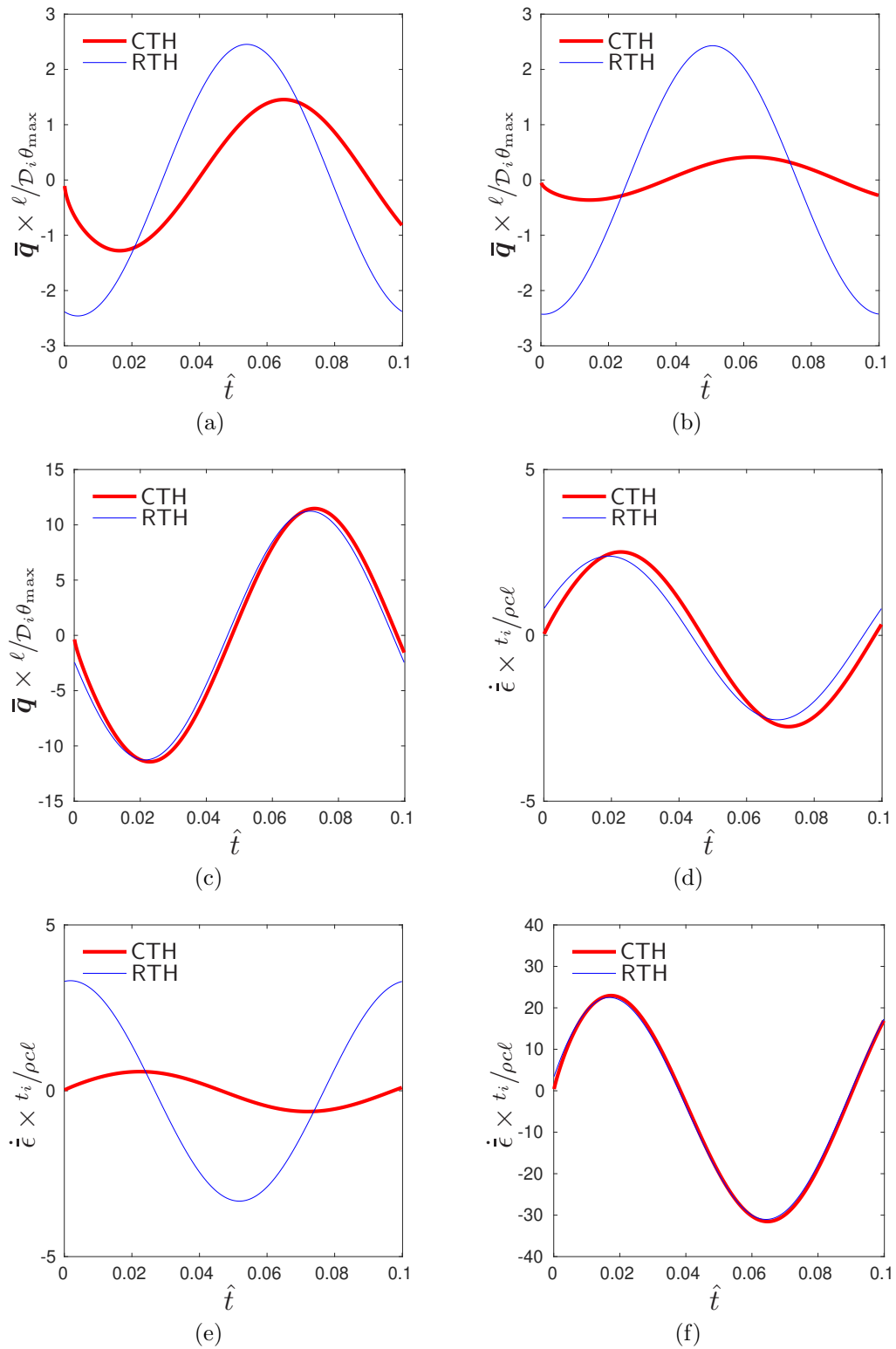


Figure 2.10: Comparison of the time evolution of the macroscopic quantities, effective heat flux - (a),(b) and (c) and the rate of change of internal energy - (d), (e) and (f), calculated using RTH and CTH with different material properties leading to different separation of scales regimes as shown in Table 2.3.

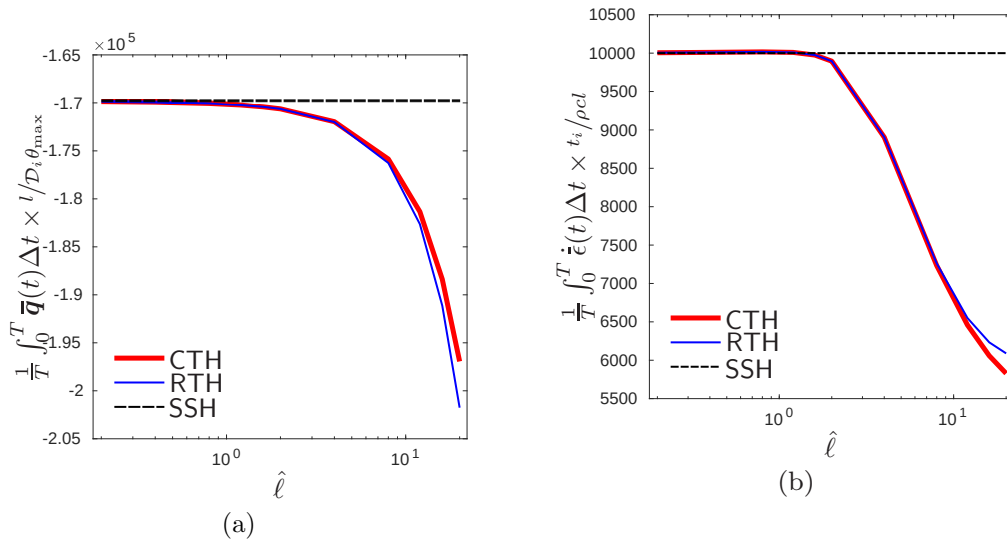


Figure 2.11: Effect of RVE size $\hat{\ell}$ on the time averaged (a) macroscopic heat flux and (b) the rate of change of macroscopic internal energy calculated with the SSH, CTH and RTH methods.

of the matrix also increases, which leads to a “stiff” response and RTH becomes slightly less accurate compared to the reference CTH solution.

2.5 Conclusions and Perspectives

A reduced model for the homogenization of transient heat conduction problems was developed. It is based on the relaxed separation of scales, under material linearity, in which the matrix always remains in steady-state and only inclusions experience transient effects. The effective macroscopic quantities for transient homogenization were obtained using the extended Hill-Mandel condition adopted for the transient thermal problems. The main contribution of this work is the development of a model reduction approach at the micro-scale, where the microscopic solution and the macroscopic quantities are represented in terms of the steady-state and transient reduced bases along with their corresponding coefficients. This reduced homogenization technique adequately captures microscopic transient effects in its target regime of scale separation. Significant computational gain was observed as compared to the conventional transient homogenization scheme. In future work, the enriched-continuum formulation resulting from the reduced transient homogenization procedure will be used to solve macroscopic boundary value problems. A reduced model for coupled thermo-mechanical problems can also be

formulated in which both the thermal and mechanical problems can be solved with a similar reduced approach.

CHAPTER 3

**Two-scale Analysis of Transient
Diffusion Problems Through a
Homogenized
Enriched-Continuum**

Abstract

This chapter addresses the two-scale problem underlying the enriched-continuum for transient diffusion problems, which was previously developed and tested at the single scale level only. For a linear material model exhibiting a relaxed separation of scales, a model reduction was proposed at the micro-scale that replaces the micro-scale problem with a set of uncoupled ordinary differential equations (ODEs). At the macro-scale, the balance law, the ODEs and the macroscopic constitutive equations collectively represent an enriched-continuum description. Examining different discretization techniques, distinct solution methods are presented for the macro-scale enriched-continuum. Proof-of-principle examples are solved for a mass diffusion system in which species diffuse slower in the inclusion than in the matrix. The results from the enriched-continuum formulation are compared with the computational transient homogenization (CTH) and direct numerical simulations (DNS). Without compromising the solution accuracy, significant computational gains are obtained through the enriched-continuum approach.

3.1 Introduction

Composite materials are used in a wide range of applications from large structures to micrometer size components [53]. The contrast between the properties of the constituents may differ by several orders of magnitude [54]. In general, it is computationally very expensive to simulate such heterogeneous materials at the micro-scale since the analysis involves a large number of degrees of freedom to capture the physical phenomena. Homogenization can be used instead, which provides the effective properties through an averaging procedure. Various homogenization methods can be found in the literature, i.e., analytical bounds [55, 56], self-consistent methods [57] and asymptotic homogenization [23, 24, 28]. Most of these homogenization methods assume a steady-state condition at the micro-scale to calculate the effective properties. However, in reality, due to the high contrast in material properties and time varying loading conditions, this assumption is often not valid. For example, the steady-state assumption is not appropriate in the case of diffusing species in polycrystalline materials, where the diffusion process in the grain boundaries reaches steady-state while the grain interior still remains transient [5]. Similar phenomena are observed for fluid and solute transport in

geo-materials [58], diffusion in porous gels [59] and diffusion of Lithium-ions in electrode-electrolyte systems of Li-ion batteries [60].

Computational homogenization (CH) [7, 32, 34, 61] is a more recent and robust homogenization procedure, which has been extended to transient problems [38], including diffusion [8, 9]. For a detailed review and perspectives of CH see [62–64]. Computational homogenization for transient problems, despite its robustness, suffers from a high computational cost. It requires the solution of a micro-scale problem at each macroscopic material point, which in transient problems must be solved at each time increment. To circumvent this problem, reduced models for the effective diffusion response in transient regimes have recently been proposed [65, 66], in which a chemical creep function is obtained. This chemical creep function behaves similar to phenomenological models of viscoelasticity and consists of an infinite number of Kelvin-Voigt units. A reduced model is then obtained by selecting a finite number of Kelvin-Voigt units. In [66], an analytical expression is obtained for a transient inclusion, embedded in an infinitely fast matrix, which is only possible for certain inclusion morphologies.

In the previous chapter, an alternative reduced order model was proposed for the micro-scale problem, first for dynamics [43] and then for diffusion problems in the context of heat conduction [67]. It is based on computational homogenization and applies a reduction technique to the whole unit-cell (as opposed to the inclusion only in [66]). This numerical approach accounts for different complex RVE morphologies. It is applicable in the relaxed separation of scales regime in which the characteristic diffusion time τ_m of species in the matrix is much smaller than the characteristic diffusion time τ_i in the inclusions. Moreover, the macroscopic loading time T is such that the matrix can be assumed in a steady-state regime while the inclusion exhibits transient inertia effects. The relaxed separation of scales can be expressed in terms of the characteristic diffusion times of the constituents and the characteristic loading time as follows

$$\tau_m \ll (T \sim \tau_i), \quad (3.1)$$

For more discussion on the relaxed separation of scales in diffusion problems, see [28, 66]. Assuming a linear material model for both the matrix and inclusions, allows to perform an additive decomposition of the microscopic solution field into a steady-state and a transient part. The reduced model is defined by means of a static condensation of the steady-state part of the response, and by projecting the transient part onto a reduced (eigen)basis. The size of the microscopic

system of equations is thereby reduced from \mathcal{N} coupled finite element degrees of freedom (d.o.f) to just a few \mathcal{N}_q decoupled d.o.f with $\mathcal{N}_q \ll \mathcal{N}$. An averaging is performed to obtain the macroscopic constitutive equations in terms of the coefficients of the reduced basis and the emerging macroscopic (internal) variables. The resulting set of equations to be solved at the macro-scale describes what is called an *enriched-continuum*, consisting of the macroscopic mass balance, constitutive equations obtained by homogenization and an evolution equation for the enrichment-variables. The coefficients of the micro-scale reduced basis are called *enrichment-variables* and the vectors, constituting the micro-scale reduced basis are called *enrichment-functions*. For a certain microscopic domain and material properties, the enrichment-functions and the coupling terms in the macroscopic constitutive equations are computed once and for all, and the subsequent on-line computation only consists in solving \mathcal{N}_q decoupled ordinary differential equations along with the macroscopic mass balance equation. Such an enriched-continuum formulation can be applied to a heterogeneous medium which exhibits transient diffusion phenomena within the assumption of linear material properties and the relaxed separation of scales, for example mass diffusion problems in batteries where these assumptions are valid in application for some ranges.

The enriched-continuum formulation for (heat) diffusion problems was developed in [67] and validated at the micro-scale unit-cell level against full transient computational homogenization results. No macro-scale enriched-continuum simulations were used in [67]. The aim of this work is to demonstrate the applicability of the reduced order framework to the solution of transient problems with an underlying microstructure obeying the relaxed separation of scales. Since the resulting macroscopic problem consists of an enriched-continuum with enrichment-variables and corresponding evolution equations, dedicated solution techniques have to be adopted. To this end, two solution methods based on different spatial discretization schemes are analyzed. First, a *multi-field* solution method is presented, in which both the enrichment-variables and the primary macroscopic field are computed on the nodes and interpolated using finite element shape functions. Next, an *internal-variable* solution method is presented, in which the enrichment-variables are evaluated at the macroscopic quadrature points and considered as internal variables, while the macroscopic primary field variable is interpolated in a classical manner using the finite element shape functions, as shown in Figure 3.1. The advantage of the multi-field solution method is that the macroscopic primary variable and the enrichment-variables are solved in a coupled manner at each time

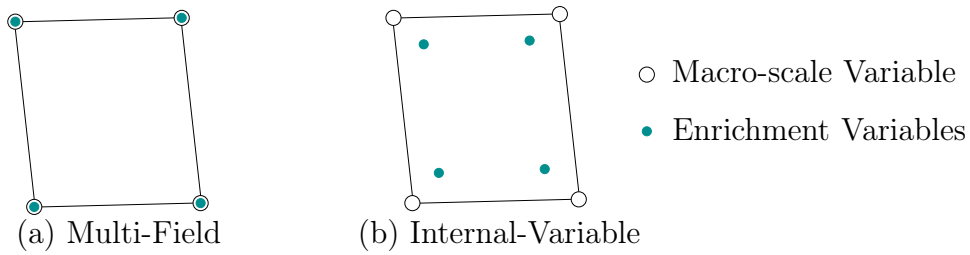


Figure 3.1: Spatial discretizations schemes for the enriched-continuum. (a) Multi-field: both the macro-scale and enrichment-variables are interpolated using bi-linear quadrilateral finite elements. (b) Internal-variable: the macro-scale variable is interpolated by bi-linear quadrilateral finite elements while the enrichment-variables are computed at the Gauss quadrature points.

step; the disadvantage is the significantly increased size of the finite element system of equations. In the internal-variable method, the enrichment-variables are eliminated by substitution and only the macroscopic primary field is solved at the current time step. Once the solution of the macroscopic variable field is available, the enrichment-variables are evaluated and stored for the next time increment, i.e., a staggered approach in time is used. This allows to use different time integration schemes for the enrichment-variables as opposed to the primary field, e.g., to better capture micro-scale transient effects. These two solution methods will be assessed here. The novel contributions of the work presented here are:

- the two-scale enriched macroscopic continuum implementation emerging from the model order reduction approach, applied to the solution of diffusion boundary value problems with incorporation of micro-structural transient effects;
- the proposed different solution methods for the enriched-continuum for transient diffusion problems;
- a comparison between the two-scale diffusion enriched-continuum macroscopic solution, the conventional transient homogenization and direct numerical simulations, allowing to evaluate the associated computational cost reduction.

3.1.1 Outline

Section 3.2 summarizes the enriched-continuum equations with expressions for the effective mass flux and the effective concentration rate. Section 3.3 presents the analyzed solution methods for the macro-scale enriched-continuum. First, the time integration schemes are presented and, subsequently, the multi-field and

the internal-variable solution methods are derived. In section 3.4, proof-of-concept numerical examples are solved for species diffusion in a material with high contrast material properties. This will demonstrate the ability of the enriched-continuum formulation to reliably reproduce the results obtained by conventional transient homogenization (CTH) or direct numerical simulations (DNS), which are both will be shown to be outperformed in terms of computational efficiency.

3.1.2 Symbols and Notations

The (homogenized) macroscopic quantities are shown with a bar on top, e.g., a scalar, a vector and a second-order tensor are represented with \bar{a} , $\bar{\mathbf{a}}$, $\bar{\mathbf{A}}$. There is no bar on top of a quantity belonging to the heterogeneous micro-scale problem, i.e., a scalar, a vector and a second-order tensor are written as a , \mathbf{a} , \mathbf{A} . The same Cartesian coordinate system is used at the micro- and macro-scale. Standard calculus operators are used in this work. For example, the dot product between two vectors is $\mathbf{a} \cdot \mathbf{b} = a_i b_i$, between a second-order tensor and a vector is $\mathbf{A} \cdot \mathbf{b} = A_{ij} b_j \mathbf{e}_i$. The tensorial dyadic product between two vectors is $\mathbf{a} \otimes \mathbf{b} = a_i b_j \mathbf{e}_i \otimes \mathbf{e}_j$ and between a second-order tensor and a vector is $\mathbf{A} \otimes \mathbf{b} = A_{ij} b_k \mathbf{e}_i \otimes \mathbf{e}_j \otimes \mathbf{e}_k$, where \mathbf{e}_i represent the vectors of the Cartesian basis. The gradient of a scalar, a vector and a second-order tensor is defined as $\nabla a := \frac{\partial a}{\partial x_i} \mathbf{e}_i$, $\nabla \mathbf{a} := \frac{\partial a_i}{\partial x_j} \mathbf{e}_i \otimes \mathbf{e}_j$ and $\nabla \mathbf{A} := \frac{\partial A_{ij}}{\partial x_k} \mathbf{e}_i \otimes \mathbf{e}_j \otimes \mathbf{e}_k$, respectively. Similarly, the divergence operates as $\nabla \cdot \mathbf{a} := \frac{\partial a_i}{\partial x_i}$ and $\nabla \cdot \mathbf{A} := \frac{\partial A_{ij}}{\partial x_i} \mathbf{e}_j$. For linear algebra notation, columns are represented with a tilde underneath a lowercase letter, e.g., \underline{a} , and matrices with a bar underneath an uppercase letter, e.g., $\underline{\underline{A}}$. A tensorial product between two column arrays of vectors is defined as $\underline{\underline{a}}^T \underline{\underline{b}}$, where

$$\underline{\underline{\otimes}} := \begin{bmatrix} \otimes & 0 & \dots & 0 \\ 0 & \otimes & & \vdots \\ \vdots & & \ddots & \\ 0 & 0 & \dots & \otimes \end{bmatrix}. \quad (3.2)$$

The microscopic domain and its boundary are represented by Ω_{\square} and $\partial\Omega_{\square}$, respectively. The volume average of a microscopic quantity \bullet is defined as

$$\langle \bullet \rangle := \frac{1}{V} \int_{\Omega_{\square}} \bullet \, d\Omega_{\square}, \quad (3.3)$$

where, $V = \int_{\Omega_{\square}} d\Omega_{\square}$ is the volume of the microscopic domain Ω_{\square} .

3.2 Enriched-Continuum Formulation

In this section, the transient mass diffusion problem is presented briefly, first for a heterogeneous domain and then for a homogenized domain, for which the two-scale computational homogenization and the resulting enriched-continuum will be considered.

3.2.1 Direct Numerical Simulation

The diffusion of species in solids is governed by the mass balance equation,

$$\nabla \cdot \mathbf{j} + \dot{c} = 0, \quad \text{in } \Omega, \quad (3.4)$$

where, \dot{c} is the rate of change of the concentration field c , $\mathbf{j} = -\mathbf{M} \cdot \nabla \mu$ is the mass flux, $\mu = \Lambda(c - c_0)$ is the chemical potential, Λ is the chemical modulus, c_0 is the reference concentration of a specie, \mathbf{M} is the mobility tensor; Ω is the heterogeneous macro-scale domain, as shown in Figure 3.2(a). The numerical procedure to solve the diffusion equation (3.4) in Ω , with corresponding initial and boundary conditions

$$\begin{aligned} \mu(0) &= \mu_0, & \text{in } & \Omega, \\ \mu &= \hat{\mu}, & \text{on } & \partial\Omega_\mu, \\ -\mathbf{j} \cdot \mathbf{n} &= j_n, & \text{on } & \partial\Omega_j. \end{aligned} \quad (3.5)$$

is referred to as the direct numerical simulation (DNS) in this work. In here, $\partial\Omega_\mu$ and $\partial\Omega_j$ are the Dirichlet and Neumann parts of the heterogeneous domain Ω , respectively, and \mathbf{n} is the outward unit-normal vector on its boundary $\partial\Omega$.

3.2.2 Computational Homogenization

Given its exorbitant computational cost, the DNS problem is commonly replaced by a computationally homogenized problem which represents an equivalent homogeneous problem by solving a coupled two-scale (macro-scale and a micro-scale) problem, as shown in Figure 3.2(b). The heterogeneous domain, in Figure 3.2(a), is replaced by a homogeneous one $\bar{\Omega}$, to which at each point, a microscopic domain Ω_\square is attached. This microscopic domain is a representative volume element (RVE) or a unit-cell in the case of a periodic medium. In transient computational homogenization, at the macro-scale a transient mass balance equation is solved

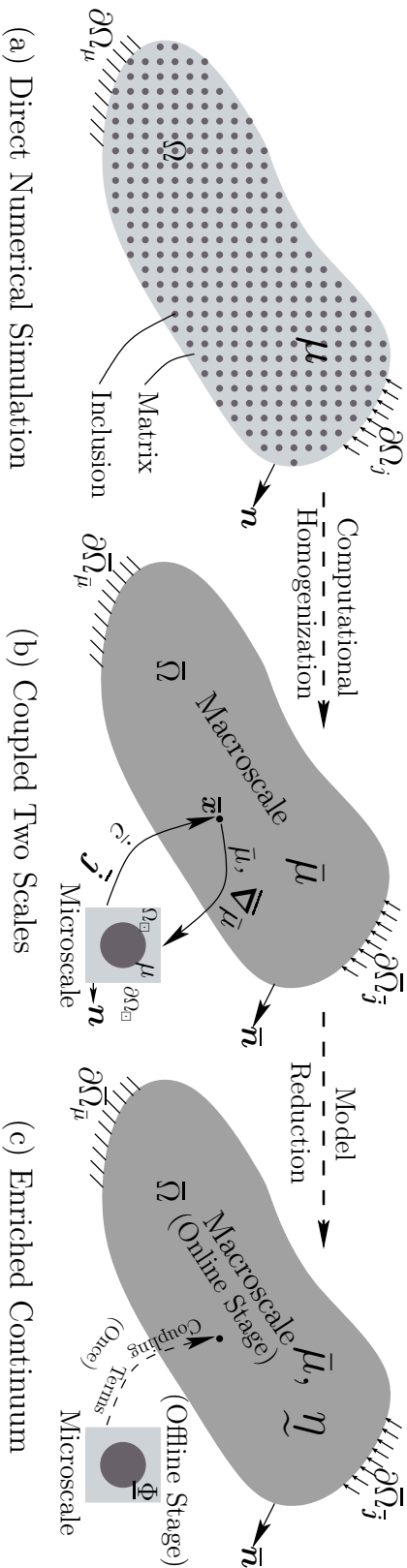


Figure 3.2: Schematic representation of the development of the enriched-continuum formulation: by performing computational homogenization: the DNS problem (a) is replaced by the coupled two-scale problem (b), followed by a model reduction on the micro-scale to obtain an enriched-continuum formulation (c).

which is complemented by the initial and boundary conditions i.e. ,

$$\begin{aligned}
 \bar{\nabla} \cdot \bar{\mathbf{j}} + \dot{\bar{c}} &= 0, & \text{in } & \bar{\Omega}, \\
 \bar{\mu}(0) &= \bar{\mu}_0, & \text{in } & \bar{\Omega}, \\
 \bar{\mu} &= \hat{\bar{\mu}}, & \text{on } & \partial\bar{\Omega}_{\bar{\mu}}, \\
 -\bar{\mathbf{j}} \cdot \bar{\mathbf{n}} &= \bar{j}_{\bar{n}}, & \text{on } & \partial\bar{\Omega}_{\bar{j}}.
 \end{aligned} \tag{3.6}$$

Where, $\partial\bar{\Omega}_{\bar{\mu}}$ and $\partial\bar{\Omega}_{\bar{j}}$ are the Dirichlet and Neumann parts of the macroscopic domain $\bar{\Omega}$, respectively, $\bar{\mathbf{n}}$ is the outward unit-normal vector to the macroscopic boundary $\partial\bar{\Omega}$, $\bar{j}_{\bar{n}}$ is the prescribed mass influx and $\hat{\bar{\mu}}$ is the prescribed chemical potential. The constitutive responses for the macroscopic mass flux $\bar{\mathbf{j}}$ and the macroscopic rate of change of concentration field $\dot{\bar{c}}$ are obtained by solving a micro-scale problem for the microscopic chemical potential field μ , which in the first-order computational homogenization is based on the following ansatz

$$\mu = \bar{\mu} + \bar{\nabla}\bar{\mu} \cdot (\mathbf{x} - \bar{\mathbf{x}}) + \tilde{\mu}, \tag{3.7}$$

where, $\tilde{\mu}$ is the fluctuation in the chemical potential at the micro-scale due to the difference in material properties of the microconstituents properties and transient loading conditions, imposed through the macroscopic chemical potential $\bar{\mu}$ and its gradient $\bar{\nabla}\bar{\mu}$, see Figure 3.2(b). The transient mass diffusion problem which is solved at the micro-scale is accompanied by specific boundary conditions that satisfy the extended Hill-Mandel condition. In computational homogenization it is assumed that the average of the microscopic chemical potential equals to the macroscopic chemical potential and the gradient of the microscopic chemical potential to be equal to the gradient of the macroscopic chemical potential.

$$\begin{aligned}
 \nabla \cdot \mathbf{j} + \dot{c} &= 0, & \text{in } & \Omega_{\square}, \\
 \langle \mu \rangle &= \bar{\mu}, & \text{in } & \Omega_{\square}, \\
 \langle \nabla \mu \rangle &= \bar{\nabla}\bar{\mu}, & \text{in } & \Omega_{\square}.
 \end{aligned} \tag{3.8}$$

The constitutive response of the microscopic mass flux $\mathbf{j} = -\mathbf{M} \cdot \nabla\mu$ and $\mu = \Lambda(c - c_0)$ are the same as used in the DNS. By using the equivalence of virtual power between the micro-scale and the macroscopic material point $\bar{\mathbf{x}}$ (the extended Hill-Mandel conditions) the macroscopic flux and concentration can be obtained

from the micro-scale fields as

$$\bar{\mathbf{j}} = \langle \mathbf{j} - \dot{c}(\mathbf{x} - \bar{\mathbf{x}}) \rangle, \quad \text{and} \quad \dot{\bar{c}} = \langle \dot{c} \rangle. \quad (3.9)$$

Despite of its robustness, computational homogenization is still very expensive in solving a transient mass diffusion problem, since it requires the solution of a microscopic problem (3.8) at each macroscopic point $\bar{\mathbf{x}}$ at each time instance (increment). For more details on the transient computational homogenization and its solution schemes, the reader is referred to [8, 9].

3.2.3 Enriched-Continuum

To alleviate the computational cost of the transient computational homogenization scheme, for linear problems, a model reduction technique was presented for heat conduction in [67], which provides an enriched-continuum at the macro-scale. It replaces the microscopic problem (3.8) with a set of uncoupled ordinary differential equations by projecting the weak Galerkin form of (3.8) onto an orthogonal set of reduced basis functions Φ , here called enrichment-functions. The microscopic chemical potential field is written in terms of the macroscopic quantities and the enrichment-functions as

$$\mu(\mathbf{x}) = S (\bar{\mu} + \bar{\nabla} \bar{\mu} \cdot (\mathbf{x} - \bar{\mathbf{x}})) + \sum_{k=1}^{\mathcal{N}_q} \Phi^{(k)}(\mathbf{x}) \eta^{(k)}, \quad (3.10)$$

where $\eta^{(k)}$, called enrichment-variables, are the coefficients of the corresponding enrichment-function $\Phi^{(k)}$. \mathcal{N}_q is the number of enrichment-functions used, which is much smaller than the number of degrees of freedom \mathcal{N} used to solve the microscopic problem (3.8) in computational homogenization, i.e., $\mathcal{N}_q \ll \mathcal{N}$. S represents the steady-state counter part of the $\Phi^{(k)}$ and it is obtained through static-condensation. It maps the loading applied on the boundary of the micro-scale to the inside of the micro-scale and in its discrete form, S has the dimension of free times prescribed d.o.f. This reduction in the number of the degrees of freedom at each macroscopic point $\bar{\mathbf{x}}$ provides a significant reduction in computational time. The effective macroscopic transient mass balance equation remains consistent with the one used in transient computational homogenization scheme, i.e., equation (3.6). However, the expression for the macroscopic mass flux $\bar{\mathbf{j}}$ and the macroscopic rate of change of concentration field $\dot{\bar{c}}$ are now written in terms of the

(reduced) enrichment-variables $\underline{\eta}$ i.e. ,

$$\bar{\mathbf{j}} = -\bar{\underline{\mathbf{a}}}^T \dot{\underline{\eta}} - \bar{\mathbf{B}} \cdot \nabla \dot{\bar{\mu}} - \bar{\underline{\mathbf{c}}}\dot{\bar{\mu}} - \bar{\mathbf{C}} \cdot \nabla \dot{\bar{\mu}}, \quad (3.11)$$

and

$$\dot{\bar{\mathbf{c}}} = \bar{\underline{\mathbf{d}}}^T \dot{\underline{\eta}} + \bar{\underline{\mathbf{e}}} \cdot \nabla \dot{\bar{\mu}} + \bar{\underline{\mathbf{f}}}\dot{\bar{\mu}} + \bar{\mathbf{f}} \cdot \nabla \dot{\bar{\mu}}. \quad (3.12)$$

The coefficients in (3.11) and (3.12) are computed only once for a given microstructure in an off-line computation stage and used at the macro-scale during the on-line stage where $\bar{\mu}$ and $\underline{\eta}$ are solved for. A detailed derivation of the expressions for the coefficients in equation (3.11) and (3.12) are provided in Appendix A.1 for mass diffusion problems. For more details on the enriched-continuum formulation and its derivation the readers are directed to our prior work on heat conduction [67]. Through model reduction of the micro-scale problem, evolution equations for $\underline{\eta}$ emerge, which are a set of (uncoupled) ordinary differential equations, given by

$$\dot{\underline{\eta}} = -\underline{\alpha} \underline{\eta} - \bar{\underline{\mathbf{a}}}^* \cdot \nabla \dot{\bar{\mu}} - \bar{\underline{\mathbf{d}}}\dot{\bar{\mu}}, \quad (3.13)$$

where $\underline{\alpha}$ is the diagonal matrix of size $(\mathcal{N}_q \times \mathcal{N}_q)$ containing the eigenvalues which are obtained by solving a generalized eigenvalue problem at the micro-scale during the off-line stage, expressions for $\bar{\underline{\mathbf{a}}}^*$ and $\bar{\underline{\mathbf{d}}}$ are given in Appendix A.1. Equations (3.6), (3.11), (3.12) and (3.13) represent the enriched-continuum model capturing the diffusion problem in the relaxed separation of scales regime (3.1). Next, we discuss the solution methods for the set of equations for the enriched-continuum.

3.3 Solution Methods

In this section, first the time integration schemes are presented for the macroscopic variable $\bar{\mu}$ and the enrichment-variables $\underline{\eta}$. Then, the multi-field and the internal-variable solution methods are derived.

3.3.1 Time Integration Schemes

The rate of change of the macroscopic chemical potential $\dot{\bar{\mu}}$ is integrated in time using a backward-Euler time integration scheme. For example, the general equation

$$\dot{\bar{\mu}} = \mathcal{F}(t), \quad (3.14)$$

can be discretized as

$$\frac{\bar{\mu}^{n+1} - \bar{\mu}^n}{\Delta t} = \mathcal{F}(t^{n+1}). \quad (3.15)$$

In the enriched-continuum formulation, the microscopic transient effects are captured at the macro-scale through the enrichment-variables $\underline{\eta}$. This allows to compute the transient effects, present at the micro-scale, on a coarse macroscopic mesh. In the internal-variable solution method, the internal-variables $\underline{\eta}$ are condensed out of the final system of equations, therefore different time integration schemes can be used for equations (3.6) and (3.13). Following the literature on visco-elasticity, as recalled in [68], a one-step second-order accurate time integrator can be obtained by writing equation (3.13) in a convolution form

$$\underline{\eta} = \exp^{[-\alpha t]} \int_0^t \exp^{[\alpha s]} \left[-\underline{\underline{\mathbf{a}}}^* \cdot \nabla \dot{\bar{\mu}}(s) - \underline{\underline{\mathbf{d}}}^* \dot{\bar{\mu}}(s) \right] ds. \quad (3.16)$$

Using the semi-group property of an exponential and the additive property of an integral, the approximation in (3.16) can be written as

$$\underline{\eta}^{n+1} = \underline{\eta}^n \exp^{[-\alpha \Delta t]} + \int_{t^n}^{t^{n+1}} \exp^{[-\alpha(t+\Delta t-s)]} \left[-\underline{\underline{\mathbf{a}}}^* \cdot \nabla \dot{\bar{\mu}}(s) - \underline{\underline{\mathbf{d}}}^* \dot{\bar{\mu}}(s) \right] ds. \quad (3.17)$$

A midpoint approximation of the integral in equation (3.17) provides a one-step second-order accurate time integration scheme to evaluate $\underline{\eta}^{n+1}$,

$$\underline{\eta}^{n+1} = \underline{\eta}^n \exp^{[-\alpha \Delta t]} + \exp^{[-\alpha \Delta t/2]} \left[-\underline{\underline{\mathbf{a}}}^* \cdot (\nabla \bar{\mu}^{n+1} - \nabla \bar{\mu}^n) - \underline{\underline{\mathbf{d}}}^* (\bar{\mu}^{n+1} - \bar{\mu}^n) \right], \quad (3.18)$$

which, as argued in [68], is unconditionally stable. This second-order accurate scheme will be compared to the first-order accurate backward-Euler scheme for which the approximation for $\underline{\eta}^{n+1}$ is given by

$$\underline{\eta}^{n+1} = (\underline{I} + \Delta t \underline{\alpha})^{-1} \left[\underline{\eta}^n - \underline{\underline{\mathbf{a}}}^* \cdot (\nabla \bar{\mu}^{n+1} - \nabla \bar{\mu}^n) - \underline{\underline{\mathbf{d}}}^* (\bar{\mu}^{n+1} - \bar{\mu}^n) \right]. \quad (3.19)$$

3.3.2 Multi-Field Method

In a multi-field approach, the primary field $\bar{\mu}$ as well as the enrichment field $\underline{\eta}$, are discretized on a finite element mesh. A combined residual $\bar{\mathcal{Q}}(\bar{\mu}, \delta \bar{\mu}, \underline{\eta}, \delta \underline{\eta})$ is formulated by multiplying the macroscopic mass balance equation (3.6) and the evolution equation (3.13) with the appropriate admissible test functions $\delta \bar{\mu}$ and

$\delta\eta$, respectively

$$\begin{aligned}\bar{\mathcal{Q}}(\bar{\mu}, \delta\bar{\mu}; \underline{\eta}, \delta\underline{\eta}) &= \bar{\mathcal{R}}(\bar{\mu}, \delta\bar{\mu}) + \bar{\mathcal{E}}(\underline{\eta}, \delta\underline{\eta}) = 0 \\ &= \int_{\bar{\Omega}} \delta\bar{\mu} (\nabla \cdot \bar{\mathbf{j}} + \dot{\bar{c}}) \, d\bar{v} + \int_{\bar{\Omega}} \delta\underline{\eta} \left(\dot{\underline{\eta}} + \underline{\alpha}\underline{\eta} + \underline{\bar{\mathbf{a}}} \cdot \nabla \dot{\underline{\mu}} + \underline{\bar{d}}\dot{\underline{\mu}} \right) \, d\bar{v} = 0.\end{aligned}\quad (3.20)$$

where, $\bar{\mathcal{R}}(\bar{\mu}, \delta\bar{\mu})$ and $\bar{\mathcal{E}}(\underline{\eta}, \delta\underline{\eta})$ are the individual residuals for the weighted residual form of the equations (3.6) and (3.13). Integrating by parts and applying the divergence theorem on $\bar{\mathcal{R}}(\bar{\mu}, \delta\bar{\mu})$, provides the weak form as follows

$$\begin{aligned}\bar{\mathcal{Q}}(\bar{\mu}, \delta\bar{\mu}; \underline{\eta}, \delta\underline{\eta}) &= - \int_{\bar{\Omega}} \nabla \delta\bar{\mu} \cdot \bar{\mathbf{j}} \, d\bar{v} + \int_{\bar{\Omega}} \delta\bar{\mu} \dot{\bar{c}} \, d\bar{v} + \int_{\partial\bar{\Omega}} \delta\bar{\mu} \bar{j}_{\bar{\mathbf{n}}} \, d\bar{a} \\ &\quad + \int_{\bar{\Omega}} \delta\underline{\eta} \left(\dot{\underline{\eta}} + \underline{\alpha}\underline{\eta} + \underline{\bar{\mathbf{a}}} \cdot \nabla \dot{\underline{\mu}} + \underline{\bar{d}}\dot{\underline{\mu}} \right) \, d\bar{v} = 0,\end{aligned}\quad (3.21)$$

where $\bar{j}_{\bar{\mathbf{n}}} = -\bar{\mathbf{j}} \cdot \bar{\mathbf{n}}$ is the mass flux through the macroscopic boundary $\partial\bar{\Omega}_{\bar{\mathbf{j}}}$, $\bar{\mathbf{n}}$ is the outward unit normal, $d\bar{v}$ and $d\bar{a}$ is the small differential volume and area elements associated to the domain $\bar{\Omega}$. Substituting the constitutive expressions (3.11) and (3.12) for the macroscopic flux $\bar{\mathbf{j}}$ and the macroscopic chemical concentration rate $\dot{\bar{c}}$ yields a coupled system in terms of $\bar{\mu}$ and $\underline{\eta}$,

$$\begin{aligned}\bar{\mathcal{Q}}(\bar{\mu}, \delta\bar{\mu}; \underline{\eta}, \delta\underline{\eta}) &= \int_{\bar{\Omega}} \nabla \delta\bar{\mu} \cdot \left[\underline{\bar{\mathbf{a}}}^T \underline{\eta} + \bar{\mathbf{B}} \cdot \nabla \bar{\mu} + \bar{\mathbf{c}}\dot{\bar{\mu}} + \bar{\mathbf{C}} \cdot \nabla \dot{\bar{\mu}} \right] \, d\bar{v} \\ &\quad + \int_{\bar{\Omega}} \delta\bar{\mu} \left[\underline{\bar{d}}^T \underline{\eta} + \bar{\mathbf{e}} \cdot \nabla \bar{\mu} + \bar{\mathbf{f}}\dot{\bar{\mu}} + \bar{\mathbf{f}} \cdot \nabla \dot{\bar{\mu}} \right] \, d\bar{v} \\ &\quad + \int_{\bar{\Omega}} \delta\underline{\eta} \left(\dot{\underline{\eta}} + \underline{\alpha}\underline{\eta} + \underline{\bar{\mathbf{a}}} \cdot \nabla \dot{\underline{\mu}} + \underline{\bar{d}}\dot{\underline{\mu}} \right) \, d\bar{v} + \int_{\partial\bar{\Omega}} \delta\bar{\mu} \bar{j}_{\bar{\mathbf{n}}} \, d\bar{a} = 0.\end{aligned}\quad (3.22)$$

3.3.2.1 Finite element implementation

In the multi-field solution method, the macroscopic variable $\bar{\mu}$ and the enrichment-variables $\underline{\eta}$ are interpolated using the finite element nodal shape functions

$$\bar{\mu} = \sum_{I=1}^{\mathcal{N}_e} N^I \bar{\mu}^I = \underline{N}_{\bar{\mu}}^T \underline{\bar{\mu}}, \quad \text{and} \quad \underline{\eta} = \sum_{I=1}^{\mathcal{N}_e} N^I \underline{\eta}^I = \underline{N}_{\underline{\eta}}^T \{\underline{\eta}\}, \quad (3.23)$$

where, N^I is the shape function value associated to the I -th node of an element and \mathcal{N}_e is the number of nodes in an element. $\underline{N}_{\bar{\mu}}$ and $\underline{N}_{\underline{\eta}}$ are the column and

matrix, respectively, containing the respective shape functions and $\underline{\tilde{\mu}}$ is the column of the degrees of freedom of $\bar{\mu}$, while $\{\eta\} = \{\eta_1^{(1)} \dots \eta_{N_q}^{(1)}, \eta_1^{(2)} \dots \eta_{N_q}^{(2)}, \dots, \eta_1^{(N_e)} \dots \eta_{N_q}^{(N_e)}\}$ is the column vector of degrees of freedom of the vector fields $\underline{\eta}$ containing the nodal enrichment degree of freedoms. Equation (3.22), can then be written in discrete form as

$$\delta \underline{\tilde{\mu}}^T \underbrace{(\underline{B}_1 + \underline{E}_1)}_{\mathbb{K}} \underline{\tilde{\mu}} + \delta \underline{\tilde{\mu}}^T \underbrace{(\underline{C}_1 + \underline{C}_2 + \underline{F}_1 + \underline{F}_2)}_{\mathbb{M}} \dot{\underline{\tilde{\mu}}} + \delta \underline{\tilde{\mu}}^T \underbrace{(\underline{A} + \underline{D})}_{\mathbb{N}} \{\dot{\eta}\} + \delta \{\eta\}^T \underline{\mathcal{E}} \{\dot{\eta}\} + \delta \{\eta\}^T \underline{\mathcal{A}} \{\eta\} + \delta \{\eta\}^T \underbrace{\left(\underline{\overset{*}{A}}^T + \underline{\overset{*}{D}}^T \right)}_{\overset{*}{\mathbb{N}}^T} \dot{\underline{\tilde{\mu}}} = \delta \underline{\tilde{\mu}}^T \underline{F}_{\bar{\mu}}. \quad (3.24)$$

The matrices in the above equation are given by

$$\begin{aligned} \underline{A} &= \int_{\Omega} \underline{N}_{\underline{\eta}}^T \underline{\tilde{\mathbf{a}}}^T \cdot \nabla \underline{N}_{\bar{\mu}} \, d\bar{v}, & \underline{B}_1 &= \int_{\Omega} (\nabla \underline{N}_{\bar{\mu}}^T \cdot \underline{\bar{\mathbf{B}}}) \cdot \nabla \underline{N}_{\bar{\mu}} \, d\bar{v}, \\ \underline{C}_1 &= \int_{\Omega} \underline{N}_{\bar{\mu}}^T \underline{\tilde{\mathbf{c}}} \cdot \nabla \underline{N}_{\bar{\mu}} \, d\bar{v}, & \underline{C}_2 &= \int_{\Omega} (\nabla \underline{N}_{\bar{\mu}}^T \cdot \underline{\bar{\mathbf{C}}}) \cdot \nabla \underline{N}_{\bar{\mu}} \, d\bar{v}, \\ \underline{D} &= \int_{\Omega} \underline{N}_{\underline{\eta}}^T \underline{\tilde{\mathbf{d}}}^T \underline{N}_{\bar{\mu}} \, d\bar{v}, & \underline{E}_1 &= \int_{\Omega} \nabla \underline{N}_{\bar{\mu}}^T \cdot \underline{\tilde{\mathbf{e}}} \underline{N}_{\bar{\mu}} \, d\bar{v}, \\ \underline{F}_1 &= \int_{\Omega} \underline{N}_{\bar{\mu}}^T \underline{\tilde{\mathbf{f}}} \underline{N}_{\bar{\mu}} \, d\bar{v}, & \underline{F}_2 &= \int_{\Omega} \nabla \underline{N}_{\bar{\mu}}^T \cdot \underline{\tilde{\mathbf{f}}} \underline{N}_{\bar{\mu}} \, d\bar{v}, \\ \underline{\mathcal{E}} &= \int_{\Omega} \underline{N}_{\underline{\eta}}^T \underline{N}_{\underline{\eta}} \, d\bar{v}, & \underline{\mathcal{A}} &= \int_{\Omega} \underline{N}_{\underline{\eta}}^T \underline{\alpha} \underline{N}_{\underline{\eta}} \, d\bar{v}, \\ \underline{F}_{\bar{\mu}} &= - \int_{\partial\Omega} \underline{N}_{\bar{\mu}}^T \underline{\tilde{j}}_n^n \, d\bar{a}, & \underline{\overset{*}{D}} &= \int_{\Omega} \underline{N}_{\underline{\eta}}^T \underline{\tilde{\mathbf{d}}}^T \underline{N}_{\bar{\mu}} \, d\bar{v}, \\ \underline{\overset{*}{A}} &= \int_{\Omega} \underline{N}_{\underline{\eta}}^T \underline{\tilde{\mathbf{a}}}^T \cdot \nabla \underline{N}_{\bar{\mu}} \, d\bar{v}. \end{aligned}$$

Taking into account that equation (3.24) should hold for all admissible $\delta \underline{\tilde{\mu}}$ and $\delta \{\eta\}$ provides

$$\begin{aligned} \mathbb{K} \underline{\tilde{\mu}} + \mathbb{M} \dot{\underline{\tilde{\mu}}} + \mathbb{N} \{\dot{\eta}\} &= \underline{F}_{\bar{\mu}}, \\ \overset{*}{\mathbb{N}}^T \dot{\underline{\tilde{\mu}}} + \underline{\mathcal{E}} \{\dot{\eta}\} + \underline{\mathcal{A}} \{\eta\} &= \mathbf{0}. \end{aligned} \quad (3.25)$$

In the multi-field method, $\{\dot{\eta}\}$ appears in the final equation together with $\dot{\underline{\tilde{\mu}}}$, which suggests the same time integration scheme for both variables. Selecting the backward-Euler time integration scheme (3.15) for both $\dot{\underline{\tilde{\mu}}}$ and $\{\dot{\eta}\}$, we obtain

$$\Delta t \mathbb{K} \underline{\tilde{\mu}}^{n+1} + \mathbb{M} (\underline{\tilde{\mu}}^{n+1} - \underline{\tilde{\mu}}^n) + \mathbb{N} (\{\eta\}^{n+1} - \{\eta\}^n) = -\Delta t \underline{F}_{\bar{\mu}}, \quad (3.26)$$

$$\overset{*}{\mathbb{N}}^T (\underline{\tilde{\mu}}^{n+1} - \underline{\tilde{\mu}}^n) + \Delta t \underline{\mathcal{A}} \{\eta\}^{n+1} + \underline{\mathcal{E}} (\{\eta\}^{n+1} - \{\eta\}^n) = \mathbf{0}. \quad (3.27)$$

Rearranging terms to gather all the unknowns at time t^{n+1} on the left hand side, the coupled system of equations to be solved at each time step can be written as

$$\begin{bmatrix} \Delta t \underline{\mathbb{K}} + \underline{\mathbb{M}} & \underline{\mathbb{N}} \\ \underline{\mathbb{N}}^{*T} & \Delta t \underline{\mathcal{A}} + \underline{\mathcal{E}} \end{bmatrix} \begin{Bmatrix} \underline{\tilde{\mu}}^{n+1} \\ \{\eta\}^{n+1} \end{Bmatrix} = \begin{Bmatrix} -\Delta t \underline{\mathcal{F}}_{\tilde{\mu}} + \underline{\mathbb{M}} \underline{\tilde{\mu}}^n + \underline{\mathbb{N}} \{\eta\}^n \\ \underline{\mathbb{N}}^{*T} \underline{\tilde{\mu}}^n + \underline{\mathcal{E}} \{\eta\}^n \end{Bmatrix}. \quad (3.28)$$

3.3.3 Internal-Variable method

In the internal-variable method, the macroscopic chemical potential $\bar{\mu}$ is interpolated using finite element nodal shape functions, while the evolution equation (3.13) for $\dot{\eta}$ is integrated at the macroscopic Gauss quadrature points. The residual $\mathcal{R}(\bar{\mu}, \delta\bar{\mu})$ is built by multiplying equation (3.6) with an admissible test function $\delta\bar{\mu}$

$$\bar{\mathcal{R}}(\bar{\mu}, \delta\bar{\mu}) = \int_{\bar{\Omega}} \delta\bar{\mu} (\bar{\nabla} \cdot \bar{\mathbf{j}} + \dot{c}) d\bar{v} = 0, \quad (3.29)$$

which, after applying integration by parts and the divergence theorem, takes the following form

$$\bar{\mathcal{R}}(\bar{\mu}, \delta\bar{\mu}) = - \int_{\bar{\Omega}} \bar{\nabla} \delta\bar{\mu} \cdot \bar{\mathbf{j}} d\bar{v} + \int_{\bar{\Omega}} \delta\bar{\mu} \dot{c} d\bar{v} + \int_{\partial\bar{\Omega}} \delta\bar{\mu} \bar{j}_{\bar{n}} d\bar{a} = 0. \quad (3.30)$$

Substituting the expressions for the macroscopic flux from equation (3.11) and the concentration rate from equation (3.12), the weak form of equation (3.30) can then be written as

$$\begin{aligned} \bar{\mathcal{R}}(\bar{\mu}, \delta\bar{\mu}) = & \int_{\bar{\Omega}} \bar{\nabla} \delta\bar{\mu} \cdot \left[\bar{\underline{\mathbf{a}}}^T \dot{\eta} + \bar{\underline{\mathbf{B}}} \cdot \bar{\nabla} \bar{\mu} + \bar{\underline{\mathbf{c}}} \dot{\mu} + \bar{\underline{\mathbf{C}}} \cdot \bar{\nabla} \dot{\mu} \right] d\bar{v} \\ & + \int_{\bar{\Omega}} \delta\bar{\mu} \left[\bar{\underline{\mathbf{d}}}^T \dot{\eta} + \bar{\underline{\mathbf{e}}} \cdot \bar{\nabla} \bar{\mu} + \bar{\underline{\mathbf{f}}} \dot{\mu} + \bar{\underline{\mathbf{f}}} \cdot \bar{\nabla} \dot{\mu} \right] d\bar{v} + \int_{\partial\bar{\Omega}} \delta\bar{\mu} \bar{j}_{\bar{n}} d\bar{a} = 0. \end{aligned} \quad (3.31)$$

3.3.3.1 Finite element implementation

Here, as an example, the derivation is performed using the backward-Euler time integration scheme for both $\bar{\mu}$ and η ; a similar derivation applies to the integral form given by equation (3.18). Using the finite element discretization (3.23) only

for $\bar{\mu}$, equation (3.31) takes the following form

$$\begin{aligned}
 & \int_{\bar{\Omega}} \bar{\nabla} N_{\bar{\mu}}^T \delta \bar{\mu} \cdot (\bar{\mathbf{a}}^T \bar{\eta}^{n+1}) d\bar{v} + \int_{\bar{\Omega}} N_{\bar{\mu}}^T \delta \bar{\mu} (\bar{\mathbf{d}}^T \bar{\eta}^{n+1}) d\bar{v} \\
 & \quad + \delta \bar{\mu}^T [\Delta t \bar{\mathbf{B}} + \bar{\mathbf{c}} + \bar{\mathbf{C}} + \Delta t \bar{\mathbf{E}} + \bar{\mathbf{f}} + \bar{\mathbf{F}}] \bar{\mu}^{n+1} \\
 & = -\Delta t \int_{\partial \bar{\Omega}} N_{\bar{\mu}}^T \delta \bar{\mu} \bar{j}_{\bar{n}}^{n+1} d\bar{a} + \delta \bar{\mu}^T \bar{\mathbf{A}}^n + \delta \bar{\mu}^T \bar{\mathbf{D}}^n \\
 & \quad + \delta \bar{\mu}^T [\bar{\mathbf{c}} + \bar{\mathbf{C}} + \bar{\mathbf{f}} + \bar{\mathbf{F}}] \bar{\mu}^n, \quad (3.32)
 \end{aligned}$$

where the matrices are calculated using

$$\begin{aligned}
 \bar{\mathbf{B}} &= \int_{\bar{\Omega}} \bar{\nabla} N_{\bar{\mu}}^T \cdot \bar{\mathbf{B}} \cdot \bar{\nabla} N_{\bar{\mu}} d\bar{v}, \quad \bar{\mathbf{c}} = \int_{\bar{\Omega}} \bar{\nabla} N_{\bar{\mu}}^T \bar{\mathbf{c}} N_{\bar{\mu}} d\bar{v}, \quad \bar{\mathbf{C}} = \int_{\bar{\Omega}} \bar{\nabla} N_{\bar{\mu}}^T \cdot \bar{\mathbf{C}} \cdot \bar{\nabla} N_{\bar{\mu}} d\bar{v}, \\
 \bar{\mathbf{E}} &= \int_{\bar{\Omega}} N_{\bar{\mu}}^T \bar{\mathbf{e}} \cdot \bar{\nabla} N_{\bar{\mu}} d\bar{v}, \quad \bar{\mathbf{f}} = \int_{\bar{\Omega}} N_{\bar{\mu}}^T \bar{\mathbf{f}} N_{\bar{\mu}} d\bar{v}, \quad \bar{\mathbf{F}} = \int_{\bar{\Omega}} N_{\bar{\mu}}^T \bar{\mathbf{f}} \cdot \bar{\nabla} N_{\bar{\mu}} d\bar{v}, \\
 \bar{\mathbf{A}}^n &= \int_{\bar{\Omega}} \bar{\nabla} N_{\bar{\mu}}^T \cdot \bar{\mathbf{a}}^* \bar{\eta}^n d\bar{v}, \quad \bar{\mathbf{D}}^n = \int_{\bar{\Omega}} N_{\bar{\mu}}^T \bar{\mathbf{d}}^* \bar{\eta}^n d\bar{v}.
 \end{aligned}$$

Next, substitution of the expression for $\bar{\eta}^{n+1}$ from (3.19) into the above equation leads to

$$\begin{aligned}
 & \delta \bar{\mu}^T \underbrace{[\Delta t (\bar{\mathbf{B}} + \bar{\mathbf{E}}) + \bar{\mathbf{c}} + \bar{\mathbf{C}} + \bar{\mathbf{f}} + \bar{\mathbf{F}} + \bar{\mathbf{A}}^1 + \bar{\mathbf{A}}^2 + \bar{\mathbf{A}}^4 + \bar{\mathbf{A}}^5]}_{\bar{\mathbf{K}}} \bar{\mu}^{n+1} \\
 & = \underbrace{\delta \bar{\mu}^T \bar{\mathbf{A}}^n + \delta \bar{\mu}^T \bar{\mathbf{D}}^n + \delta \bar{\mu}^T \bar{\mathbf{A}}^3 + \delta \bar{\mu}^T \bar{\mathbf{A}}^6 + \delta \bar{\mu}^T [\bar{\mathbf{c}} + \bar{\mathbf{C}} + \bar{\mathbf{f}} + \bar{\mathbf{F}}] \bar{\mu}^n}_{\delta \bar{\mu}^T \bar{\mathbf{F}}_{\text{int}}^n} + \\
 & \quad \underbrace{-\Delta t \int_{\partial \bar{\Omega}} N_{\bar{\mu}}^T \delta \bar{\mu} \bar{j}_{\bar{n}}^{n+1} d\bar{a}}_{\delta \bar{\mu}^T \bar{\mathbf{F}}_{\text{ext}}^{n+1}} \quad (3.33)
 \end{aligned}$$

where the finite element matrices are recognized as

$$\begin{aligned}
 \bar{\mathbf{A}}^1 &= \int_{\bar{\Omega}} \bar{\nabla} N_{\bar{\mu}}^T \cdot (\bar{\mathbf{a}}^T \bar{\mathcal{A}} \bar{\mathbf{a}}^*) \cdot \bar{\nabla} N_{\bar{\mu}} d\bar{v}, & \bar{\mathbf{A}}^2 &= \int_{\bar{\Omega}} \bar{\nabla} N_{\bar{\mu}}^T \cdot (\bar{\mathbf{a}}^T \bar{\mathcal{A}} \bar{\mathbf{d}}^*) N_{\bar{\mu}} d\bar{v}, \\
 \bar{\mathbf{A}}^3 &= \int_{\bar{\Omega}} \bar{\nabla} N_{\bar{\mu}}^T \cdot (\bar{\mathbf{a}}^T \bar{\mathcal{A}} \bar{\eta}^n) d\bar{v}, & \bar{\mathbf{A}}^4 &= \int_{\bar{\Omega}} N_{\bar{\mu}}^T (\bar{\mathbf{d}}^T \bar{\mathcal{A}} \bar{\mathbf{a}}^*) \cdot \bar{\nabla} N_{\bar{\mu}} d\bar{v}, \\
 \bar{\mathbf{A}}^5 &= \int_{\bar{\Omega}} N_{\bar{\mu}}^T (\bar{\mathbf{d}}^T \bar{\mathcal{A}} \bar{\mathbf{d}}^*) N_{\bar{\mu}} d\bar{v}, & \bar{\mathbf{A}}^6 &= \int_{\bar{\Omega}} N_{\bar{\mu}}^T (\bar{\mathbf{d}}^T \bar{\mathcal{A}} \bar{\eta}^n) d\bar{v}.
 \end{aligned}$$

here $\bar{\mathcal{A}} = (\bar{\mathbf{I}} + \Delta t \bar{\alpha})^{-1}$. Finally, taking into account that equation (3.33) should hold for all $\delta \bar{\mu}$, the system of linear equations to be solved at each time step is given by

$$\bar{\mathbf{K}} \bar{\mu}^{n+1} = \bar{\mathbf{F}}_{\text{ext}}^{n+1} + \bar{\mathbf{F}}_{\text{int}}^n. \quad (3.34)$$

Once the solution for the chemical potential field $\underline{\mu}^{n+1}$ is known, $\underline{\eta}^{n+1}$ is calculated using equation (3.19) (or (3.18) if the second-order accurate scheme is used for $\underline{\eta}$) at the Gauss integration point.

3.4 Numerical Examples

Numerical examples are conducted for species diffusion in a heterogeneous material with high contrast in properties, with slower diffusion in the inclusion than in the matrix. The microscopic domain is chosen to be a square unit-cell with a single centered circular inclusion, as shown in Figure 3.3. A chemical potential $\hat{\mu}$, harmonically varying in time is prescribed on the left side of the macroscopic boundary $\partial\bar{\Omega}_{\bar{\mu}}$ while a zero-flux boundary condition is applied on the top, right and bottom sides of the macroscopic boundary $\partial\bar{\Omega}_{\bar{j}}$. The prescribed chemical potential field and the boundary fluxes are given by

$$\begin{aligned} \hat{\mu}(t) &= \bar{\mu}_{\max}(1 - ax_2) \sin(\omega t), & \text{on } \partial\bar{\Omega}_{\bar{\mu}}, \forall x_2 \in [0, L_{x_2}] \\ \bar{j}_{\bar{n}} &= -\bar{j} \cdot \bar{n} = 0, & \text{on } \partial\bar{\Omega}_{\bar{j}}. \end{aligned} \quad (3.35)$$

$\bar{\mu}_{\max}$ is the maximum achievable chemical potential in the matrix, given by $\bar{\mu}_{\max} = \Lambda(c_{\max} - c_0)$, where $\Lambda = k_b T / c_0$ is the chemical modulus, c_{\max} and $c_0 = 0.19c_{\max}$ is the maximum and reference concentration values in the matrix, respectively. Using a non-zero parameter ‘ a ’ in equation (3.35) implies that the chemical potential field can be linearly varied along $\partial\bar{\Omega}_{\bar{\mu}}$; in (3.35) $\omega = \frac{2\pi}{T}$ is the angular loading frequency and T is the total loading time. The material properties, length scales and the loading conditions are such that the relaxed separation of scales (3.1) is satisfied. The default parameters for the geometry, material and mesh are given in Table 3.1. To obtain the enrichment-functions and construct the coefficient terms for equations (3.11), (3.12) and (3.13), according to the expressions given in Appendix A.1, an eigenvalue problem with the periodic boundary conditions is solved on the unit-cell. The eigenvectors corresponding to the relatively higher values of the coupling terms \bar{d} and \bar{a} are chosen to constitute a reduced basis set; for more discussion on the selection of the reduced basis see [67]. The selected enrichment-functions $\Phi^{(k)}$ for the considered unit-cell are shown in Figure 3.4. To solve the eigenvalue problem, a converged unit-cell mesh consisting of ~ 4400 linear triangular elements (~ 2200 nodes) was used. The DNS domain was discretized accordingly, with approximately the same number of linear triangular elements in each unit-cell. The macroscopic homogenized domain $\bar{\Omega}$, replacing the DNS

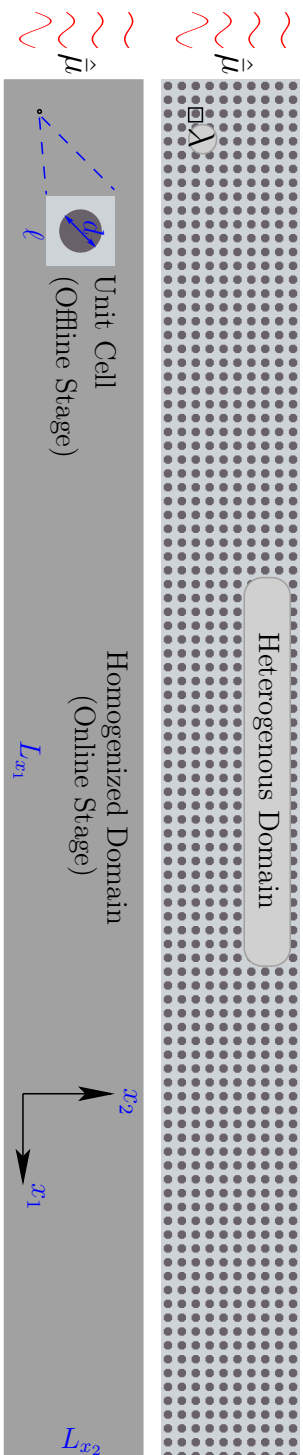


Figure 3.3: Problem settings: Top: a heterogeneous domain with 1000 unit-cells. 100 in x_1 -direction and 10 in x_2 -direction. Bottom: corresponding homogenized domain for the solution of the enriched-continuum formulation. The unit-cell shown inside is used to obtain the coupling terms in equations (3.11) and (3.12) in the off-line stage. The material properties and geometrical parameters are provided in Table 3.1.

Table 3.1: Parameters used in the simulation.

Parameter	Symbol	Value	Units
Characteristic unit-cell length	ℓ	1×10^{-2}	[m]
Inclusion diameter	d	0.6×10^{-2}	[m]
Mobility in matrix	M_m	1.1×10^{-4}	$[\text{mol}^2 \text{J}^{-1} \text{m}^{-1} \text{s}^{-1}]$
Mobility in inclusion	M_i	1.85×10^{-9}	$[\text{mol}^2 \text{J}^{-1} \text{m}^{-1} \text{s}^{-1}]$
Reference temperature	θ_0	298	[K]
Boltzman's constant	k_b	8.314	$[\text{J K}^{-1} \text{mol}^{-1}]$
Maximum concentration	c_{\max}	24161	$[\text{mol m}^{-3}]$
Minimum concentration	c_0	$0.19c_{\max}$	$[\text{mol m}^{-3}]$
Chemical modulus	$\Lambda = k_b \theta_0 / c_0$	1.83	$[\text{J m}^3 \text{mol}^{-2}]$
Macroscopic length in x_1 -direction	L_{x_1}	100×10^{-2}	[m]
Macroscopic length in x_2 -direction	L_{x_2}	10×10^{-2}	[m]
Parameter in equation (3.35)	a	0.03	
Characteristic diffusion time of inclusion	τ_i	$\frac{d^2}{M_i \Lambda} = 36000$	[s]
Characteristic diffusion time of matrix	τ_m	$\frac{\ell^2}{M_m \Lambda} = 1.69$	[s]
Total loading time	T	$0.1\tau_i$	[s]
Number of nodes in unit-cell mesh		$\sim 2.2 \times 10^3$	
Number of nodes in DNS mesh		$\sim 2.1 \times 10^6$	

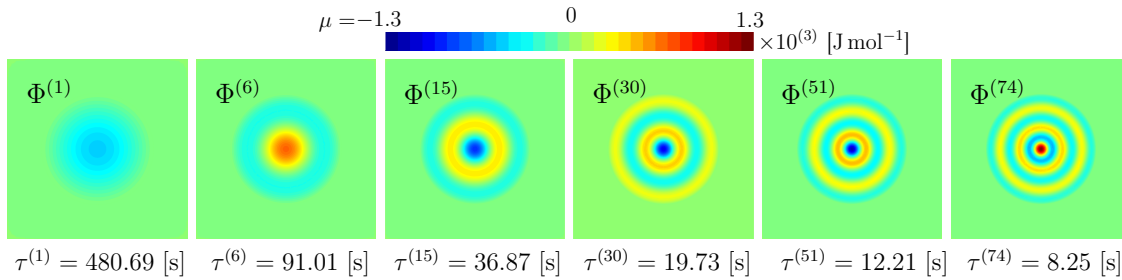


Figure 3.4: The selected enrichment-functions $\Phi^{(k)}$ obtained by solving the generalized eigenvalue problem (A.7) for mass diffusion equation (3.8). An associated decay/rise time $\tau^{(k)} = \frac{1}{\alpha^{(k)}}$, with $\alpha^{(k)}$ the k-th eigenvalue, is also given for each enrichment-function $\Phi^{(k)}$.

domain, is discretized with rectangular four node bi-linear elements for both $\bar{\mu}$ and $\underline{\eta}$ in the multi-field method, or for $\bar{\mu}$ only in the internal variable method. The effect of the macroscopic mesh size on the homogenized results will be discussed in section 3.4.3. The smallest and the largest element size in the macroscopic domain are ℓ and 10ℓ , respectively. A default time step size of $\Delta t = 3.6 \text{ [s]}$ is used in all the simulations unless otherwise stated.

3.4.1 Accuracy of the Time Integration Schemes for the Internal-Variable Method

In the internal variable method, the time integration for $\dot{\bar{\mu}}$ and $\dot{\underline{\eta}}$ can be chosen independently. In section 3.3, two different time integration schemes for the approximation of $\dot{\underline{\eta}}$ were presented, i.e., a second-order accurate approximation in equation (3.18) and a first-order accurate approximation in equation (3.19). In this regard, simulations were performed using the internal-variable method on a mesh of $nel_{x_1} \times nel_{x_2} = 50 \times 5$ elements, where nel_{x_1} and nel_{x_2} are the number of elements in x_1 and x_2 direction, respectively. For each time integration scheme, a reference solution $\underline{\eta}_{ref}^{(1)}(t)$, which is the column of enrichment-variables in time, is taken as the one with a time step size of $\Delta t = 3.6 \times 10^{-2} \text{ [s]}$. Then, a relative error for the first enrichment-variable $\underline{\eta}^{(1)}(t)$ is computed by

$$err_{\Delta t} := \frac{\|\underline{\eta}^{(1)}(t) - \underline{\eta}_{ref}^{(1)}(t)\|}{\|\underline{\eta}_{ref}^{(1)}(t)\|}. \quad (3.36)$$

where, $\|\bullet\|$ is the vector Frobenius norm. The enrichment variable $\underline{\eta}^{(1)}(t)$ was stored at the Gauss integration point located at $\mathbf{x} = (4.2, 4.2) \times 10^{-4} \text{ [m]}$ in the

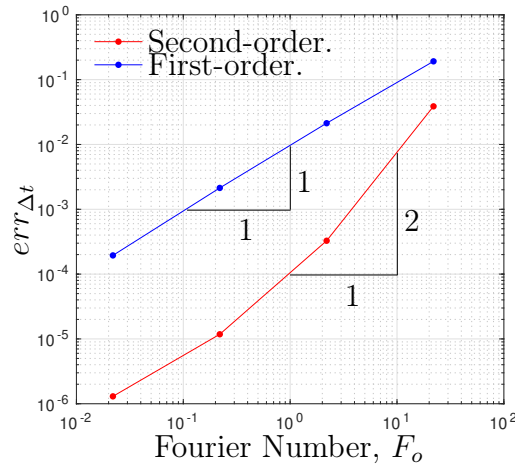


Figure 3.5: Error analysis for the local time integration schemes, to be used with the internal variable method. The one step second-order accurate time integrator, equation (3.18) reveals a higher accuracy than the first-order backward-Euler time integrator, (3.19). The expression for $err_{\Delta t}$ is given in equation (3.36).

first element. In this example, a characteristic element length $\ell_e = 1 \times 10^{-2}$ [m] was used and the time step size Δt was varied resulting in different values of the Fourier number $F_o = \mathcal{D}_{11}^{eff} \frac{\Delta t}{\ell_e^2}$, where \mathcal{D}_{11}^{eff} is the first component of the effective macroscopic diffusivity tensor $\mathcal{D}^{eff} = \Lambda \bar{\mathbf{B}}$, the effective mobility $\bar{\mathbf{B}}$ is given in (A.9). The results are shown in Figure 3.5. As expected, the backward-Euler first-order time integration scheme converges with a rate of convergence equal to one, while the time integration scheme given in equation (3.18) converges with a rate of convergence of almost two, providing a more accurate approximation of $\dot{\eta}$. However, the second-order method changes towards to first-order accuracy, which due to the backward-Euler time integration scheme used at the macro-scale which limits the overall convergence rate. For example, for the default time step size of $\Delta t = 3.6$ [s], the second-order scheme provides three orders more accurate result than the backward-Euler time integration method. Since the second-order scheme given by equation (3.18) is a one-step time integration scheme, no extra memory or computational costs are associated with it. Therefore, it is suggested to use the second-order accurate time integration scheme whenever possible to capture the transient effects more accurately.

3.4.2 Homogenized Solution

Next, the results computed using the homogenized enriched-continuum formulation are compared to the direct numerical simulations (DNS). To do so, the DNS

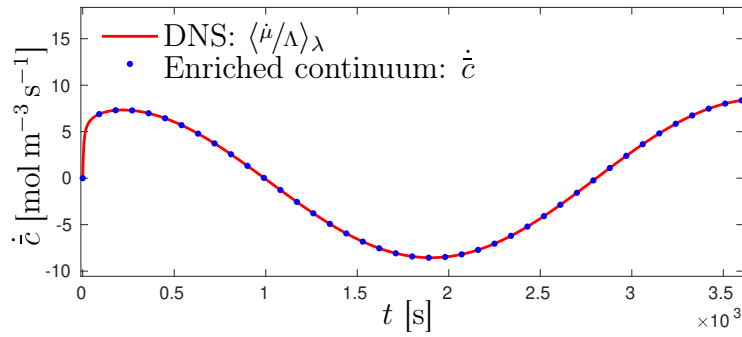


Figure 3.6: Comparison between the macroscopic concentration rate $\dot{\bar{c}}(\bar{\mathbf{x}}, t)$, computed with equation (3.12), and the DNS solution $\langle \dot{\mu} \rangle_{\lambda}$ averaged over the unit-cell sized domain λ around a point $\mathbf{x} = \bar{\mathbf{x}} = (2.5, 2.5) \times 10^{-2}[\text{m}]$. The homogenized solution is computed using the internal-variable method and plotted with a blue marker every 25th time step.

solution $\mu(\mathbf{x}, t)$ is averaged over the heterogeneous unit-cell sized domain λ around the point $\mathbf{x} = (2.5, 2.5) \times 10^{-2}[\text{m}]$, as shown in Figure 3.3 with a small square. In this example, the homogenized domain was discretized with $nel_{x_1} \times nel_{x_2} = 10 \times 3$ elements, with four Gauss quadrature points (ngp) per element. Figure 3.6 shows the time evolution of the macroscopic concentration rate $\dot{\bar{c}}(\bar{\mathbf{x}}, t)$, given by equation (3.12), and the averaged DNS solution $\langle \dot{\mu} \rangle_{\lambda}$. These results are in perfect agreement with each other, which demonstrates the ability of the enriched-continuum formulation to capture the transient DNS solution.

3.4.3 Macroscopic Discretization Effect

In this section, the effect of the macroscopic mesh size (in both x_1 - and x_2 - directions), on the accuracy of the macroscopic solution, $\bar{\mu}$ is examined. The DNS solution is taken as the reference. The homogenization level ‘ h ’ is defined as the ratio between the number of unit-cells ‘ nuc ’ composing the DNS domain to the number of integration points to be solved in the homogenized domain. This provides an indicator for the trade-off between the accuracy and the computational cost. A higher h value indicates more homogenization, and thus lower computational costs. In a two-dimensional setting, with a quadrilateral discretization, the homogenization level can be written as

$$h := \frac{nuc}{nel_{x_1} \times nel_{x_2} \times ngp}. \quad (3.37)$$

In the subsequent simulations, the parameters, $nuc = 1000$ and $ngp = 4$ per element are fixed. The number of elements in x_1 - and x_2 -directions, nel_{x_1} and nel_{x_2} , are varied, resulting in a different value of h .

In figure 3.7, the heterogeneous chemical potential field μ , calculated with the direct numerical simulation (DNS) is compared with the homogenized chemical potential field $\bar{\mu}$, obtained by the enriched-continuum formulation solved with the multi-field method. The homogenization level h given in equation (3.37) is increased by decreasing the number of elements in the macroscopic domain, while keeping the ratio $nel_{x_2} = \frac{nel_{x_1}}{10}$ fixed. Different numbers of elements in x_1 -direction $nel_{x_1} = 50, 40, 30, 20, 10$ imply the following homogenization levels $h = 1, 1.56, 2.78, 6.25, 25$. At $h = 1$, where the number of unit-cells is the same in both the heterogeneous and homogenized domains, the enriched-continuum response captures the DNS almost perfectly. In this example, due to a non-homogeneous boundary condition on $\partial\bar{\Omega}_{\bar{\mu}}$, as given in equation (3.35), the homogenization problem requires high finite element density in x_2 -direction in the vicinity of $\partial\bar{\Omega}_{\bar{\mu}}$, lower element density is needed in x_1 -direction.

3.4.4 Computational Efficiency

Next, the efficiency of the proposed approach compared to the direct numerical simulations (DNS) and conventional computational transient homogenization (CTH) scheme is investigated. All simulations were performed on a computer with a core-i5@3.2GHz processor and 8Gb RAM using Matlab 2018b. It can be seen in Figure 3.8, that the CPU time increases for all the homogenization methods as $h \rightarrow 1$. The CTH is the most expensive among the considered methods, since (when implemented in its standard form) for each time increment at each macroscopic Gauss quadrature point it requires the solution of a micro-scale finite element problem (one computation of the effective flux and two sensitivity problems) followed by the assembly of the internal flux vector. For the complete solution procedure of the CTH see [8] and [9]. For low levels of homogenization, it becomes even more expensive than the DNS problem.

Since the enriched-continuum formulation replaces the microscopic finite element problem with a set of ordinary differential equations, the computational gains are remarkably high. The internal-variable solution method is a little more expensive than the multi-field method because it requires the assembly of the internal flux vector at each time increment using the data from the previous time step. In the internal variable method, the enrichment-variables are computed at

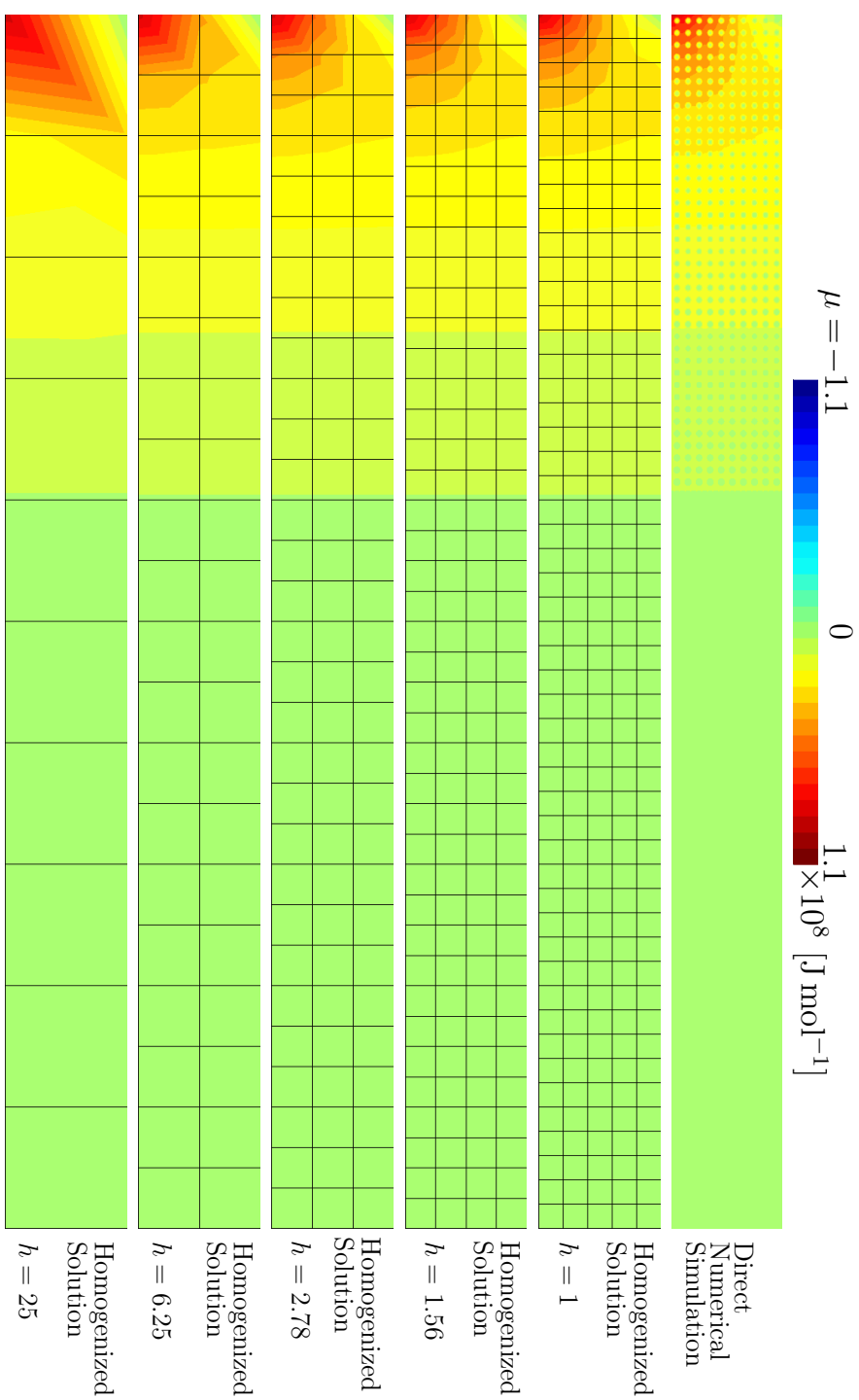


Figure 3.7: The chemical potential field μ in the heterogeneous domain (top plot) obtained by the direct numerical simulation (DNS). The homogenized chemical potential field $\bar{\mu}$ obtained by enriched-continuum formulation solved using multi-field method with increasing homogenization levels h (from the second plot to the bottom).

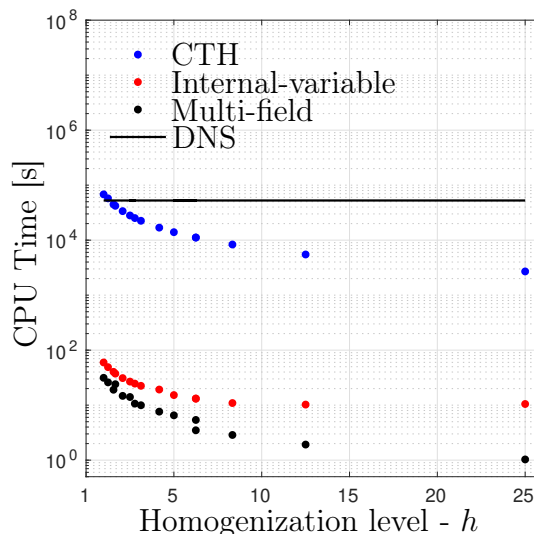


Figure 3.8: Computational effort in CPU time for different solution techniques (internal-variable and multi-field) for the enriched-continuum formulation, conventional computational transient homogenization (CTH) and direct numerical simulation (DNS).

the macroscopic Gauss quadrature points entailing higher memory requirements than the multi-field method, since the total number of integration points in the model is usually (much) larger than the total number of finite element nodes. The multi-field method is the least expensive because the finite element assembly is performed only once and it does not require the assembly of the internal flux vector at each time step. Moreover, if a reordering algorithm is used, such as Cuthill-McKee [69], the direct linear solvers can be optimized resulting in even lower computation times. The CPU time comparison has been performed for the same time integration scheme, i.e., backward-Euler, for all considered methods. Notice, however, that as discussed before, the internal variable methods allows for more flexibility, e.g., in the choice of different time integration schemes.

3.5 Conclusions

In this work, the enriched-continuum formulation, which emerges from model reduction at the micro-scale, is applied to the solution of a heterogeneous diffusion boundary value problem with pronounced microstructural transient effects. Different solution methods for the enriched-continuum transient diffusion problem formulation are discussed. These solution methods make use of two discrete spatial discretization schemes for the enrichment-variables. The primary macroscopic

field variable is always interpolated using the finite element shape functions, while the field of enrichment-variables can either be discretized using finite elements, leading to a multi-field solution method, or evaluated at the Gauss quadrature points, leading to an internal-variable solution method. To capture the transient effects more accurately, a one-step second-order accurate time integration scheme is proposed for the internal-variable method. Results for the enriched-continuum formulation with the proposed solution methods are compared with the conventional computational transient homogenization (CTH) scheme and direct numerical simulations (DNS). The proposed solution methods provide the same accuracy with respect to DNS as the expensive CTH with high gains in computational times. The CPU time and the memory requirements for the multi-field method was the lowest among the proposed solution methods.

Enriched-Continuum for Multi-scale Transient Diffusion Coupled to Mechanics

Reproduced from:

A. Waseem, T. Heuzé, L. Stainier, M.G.D. Geers, and V.G. Kouznetsova

Advanced Modeling and Simulation in Engineering Sciences, 7(1), 1-32, 2020

<https://doi.org/10.1186/s40323-020-00149-2>

Abstract

In this chapter, we present a computationally efficient homogenization technique for linear coupled diffusion-mechanics problems. It considers a linear chemo-mechanical material model at the fine scale, and relies on a full separation of scales between the time scales governing diffusion and mechanical phenomena, and a relaxed separation of scales for diffusion between the matrix and the inclusion. When the characteristic time scales associated with mass diffusion are large compared to those linked to the deformation, the mechanical problem can be considered to be quasi-static, and a full separation of scales can be assumed, whereas the diffusion problem remains transient. Using equivalence of the sum of virtual powers of internal and transient forces between the micro-scale and the macro-scale, a homogenization framework is derived for the mass diffusion, while for the mechanical case, considering its quasi-static nature, the classical equivalence of the virtual work of internal forces is used instead. Model reduction is then applied at the micro-scale. Assuming a relaxed separation of scales for diffusion phenomena, the microscopic fields are split into steady-state and transient parts, for which distinct reduced bases are extracted, using static condensation for the steady-state part and the solution of an eigenvalue problem for the transient part. The model reduction at the micro-scale results in emergent macroscopic enrichment field variables, evolution of which is described with a set of ordinary differential equations which are inexpensive to solve. The net result is a coupled diffusion-mechanics enriched-continuum at the macro-scale. Numerical examples are conducted for the cathode-electrolyte system characterizing of a lithium-ion battery. The proposed reduced order homogenization method is shown to be able to capture the coupled behavior of this system, whereby high computational gains are obtained relative to a full computational homogenization method.

4.1 Introduction

Coupled diffusion-mechanics problems arise in many application areas, when the diffusion of solute particles causes volumetric swelling of a host material, inducing chemical stresses which in turn affect the mass flux [70, 71]. It has a broad range of applications ranging from biological tissues to microelectromechanical systems devices. For example, the swelling of brain tissues, known as edema, due to water diffusion [72] or the bending of thin plates due to chemical saturation [73]. Another

typical example is the swelling of the active material due to the lithiation process in lithium-ion batteries [74], which is also governed by coupled diffusion-mechanics phenomena.

The fundamental physics behind coupled diffusion-mechanics takes place at the atomic scale where the atomic or ionic diffusion occurs [70, 75]. The diffusion rate of the solute particles and the swelling of the host material depends on the atomic size of the materials involved [76] and on the activation energy which causes the jump of atoms inside the crystal lattice [77]. The jump directions and the frequencies are affected by the stresses inside the material, which in turn alter the activation energy and hence the mass flux. At the continuum level, the diffusion of species are described as driven by the gradient of the chemical potential [78]. The induced chemical stresses affect the chemical potential, which in turn influences the mass flux in the material [78–81]; this is known as the Gorsky effect [82].

This chapter addresses the application of coupled diffusion-mechanics described by the simulation of swelling in lithium-ion batteries. A lithium-ion battery consists of four components: two electrodes - a cathode and an anode, an electrolyte and the separator. Through an electro-chemical reaction, the chemical energy is converted to electrical energy in a discharge cycle; the reverse reaction takes place during the charging cycle. During charging the chemical potential across the cell forces the lithium-ions to diffuse towards the anode compartment via the electrolyte while passing through the separator [83]. At the anode, the lithium-ions are deposited in the active particles during an intercalation process which increases the volume of the active particle. Upon discharging, a similar reaction occurs in which the lithium in the anode is oxidized into lithium-ions and electrons. The electrons flow through the external circuit to the cathode and lithium-ions diffuse towards the cathode where they intercalate into the active particles.

The amount of swelling of the active particles depends on the cathode and anode materials. For example, swelling in the cathode of up to 6.5% is reported in different lithium-metal-oxides and up to 10% in lithium-cobalt-oxide [84], Silicon-based anode active particles can swell up to 300% [85]. Even when the deformation of cathode materials is small, e.g., LiCoO_2 , LiMn_2O_3 and LiFePO_4 , the cyclic lithiation and delithiation of active particles leads to cracks and loss of contact with the matrix, which gradually results in a capacity loss and eventually failure of the battery [4, 86]. Hence, to design a longer lifetime and higher energy density batteries, simulation of coupled diffusion-mechanics is of primary importance [87, 88].

Most of the work done in the literature on the simulation of coupled diffusion-mechanics in batteries is based on the pioneering works of Larche and Cahn [89], in which a framework for solid-state diffusion was developed for compositional changes in the solid state [74]. In general, due to its multiphysics and multiscale nature, the simulation of lithium-ion batteries is a challenging task [4]. Analytical methods for the solution of coupled diffusion-mechanics problems are limited to simple geometrical shapes [90], therefore approximate solutions using numerical techniques such as finite elements are often required [4]. However, with a complex microstructures [91] and transient phenomena [92], the direct numerical simulations (DNS) become prohibitively expensive.

Computational homogenization is a well known technique to reduce the computational costs associated with the modeling of physical phenomena in complex microstructures [93, 94]. It replaces a highly heterogeneous medium with an equivalent homogeneous one by decomposing the problem into smooth macro-scale and highly oscillatory micro-scale problems. The effective behavior is computed from a representative microscopic element (RVE) [95] and transferred to the macro-scale. The computational homogenization of transient phenomena, as associated with lithium diffusion in batteries, has been the focus of research recently [66, 92]. Effective responses have to be computed at each macroscopic material point at each time step, making homogenization of transient phenomena computationally demanding. For a general overview of multi-scale computational modeling of lithium-ion batteries, see [96, 97].

In this work, we propose a computationally efficient method for the homogenization of coupled diffusion-mechanics for the cathode material of a lithium-ion battery. The homogenization of the underlying diffusion and mechanical problems is performed separately by using the method proposed in [92]. For the diffusion problem, equivalence of virtual power (extended Hill-Mandel condition) is considered, while for the mechanical problem equivalence of virtual work is used (standard Hill-Mandel). Assuming linear material properties and small strains, the relaxed separation of scales allows the decomposition of the microscopic fields into their steady-state and transient parts. The mechanical response relies on the assumption of full scale separation since the characteristic time of the elastic deformation for the considered problem is very small compared to the characteristic diffusion time [71, 78]. Moreover, the characteristic diffusion time in the active material particles is several orders of magnitude larger, than the one of electrolyte (considered here as a matrix in which active particles are embedded) [66].

Therefore, the lithium-ions travel instantly in the electrolyte as compared to their diffusion in the active material. This allows for a so-called relaxed separation of scales, in which diffusive species migrate instantly in the matrix and very slowly in the inclusions [67]. Next, a model reduction technique, inspired by [43] for elasto-dynamic problems and applied in [67] to heat conduction problems, can be performed to extract the reduced bases for the steady-state and transient parts of the microscopic response. Although mechanical inertia effects can be neglected, the mechanical deformation is coupled to the transient diffusion, i.e., it evolves in time with the concentration field. Hence, a decomposition of the microscopic displacement field into a steady-state and a transient part is also required.

Through model reduction, the fine scale coupled-diffusion equations are replaced by a set of ordinary differential equations for the emergent macroscopic field variables, giving rise to an enriched-continuum at the macro-scale. These equations are to be solved at the macro-scale together with the macroscopic mass and linear momentum conservation and the constitutive effective mass flux, rate of change of concentration and stress, obtained through the reduced order homogenization. The resulting enriched-continuum macroscopic problem is computationally significantly less expensive than the original fully resolved problem or the direct transient computational homogenization.

4.1.1 Outline

The general framework of the coupled diffusion-mechanics framework is presented in section 4.2, where the classical formulation in terms of concentration and strain is summarized. Next, a computationally more convenient formulation expressed in the terms of the chemical potential and strain is derived. Section 4.3 presents the homogenization framework, in which the relaxed separation of scales is defined. The downscaling is performed and the macroscopic effective constitutive responses are obtained through an upscaling procedure. The model reduction is carried out in section 4.4. First, a finite element discretization is introduced and the partitioned equations are shown. The reduced bases are identified, the macroscopic quantities are written in terms of the coefficients of the reduced bases and finally mode selection criteria are discussed. Numerical examples for the cathode material of a lithium-ion battery are presented in section 4.5.

4.1.2 Symbols and Notation

Macroscopic quantities are represented with a bar on top: for example scalar, vector and second-order tensor macroscopic quantities are written as \bar{a} , $\bar{\mathbf{a}}$, and $\bar{\mathbf{A}}$, respectively. Microscopic quantities are represented without a bar; microscopic scalar, vector and second-order tensorial quantities are written as a , \mathbf{a} and \mathbf{A} , respectively. The same Cartesian basis is adopted at the macro and micro scales. The dot products between two vectors, and between a second-order tensor and a vector are represented as $\mathbf{a} \cdot \mathbf{b} := a_i b_i$ and $\mathbf{A} \cdot \mathbf{a} := A_{ij} a_j \mathbf{e}_i$, respectively. A tensorial dyadic product is denoted as $\mathbf{a} \otimes \mathbf{b} := a_i b_j \mathbf{e}_i \otimes \mathbf{e}_j$ and $\mathbf{A} \otimes \mathbf{a} := A_{ij} a_k \mathbf{e}_i \otimes \mathbf{e}_j \otimes \mathbf{e}_k$. The gradient of a scalar and a vector is defined as $\nabla a := \frac{\partial a}{\partial x_i} \mathbf{e}_i$ and $\nabla \mathbf{a} := \frac{\partial a_i}{\partial x_j} \mathbf{e}_i \otimes \mathbf{e}_j$. Similarly, the divergence operates as $\nabla \cdot \mathbf{a} := \frac{\partial a_i}{\partial x_i}$ and $\nabla \cdot \mathbf{A} := \frac{\partial A_{ij}}{\partial x_i} \mathbf{e}_j$. For linear algebra operations, columns are represented with a tilde underneath a lowercase letter, e.g., $\underline{\mathbf{a}}$, and matrices are represented with a bar underneath an uppercase letter e.g., $\underline{\mathbf{A}}$. The matrices and columns of vectors and tensor quantities are written with bold symbol, for example a matrix of a vector or a tensor quantity is written as $\underline{\mathbf{A}}$. A tensorial product between two column arrays of vectors is defined as $\underline{\mathbf{a}}^T \underline{\otimes} \underline{\mathbf{b}}$, where

$$\underline{\otimes} := \begin{bmatrix} \otimes & 0 & \dots & 0 \\ 0 & \otimes & & \vdots \\ \vdots & & \ddots & \\ 0 & 0 & \dots & \otimes \end{bmatrix}. \quad (4.1)$$

The microscopic domain and its boundary are represented by Ω_{\square} and $\partial\Omega_{\square}$, respectively. The volume average of a microscopic quantity \bullet is defined as

$$\langle \bullet \rangle := \frac{1}{V} \int_{\Omega_{\square}} \bullet \, d\Omega_{\square}, \quad (4.2)$$

where $V = \int_{\Omega_{\square}} d\Omega_{\square}$ is the volume of the microscopic domain Ω_{\square} .

4.2 Coupled Diffusion-Mechanics Formulation:

Coupled diffusion-mechanics equations describing the fully resolved (heterogeneous) problem are presented in this section. The conservation laws and the boundary conditions are written for the chemical and mechanical problems, followed by the derivation of the form of the constitutive equations [78]. First, the formulation considering the concentration and the displacement (strain) as the

primary field variables is presented, which requires C^1 -continuity and is therefore cumbersome to implement numerically. Next, using a Legendre transform, the primal field variables are transformed to the chemical potential and strain [92]. This formulation requires only C^0 -continuity and standard finite elements can be used for the implementation. Finally, the material model to be used for the micro-scale constituents is presented.

4.2.1 Conservation Laws

To take into account the large time scales associated with the mass diffusion problem a transient mass conservation equation is considered (without the volumetric source/sink term)

$$\nabla \cdot \mathbf{j} + \dot{c} = 0 \quad \text{in} \quad \Omega, \quad (4.3)$$

which states that the divergence of the mass flux \mathbf{j} in a domain Ω ¹ is opposite to the time rate of the concentration field \dot{c} . Equation (4.3) is supplemented with Dirichlet and Neumann boundary conditions, plus an initial condition

$$\begin{aligned} c &= \widehat{c} & \text{on} & \quad \partial\Omega_{\widehat{c}}, \\ \mathbf{j} \cdot \mathbf{n} &= \widehat{j}_n & \text{on} & \quad \partial\Omega_{\widehat{j}_n}, \\ c(0) &= c_0 & \text{at} & \quad t = 0, \end{aligned} \quad (4.4)$$

where \widehat{c} is the prescribed value of the concentration field on the Dirichlet part of the boundary $\partial\Omega_{\widehat{c}}$, and \widehat{j}_n is the prescribed normal outward mass flux on the Neumann part of the boundary $\partial\Omega_{\widehat{j}_n}$ such that $\partial\Omega_{\widehat{c}} \cup \partial\Omega_{\widehat{j}_n} = \partial\Omega$ and $\partial\Omega_{\widehat{c}} \cap \partial\Omega_{\widehat{j}_n} = \emptyset$. The initial value of the concentration at time $t = 0$ is denoted by c_0 .

Considering the short characteristic times of phenomena associated with the mechanical problem, it is justified to assume a conservation of linear momentum neglecting inertial terms, which without volumetric forces reads

$$\nabla \cdot \boldsymbol{\sigma} = \mathbf{0} \quad \text{in} \quad \Omega, \quad (4.5)$$

requiring the divergence of stress field $\boldsymbol{\sigma}$ in a body Ω vanish. Conservation of linear momentum (4.5) is also supplemented with the Dirichlet and Neumann boundary

¹Here, the domain Ω is used as a general description of a continuum body and should not be confused with the description of a microscopic domain Ω_{\square} used in computational homogenization.

conditions

$$\begin{aligned} \mathbf{u} &= \hat{\mathbf{u}} & \text{on} & \partial\Omega_{\hat{\mathbf{u}}}, \\ \boldsymbol{\sigma} \cdot \mathbf{n} &= \hat{\mathbf{t}}_n & \text{on} & \partial\Omega_{\hat{\mathbf{t}}_n}, \end{aligned} \quad (4.6)$$

where \mathbf{u} is the displacement field, $\hat{\mathbf{u}}$ is the prescribed displacement value on the Dirichlet part of the boundary $\partial\Omega_{\hat{\mathbf{u}}}$, and $\hat{\mathbf{t}}_n$ is the traction force applied on the Neumann part of the boundary $\partial\Omega_{\hat{\mathbf{t}}_n}$ such that $\partial\Omega_{\hat{\mathbf{u}}} \cup \partial\Omega_{\hat{\mathbf{t}}_n} = \partial\Omega$ and $\partial\Omega_{\hat{\mathbf{u}}} \cap \partial\Omega_{\hat{\mathbf{t}}_n} = \emptyset$. Constitutive equations for the mass flux \mathbf{j} , the concentration c and the stress $\boldsymbol{\sigma}$ are required to close the problem (4.3)–(4.6).

4.2.2 $(c, \boldsymbol{\varepsilon})$ Formulation

Following [78], the dissipation inequality for a coupled diffusion-mechanics problem can be written as

$$\varphi = \boldsymbol{\sigma} : \dot{\boldsymbol{\varepsilon}} + \mu \dot{c} - \dot{\psi} - \mathbf{j} \cdot \nabla \mu \geq 0, \quad (4.7)$$

where, μ is the chemical potential, φ is the dissipation density at a material point \mathbf{x} and $\dot{\psi}$ is the time derivative of the Helmholtz's free energy density. For coupled diffusion-mechanics problems, the Helmholtz's free energy density ψ depends on the concentration field c and the strain $\boldsymbol{\varepsilon}$, related to the displacement field \mathbf{u} by $\boldsymbol{\varepsilon} = \text{sym}(\nabla \mathbf{u})$ (assuming linear kinematics). Using the chain-rule, its material time derivative can be written as

$$\dot{\psi} = \dot{\psi}(c, \boldsymbol{\varepsilon}) = \frac{\partial \psi}{\partial c} \dot{c} + \frac{\partial \psi}{\partial \boldsymbol{\varepsilon}} : \dot{\boldsymbol{\varepsilon}}, \quad (4.8)$$

substituting the expression of $\dot{\psi}$ from equation (4.8) into the dissipation inequality (4.7) and rearranging terms yields

$$\varphi = \left(\boldsymbol{\sigma} - \frac{\partial \psi}{\partial \boldsymbol{\varepsilon}} \right) : \dot{\boldsymbol{\varepsilon}} + \left(\mu - \frac{\partial \psi}{\partial c} \right) \dot{c} - \mathbf{j} \cdot \nabla \mu \geq 0. \quad (4.9)$$

In the inequality (4.9), the restriction on the dissipation density to be positive is partially fulfilled by setting

$$\boldsymbol{\sigma} = \frac{\partial \psi}{\partial \boldsymbol{\varepsilon}} \quad \text{and} \quad \mu = \frac{\partial \psi}{\partial c}, \quad (4.10)$$

which provides, for a given expression for the Helmholtz potential ψ , the constitutive equations for the stress and the chemical potential, respectively. Considering

a quadratic Helmholtz free energy density [78]

$$\psi = \psi(c, \boldsymbol{\varepsilon}) = \frac{1}{2} \boldsymbol{\varepsilon} : \mathbb{C} : \boldsymbol{\varepsilon} + \mathbf{S} : \boldsymbol{\varepsilon} (c - c_0) + \frac{1}{2} \Lambda (c - c_0)^2, \quad (4.11)$$

results in linear constitutive expressions for the stress and the chemical potential given by

$$\boldsymbol{\sigma} = \frac{\partial \psi}{\partial \boldsymbol{\varepsilon}} = \mathbb{C} : \boldsymbol{\varepsilon} + \mathbf{S} (c - c_0), \quad (4.12)$$

and

$$\mu = \frac{\partial \psi}{\partial c} = \mathbf{S} : \boldsymbol{\varepsilon} + \Lambda (c - c_0), \quad (4.13)$$

where \mathbb{C} is the elastic stiffness tensor, \mathbf{S} the chemical strain modulus tensor, c_0 the initial concentration and Λ is the chemical modulus. The constitutive model based on energy density function given in equation (4.11) is an alternative approach to the approach in which the microscopic strain field is decomposed in an elastic and volumetric swelling part, for more details see [98]. The remaining dissipation term in (4.9)

$$- \mathbf{j} \cdot \nabla \mu \geq 0, \quad (4.14)$$

asserts a restriction on the constitutive form of the mass flux \mathbf{j} . Here, we use Fick's second law which states that the mass flux \mathbf{j} depends linearly on the gradient of the chemical potential $\nabla \mu$ i.e.,

$$\mathbf{j} = -\mathbf{M} \cdot \nabla \mu, \quad (4.15)$$

where \mathbf{M} is the second-order mobility tensor which has to be positive definite to satisfy (4.14). Next, the constitutive equations (4.12), (4.13) and (4.15) can be introduced in the mass conservation equation (4.3),

$$\nabla \cdot [\mathbf{M} \cdot \nabla (\Lambda (c - c_0) + \mathbf{S} : \boldsymbol{\varepsilon})] - \dot{c} = 0, \quad (4.16)$$

and in the conservation of linear momentum (4.5)

$$\nabla \cdot [\mathbb{C} : \boldsymbol{\varepsilon} + \mathbf{S} (c - c_0)] = \mathbf{0}. \quad (4.17)$$

The mass and the linear momentum conservation equations (4.16) and (4.17) can be solved together for the concentration and displacement fields (c, \mathbf{u}) . Equation (4.16), however, involves the third-order derivative of \mathbf{u} and its numerical solution therefore requires a C^1 -continuous finite element formulation. Various other

solution techniques have also been proposed in the literature for this type of problems, see for example [92, 99]. In the current work, following [92], a Legendre transform is performed on the Helmholtz's free energy density function $\psi(c, \boldsymbol{\varepsilon})$ to obtain a dual energy density function ζ , for which the primary field variables are the chemical potential μ and the strain $\boldsymbol{\varepsilon}$.

4.2.3 $(\mu, \boldsymbol{\varepsilon})$ Formulation

Now, we derive the constitutive equations for stress $\boldsymbol{\sigma}$, concentration c and mass flux \mathbf{j} considering $(\mu, \boldsymbol{\varepsilon})$ as the primary field variables. A Legendre transform can be performed on the Helmholtz's free energy density function (4.11) to obtain the dual energy density function ζ

$$\zeta(\mu, \boldsymbol{\varepsilon}) = \psi(c(\mu, \boldsymbol{\varepsilon}), \boldsymbol{\varepsilon}) - \mu c(\mu, \boldsymbol{\varepsilon}), \quad (4.18)$$

which is now a function of the chemical potential μ and the strain $\boldsymbol{\varepsilon}$. The constitutive equations for the concentration and the stress fields $(c, \boldsymbol{\sigma})$ can be obtained by the standard Coleman-Noll procedure. Substituting $\psi = \zeta + \mu c$ from (4.18) into (4.7) provides the dissipation inequality

$$\varphi = \boldsymbol{\sigma} : \dot{\boldsymbol{\varepsilon}} - \dot{\zeta} - \dot{\mu}c - \mathbf{j} \cdot \nabla \mu \geq 0. \quad (4.19)$$

Using the chain-rule, the time derivative of the dual energy density $\dot{\zeta}$ can be written as

$$\dot{\zeta}(\mu, \boldsymbol{\varepsilon}) = \frac{\partial \zeta}{\partial \mu} \dot{\mu} + \frac{\partial \zeta}{\partial \boldsymbol{\varepsilon}} : \dot{\boldsymbol{\varepsilon}}. \quad (4.20)$$

Substituting the expression for $\dot{\zeta}$, from equation (4.20), into the dissipation inequality (4.19) and rearranging terms yields

$$\varphi = \left(\boldsymbol{\sigma} - \frac{\partial \zeta}{\partial \boldsymbol{\varepsilon}} \right) : \dot{\boldsymbol{\varepsilon}} - \left(c + \frac{\partial \zeta}{\partial \mu} \right) \dot{\mu} - \mathbf{j} \cdot \nabla \mu \geq 0. \quad (4.21)$$

From here, the constitutive forms for the stress $\boldsymbol{\sigma}$ and the concentration field c are found as

$$\boldsymbol{\sigma} = \frac{\partial \zeta}{\partial \boldsymbol{\varepsilon}} \quad \text{and} \quad c = -\frac{\partial \zeta}{\partial \mu}. \quad (4.22)$$

Using constitutive equations (4.22) in conjunction with (4.18) and (4.11) provides the constitutive equations for the stress

$$\boldsymbol{\sigma} = \frac{\partial \zeta}{\partial \boldsymbol{\varepsilon}} = \left(\mathbb{C} - \frac{\mathbf{S} \otimes \mathbf{S}}{\Lambda} \right) : \boldsymbol{\varepsilon} + \frac{\mu \mathbf{S}}{\Lambda}, \quad (4.23)$$

and for the concentration field

$$c = -\frac{\partial \zeta}{\partial \mu} = \frac{\mu}{\Lambda} - \frac{\mathbf{S}}{\Lambda} : \boldsymbol{\varepsilon} + c_0. \quad (4.24)$$

For the remaining dissipation term $-\mathbf{j} \cdot \nabla \mu \geq 0$, again Fick's second law (4.15) can be used. Introducing the stress (4.23), the concentration field (4.24) and the mass flux (4.15) into the mass conservation (4.3) gives

$$\nabla \cdot (\mathbf{M} \cdot \nabla \mu) + \frac{\mathbf{S} : \dot{\boldsymbol{\varepsilon}}}{\Lambda} - \frac{\dot{\mu}}{\Lambda} = 0, \quad (4.25)$$

while the conservation of linear momentum (4.5) reads

$$\nabla \cdot \left[\left(\mathbb{C} - \frac{\mathbf{S} \otimes \mathbf{S}}{\Lambda} \right) : \boldsymbol{\varepsilon} + \frac{\mu \mathbf{S}}{\Lambda} \right] = \mathbf{0}, \quad (4.26)$$

Equations (4.25) and (4.26) are solved for the chemical potential μ and the displacement \mathbf{u} . The requirement of C^1 -continuity on \mathbf{u} is now relaxed by using the $(\mu, \boldsymbol{\varepsilon})$ formulation, as can be seen from (4.26), for which a standard C^0 -continuous finite element formulation can be used.

4.2.4 Linear Isotropic Constitutive Model

A isotropic material model is considered for both mass diffusion and mechanical problems. The isotropic mobility tensor is given by

$$\mathbf{M} = M \mathbf{I}, \quad (4.27)$$

where \mathbf{I} is the second order identity tensor and M is the scalar mobility coefficient. The chemical strain modulus \mathbf{S} is assumed to have the following form [71]

$$\mathbf{S} = -\gamma K \mathbf{I}, \quad (4.28)$$

where $K = \frac{3\lambda+2G}{3}$ is the bulk modulus, λ , G are Lamé's constants and γ is the partial molar volume of the material, which is the volumetric increase of a material

by the introduction of one mole of other substance. The linear elastic stiffness tensor \mathbb{C} is expressed in terms of Lamé's constants as

$$\mathbb{C} = \lambda \mathbf{I} \otimes \mathbf{I} + 2G\mathbb{I}, \quad (4.29)$$

where \mathbb{I} is the fourth order identity tensor. Next, the computational homogenization framework for the two-scale coupled diffusion-mechanics problem will be presented.

4.3 Computational Homogenization

In this section, the computational homogenization of a two-scale coupled diffusion-mechanics problem is presented. First, the separation of scales regimes are defined for the mass diffusion and mechanics problems. Then, the governing equations at the micro- and the macro-scales are presented. The boundary conditions on the microscopic domain are defined through the constraints imposed by the downscaling relations. Finally, the upscaling is performed via equivalence of the virtual powers of the macro- and micro-scales providing the constitutive forms for the macroscopic quantities.

The solution of the coupled diffusion mechanics problem on the fully resolved heterogeneous domain, as shown in Figure 4.1(a), is referred to as direct numerical simulation (DNS). Due to the computational expense of the DNS problem it is preferred, when possible, to divide the problem into micro and macro scales and solve a homogenized problem in a two-scale manner, as shown in Figure 4.1(b). The homogenizability of the DNS problem depends on the separation of scales, which is discussed next.

4.3.1 Separation of Scales

The separation of scales can be defined through the material properties of the constituents, their characteristic length and time scales, and the characteristic scales of the physical phenomena under consideration [28]. For the coupled problem studied here, *coupled scales* for the mass diffusion, have to be considered, while for the mechanical phenomena a *full separation of scales* can be assumed. For more details on separation of scales see for example [28].

Mechanics: For the mechanical problem, a full separation of scales is adopted since the microscopic characteristic length scales ($\ell_i < \ell_m$) are much smaller than the

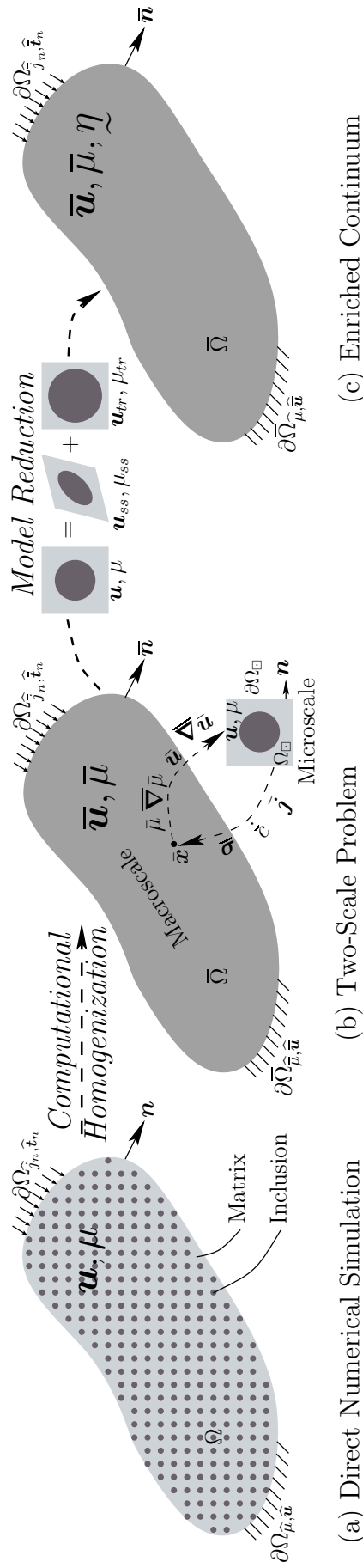


Figure 4.1: Steps involved in the development of the enriched-continuum formulation: first, performing computational homogenization, the solution of a highly heterogeneous problem also known as the direct numerical simulation (a) is replaced by a two-scale macro and micro-scale coupled problem (b), next model reduction is performed at the micro-scale yielding an enriched-continuum formulation (c).

macroscopic characteristic length scale L , which is typically the length over which the macroscopic fields vary over time i.e. ,

$$(\ell_i < \ell_m) \ll L, \quad (4.30)$$

where ℓ_m and ℓ_i are the characteristic lengths of the microstructural components (matrix and inclusions, respectively) and L is the characteristic size of the macroscopic domain.

Mass diffusion: In the mass diffusion problem, the separation of scales can be quantified based on the characteristic times associated with each material constituent. The characteristic times for the matrix t_m and the inclusion t_i can be written as

$$t_m := \frac{\ell_m^2}{\mathcal{D}_m} \quad \text{and} \quad t_i := \frac{\ell_i^2}{\mathcal{D}_i}, \quad (4.31)$$

where \mathcal{D}_m and \mathcal{D}_i are the mass diffusivity coefficients of the matrix and inclusions, respectively. In the present work, a *relaxed separation of scales* is considered for the diffusion problem, which is a special case of coupled scales. In the regime of relaxed separation of scales, the characteristic diffusion time of the matrix t_m is very small compared to the one of the inclusion t_i , and the macroscopic loading time T :

$$t_m \ll (T \sim t_i). \quad (4.32)$$

A relaxed separation of scales is applicable to the homogenization of mass diffusion problems in lithium-ion batteries, where the lithium-ions diffuse essentially instantaneously through the electrolyte material (matrix) in contrast to the very slow diffusion in the active particles (inclusions). The relaxed separation of scales has a direct implication for the model reduction presented in section 4.4, since it allows the decomposition of the microscopic solution fields into the steady-state and transient parts. The separation of scales also indicates whether the transient terms in the conservation laws at the micro- and macro-scales should be included or not. These conservation laws are stated next.

4.3.2 Conservation Laws at Micro and Macro-scales

Mass conservation: the mass conservation at the macro-scale reads:

$$\bar{\nabla} \cdot \bar{\mathbf{j}} + \dot{\bar{c}} = 0 \quad \text{in} \quad \bar{\Omega}, \quad (4.33)$$

where $\bar{\mathbf{j}}$ and $\dot{\bar{c}}$ are the macroscopic mass flux and the macroscopic rate of change of the concentration field, respectively. To capture the time dependent mass diffusion behavior inside transient inclusions, the mass conservation is considered at the micro-scale:

$$\nabla \cdot \mathbf{j} + \dot{c} = 0 \quad \text{in} \quad \Omega_{\square}, \quad (4.34)$$

where \mathbf{j} and \dot{c} are the mass flux and the rate of change of concentration at the micro-scale.

Conservation of Linear Momentum: For the considered problem, mechanical inertia can be neglected, for which the macroscopic linear momentum balance equation reads:

$$\bar{\nabla} \cdot \bar{\boldsymbol{\sigma}} = \mathbf{0} \quad \text{in} \quad \bar{\Omega}, \quad (4.35)$$

where $\bar{\boldsymbol{\sigma}}$ is the macroscopic stress tensor. Given the full separation of scales for the mechanical problem, the conservation of linear momentum at the micro-scale also does not include transient terms neither and reads

$$\nabla \cdot \boldsymbol{\sigma} = \mathbf{0} \quad \text{in} \quad \Omega_{\square}. \quad (4.36)$$

where $\boldsymbol{\sigma}$ is the microscopic stress tensor.

The constitutive equations for the macroscopic quantities $\bar{\boldsymbol{\sigma}}$, $\bar{\mathbf{j}}$ and $\dot{\bar{c}}$ are yet unknown; in the computational homogenization, these are obtained through an upscaling procedure. The boundary and initial conditions at the macro-scale are given by the particular problem at hand. At the micro-scale, the constitutive equation for $\boldsymbol{\sigma}$, \mathbf{j} and c are assumed to be known, as presented in section 4.2. The boundary conditions at the micro-scale are obtained by downscaling relations, which will be presented next.

4.3.3 Downscaling

In first-order computational homogenization, the microscopic fields are approximated as the first-order Taylor's series expansion around a macroscopic point $\bar{\mathbf{x}}$. The chemical potential μ in a microscopic domain Ω_{\square} can then be written as

$$\mu(\bar{\mathbf{x}}, \mathbf{x}, t) := \bar{\mu}(\bar{\mathbf{x}}, t) + \bar{\nabla} \bar{\mu}(\bar{\mathbf{x}}, t) \cdot [\mathbf{x} - \bar{\mathbf{x}}] + \tilde{\mu}(\bar{\mathbf{x}}, \mathbf{x}, t), \quad (4.37)$$

where $\bar{\mu}$ and $\bar{\nabla} \bar{\mu}$ are the macroscopic chemical potential and its gradient, respectively, and $\tilde{\mu}$ is the fluctuation field of the chemical potential at the micro-scale. The latter is due to the difference in material properties of the constituents, and

the transient loading conditions at the macro-scale. Similarly, the microscopic displacement field \mathbf{u} can also be expressed as the first order Taylor's series expansion around a macroscopic point $\bar{\mathbf{x}}$

$$\mathbf{u}(\bar{\mathbf{x}}, \mathbf{x}, t) := \bar{\mathbf{u}}(\bar{\mathbf{x}}, t) + \bar{\nabla} \bar{\mathbf{u}}(\bar{\mathbf{x}}, t) \cdot [\mathbf{x} - \bar{\mathbf{x}}] + \tilde{\mathbf{u}}(\bar{\mathbf{x}}, \mathbf{x}, t), \quad (4.38)$$

where $\bar{\mathbf{u}}$ and $\bar{\nabla} \bar{\mathbf{u}}$ are the macroscopic displacement field and its gradient, respectively, and $\tilde{\mathbf{u}}$ is the microfluctuation of the displacement field.

In computational homogenization, downscaling is referred to as the transfer of macroscopic quantities to the micro-scale, as shown in Figure 4.1(b). Macroscopic quantities which are to be transferred to the micro-scale depend on the physical phenomena under consideration. For instance, in first-order transient computational homogenization, both for diffusion processes [8] and dynamics [38, 40], both the primary macroscopic field and its gradient are transferred to the micro-scale. In a steady-state/static computational homogenization scheme, only the gradient information needs to be transferred to the micro-scale.

In transient computational homogenization, the first constraint on the micro-scale solution is that the volume average of the microscopic primary field is enforced to be equal to the corresponding macroscopic field

$$\begin{aligned} \langle \mu(\bar{\mathbf{x}}, \mathbf{x}, t) \rangle &= \bar{\mu}(\bar{\mathbf{x}}, t), \\ \langle \mathbf{u}(\bar{\mathbf{x}}, \mathbf{x}, t) \rangle &= \bar{\mathbf{u}}(\bar{\mathbf{x}}, t), \end{aligned} \quad (4.39)$$

which, by using the definitions (4.37) and (4.38) a chosen positioning of the microscopic domain such that $\langle \mathbf{x} - \bar{\mathbf{x}} \rangle = \mathbf{0}$, requires that the average of the microfluctuations over the microscopic domain vanishes

$$\begin{aligned} \langle \tilde{\mu}(\bar{\mathbf{x}}, \mathbf{x}, t) \rangle &= 0, \\ \langle \tilde{\mathbf{u}}(\bar{\mathbf{x}}, \mathbf{x}, t) \rangle &= \mathbf{0}. \end{aligned} \quad (4.40)$$

The second constraint on the microscopic solution fields is that the average of the microscopic gradient fields should be equal to the corresponding macroscopic gradients

$$\begin{aligned} \langle \nabla \mu(\bar{\mathbf{x}}, \mathbf{x}, t) \rangle &= \bar{\nabla} \bar{\mu}(\bar{\mathbf{x}}, t), \\ \langle \nabla \mathbf{u}(\bar{\mathbf{x}}, \mathbf{x}, t) \rangle &= \bar{\nabla} \bar{\mathbf{u}}(\bar{\mathbf{x}}, t), \end{aligned} \quad (4.41)$$

which by using equation (4.37) and (4.38) and the identity $\nabla(\mathbf{x} - \bar{\mathbf{x}}) = \mathbf{I}$ can be written as

$$\begin{aligned} \langle \nabla \mu(\bar{\mathbf{x}}, \mathbf{x}, t) \rangle &= \bar{\nabla} \bar{\mu}(\bar{\mathbf{x}}, t) + \langle \nabla \tilde{\mu}(\bar{\mathbf{x}}, \mathbf{x}, t) \rangle, \\ \langle \nabla \mathbf{u}(\bar{\mathbf{x}}, \mathbf{x}, t) \rangle &= \bar{\nabla} \bar{\mathbf{u}}(\bar{\mathbf{x}}, t) + \langle \nabla \tilde{\mathbf{u}}(\bar{\mathbf{x}}, \mathbf{x}, t) \rangle. \end{aligned} \quad (4.42)$$

The last terms in the above equations, i.e., the average of the gradient of the microfluctuation fields $\langle \nabla \tilde{\mu} \rangle$ and $\langle \nabla \tilde{\mathbf{u}} \rangle$ should vanish to satisfy the requirements (4.41). After applying Gauss's theorem, these can be written as

$$\begin{aligned} \int_{\partial\Omega_{\square}} \tilde{\mu} \mathbf{n} \, da &= \mathbf{0}, \\ \int_{\partial\Omega_{\square}} \tilde{\mathbf{u}} \otimes \mathbf{n} \, da &= \mathbf{0}. \end{aligned} \quad (4.43)$$

where \mathbf{n} is the outward unit-normal vector to the microscopic boundary $\partial\Omega_{\square}$ with an infinitesimal surface area da .

Constraints (4.40) can be applied by prescribing the respective fields at one point in the microscopic domain, along with the elimination of rigid body motion, to the corresponding macroscopic field values. To apply constraints (4.43), specific types of boundary conditions are used at the micro-scale. Typical choices for these boundary conditions are (i) zero fluctuation boundary conditions or (ii) periodic fluctuation boundary conditions as used later in this work.

4.3.4 Upscaling

Next, we discuss the upscaling relations which provide the constitutive equations for the macroscopic quantities. In computational homogenization, upscaling refers to the transfer of information from the micro-scale to the macro-scale by requiring equality of the macroscopic and volume averaged microscopic (virtual) powers, known as the (extended) Hill-Mandel conditions in the literature [9, 40, 67]. The microscopic primary field ansatz e.g., (4.37) and (4.38), is then injected in the expression of the virtual power average and the macroscopic quantities are obtained by applying proper boundary conditions.

Mass Diffusion: The micro-macro scale equivalence of the virtual power due to mass diffusion

$$-\bar{\nabla} \delta \bar{\mu} \cdot \bar{\mathbf{j}} + \delta \bar{\mu} \dot{\bar{c}} = \left\langle -\nabla \delta \mu \cdot \mathbf{j} + \delta \mu \dot{c} \right\rangle. \quad (4.44)$$

Substituting the variation of the microscopic chemical potential $\delta\mu$ using (4.37) in the right hand side of (4.44) yields

$$-\overline{\nabla\delta\bar{\mu}\cdot\bar{\mathbf{j}}+\delta\bar{\mu}\dot{c}} = \left\langle -\overline{\nabla\delta\bar{\mu}\cdot\mathbf{j}} - \overline{\nabla\delta\tilde{\mu}\cdot\mathbf{j}} + \delta\bar{\mu}\dot{c} + \overline{\nabla\delta\bar{\mu}\cdot(\mathbf{x}-\bar{\mathbf{x}})\dot{c}} + \delta\tilde{\mu}\dot{c} \right\rangle. \quad (4.45)$$

Rearranging the above expression for $\delta\bar{\mu}$ and $\delta\tilde{\mu}$ yields

$$-\overline{\nabla\delta\bar{\mu}\cdot\bar{\mathbf{j}}+\delta\bar{\mu}\dot{c}} = \left\langle -\overline{\nabla\delta\bar{\mu}\cdot[\mathbf{j}-\dot{c}(\mathbf{x}-\bar{\mathbf{x}})]+\delta\bar{\mu}\dot{c}} \right\rangle + \left\langle -\overline{\nabla\delta\tilde{\mu}\cdot\mathbf{j}} + \delta\tilde{\mu}\dot{c} \right\rangle. \quad (4.46)$$

The last term in the above expression, after applying the chain rule and the divergence theorem, reflects the weak form of the microfluctuation mass conservation

$$\left\langle -\overline{\nabla\delta\tilde{\mu}\cdot\mathbf{j}} + \delta\tilde{\mu}\dot{c} \right\rangle = \left\langle \delta\tilde{\mu}(\nabla\cdot\mathbf{j} + \dot{c}) \right\rangle - \frac{1}{V} \int_{\partial\Omega_{\square}} \delta\tilde{\mu}\mathbf{j}\cdot\mathbf{n} \, da. \quad (4.47)$$

The first term on the right hand side of the above expression is the weighted residual of the microscopic conservation of mass (4.34), whose solution at the micro-scale should vanish. For the prescribed zero microfluctuation boundary condition or the periodic boundary conditions, the second term also vanishes and equation (4.46) reduces to

$$-\overline{\nabla\delta\bar{\mu}\cdot\mathbf{j}} + \delta\bar{\mu}\dot{c} = -\overline{\nabla\delta\bar{\mu}\cdot\langle\mathbf{j}-\dot{c}(\mathbf{x}-\bar{\mathbf{x}})\rangle} + \delta\bar{\mu}\langle\dot{c}\rangle, \quad (4.48)$$

from where the macroscopic mass flux can be recognized as

$$\bar{\mathbf{j}} = \langle\mathbf{j}-\dot{c}(\mathbf{x}-\bar{\mathbf{x}})\rangle, \quad (4.49)$$

and the rate of change of the macroscopic concentration as

$$\dot{c} = \langle\dot{c}\rangle. \quad (4.50)$$

The volume averages in equation (4.49) and (4.50) can also be converted to boundary integrals using the divergence theorem and the microscopic mass conservation (4.34)

$$\bar{\mathbf{j}} = \frac{1}{V} \int_{\partial\Omega_{\square}} j_n(\mathbf{x}-\bar{\mathbf{x}}) \, da, \quad (4.51)$$

and

$$\dot{c} = -\frac{1}{V} \int_{\partial\Omega_{\square}} j_n \, da. \quad (4.52)$$

with $j_n = \mathbf{j}\cdot\mathbf{n}$ the normal outward mass flux.

Mechanics: In the absence of inertia effects, the standard Hill-Mandel condition

$$\overline{\nabla \delta \bar{\mathbf{u}} : \bar{\boldsymbol{\sigma}}} = \left\langle \nabla \delta \mathbf{u} : \boldsymbol{\sigma} \right\rangle, \quad (4.53)$$

applies for the homogenization of the mechanical problem. Following similar steps as described above, allows identification of the (standard) macroscopic stress

$$\bar{\boldsymbol{\sigma}} = \left\langle \boldsymbol{\sigma} \right\rangle, \quad (4.54)$$

which can be converted to an expression in terms of tractions at the microscopic boundary

$$\bar{\boldsymbol{\sigma}} = \frac{1}{V} \int_{\partial \Omega_{\square}} \mathbf{t}_n \otimes (\mathbf{x} - \bar{\mathbf{x}}) da. \quad (4.55)$$

Once the solution to the microscopic problem (4.34) and (4.36) is known, the reaction mass fluxes j_n and the reaction forces \mathbf{t}_n can be computed and post-processed to obtain the macroscopic quantities $\bar{\mathbf{j}}$, $\dot{\bar{c}}$ and $\bar{\boldsymbol{\sigma}}$. Next, we discuss the solution procedure to obtain the reaction fluxes j_n and forces \mathbf{t}_n through a reduced order model, rather than the fully resolved model of the microscopic domain.

An alternative homogenization route is to average the dissipation, given in equation (4.7), at the micro-scale and equating it to an assumed macroscopic dissipation expression. For a first-order computational homogenization approach, the ansatz in equations (4.40) and (4.43) can be inserted into the microscopic dissipation. Expanding and applying the required boundary conditions to eliminate the fluctuation fields, the corresponding macroscopic quantities can be obtained along with the weak forms of the balance laws at the micro-scale.

4.4 Model Reduction Leading to an Enriched-Continuum

In this section, a model reduction of the microscopic coupled diffusion-mechanics problem is presented. The microscopic chemical potential and displacement fields are first decomposed into their steady-state and transient parts and reduced bases are identified. The reaction fluxes and tractions, which are required to compute the macroscopic quantities, are written in terms of the coefficients of these reduced bases. Next, the expressions for the macroscopic quantities are derived explicitly. Finally, an emergent macroscopic enriched-continuum formulation, which arises as a consequence of model reduction at the micro-scale, is presented.

4.4.1 Finite Element Discretization

Using the finite element discretization, the linear momentum balance (4.36), the mass conservation (4.34) and the constitutive models (4.27)–(4.29), the discretized coupled diffusion-mechanics problem in terms of the unknown nodal values of the chemical potential $\underline{\mu}$ and displacements $\underline{\mathbf{u}}$ can be written as

$$\underline{K}_{\mu\mu}\underline{\mu} + \underline{M}_{\mu\mu}\dot{\underline{\mu}} + \underline{K}_{\mu\mathbf{u}} \cdot \dot{\underline{\mathbf{u}}} = -\underline{j}_n, \quad (4.56)$$

$$\underline{K}_{\mathbf{u}\mu}\underline{\mu} + \underline{K}_{\mathbf{u}\mathbf{u}} \cdot \underline{\mathbf{u}} = \underline{\mathbf{t}}_n, \quad (4.57)$$

where $\underline{K}_{\mu\mu}$, $\underline{M}_{\mu\mu}$, $\underline{K}_{\mathbf{u}\mathbf{u}}$ and $\underline{K}_{\mathbf{u}\mu}$ are the mobility, mass, stiffness and coupling matrices, respectively, and $\underline{K}_{\mu\mathbf{u}} = -[\underline{K}_{\mathbf{u}\mu}]^T$. The right hand sides \underline{j}_n and $\underline{\mathbf{t}}_n$ are the vector of reaction fluxes and reaction forces.

In the computational homogenization framework, once the solution for the microscopic primary fields $\underline{\mu}$ and $\underline{\mathbf{u}}$ is known, the reaction fluxes \underline{j}_n and reaction forces $\underline{\mathbf{t}}_n$ can be computed. In a two-scale setting, this is an expensive task, especially in the transient regime, since it requires the solution of a coupled problem at each macroscopic material point at each time step. Hence, an approximate solution based on a model reduction technique is called for.

To apply the model reduction, instead of solving a coupled system of equation (4.56)–(4.57), we first analyze each equation separately and then the coupling effect is taken into account when the reduced bases are constructed. The homogenization conditions in equation (4.40) amounts to kinematically constraint the micro-scale to the macroscopic point $\bar{\mathbf{x}}$ and requires the macroscopic chemical potential $\bar{\mu}$ to be the average value of the microscopic chemical potential field μ . In a discrete setting, it can be achieved by prescribing the microscopic fields μ and \mathbf{u} degrees of freedom (DOF), at a point \mathbf{x} in the microscopic domain, equal to the corresponding reference values of macroscopic fields $\bar{\mu}$ and $\bar{\mathbf{u}}$. It is allowed to fix the displacement field and the chemical potential at a point in the micro-scale because all the material properties i.e., \mathbb{C} , \mathbf{S} , \mathbf{M} and Λ are independent of these solution fields. Also, the displacement field \mathbf{u} at the micro-scale are defined up to the rigid body motion and the chemical potential μ can also be defined up to a constant since the microscopic flux \mathbf{j} , given in equation (4.15), depends on the gradient of chemical potential $\nabla\mu$ and linear momentum balance, given in equation (4.26), is not affected by adding a constant term to the chemical potential. In this study this point is chosen to be \mathbf{x}_1 which is at the lower left corner

of the rectangular microscopic domain. The constraint (4.43) is satisfied by applying the periodic boundary conditions on the fluctuation fields $\tilde{\mu}$ and $\tilde{\mathbf{u}}$. Due to the applied periodicity, the DOFs at the other three corner nodes, denoted as points \mathbf{x}_2 , \mathbf{x}_3 and \mathbf{x}_4 , are also fully prescribed, while the rest of the DOFs in the microscopic domain are considered free. More details on applying the boundary conditions in a discrete setting for a scalar field like μ can be found in [67] and for a vector field like \mathbf{u} in [43]. The discretized mass diffusion equation (4.56) partitioned into prescribed ‘ p ’ and free ‘ f ’ degree of freedoms takes the form

$$\begin{bmatrix} \underline{K}_{\mu\mu}^{pp} & \underline{K}_{\mu\mu}^{pf} \\ \underline{K}_{\mu\mu}^{fp} & \underline{K}_{\mu\mu}^{ff} \end{bmatrix} \begin{bmatrix} \tilde{\mu}^p \\ \tilde{\mu}^f \end{bmatrix} + \begin{bmatrix} \underline{M}_{\mu\mu}^{pp} & \underline{M}_{\mu\mu}^{pf} \\ \underline{M}_{\mu\mu}^{fp} & \underline{M}_{\mu\mu}^{ff} \end{bmatrix} \begin{bmatrix} \dot{\tilde{\mu}}^p \\ \dot{\tilde{\mu}}^f \end{bmatrix} + \begin{bmatrix} \underline{K}_{\mu\mathbf{u}}^{pp} & \underline{K}_{\mu\mathbf{u}}^{pf} \\ \underline{K}_{\mu\mathbf{u}}^{fp} & \underline{K}_{\mu\mathbf{u}}^{ff} \end{bmatrix} \cdot \begin{bmatrix} \dot{\tilde{\mathbf{u}}}^p \\ \dot{\tilde{\mathbf{u}}}^f \end{bmatrix} = \begin{bmatrix} -\underline{j}_n^p \\ \underline{0}^f \end{bmatrix}. \quad (4.58)$$

Similarly, the mechanical equation after partitioning into its prescribed and free DOF can be written as

$$\begin{bmatrix} \underline{K}_{\mathbf{u}\mu}^{pp} & \underline{K}_{\mathbf{u}\mu}^{pf} \\ \underline{K}_{\mathbf{u}\mu}^{fp} & \underline{K}_{\mathbf{u}\mu}^{ff} \end{bmatrix} \begin{bmatrix} \tilde{\mu}^p \\ \tilde{\mu}^f \end{bmatrix} + \begin{bmatrix} \underline{K}_{\mathbf{u}\mathbf{u}}^{pp} & \underline{K}_{\mathbf{u}\mathbf{u}}^{pf} \\ \underline{K}_{\mathbf{u}\mathbf{u}}^{fp} & \underline{K}_{\mathbf{u}\mathbf{u}}^{ff} \end{bmatrix} \cdot \begin{bmatrix} \tilde{\mathbf{u}}^p \\ \tilde{\mathbf{u}}^f \end{bmatrix} = \begin{bmatrix} \underline{t}_n^p \\ \underline{0}^f \end{bmatrix}. \quad (4.59)$$

For the microscopic response, both the chemical potential μ and displacement \mathbf{u} are next split into their steady-state and transient parts.

4.4.2 Microscopic Fields Decomposition

According to the relaxed separation of scales, the transient response of the system evolves independently from the steady-state one. The steady-state response depends on the macroscopic input parameters ($\bar{\mu}$, $\bar{\mathbf{u}}$, $\bar{\nabla}\bar{\mu}$, and $\bar{\nabla}\bar{\mathbf{u}}$) through the prescribed DOFs $\tilde{\mu}^p$ and $\tilde{\mathbf{u}}^p$, whereas the transient response only affects the inclusions that are part of the free DOFs. (In a discrete setting this requires that the prescribed DOFs always reside in the matrix material so that the transient response can evolve independently.) Consequently, the free parts of the microscopic solution fields are decomposed into a steady-state and a transient part. The free part of the chemical potential field can be written as

$$\tilde{\mu}^f = \tilde{\mu}_{ss}^f + \tilde{\mu}_{tr}^f, \quad (4.60)$$

where $\tilde{\mu}_{ss}^f$ is the steady-state and $\tilde{\mu}_{tr}^f$ is the transient part. Since the mechanical response is coupled to that of the mass diffusion, the displacement field will also evolve in time due to the change of the chemical potential. The free part of the

microscopic displacement field $\underline{\mathbf{u}}^f$ is also decomposed into its steady-state $\underline{\mathbf{u}}_{ss}^f$ and transient $\underline{\mathbf{u}}_{tr}^f$ part

$$\underline{\mathbf{u}}^f = \underline{\mathbf{u}}_{ss}^f + \underline{\mathbf{u}}_{tr}^f, \quad (4.61)$$

Next, the steady-state and transient reduced bases have to be determined for both the chemical and mechanical fields.

4.4.3 Steady-State Response

The steady-state part of the micro-scale solution follows the macro-scale solution instantaneously. To obtain the steady-state response, the discrete systems of equation (4.58) and (4.59) are written considering the steady-state contributions $\underline{\mu}_{ss}$ and $\underline{\mathbf{u}}_{ss}$ only.

4.4.3.1 Mass Diffusion

Substituting the steady-state chemical potential field μ_{ss} in the second line of equation (4.58) yields

$$\underline{\mathbf{K}}_{\mu\mu}^{fp} \underline{\mu}^p + \underline{\mathbf{K}}_{\mu\mu}^{ff} \underline{\mu}_{ss}^f + \underline{\mathbf{M}}_{\mu\mu}^{fp} \dot{\underline{\mu}}^p + \underline{\mathbf{M}}_{\mu\mu}^{ff} \dot{\underline{\mu}}_{ss}^f + \underline{\mathbf{K}}_{\mu\mathbf{u}}^{fp} \cdot \dot{\underline{\mathbf{u}}}^p + \underline{\mathbf{K}}_{\mu\mathbf{u}}^{ff} \cdot \dot{\underline{\mathbf{u}}}_{ss}^f = \underline{\mathbf{Q}}^f. \quad (4.62)$$

Equation (4.62) is the evolution equation for μ_{ss}^f . Under the steady-state condition it holds that

$$\underline{\mathbf{M}}_{\mu\mu}^{fp} \dot{\underline{\mu}}^p + \underline{\mathbf{M}}_{\mu\mu}^{ff} \dot{\underline{\mu}}_{ss}^f + \underline{\mathbf{K}}_{\mu\mathbf{u}}^{fp} \cdot \dot{\underline{\mathbf{u}}}^p + \underline{\mathbf{K}}_{\mu\mathbf{u}}^{ff} \cdot \dot{\underline{\mathbf{u}}}_{ss}^f = \underline{\mathbf{Q}}^f, \quad (4.63)$$

The steady-state part of the chemical potential $\underline{\mu}_{ss}$ can then be expressed in terms of the prescribed DOF $\underline{\mu}^p$ as

$$\underline{\mu}_{ss}^f = \underline{\mathbf{S}}_{\mu\mu}^{fp} \underline{\mu}^p, \quad (4.64)$$

where $\underline{\mathbf{S}}_{\mu\mu}^{fp} = -[\underline{\mathbf{K}}_{\mu\mu}^{ff}]^{-1} \underline{\mathbf{K}}_{\mu\mu}^{fp}$ is the Schur-complement. When multiplied with the macroscopic quantities $\underline{\mathbf{S}}_{\mu\mu}^{fp}$ provides the steady-state homogenized response for the linear material model and thus can be considered as the steady-state reduced basis for the chemical potential field.

4.4.3.2 Mechanics

Similarly, to obtain the steady-state displacement field $\underline{\underline{\boldsymbol{u}}}_{ss}^f$ the second line of equation (4.59) is considered

$$\underline{\underline{\mathbf{K}}}_{\underline{\underline{\boldsymbol{u}}}\underline{\underline{\boldsymbol{\mu}}}}^{fp}\underline{\underline{\boldsymbol{\mu}}}^p + \underline{\underline{\mathbf{K}}}_{\underline{\underline{\boldsymbol{u}}}\underline{\underline{\boldsymbol{\mu}}}}^{ff}\underline{\underline{\boldsymbol{\mu}}}_{ss}^f + \underline{\underline{\mathbf{K}}}_{\underline{\underline{\boldsymbol{u}}}\underline{\underline{\boldsymbol{u}}}}^{fp} \cdot \underline{\underline{\boldsymbol{u}}}^p + \underline{\underline{\mathbf{K}}}_{\underline{\underline{\boldsymbol{u}}}\underline{\underline{\boldsymbol{u}}}}^{ff} \cdot \underline{\underline{\boldsymbol{u}}}_{ss}^f = \underline{\underline{\mathbf{0}}}^f. \quad (4.65)$$

Substituting expression (4.64) for $\underline{\underline{\boldsymbol{\mu}}}_{ss}^f$ in the equation (4.65) yields

$$\underline{\underline{\mathbf{K}}}_{\underline{\underline{\boldsymbol{u}}}\underline{\underline{\boldsymbol{\mu}}}}^{fp}\underline{\underline{\boldsymbol{\mu}}}^p + \underline{\underline{\mathbf{K}}}_{\underline{\underline{\boldsymbol{u}}}\underline{\underline{\boldsymbol{\mu}}}}^{ff}\underline{\underline{\mathbf{S}}}_{\underline{\underline{\boldsymbol{\mu}}}\underline{\underline{\boldsymbol{\mu}}}}^{fp}\underline{\underline{\boldsymbol{\mu}}}^p + \underline{\underline{\mathbf{K}}}_{\underline{\underline{\boldsymbol{u}}}\underline{\underline{\boldsymbol{u}}}}^{fp} \cdot \underline{\underline{\boldsymbol{u}}}^p + \underline{\underline{\mathbf{K}}}_{\underline{\underline{\boldsymbol{u}}}\underline{\underline{\boldsymbol{u}}}}^{ff} \cdot \underline{\underline{\boldsymbol{u}}}_{ss}^f = \underline{\underline{\mathbf{0}}}^f, \quad (4.66)$$

from where the expression for $\underline{\underline{\boldsymbol{u}}}_{ss}^f$ can be computed in terms of $\underline{\underline{\boldsymbol{\mu}}}^p$ and $\underline{\underline{\boldsymbol{u}}}^p$

$$\underline{\underline{\boldsymbol{u}}}_{ss}^f = \underline{\underline{\mathbf{S}}}_{\underline{\underline{\boldsymbol{u}}}\underline{\underline{\boldsymbol{\mu}}}}^{fp}\underline{\underline{\boldsymbol{\mu}}}^p + \underline{\underline{\mathbf{S}}}_{\underline{\underline{\boldsymbol{u}}}\underline{\underline{\boldsymbol{u}}}}^{fp} \cdot \underline{\underline{\boldsymbol{u}}}^p, \quad (4.67)$$

where $\underline{\underline{\mathbf{S}}}_{\underline{\underline{\boldsymbol{u}}}\underline{\underline{\boldsymbol{\mu}}}}^{fp} = -[\underline{\underline{\mathbf{K}}}_{\underline{\underline{\boldsymbol{u}}}\underline{\underline{\boldsymbol{u}}}}^{ff}]^{-1} (\underline{\underline{\mathbf{K}}}_{\underline{\underline{\boldsymbol{u}}}\underline{\underline{\boldsymbol{\mu}}}}^{fp} + \underline{\underline{\mathbf{K}}}_{\underline{\underline{\boldsymbol{u}}}\underline{\underline{\boldsymbol{\mu}}}}^{ff}\underline{\underline{\mathbf{S}}}_{\underline{\underline{\boldsymbol{\mu}}}\underline{\underline{\boldsymbol{\mu}}}}^{fp})$ and $\underline{\underline{\mathbf{S}}}_{\underline{\underline{\boldsymbol{u}}}\underline{\underline{\boldsymbol{u}}}}^{fp} = -[\underline{\underline{\mathbf{K}}}_{\underline{\underline{\boldsymbol{u}}}\underline{\underline{\boldsymbol{u}}}}^{ff}]^{-1}\underline{\underline{\mathbf{K}}}_{\underline{\underline{\boldsymbol{u}}}\underline{\underline{\boldsymbol{u}}}}^{fp}$.

4.4.4 Transient Response

As stated in section 4.4.2, due to the relaxed separation of scales, to identify the transient reduced basis it is justified to use the free DOFs only. From equation (4.58) with account for (4.64), the free part of the discrete mass conservation equation can be written as

$$\underline{\underline{\mathbf{K}}}_{\underline{\underline{\boldsymbol{\mu}}}\underline{\underline{\boldsymbol{\mu}}}}^{ff}\underline{\underline{\boldsymbol{\mu}}}_{tr}^f + \underline{\underline{\mathbf{M}}}_{\underline{\underline{\boldsymbol{\mu}}}\underline{\underline{\boldsymbol{\mu}}}}^{ff}\dot{\underline{\underline{\boldsymbol{\mu}}}}_{tr}^f + \underline{\underline{\mathbf{K}}}_{\underline{\underline{\boldsymbol{\mu}}}\underline{\underline{\boldsymbol{u}}}}^{ff} \cdot \dot{\underline{\underline{\boldsymbol{u}}}}_{tr}^f = \underline{\underline{\mathbf{0}}}^f, \quad (4.68)$$

and from equation (4.59) with account for (4.65), the free part of the discrete conservation of linear momentum can be written as

$$\underline{\underline{\mathbf{K}}}_{\underline{\underline{\boldsymbol{u}}}\underline{\underline{\boldsymbol{\mu}}}}^{ff}\underline{\underline{\boldsymbol{\mu}}}_{tr}^f + \underline{\underline{\mathbf{K}}}_{\underline{\underline{\boldsymbol{u}}}\underline{\underline{\boldsymbol{u}}}}^{ff} \cdot \underline{\underline{\boldsymbol{u}}}_{tr}^f = \underline{\underline{\mathbf{0}}}^f, \quad (4.69)$$

from where

$$\underline{\underline{\boldsymbol{u}}}_{tr}^f = \underline{\underline{\mathbf{S}}}_{\underline{\underline{\boldsymbol{u}}}\underline{\underline{\boldsymbol{\mu}}}}^{ff}\underline{\underline{\boldsymbol{\mu}}}_{tr}^f, \quad (4.70)$$

with $\underline{\underline{\mathbf{S}}}_{\underline{\underline{\boldsymbol{u}}}\underline{\underline{\boldsymbol{\mu}}}}^{ff} = -[\underline{\underline{\mathbf{K}}}_{\underline{\underline{\boldsymbol{u}}}\underline{\underline{\boldsymbol{u}}}}^{ff}]^{-1}\underline{\underline{\mathbf{K}}}_{\underline{\underline{\boldsymbol{u}}}\underline{\underline{\boldsymbol{\mu}}}}^{ff}$.

Assuming that the transient part of the microscopic solution fields, $\underline{\underline{\boldsymbol{\mu}}}_{tr}^f$ and $\underline{\underline{\boldsymbol{u}}}_{tr}^f$, can be expressed in terms of a set of reduced basis functions, the transient chemical potential $\underline{\underline{\boldsymbol{\mu}}}_{tr}^f$ is written in terms of these reduced basis functions $\underline{\underline{\Phi}}_{\underline{\underline{\boldsymbol{\mu}}}}^{(k)}$ and

the corresponding coefficients $\eta_\mu^{(k)}$ as

$$\underline{\mu}_{tr}^f \approx \sum_{k=1}^{\mathcal{N}_q^\mu} \underline{\Phi}_\mu^{(k)} \eta_\mu^{(k)} = \underline{\Phi}_\mu^* \eta_\mu, \quad (4.71)$$

where $\underline{\Phi}_\mu^*$ is the matrix containing the columns of the reduced transient functions $\underline{\Phi}_\mu^{(k)}$ and \mathcal{N}_q^μ is the number of reduced basis functions for the chemical potential, which is much smaller than the total number of the free DOF \mathcal{N}_f , i.e., $\mathcal{N}_q^\mu \ll \mathcal{N}_f$. Similarly, the transient displacement field $\underline{\mathbf{u}}_{tr}$ can also be written in terms of the reduced basis functions $\underline{\Phi}_u^{(k)}$ and their corresponding coefficients $\eta_u^{(k)}$ as

$$\underline{\mathbf{u}}_{tr}^f \approx \sum_{k=1}^{\mathcal{N}_q^u} \underline{\Phi}_u^{(k)} \eta_u^{(k)} = \underline{\Phi}_u^* \eta_u. \quad (4.72)$$

where \mathcal{N}_q^u is the number of reduced basis for the displacement field. We will show later that \mathcal{N}_q^μ and \mathcal{N}_q^u and η_u and η_μ are the same. The selection criteria for the set of \mathcal{N}_q basis functions will also be presented later. Next, the reduced basis functions in equations (4.71) and (4.72) are identified using a spectral decomposition scheme.

4.4.4.1 Mass Diffusion

Substituting $\underline{\mu}_{tr}^f$ from equation (4.70) into equation (4.68) provides

$$\underline{K}_{\mu\mu}^{ff} \underline{\mu}_{tr}^f + \underline{M}_{\mu\mu}^{ff*} \underline{\mu}_{tr}^f = \underline{\mathcal{Q}}^f, \quad (4.73)$$

where $\underline{M}_{\mu\mu}^{ff*} = \underline{M}_{\mu\mu}^{ff} + \underline{\mathbf{K}}_{\mu u}^{ff} \underline{\mathbf{S}}_{u\mu}^{ff}$ is the coupled mass matrix. The mass conservation (4.34) is a parabolic partial differential equation which has a natural solution that decays exponentially in time, i.e., $\underline{\mu} = \underline{\Phi}^{(k)} \exp[-\alpha^{(k)}t]$, substituting it in equation (4.73) yields the eigenvalue problems

$$(\underline{K}_{\mu\mu}^{ff} - \alpha^{(k)} \underline{M}_{\mu\mu}^{ff*}) \underline{\Phi}^{(k)} = \underline{\mathcal{Q}}^f, \quad (4.74)$$

where $\underline{\Phi}^{(k)}$ is the k -th eigenvector and $\alpha^{(k)}$ the associated k -th eigenvalue. For the diffusion problem (4.34), the eigenvectors are the chemical potential distribution modes inside the domain and the corresponding eigenvalues are the inverse of a decay/rise time, i.e., $\tau^{(k)} = \frac{2\pi}{\alpha^{(k)}}$. Normalizing the eigenvectors $\underline{\Phi}^{(k)}$ with respect

to the mass matrix $\underline{M}_{\mu\mu}^{*ff}$,

$$[\underline{\Phi}^{(k)}]^T \underline{M}_{\mu\mu}^{*ff} \underline{\Phi}^{(k)} = 1, \quad (4.75)$$

yields

$$[\underline{\Phi}^{(k)}]^T \underline{K}_{\mu\mu}^{ff} \underline{\Phi}^{(k)} = \alpha^{(k)}. \quad (4.76)$$

The transient basis functions $\underline{\Phi}_{\mu}^{*}$ in equation (4.71) can now be identified as the eigenvectors $\underline{\Phi}^{*}$ obtained from the solution of the eigenvalue problem (4.74) i.e. ,

$$\underline{\mu}_{tr}^f = \sum_{k=1}^{\mathcal{N}_q} \underline{\Phi}^{(k)} \eta_k = \underline{\Phi}^{*} \underline{\eta}, \quad (4.77)$$

where $\eta^{(k)}$ can be interpreted as the modal amplitude, and $\underline{\eta}$ is a column of size \mathcal{N}_q .

4.4.4.2 Mechanics

Substituting the expression of $\underline{\mu}_{tr}^f$ from equation (4.77) in (4.70) provides the transient mechanical response

$$\underline{\mathbf{u}}_{tr} = \sum_{k=1}^{\mathcal{N}_q} \underline{\mathbf{S}}_{\mathbf{u}\mu}^{ff} \underline{\Phi}^{(k)} \eta^{(k)} = \underline{\mathbf{S}}_{\mathbf{u}\mu}^{ff} \underline{\Phi}^{*} \underline{\eta}. \quad (4.78)$$

with $\underline{\Phi}_{\mathbf{u}}^{*} = \underline{\mathbf{S}}_{\mathbf{u}\mu}^{ff} \underline{\Phi}^{*}$. Next, we reconstruct the total solution for the chemical potential and displacement fields from their respective transient and steady-state responses.

4.4.5 Linear Superposition

Substituting the expressions for $\underline{\mu}_{ss}$ from (4.64) and $\underline{\mu}_{tr}$ from (4.77) into (4.60), the total chemical potential field at the micro-scale can be written as

$$\underline{\mu} = \underline{\mu}_{ss} + \underline{\mu}_{tr} = \underline{S}_{\mu\mu}^{fp} \underline{\mu}^p + \underline{\Phi}^{*} \underline{\eta}, \quad (4.79)$$

where only the reduced basis $\underline{\Phi}^{*}$ is coupled to the microscopic mechanical problem via the coupled mass matrix $\underline{M}_{\mu\mu}^{*ff}$ appearing in the eigenvalue problem (4.74).

Similarly, the total microscopic displacement field $\underline{\mathbf{u}}$ can be reconstructed by substituting the expression for $\underline{\mathbf{u}}_{ss}$ from (4.67) and $\underline{\mathbf{u}}_{tr}$ from (4.78) into equation

(4.61) i.e. ,

$$\underline{\mathbf{u}} = \underline{\mathbf{u}}_{ss} + \underline{\mathbf{u}}_{tr} = \underline{\mathbf{S}}_{\underline{\mathbf{u}}\underline{\mu}}^{fp} \underline{\mu}^p + \underline{\mathbf{S}}_{\underline{\mathbf{u}}\underline{\mathbf{u}}}^{fp} \cdot \underline{\mathbf{u}}^p + \underline{\mathbf{S}}_{\underline{\mathbf{u}}\underline{\mu}}^{ff} \underline{\Phi}^* \underline{\eta}. \quad (4.80)$$

Both, the steady-state and transient parts of the microscopic displacement field are coupled to the chemical problem as the coupling matrix $\underline{\mathbf{K}}_{\underline{\mathbf{u}}\underline{\mu}}$ appears in the matrices $\underline{\mathbf{S}}_{\underline{\mathbf{u}}\underline{\mu}}^{ff}$, $\underline{\mathbf{S}}_{\underline{\mathbf{u}}\underline{\mu}}^{ff}$ and $\underline{\Phi}^*$. Equations (4.79) and (4.80) shows that the microscopic solution fields, $\underline{\mu}$ and $\underline{\mathbf{u}}$, are completely given by the chemical potential $\underline{\mu}^p$, the displacement $\underline{\mathbf{u}}^p$ at the prescribed DOFs and the coefficients of the transient reduced basis $\underline{\eta}$. Generally, in a two-scale setting, the microscopic fields at the prescribed DOFs, where the microfluctuations $\tilde{\mu}$ and $\tilde{\mathbf{u}}$ are zero, are given by the macroscopic quantities, as can be seen in equation (4.37) and (4.38). Therefore, the only remaining unknown fields at the micro-scale are $\underline{\eta}$ which can be obtained from the evolution equation, derived in the next subsection.

4.4.6 Evolution Equation

The time evolution of $\underline{\eta}$ can be obtained from the free part of equation (4.58)

$$\underline{\mathbf{K}}_{\underline{\mu}\underline{\mu}}^{fp} \underline{\mu}^p + \underline{\mathbf{K}}_{\underline{\mu}\underline{\mu}}^{ff} \underline{\mu}^f + \underline{\mathbf{M}}_{\underline{\mu}\underline{\mu}}^{fp} \dot{\underline{\mu}}^p + \underline{\mathbf{M}}_{\underline{\mu}\underline{\mu}}^{ff} \dot{\underline{\mu}}^f + \underline{\mathbf{K}}_{\underline{\mu}\underline{\mathbf{u}}}^{fp} \cdot \underline{\dot{\mathbf{u}}}^p + \underline{\mathbf{K}}_{\underline{\mu}\underline{\mathbf{u}}}^{ff} \cdot \underline{\dot{\mathbf{u}}}^f = \underline{\mathcal{Q}}^f, \quad (4.81)$$

Substituting the expressions for $\underline{\mu}^f$ from equation (4.79) and $\underline{\mathbf{u}}^f$ from equation (4.80) into (4.81) and rearranging terms

$$\begin{aligned} (\underline{\mathbf{K}}_{\underline{\mu}\underline{\mu}}^{ff} \underline{\Phi}^*) \underline{\eta} + (\underline{\mathbf{M}}_{\underline{\mu}\underline{\mu}}^{ff} \underline{\Phi}^* + \underline{\mathbf{K}}_{\underline{\mu}\underline{\mathbf{u}}}^{ff} \underline{\mathbf{S}}_{\underline{\mathbf{u}}\underline{\mu}}^{ff} \underline{\Phi}^*) \dot{\underline{\eta}} = & -(\underline{\mathbf{K}}_{\underline{\mu}\underline{\mu}}^{fp} + \underline{\mathbf{K}}_{\underline{\mu}\underline{\mu}}^{ff} \underline{\mathbf{S}}_{\underline{\mu}\underline{\mu}}^{fp}) \underline{\mu}^p \\ & - (\underline{\mathbf{M}}_{\underline{\mu}\underline{\mu}}^{fp} + \underline{\mathbf{M}}_{\underline{\mu}\underline{\mu}}^{ff} \underline{\mathbf{S}}_{\underline{\mu}\underline{\mu}}^{fp} + \underline{\mathbf{K}}_{\underline{\mu}\underline{\mathbf{u}}}^{ff} \underline{\mathbf{S}}_{\underline{\mathbf{u}}\underline{\mu}}^{fp}) \dot{\underline{\mu}}^p - (\underline{\mathbf{K}}_{\underline{\mu}\underline{\mathbf{u}}}^{fp} + \underline{\mathbf{K}}_{\underline{\mu}\underline{\mathbf{u}}}^{ff} \underline{\mathbf{S}}_{\underline{\mathbf{u}}\underline{\mathbf{u}}}^{fp}) \cdot \underline{\dot{\mathbf{u}}}^p. \end{aligned} \quad (4.82)$$

Using the definition $\underline{\mathbf{S}}_{\underline{\mu}\underline{\mu}}^{fp} = -[\underline{\mathbf{K}}_{\underline{\mu}\underline{\mu}}^{ff}]^{-1} \underline{\mathbf{K}}_{\underline{\mu}\underline{\mu}}^{fp}$, the first term on the right hand side of (4.82) drops out. Pre-multiplying the remaining equation with $[\underline{\Phi}^*]^T$, equation (4.82) is written as

$$\begin{aligned} [\underline{\Phi}^*]^T \underline{\mathbf{K}}_{\underline{\mu}\underline{\mu}}^{ff} \underline{\Phi}^* \underline{\eta} + [\underline{\Phi}^*]^T (\underline{\mathbf{M}}_{\underline{\mu}\underline{\mu}}^{ff} + \underline{\mathbf{K}}_{\underline{\mu}\underline{\mathbf{u}}}^{ff} \underline{\mathbf{S}}_{\underline{\mathbf{u}}\underline{\mu}}^{ff}) \underline{\Phi}^* \dot{\underline{\eta}} = \\ - [\underline{\Phi}^*]^T (\underline{\mathbf{M}}_{\underline{\mu}\underline{\mu}}^{fp} + \underline{\mathbf{M}}_{\underline{\mu}\underline{\mu}}^{ff} \underline{\mathbf{S}}_{\underline{\mu}\underline{\mu}}^{fp} + \underline{\mathbf{K}}_{\underline{\mu}\underline{\mathbf{u}}}^{ff} \underline{\mathbf{S}}_{\underline{\mathbf{u}}\underline{\mu}}^{fp}) \dot{\underline{\mu}}^p - [\underline{\Phi}^*]^T (\underline{\mathbf{K}}_{\underline{\mu}\underline{\mathbf{u}}}^{fp} + \underline{\mathbf{K}}_{\underline{\mu}\underline{\mathbf{u}}}^{ff} \underline{\mathbf{S}}_{\underline{\mathbf{u}}\underline{\mathbf{u}}}^{fp}) \cdot \underline{\dot{\mathbf{u}}}^p, \end{aligned} \quad (4.83)$$

which after using the normalization conditions in (4.75) and (4.76) takes the form

$$\underline{\alpha} \underline{\eta} + \dot{\underline{\eta}} = - \left(\underline{\mathbf{M}}_{\underline{\mu}\underline{\mu}}^{qp} \dot{\underline{\mu}}^p + \underline{\mathbf{K}}_{\underline{\mu}\underline{\mathbf{u}}}^{qp} \cdot \underline{\dot{\mathbf{u}}}^p \right), \quad (4.84)$$

where,

$$\begin{aligned}\underline{\underline{M}}_{\mu\mu}^{qp} &= [\underline{\underline{\Phi}}]^T (\underline{\underline{M}}_{\mu\mu}^{fp} + \underline{\underline{M}}_{\mu\mu}^{ff} \underline{\underline{S}}_{\mu\mu}^{fp} + \underline{\underline{K}}_{\mu u}^{ff} \underline{\underline{S}}_{u\mu}^{fp}) , \\ \underline{\underline{K}}_{\mu u}^{qp} &= [\underline{\underline{\Phi}}]^T (\underline{\underline{K}}_{\mu u}^{fp} + \underline{\underline{K}}_{\mu u}^{ff} \underline{\underline{S}}_{u\mu}^{fp}) .\end{aligned}\quad (4.85)$$

Equation (4.84) is a set of \mathcal{N}_q decoupled ordinary differential equations (ODEs) which represent the reduced order model for the evolution of diffusion-mechanics behavior at the micro-scale. The right hand side of (4.84) acts as the forcing term to the set of ODEs in terms of macroscopic fields present in $\underline{\underline{\mu}}^p$ and $\underline{\underline{u}}^p$.

4.4.7 Reaction Fluxes and Forces

Next, we write the reaction mass fluxes j_n^p and tractions $\underline{\underline{t}}_n^p$ in terms of the coefficients of the steady-state and transient bases functions.

4.4.7.1 Reaction Fluxes

The reaction mass fluxes j_n^p can be obtained from the first line of the discrete mass conservation equation (4.58)

$$\underline{\underline{K}}_{\mu\mu}^{pp} \underline{\underline{\mu}}^p + \underline{\underline{K}}_{\mu\mu}^{pf} \underline{\underline{\mu}}^f + \underline{\underline{M}}_{\mu\mu}^{pp} \dot{\underline{\underline{\mu}}}^p + \underline{\underline{M}}_{\mu\mu}^{pf} \dot{\underline{\underline{\mu}}}^f + \underline{\underline{K}}_{\mu u}^{pp} \cdot \dot{\underline{\underline{u}}}^p + \underline{\underline{K}}_{\mu u}^{pf} \cdot \dot{\underline{\underline{u}}}^f = -j_n^p . \quad (4.86)$$

Substituting the expressions for $\underline{\underline{\mu}}^f$ and $\underline{\underline{u}}^f$ from equation (4.79) and (4.80) respectively yields

$$\begin{aligned}\underline{\underline{K}}_{\mu\mu}^{pp} \underline{\underline{\mu}}^p + \underline{\underline{K}}_{\mu\mu}^{pf} \underline{\underline{S}}_{\mu\mu}^{fp} \underline{\underline{\mu}}^p + \underline{\underline{K}}_{\mu\mu}^{pf} \underline{\underline{\Phi}}^* \underline{\underline{\eta}} + \underline{\underline{M}}_{\mu\mu}^{pp} \dot{\underline{\underline{\mu}}}^p + \underline{\underline{M}}_{\mu\mu}^{pf} \underline{\underline{S}}_{\mu\mu}^{fp} \dot{\underline{\underline{\mu}}}^p + \underline{\underline{M}}_{\mu\mu}^{pf} \underline{\underline{\Phi}}^* \dot{\underline{\underline{\eta}}} \\ + \underline{\underline{K}}_{\mu u}^{pp} \cdot \dot{\underline{\underline{u}}}^p + \underline{\underline{K}}_{\mu u}^{pf} \underline{\underline{S}}_{u\mu}^{fp} \dot{\underline{\underline{\mu}}}^p + \underline{\underline{K}}_{\mu u}^{pf} \underline{\underline{S}}_{u\mu}^{fp} \cdot \dot{\underline{\underline{u}}}^p + \underline{\underline{K}}_{\mu u}^{pf} \underline{\underline{S}}_{u\mu}^{ff} \underline{\underline{\Phi}}^* \dot{\underline{\underline{\eta}}} = -j_n^p .\end{aligned}\quad (4.87)$$

Making use of $\underline{\underline{\mu}}^f = \underline{\underline{\Phi}}^* \underline{\underline{\eta}}$ in the free part of the mass conservation equation (4.73), then pre-multiplying it with $[\underline{\underline{S}}_{\mu\mu}^{fp}]^T$ and using $\underline{\underline{S}}_{\mu\mu}^{fp} = -[\underline{\underline{K}}_{\mu\mu}^{ff}]^{-1} \underline{\underline{K}}_{\mu\mu}^{fp}$, with account for the symmetry of $\underline{\underline{K}}_{\mu\mu}$, replaces the third term $\underline{\underline{K}}_{\mu\mu}^{pf} \underline{\underline{\Phi}}^* \underline{\underline{\eta}}$ in equation (4.87) with $[\underline{\underline{S}}_{\mu\mu}^{fp}]^T \underline{\underline{M}}_{\mu\mu}^{ff} \underline{\underline{\Phi}}^* \dot{\underline{\underline{\eta}}}$ i.e. ,

$$\begin{aligned}\underline{\underline{K}}_{\mu\mu}^{pp} \underline{\underline{\mu}}^p + \underline{\underline{K}}_{\mu\mu}^{pf} \underline{\underline{S}}_{\mu\mu}^{fp} \underline{\underline{\mu}}^p + [\underline{\underline{S}}_{\mu\mu}^{fp}]^T \underline{\underline{M}}_{\mu\mu}^{ff} \underline{\underline{\Phi}}^* \dot{\underline{\underline{\eta}}} + \underline{\underline{M}}_{\mu\mu}^{pp} \dot{\underline{\underline{\mu}}}^p + \underline{\underline{M}}_{\mu\mu}^{pf} \underline{\underline{S}}_{\mu\mu}^{fp} \dot{\underline{\underline{\mu}}}^p + \underline{\underline{M}}_{\mu\mu}^{pf} \underline{\underline{\Phi}}^* \dot{\underline{\underline{\eta}}} \\ + \underline{\underline{K}}_{\mu u}^{pp} \cdot \dot{\underline{\underline{u}}}^p + \underline{\underline{K}}_{\mu u}^{pf} \underline{\underline{S}}_{u\mu}^{fp} \dot{\underline{\underline{\mu}}}^p + \underline{\underline{K}}_{\mu u}^{pf} \underline{\underline{S}}_{u\mu}^{fp} \cdot \dot{\underline{\underline{u}}}^p + \underline{\underline{K}}_{\mu u}^{pf} \underline{\underline{S}}_{u\mu}^{ff} \underline{\underline{\Phi}}^* \dot{\underline{\underline{\eta}}} = -j_n^p .\end{aligned}\quad (4.88)$$

Now the steady-state constraint (4.63), projected onto the prescribed DOF, should be added to equation (4.88). For projecting the steady-state constraint (4.63) onto the prescribed DOF, it is first pre-multiplied with $[\underline{S}_{\mu\mu}^{fp}]^T$, then the expressions of the steady-state chemical potential from (4.64) and the steady-state displacement field from (4.67) are substituted and finally the transpose of the whole expression is performed

$$\begin{aligned}
& \underline{K}_{\mu\mu}^{pp} \underline{\mu}^p + \underline{K}_{\mu\mu}^{pf} \underline{S}_{\mu\mu}^{fp} \underline{\mu}^p + [\underline{S}_{\mu\mu}^{fp}]^T \underline{M}_{\mu\mu}^{ff} \underline{\Phi}^* \dot{\eta} + \underline{M}_{\mu\mu}^{pp} \dot{\underline{\mu}}^p + \underline{M}_{\mu\mu}^{pf} \underline{S}_{\mu\mu}^{fp} \dot{\underline{\mu}}^p + \underline{M}_{\mu\mu}^{fp} \underline{\Phi}^* \dot{\eta} \\
& + \underline{K}_{\mu u}^{pp} \cdot \dot{\underline{\mathbf{u}}}^p + \underline{K}_{\mu u}^{pf} \underline{S}_{u\mu}^{fp} \dot{\underline{\mu}}^p + \underline{K}_{\mu u}^{pf} \underline{S}_{uu}^{fp} \cdot \dot{\underline{\mathbf{u}}}^p + \underline{K}_{\mu u}^{pf} \underline{S}_{u\mu}^{ff} \underline{\Phi}^* \dot{\eta} + \\
& \underline{M}_{\mu\mu}^{pf} \underline{S}_{\mu\mu}^{fp} \dot{\underline{\mu}}^p + [\underline{S}_{\mu\mu}^{fp}]^T \underline{M}_{\mu\mu}^{ff} \underline{S}_{\mu\mu}^{fp} \dot{\underline{\mu}}^p + [\underline{S}_{u\mu}^{fp}]^T \underline{K}_{u\mu}^{ff} \underline{S}_{\mu\mu}^{fp} \dot{\underline{\mu}}^p + \\
& \left[[\underline{K}_{\mu u}^{fp}]^T \underline{S}_{\mu\mu}^{fp} \right]^T \cdot \dot{\underline{\mathbf{u}}}^p + \left[[\underline{S}_{u\mu}^{fp}]^T \underline{K}_{u\mu}^{ff} \underline{S}_{\mu\mu}^{fp} \right]^T \cdot \dot{\underline{\mathbf{u}}}^p = -\underline{j}_n^p. \quad (4.89)
\end{aligned}$$

Rearranging terms gives the resulting reaction mass flux

$$\underline{j}_n^p = -\underline{M}_{\mu\mu}^{pq} \dot{\eta} - \underline{K}_{\mu\mu}^{pp} \underline{\mu}^p - \underline{M}_{\mu\mu}^{pp} \dot{\underline{\mu}}^p - \underline{M}_{\mu u}^{pp} \cdot \dot{\underline{\mathbf{u}}}^p, \quad (4.90)$$

where

$$\begin{aligned}
\underline{M}_{\mu\mu}^{pq} &= [\underline{S}_{\mu\mu}^{fp}]^T \underline{M}_{\mu\mu}^{ff} \underline{\Phi}^* + \underline{M}_{\mu\mu}^{pf} \underline{\Phi}^* + \underline{K}_{\mu u}^{pf} \underline{S}_{u\mu}^{ff} \underline{\Phi}^*, \\
\underline{M}_{\mu\mu}^{pp} &= \underline{M}_{\mu\mu}^{pp} + \underline{M}_{\mu\mu}^{pf} \underline{S}_{\mu\mu}^{fp} + \underline{M}_{\mu\mu}^{pf} \underline{S}_{\mu\mu}^{fp} + [\underline{S}_{\mu\mu}^{fp}]^T \underline{M}_{\mu\mu}^{ff} \underline{S}_{\mu\mu}^{fp} + \\
& [\underline{S}_{u\mu}^{fp}]^T \underline{K}_{u\mu}^{ff} \underline{S}_{\mu\mu}^{fp} + \underline{K}_{\mu u}^{pf} \underline{S}_{u\mu}^{fp}, \quad (4.91) \\
\underline{K}_{\mu\mu}^{pp} &= \underline{K}_{\mu\mu}^{pp} + \underline{K}_{\mu\mu}^{pf} \underline{S}_{\mu\mu}^{fp}, \\
\underline{M}_{\mu u}^{pp} &= \underline{K}_{\mu u}^{pp} + \underline{K}_{\mu u}^{pf} \underline{S}_{uu}^{fp} + \left[[\underline{K}_{\mu u}^{fp}]^T \underline{S}_{\mu\mu}^{fp} \right]^T + \left[[\underline{S}_{u\mu}^{fp}]^T \underline{K}_{u\mu}^{ff} \underline{S}_{\mu\mu}^{fp} \right]^T.
\end{aligned}$$

4.4.7.2 Reaction Forces

Similarly, the first part of the equation (4.59) provides the expression for the reaction forces $\underline{\mathbf{t}}_n^p$ at the prescribed DOF

$$\underline{K}_{u\mu}^{pp} \underline{\mu}^p + \underline{K}_{u\mu}^{pf} \underline{\mu}^f + \underline{K}_{uu}^{pp} \cdot \underline{\mathbf{u}}^p + \underline{K}_{uu}^{pf} \cdot \underline{\mathbf{u}}^f = \underline{\mathbf{t}}_n^p. \quad (4.92)$$

Substituting the expressions for $\underline{\mu}^f$ and $\underline{\mathbf{u}}^f$ from (4.79) and (4.80) into (4.92), gives

$$\begin{aligned}
& \underline{K}_{u\mu}^{pp} \underline{\mu}^p + \underline{K}_{u\mu}^{pf} \underline{S}_{\mu\mu}^{fp} \underline{\mu}^p + \underline{K}_{u\mu}^{pf} \underline{\Phi}^* \eta + \underline{K}_{uu}^{pp} \cdot \underline{\mathbf{u}}^p \\
& + \underline{K}_{uu}^{pf} \underline{S}_{u\mu}^{fp} \underline{\mu}^p + \underline{K}_{uu}^{fp} \underline{S}_{uu}^{fp} \cdot \underline{\mathbf{u}}^p + \underline{K}_{uu}^{pf} \underline{S}_{u\mu}^{ff} \underline{\Phi}^* \eta = \underline{\mathbf{t}}_n^p, \quad (4.93)
\end{aligned}$$

which after rearranging for terms can be written as

$$\underline{\mathbf{t}}_n^p = \underline{\mathbf{K}}_{\underline{\mathbf{u}}\underline{\mu}}^{pq} \eta + \underline{\mathbf{K}}_{\underline{\mathbf{u}}\underline{\mu}}^{pp} \underline{\mu}^p + \underline{\mathbf{K}}_{\underline{\mathbf{u}}\underline{\mathbf{u}}}^{pp} \cdot \underline{\mathbf{u}}^p, \quad (4.94)$$

where

$$\begin{aligned} \underline{\mathbf{K}}_{\underline{\mathbf{u}}\underline{\mu}}^{pq} &= \underline{\mathbf{K}}_{\underline{\mathbf{u}}\underline{\mu}}^{pf} \underline{\Phi} + \underline{\mathbf{K}}_{\underline{\mathbf{u}}\underline{\mathbf{u}}}^{pf} \underline{\mathbf{S}}_{\underline{\mathbf{u}}\underline{\mu}}^{ff} \underline{\Phi}, \\ \underline{\mathbf{K}}_{\underline{\mathbf{u}}\underline{\mu}}^{pp} &= \underline{\mathbf{K}}_{\underline{\mathbf{u}}\underline{\mu}}^{pp} + \underline{\mathbf{K}}_{\underline{\mathbf{u}}\underline{\mu}}^{pf} \underline{\mathbf{S}}_{\underline{\mu}\underline{\mu}}^{fp} + \underline{\mathbf{K}}_{\underline{\mathbf{u}}\underline{\mathbf{u}}}^{pf} \underline{\mathbf{S}}_{\underline{\mathbf{u}}\underline{\mu}}^{fp}, \\ \underline{\mathbf{K}}_{\underline{\mathbf{u}}\underline{\mathbf{u}}}^{pp} &= \underline{\mathbf{K}}_{\underline{\mathbf{u}}\underline{\mathbf{u}}}^{pp} + \underline{\mathbf{K}}_{\underline{\mathbf{u}}\underline{\mathbf{u}}}^{pf} \underline{\mathbf{S}}_{\underline{\mathbf{u}}\underline{\mathbf{u}}}^{fp}. \end{aligned} \quad (4.95)$$

In the expressions of reaction fluxes (4.90) and reaction forces (4.94), the only unknown is η which needs to be solved for in combination with the evolution equation (4.84), while $\underline{\mu}^p$ and $\underline{\mathbf{u}}^p$ are written in terms of the given (prescribed) macroscopic quantities.

4.4.8 Macroscopic Quantities

Next, the expressions for the macroscopic quantities $\bar{\boldsymbol{\sigma}}$, $\bar{\mathbf{j}}$ and $\dot{\bar{c}}$ are derived in terms of macroscopic DOF, and the coefficients of the microscopic transient basis η .

4.4.8.1 Macroscopic Flux

In the discretized form, the boundary integral (4.51) of the macroscopic flux $\bar{\mathbf{j}}$ can be written as

$$\bar{\mathbf{j}} = \frac{1}{V} [\Delta \underline{\mathbf{x}}^p]^T \underline{\mathbf{j}}_n^p, \quad (4.96)$$

where $\Delta \underline{\mathbf{x}}^p = (\mathbf{x}^p - \underline{\mathbf{I}}^p \bar{\mathbf{x}})$, with $\underline{\mathbf{I}}^p$ is the column of ones with dimension $(p \times 1)$. Substituting the expression for $\underline{\mathbf{j}}_n^p$ from (4.90) in (4.96) gives

$$\bar{\mathbf{j}} = -\frac{1}{V} [\Delta \underline{\mathbf{x}}^p]^T \left(\underline{\mathbf{M}}_{\underline{\mu}\underline{\mu}}^{pq} \dot{\eta} + \underline{\mathbf{K}}_{\underline{\mu}\underline{\mu}}^{pp} \underline{\mu}^p + \underline{\mathbf{M}}_{\underline{\mu}\underline{\mu}}^{pp} \dot{\underline{\mu}}^p + \underline{\mathbf{M}}_{\underline{\mu}\underline{\mathbf{u}}}^{pp} \cdot \dot{\underline{\mathbf{u}}}^p \right), \quad (4.97)$$

which after substituting the discretized form of expression (4.37) for $\underline{\mu}^p$ gives

$$\underline{\mu}^p = \underline{\mathbf{I}}^p \bar{\mu} + \bar{\nabla} \bar{\mu} \cdot \Delta \underline{\mathbf{x}}^p, \quad (4.98)$$

and (4.38) for $\underline{\mathbf{u}}^p$ as

$$\underline{\mathbf{u}}^p = \underline{\mathbf{I}}^p \bar{\mathbf{u}} + \bar{\nabla} \bar{\mathbf{u}} \cdot \Delta \underline{\mathbf{x}}^p. \quad (4.99)$$

After rearranging terms, (4.97) takes the following form

$$\bar{\mathbf{j}} = [{}^1\underline{\mathbf{M}}^{\dot{\eta}}]^T \dot{\eta} + {}^2\underline{\mathbf{M}}^{\nabla\bar{\mu}} \cdot \nabla\bar{\mu} + {}^1\underline{\mathbf{M}}^{\dot{\mu}} \dot{\mu} + {}^2\underline{\mathbf{M}}^{\nabla\dot{\mu}} \cdot \nabla\dot{\mu} + {}^3\underline{\mathbf{M}}^{\nabla\dot{\mathbf{u}}} : [\nabla\dot{\mathbf{u}}]^T. \quad (4.100)$$

Where, in the notation ${}^n \mathbf{A}^\bullet$, n is the tensorial order and \bullet denotes the macroscopic quantity to which the coefficient \mathbf{M} belongs to. The coefficients on the right hand side of equation (4.100) are given by

$$\begin{aligned} [{}^1\underline{\mathbf{M}}^{\dot{\eta}}]^T &= -\frac{1}{V} [\Delta\mathbf{x}^p]^T \underline{\underline{\mathbf{M}}}_{\mu\mu}^{\star pq}, & (\text{Row of } \mathcal{N}_q \text{ 1st-order tensors (vectors)}) \\ {}^2\underline{\mathbf{M}}^{\nabla\bar{\mu}} &= -\frac{1}{V} [\Delta\mathbf{x}^p]^T \underline{\underline{\mathbf{K}}}_{\mu\mu}^{\star pp} \otimes \Delta\mathbf{x}^p, & (\text{2nd-order tensor}) \\ {}^1\underline{\mathbf{M}}^{\dot{\mu}} &= -\frac{1}{V} [\Delta\mathbf{x}^p]^T \underline{\underline{\mathbf{M}}}_{\mu\mu}^{\star pp} \underline{\underline{\mathbf{I}}}^p, & (\text{1st-order tensor}) \\ {}^2\underline{\mathbf{M}}^{\nabla\dot{\mu}} &= -\frac{1}{V} [\Delta\mathbf{x}^p]^T \underline{\underline{\mathbf{M}}}_{\mu\mu}^{\star pp} \otimes \Delta\mathbf{x}^p, & (\text{2nd-order tensor}) \\ {}^3\underline{\mathbf{M}}^{\nabla\dot{\mathbf{u}}} &= -\frac{1}{V} [\Delta\mathbf{x}^p]^T \otimes \underline{\underline{\mathbf{M}}}_{\mu\mathbf{u}}^{\star pp} \otimes \Delta\mathbf{x}^p. & (\text{3rd-order tensor}) \end{aligned} \quad (4.101)$$

where it has been taken into account that $[\Delta\mathbf{x}^p]^T \underline{\underline{\mathbf{K}}}_{\mu\mu}^{\star pp} \underline{\underline{\mathbf{I}}}^p = [\Delta\mathbf{x}^p]^T \otimes \underline{\underline{\mathbf{M}}}_{\mu\mathbf{u}}^{\star pp} \underline{\underline{\mathbf{I}}}^p = \mathbf{0}$.

4.4.8.2 Macroscopic Concentration Rate

In its discrete form, the expression for the rate of change of the macroscopic concentration field \dot{c} , equation (4.52), can be written as

$$\dot{c} = -\frac{1}{V} [\underline{\underline{\mathbf{I}}}^p]^T \underline{\underline{\mathbf{j}}}_n^p. \quad (4.102)$$

Substituting the expressions of $\underline{\underline{\mu}}^p$ and $\underline{\underline{\mathbf{u}}}^p$ from equation (4.98) and (4.99) in equation (4.90) for $\underline{\underline{\mathbf{j}}}_n^p$ respectively, and then rearranging terms in expression (4.102) gives

$$\dot{c} = [{}^0\underline{\underline{\mathbf{C}}}]^T \dot{\eta} + {}^0\underline{\underline{\mathbf{C}}}^{\dot{\mu}} \dot{\mu} + {}^1\underline{\underline{\mathbf{C}}}^{\nabla\dot{\mu}} \cdot \nabla\dot{\mu} + {}^2\underline{\underline{\mathbf{C}}}^{\nabla\dot{\mathbf{u}}} : [\nabla\dot{\mathbf{u}}]^T, \quad (4.103)$$

where the coefficients on the right hand side of equation (4.103) are given by

$$\begin{aligned} [{}^0\underline{\underline{\mathbf{C}}}^{\dot{\eta}}]^T &= \frac{1}{V} [\underline{\underline{\mathbf{I}}}^p]^T \underline{\underline{\mathbf{M}}}_{\mu\mu}^{\star pq}, & (\text{Row of } \mathcal{N}_q \text{ scalars}) \\ {}^0\underline{\underline{\mathbf{C}}}^{\dot{\mu}} &= \frac{1}{V} [\underline{\underline{\mathbf{I}}}^p]^T \underline{\underline{\mathbf{M}}}_{\mu\mu}^{\star pp} \underline{\underline{\mathbf{I}}}^p, & (\text{Scalar}) \\ {}^1\underline{\underline{\mathbf{C}}}^{\nabla\dot{\mu}} &= \frac{1}{V} [\underline{\underline{\mathbf{I}}}^p]^T \underline{\underline{\mathbf{M}}}_{\mu\mu}^{\star pp} \Delta\mathbf{x}^p, & (\text{1st-order tensor}) \\ {}^2\underline{\underline{\mathbf{C}}}^{\nabla\dot{\mathbf{u}}} &= \frac{1}{V} [\underline{\underline{\mathbf{I}}}^p]^T \underline{\underline{\mathbf{M}}}_{\mu\mathbf{u}}^{\star pp} \otimes \Delta\mathbf{x}^p, & (\text{2nd-order tensor}) \end{aligned} \quad (4.104)$$

where $[\underline{I}^p]^\text{T} \underline{\underline{K}}_{\mu\mu}^{\star pp} \underline{I}^p = [\underline{I}^p]^\text{T} \underline{\underline{K}}_{\mu\mu}^{\star pp} \Delta \underline{\underline{x}}^p = [\underline{I}^p]^\text{T} \underline{\underline{M}}_{\mu\mathbf{u}}^{\star pp} \underline{I}^p = \mathbf{0}$ has been used.

4.4.8.3 Macroscopic Stress

Similarly, the expression (4.55) for the macroscopic stress $\bar{\boldsymbol{\sigma}}$ in its discrete form can be written as

$$\bar{\boldsymbol{\sigma}} = \frac{1}{V} [\Delta \underline{\underline{x}}^p]^\text{T} \otimes \underline{\underline{t}}_n^p. \quad (4.105)$$

Substituting the expression for the reaction forces $\underline{\underline{t}}_n^p$ from equation (4.94) provides

$$\bar{\boldsymbol{\sigma}} = \frac{1}{V} [\Delta \underline{\underline{x}}^p]^\text{T} \otimes \left(\underline{\underline{K}}_{\mathbf{u}\eta}^{\star pq} \eta + \underline{\underline{K}}_{\mathbf{u}\mu}^{\star pp} \mu^p + \underline{\underline{K}}_{\mathbf{u}\mathbf{u}}^{\star pp} \cdot \underline{\underline{u}}^p \right), \quad (4.106)$$

which after using the discretized $\underline{\underline{\mu}}^p$ and $\underline{\underline{u}}^p$ from equations (4.98) and (4.99) take the following form

$$\bar{\boldsymbol{\sigma}} = {}^2\mathbb{C}^\eta \eta + {}^2\mathbb{C}^{\bar{\mu}} \bar{\mu} + {}^3\mathbb{C}^{\bar{\nabla}\bar{\mu}} \cdot \bar{\nabla} \bar{\mu} + {}^4\mathbb{C}^{\bar{\nabla}\bar{\mathbf{u}}} : [\bar{\nabla} \bar{\mathbf{u}}]^\text{T}. \quad (4.107)$$

The coefficients in equation (4.107) are given by

$$\begin{aligned} [{}^2\mathbb{C}^\eta]^\text{T} &= \frac{1}{V} [\Delta \underline{\underline{x}}^p]^\text{T} \otimes \underline{\underline{K}}_{\mathbf{u}\eta}^{\star pq}, & (\text{Rows of } \mathcal{N}_q \text{ 2nd-order tensors}) \\ {}^2\mathbb{C}^{\bar{\mu}} &= \frac{1}{V} [\Delta \underline{\underline{x}}^p]^\text{T} \otimes \underline{\underline{K}}_{\mathbf{u}\mu}^{\star pp} \underline{I}^p, & (2\text{nd-order tensor}) \\ {}^3\mathbb{C}^{\bar{\nabla}\bar{\mu}} &= \frac{1}{V} [\Delta \underline{\underline{x}}^p]^\text{T} \otimes \underline{\underline{K}}_{\mathbf{u}\mu}^{\star pp} \otimes \Delta \underline{\underline{x}}^p, & (3\text{rd-order tensor}) \\ {}^4\mathbb{C}^{\bar{\nabla}\bar{\mathbf{u}}} &= \frac{1}{V} [\Delta \underline{\underline{x}}^p]^\text{T} \otimes \underline{\underline{K}}_{\mathbf{u}\mathbf{u}}^{\star pp} \otimes \Delta \underline{\underline{x}}^p, & (4\text{th-order tensor}) \end{aligned} \quad (4.108)$$

where $[\Delta \underline{\underline{x}}^p]^\text{T} \otimes \underline{\underline{K}}_{\mathbf{u}\mathbf{u}}^{\star pp} \underline{I}^p = \mathbf{0}$ has been accounted for.

4.4.9 Mode Selection Criteria

The microscopic fields $\underline{\underline{\mu}}$ and $\underline{\underline{u}}$, given by equations (4.79) and (4.80), can be fully described by the macroscopic fields $(\bar{\mu}, \bar{\mathbf{u}})$, their gradients $(\bar{\nabla}\bar{\mu}, \bar{\nabla}\bar{\mathbf{u}})$ and the coefficients of the reduced bases η . The size of the original eigenvalue problem is equal to the number of free DOF \mathcal{N}_f present in the system, which provides the complete set of eigenvectors $\underline{\underline{\Phi}}$. Owing to the fact that in diffusion problems the lowest eigenvalues $\alpha^{(k)}$ are the most important ones, the eigenvectors corresponding to the first (several hundreds) lowest eigenvalues could be taken as the reduced basis. However, this would still entail a computationally inefficient scheme, since in a two-scale setting, where η is solved at the macroscopic quadrature points

as internal variables, solving hundreds of ordinary differential equations for the internal variables would still require noticeable computational efforts. Therefore, the reduced set of eigenvectors $\underline{\Phi}^*$ can be extracted from $\underline{\Phi}$ by taking into account that the right hand side of (4.84) acts as the forcing term and the modal coordinate $\eta^{(k)}$ corresponding to the forcing terms with a higher magnitude will have a higher amplitude and therefore contribute more to the homogenized behavior at the macro-scale. Substituting the expressions for the prescribed chemical potential $\underline{\mu}^p$ and displacement $\underline{\mathbf{u}}^p$ fields, equations (4.98) and (4.99), in the evolution equation (4.84) provides

$$\underline{\alpha}\underline{\eta} + \underline{\dot{\eta}} = - \left(\underline{\underline{M}}_{\mu\mu}^{qp} [I^p \dot{\underline{\mu}} + \nabla \dot{\underline{\mu}} \cdot \Delta \underline{\mathbf{x}}^p] + \underline{\underline{K}}_{\mu\mathbf{u}}^{qp} \cdot [I^p \dot{\underline{\mathbf{u}}} + \nabla \dot{\underline{\mathbf{u}}} \cdot \Delta \underline{\mathbf{x}}^p] \right), \quad (4.109)$$

which after using the definition of the coupling terms in (4.101), (4.104) and (4.108) takes the following form

$$\underline{\alpha}\underline{\eta} + \underline{\dot{\eta}} = - \left({}^0\widehat{\underline{\underline{C}}^{\dot{\eta}}} \dot{\underline{\mu}} + [{}^1\widehat{\underline{\underline{M}}^{\dot{\eta}}}]^T \cdot \nabla \dot{\underline{\mu}} + [{}^2\widehat{\underline{\underline{C}}^{\eta}}]^T : \nabla \dot{\underline{\mathbf{u}}} \right), \quad (4.110)$$

where ${}^0\widehat{\underline{\underline{C}}^{\dot{\eta}}} = V({}^0\underline{\underline{C}}^{\dot{\eta}})$, ${}^1\widehat{\underline{\underline{M}}^{\dot{\eta}}} = V({}^1\underline{\underline{M}}^{\dot{\eta}})$ and ${}^2\widehat{\underline{\underline{C}}^{\eta}} = V({}^2\underline{\underline{C}}^{\eta})$, and takes into account that $\underline{\underline{K}}_{\mu\mathbf{u}}^{qp} I^p = \underline{\underline{0}}^q$. The coefficients ${}^0\widehat{\underline{\underline{C}}^{\dot{\eta}}}$, ${}^1\widehat{\underline{\underline{M}}^{\dot{\eta}}}$ and ${}^2\widehat{\underline{\underline{C}}^{\eta}}$ couple the microscopic transient behavior, in terms of $\eta^{(k)}$, to the macro-scale fields. The higher the value of a coefficient, the higher the contribution of the respective $\eta^{(k)}$ to the macro-scale behavior. This information can be exploited to identify a reduced set of eigenvectors $\underline{\Phi}^*$. The eigenvectors associated to ${}^0\widehat{\underline{\underline{C}}^{\dot{\eta}}}$ with a relatively high contribution are identified using

$$E_{0\widehat{\underline{\underline{C}}^{\dot{\eta}},(k)}} = \frac{|{}^0\widehat{\underline{\underline{C}}^{\dot{\eta}},(k)}|}{\max |{}^0\widehat{\underline{\underline{C}}^{\dot{\eta}}}|}, \quad (4.111)$$

where $|\bullet|$ is the absolute value of \bullet . Similarly, for each component of ${}^1\widehat{\underline{\underline{M}}^{\dot{\eta}}}$ it can be stated

$$E_{1\widehat{\underline{\underline{M}}^{\dot{\eta}},(k)}} = \frac{\|{}^1\widehat{\underline{\underline{M}}^{\dot{\eta}},(k)}\|}{\max \|{}^1\widehat{\underline{\underline{M}}^{\dot{\eta}}}\|}, \quad (4.112)$$

and for each component of ${}^2\widehat{\underline{\underline{C}}^{\eta}}$ using

$$E_{2\widehat{\underline{\underline{C}}^{\eta}},(k)} = \frac{\|{}^2\widehat{\underline{\underline{C}}^{\eta}},(k)\|}{\max \|{}^2\widehat{\underline{\underline{C}}^{\eta}}\|}. \quad (4.113)$$

Then, a reduced eigenbasis $\underline{\Phi}^*$ can be obtained by requiring a minimum threshold e_\bullet for a coefficient \bullet , such that

$$\begin{aligned}
 \underline{\Phi}_{0\widehat{C}\dot{\eta},(k)}^* &= \{\underline{\Phi}^{(k)} \in \underline{\Phi} : E_{0\widehat{C}\dot{\eta},(k)} \geq e_{\widehat{C}}\}, \\
 \underline{\Phi}_{1\widehat{M}\dot{\eta},(k)}^* &= \{\underline{\Phi}^{(k)} \in \underline{\Phi} : E_{1\widehat{M}\dot{\eta},(k)} \geq e_{\widehat{M}}\}, \\
 \underline{\Phi}_{2\widehat{C}\eta,(k)}^* &= \{\underline{\Phi}^{(k)} \in \underline{\Phi} : E_{2\widehat{C}\eta,(k)} \geq e_{\widehat{C}}\}, \\
 \underline{\Phi}^* &= \underline{\Phi}_{0\widehat{C}\dot{\eta},(k)}^* \cup \underline{\Phi}_{1\widehat{M}\dot{\eta},(k)}^* \cup \underline{\Phi}_{2\widehat{C}\eta,(k)}^*.
 \end{aligned} \tag{4.114}$$

For a macroscopic simulation, during an offline stage, individual threshold value signifies the corresponding macroscopic quantity and it should be selected accordingly.

4.4.10 Macro-scale Enriched-Continuum

The model reduction at the micro-scale leads to an enriched-continuum formulation, as shown in Figure 4.1(c), at the macro-scale with $\underline{\eta}$ as the emergent (internal) variables and the set of equations (4.110) as their evolution equations. The developed reduced computational homogenization consists of two stages: an offline stage and an online stage. For a specific microstructure with given material properties and the finite element matrices (equations (4.56) and (4.57)), the offline stage consists of the solution of the eigenvalue problem (4.74), the selection of relevant eigenvectors using (4.114), and the computation of the coefficients for the macroscopic quantities (4.101), (4.104) and (4.108). Through the model reduction of the microscopic problem, (4.56)–(4.57), each macroscopic material point entails a set of \mathcal{N}_q decoupled ordinary differential equations, which are inexpensive to solve. The evolution equations (4.110) are to be solved during the online stage along with the macroscopic conservation equations (4.33) and (4.35), the constitutive equations obtained through the homogenization (4.100), (4.103) and (4.107). All together this constitutes the enriched coupled diffusion-mechanics continuum description as follows

Macroscopic mass conservation:

$$\bar{\nabla} \cdot \bar{\mathbf{j}} + \dot{\bar{c}} = 0$$

Macroscopic flux:

$$\bar{\mathbf{j}} = [{}^1\mathbf{M}^{\dot{\eta}}]^\text{T} \dot{\underline{\eta}} + {}^2\mathbf{M}^{\bar{\nabla}\bar{\mu}} \cdot \bar{\nabla}\bar{\mu} + {}^1\mathbf{M}^{\dot{\mu}} \dot{\bar{\mu}} + {}^2\mathbf{M}^{\bar{\nabla}\dot{\mu}} \cdot \bar{\nabla}\dot{\bar{\mu}} + {}^3\mathbf{M}^{\bar{\nabla}\dot{\mathbf{u}}} : [\bar{\nabla}\dot{\bar{\mathbf{u}}}]^\text{T}$$

Macroscopic concentration rate:

$$\dot{\bar{c}} = [{}^0\mathbf{C}^{\dot{\eta}}]^\text{T} \dot{\underline{\eta}} + {}^0\mathbf{C}^{\dot{\mu}} \dot{\bar{\mu}} + {}^1\mathbf{C}^{\bar{\nabla}\dot{\mu}} \cdot \bar{\nabla}\dot{\bar{\mu}} + {}^2\mathbf{C}^{\bar{\nabla}\dot{\mathbf{u}}} : [\bar{\nabla}\dot{\bar{\mathbf{u}}}]^\text{T}$$

Macroscopic momentum conservation:

$$\bar{\nabla} \cdot \bar{\boldsymbol{\sigma}} = \mathbf{0}$$

Macroscopic stress:

$$\bar{\boldsymbol{\sigma}} = [{}^2\mathbf{C}^{\eta}]^\text{T} \underline{\eta} + {}^2\mathbf{C}^{\bar{\mu}} \bar{\mu} + {}^3\mathbf{C}^{\bar{\nabla}\bar{\mu}} \cdot \bar{\nabla}\bar{\mu} + {}^4\mathbf{C}^{\bar{\nabla}\bar{\mathbf{u}}} : [\bar{\nabla}\bar{\mathbf{u}}]^\text{T}$$

Internal variable evolution:

$$\underline{\alpha}\underline{\eta} + \dot{\underline{\eta}} = - \left({}^0\widehat{\mathbf{C}}^{\dot{\eta}} \dot{\bar{\mu}} + [{}^1\widehat{\mathbf{M}}^{\dot{\eta}}]^\text{T} \cdot \bar{\nabla}\dot{\bar{\mu}} + [{}^2\widehat{\mathbf{C}}^{\eta}]^\text{T} : \bar{\nabla}\dot{\bar{\mathbf{u}}} \right)$$

Different solution methods can be adopted to solve the coupled diffusion-mechanics enriched-continuum problem, depending on whether $\underline{\eta}$ is evaluated at the macroscopic quadrature points, leading to an internal variable solution scheme, or at the nodes along with $\bar{\mu}$ and $\bar{\mathbf{u}}$, which leads to a multi-field solution scheme. Numerical analysis for the solution of the enriched-continuum formulation will be discussed in a future contribution.

4.5 Numerical Examples

In this section, the proposed reduced order homogenization for coupled transient diffusion-mechanics is analyzed at the micro-scale. First, the problem setting is presented. The coupled transient bases are identified. Then, the microscopic fields and macroscopic quantities computed with the reduced order homogenization are compared with those obtained through the expensive, fully resolved, conventional computational homogenization scheme. Finally, the computational efficiency of the proposed reduced order homogenization is assessed.

4.5.1 Problem Setting

Lithium-ion battery electrodes are majorly composed of two components: the electrolyte (matrix) and the active particles (inclusions). As an example, in this study

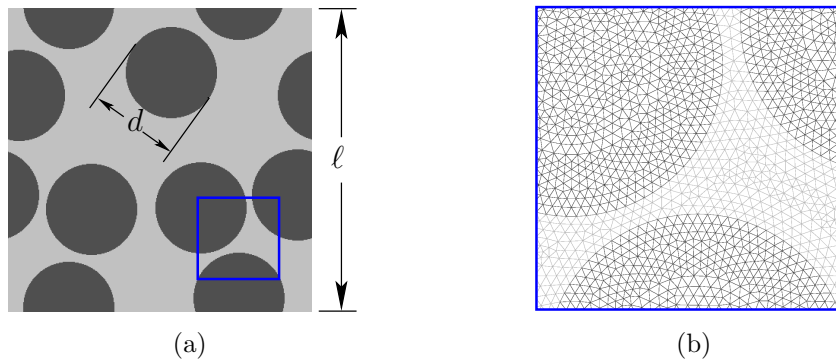


Figure 4.2: (a) Two dimensional representation of a lithium-ion battery cathode-electrolyte system with mono-dispersed circular active particles (inclusions); ℓ is the characteristic size of the RVE and d is the diameter of the inclusions. (b) A fragment of the finite element mesh corresponding to the area indicated by the box in Figure 4.2(a). The full FE mesh consists of 25498 linear triangular elements and 12494 nodes.

a cathode-electrolyte system is considered, in which the electrolyte is lithium hexafluoro phosphate (LiPF_6) and the embedded active particles are made of lithium cobalt oxide (LiCO_2). For simplicity, it is assumed that the active particles are surrounded by the electrolyte only. All the other materials, e.g., the polymer binders, conductive particles etc., are disregarded following similar simplifications made in [97, 100]. The material and geometric parameters are listed in Table 4.1. All material properties are assumed to be constant and do not change with the chemical potential or stresses in the material. For a given material, the chemical modulus Λ and the mobility coefficient M combine to form the diffusivity coefficient $\mathcal{D} = \Lambda M$ of the material. The diffusivity \mathcal{D}_m of the lithium-ions is much larger in the electrolyte as compared to the diffusivity \mathcal{D}_i in the active particles, indicating that the relaxed separation of scales (4.32) holds for the considered problem. It is assumed that the electrolyte material does not swell with the introduction of lithium-ions. The active particles are spherical in shape, vary in size and are placed randomly in the electrolyte which creates a poly-disperse heterogeneous medium [91]. In this example (for simplicity reasons), we consider a two dimensional mono-dispersed heterogeneous medium, as shown in Figure 4.2, which is generated by a level set based random sequential adsorption method [52]. In the simulations, all the parameters were non-dimensionalized, the time was normalized with respect to the characteristic diffusion time of the inclusion, i.e., $\hat{t} = \frac{t}{t_i}$, the lengths are normalized with respect to the characteristic length of the microscopic domain, i.e., $\hat{x} = \frac{x}{\ell}$, the chemical potential is normalized with respect

to the maximum attainable chemical potential in the inclusion $\hat{\mu} = \frac{\mu}{\mu_{\max}}$, where $\mu_{\max} = \Lambda_i(c_{\max} - c_0)$, the displacement field is normalized with respect to the characteristic length of the microscopic domain, i.e., $\hat{\mathbf{u}} = \frac{\mathbf{u}}{\ell}$ and the stresses are normalized with respect to the Young's modulus of the inclusion E_i .

The microscopic domain is excited by the chemical loading given in terms of the macroscopic chemical potential $\bar{\mu}$ and the gradient of the macroscopic chemical potential $\bar{\nabla}\bar{\mu}$ as a function of time

$$\begin{aligned}\bar{\mu}(t) &= \bar{\mu} \sin \omega t, \\ \bar{\nabla}\bar{\mu}(t) &= \bar{\nabla}\bar{\mu} \sin \omega t,\end{aligned}\tag{4.115}$$

where $\omega = \frac{2\pi}{T}$ is the angular loading frequency, T is the time of one period and $\bar{\mu} = \mu_{\max}$ and $\bar{\nabla}\bar{\mu} = 0.1\mu_{\max}$ are assumed. Externally applied mechanical loads to the micro-scale are neglected here. At the micro-scale, periodic boundary conditions are used to satisfy the Hill-Mandel conditions for both the mass diffusion and mechanical problems. The microscopic domain, shown in Figure 4.2(b), is discretized with linear triangular finite elements. For time integration, the backward-Euler method was used with a time step $\Delta t = 1 \times 10^{-3}T$ [s].

4.5.2 Reduced Basis Identification

After assembling the finite element matrices and applying the boundary conditions at the micro-scale, the first step of the reduced order homogenization is the solution of the coupled eigenvalue problem (4.74). This eigenvalue problem is solved for the first two hundred smallest eigenvalues and the corresponding eigenvectors $\underline{\Phi}$. Then, using the mode selection criteria given by equation (4.114), the reduced basis $\underline{\Phi}^* \in \underline{\Phi}$ is based on the coupling terms ${}^0\widehat{C}^{\dot{\eta},(k)}$, ${}^1\widehat{M}^{\dot{\eta},(k)}$ and ${}^2\widehat{C}^{\eta,(k)}$ with the threshold value $e_{\widehat{C}} = e_{\widehat{M}} = e_{\widehat{C}} = 0.1$. The number of eigenvectors selected in the eigenbasis $\underline{\Phi}^*$ depends on the topology of the micro-structure, the strength of the coupling in diffusion-mechanics and the material contrast between the matrix and the inclusions. For each selected eigenvector $\Phi_{\mu}^{(k)}$, there is a corresponding coupled mechanical eigenvector $\underline{\Phi}_{\mathbf{u}}^{(k)} = \underline{\mathbf{S}}_{\mathbf{u}\mu}^{ff} \Phi_{\mu}^{(k)}$, both $\underline{\Phi}_{\mu}^*$ and $\underline{\Phi}_{\mathbf{u}}^*$ are shown for the considered micro-structure in a coupled manner in Figure 4.3. The ten modes selected are not the modes corresponding to the 10 consecutive smallest eigenvalues. The inclusions swell where the chemical potential is high, indicated by the red regions inside the domain and the inclusions shrink where the chemical potential is low, indicated by the blue regions. The modes have contributions

Table 4.1: Default parameters used in the simulation.

Parameter	Symbol	Value	Units
RVE length	ℓ	1.0	[mm]
Inclusion diameter	d	0.3	[mm]
Inclusion volume fraction	V_{f_i}	~ 0.5	
Maximum attainable concentration in inclusion[101]	c_{\max}	24161	[mol m ⁻³]
Minimum attainable concentration in inclusion[101]	$c_0 = 0.19c_{\max}$	4590.59	[mol m ⁻³]
Absolute temperature	θ_0	298	[K]
Boltzmann constant	k_b	1.3806×10^{-23}	[m ² kg s ⁻² K ⁻¹]
Inclusion chemical modulus [66]	$\Lambda_i = k_b \theta_0 / c_0$	10202	[J m ⁻³ / (mol m ⁻³) ²]
Maximum chemical potential in inclusion	$\mu_{\max} = \Lambda_i (c_{\max} - c_0)$	1.99×10^8	[J / m ³ / (mol m ⁻³)]
Matrix diffusivity [66]	\mathcal{D}_m	6×10^{-11}	[m ² s ⁻¹]
Inclusion diffusivity [66]	\mathcal{D}_i	1×10^{-16}	[m ² s ⁻¹]
Matrix characteristic time	$t_m = \frac{\ell^2}{\mathcal{D}_m}$	1.6×10^4	[s]
Inclusion characteristic time	$t_i = \frac{d^2}{\mathcal{D}_i}$	3×10^{12}	[s]
Matrix Young's modulus [101]	E_m	1	[GPa]
Inclusion Young's modulus [101]	E_i	10	[GPa]
Poisson's ratio [101]	ν_m & ν_i	0.3	
Inclusions partial molar volume[101]	γ	3.497×10^{-6}	[m ³ mol ⁻¹]
Number of elements		25498 TRI3	
Number of nodes		12494	
Total loading time	T	$0.1t_i$	[s]
Loading frequency	ω	1	[Hz]

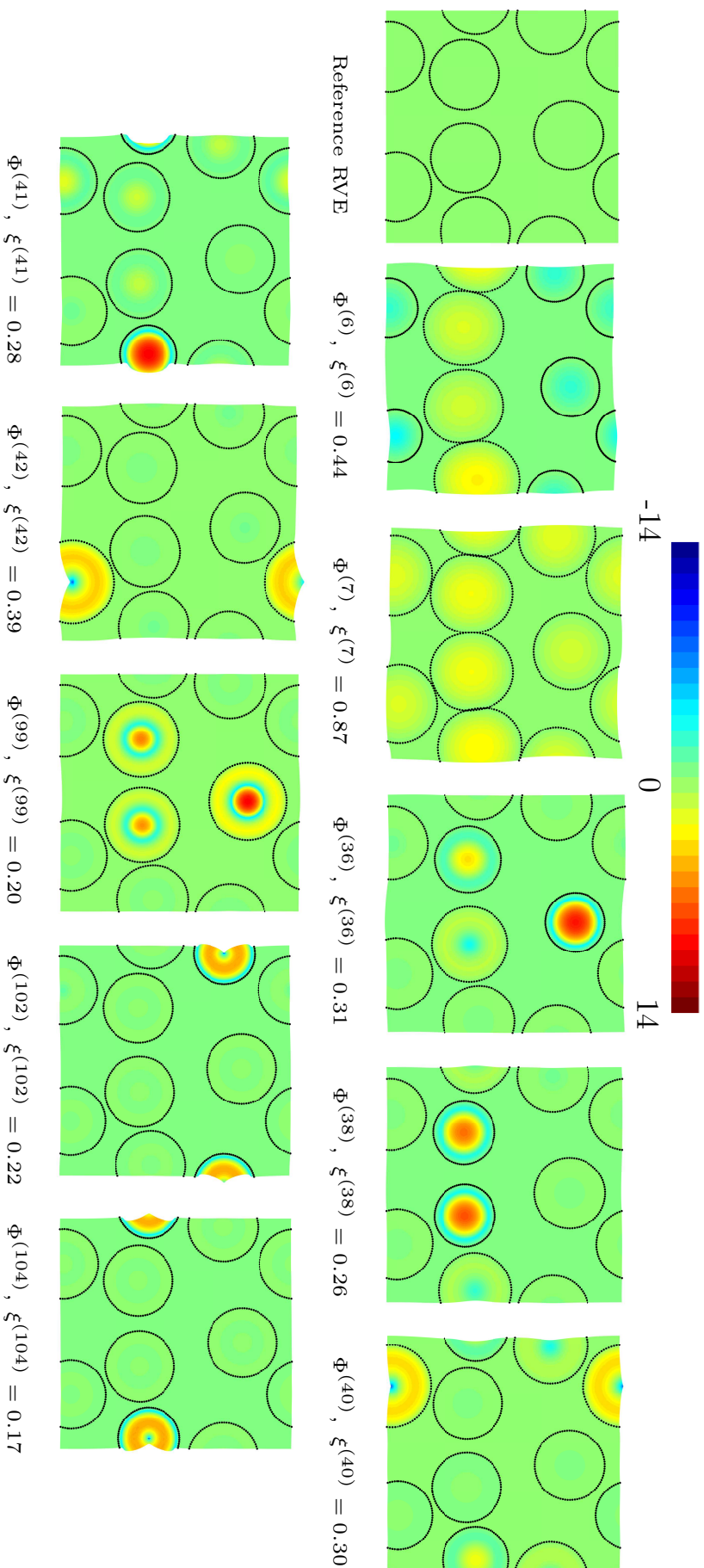


Figure 4.3: eigenvectors $\underline{\Phi}_\mu^*$ and $\underline{\Phi}_u^*$ are shown in a coupled manner: the color map indicates the chemical potential value and the corresponding mechanical modes are indicated by the geometry change (swelling or shrinkage) of the inclusions. The displacement field is scaled 5 times relative to the reference configuration. The quantitative contribution $\xi^{(k)}$ of the mode is defined in equation (4.116).

in the inclusions only, in accordance with the relaxed separation of scales. If the material properties do not fulfill the requirements of relaxed separation of scales (4.32) then the eigenvectors might have contributions in the matrix and consequently the proposed reduced homogenization method will not capture the phenomena adequately.

Among the selected eigenvectors, shown in Figure 4.3, there is one eigenvector with the highest relative importance of the eigenmodes in terms of their contribution to the macro-scale, which can be quantified by a measure $\xi^{(k)}$

$$\xi^{(k)} = \frac{1}{3} \left(\frac{|\widehat{\mathbf{C}}^{\dot{\eta},(k)}|}{\max|\widehat{\mathbf{C}}^{\dot{\eta}}|} + \frac{\|\widehat{\mathbf{M}}^{\dot{\eta},(k)}\|}{\max\|\widehat{\mathbf{M}}^{\dot{\eta}}\|} + \frac{\|\widehat{\mathbf{C}}^{\eta,(k)}\|}{\max\|\widehat{\mathbf{C}}^{\eta}\|} \right), \quad (4.116)$$

where $|\bullet|$ and $\|\bullet\|$ are the absolute value and Frobenius norm of a quantity \bullet . In this example, eigenvector numbered 7 has the highest contribution to the macro-scale, while other eigenvectors in $\underline{\Phi}^*$ make only small improvements in capturing the phenomena. For a more detailed mode selection analysis, in the case of heat diffusion, the reader is referred to [67].

4.5.3 Micro-scale Simulations

Next, we compare the microscopic fields computed by the model reduction method and the (expensive) fully resolved finite element calculations. For the fully resolved finite element analysis, the coupled system of equations (4.56)–(4.57) is solved for $\underline{\mu}$ and $\underline{\mathbf{u}}$, directly on the finite element mesh of the considered RVE 4.2(b). For the reduced model, the coefficients $\underline{\eta}$ are solved by using equation (4.110); subsequently, the microscopic fields $\underline{\mu}$ and $\underline{\mathbf{u}}$, are reconstructed (localization operation) by post-processing through equations (4.79) and (4.80), respectively. Note that, in a two-scale simulation the post-processing of microscopic fields $\underline{\mu}$ and $\underline{\mathbf{u}}$, is generally not done, unless the microscopic fields are also the quantities of interest in addition to the macroscopic field. Figure 4.4 shows the contour plots of the normalized chemical potential $\hat{\mu}$ and Figure 4.5 shows the contour plots of the normalized hydrostatic stress $\hat{\sigma}_{hyd} = \frac{\hat{\sigma}_{11} + \hat{\sigma}_{22}}{3}$ at time $\hat{t} = 250\Delta\hat{t}$. The minor differences between the fully resolved solution and the reduced order model are due to the approximate nature of the model reduction.

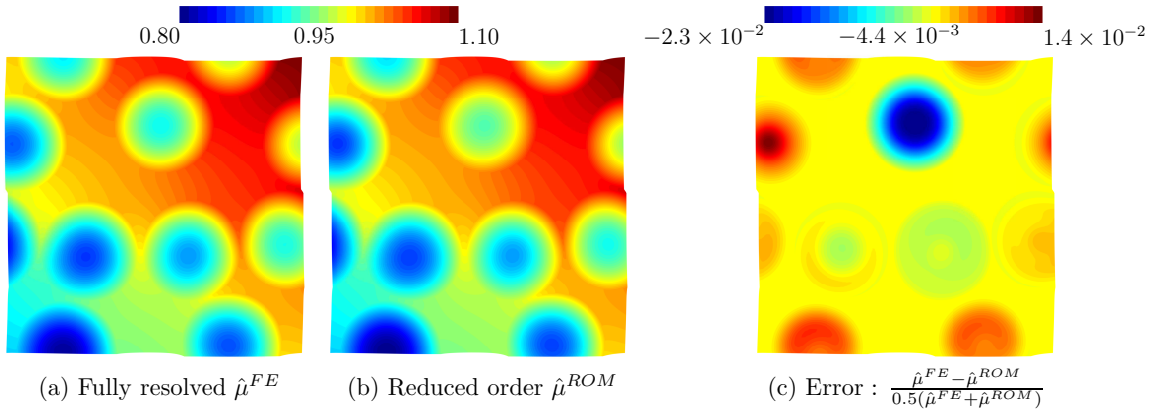


Figure 4.4: Chemical potential field $\hat{\mu} = \mu/\mu_{\max}$ in the microscopic domain at time step $\hat{t} = 250\Delta\hat{t}$. (a) Fully resolved finite element solution $\hat{\mu}^{FE}$ (b) reduced order solution $\hat{\mu}^{ROM}$ and (c) the relative error with respect to their average $\frac{\hat{\mu}^{FE} - \hat{\mu}^{ROM}}{0.5(\hat{\mu}^{FE} + \hat{\mu}^{ROM})}$.

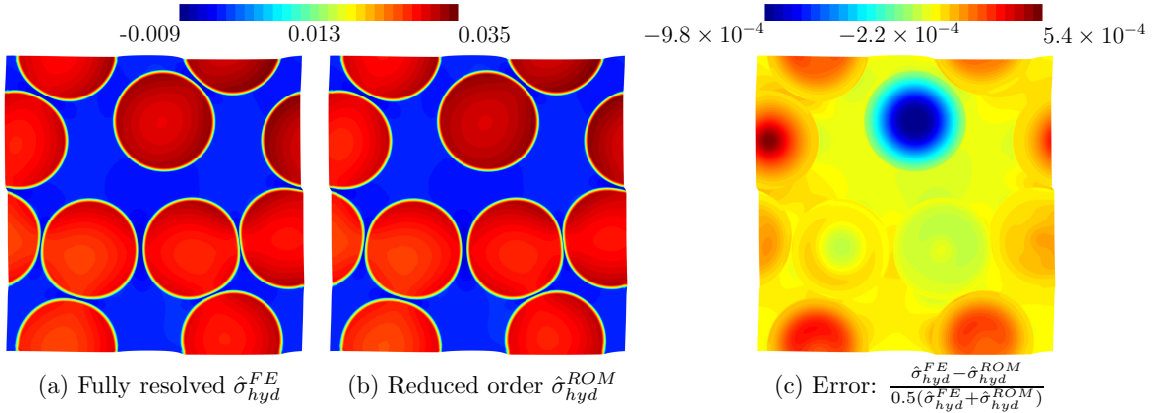


Figure 4.5: Hydrostatic stress $\hat{\sigma}_{hyd} = \frac{\hat{\sigma}_{11} + \hat{\sigma}_{22}}{3}$ induced at the micro-scale due to diffusion mechanical coupling at time $\hat{t} = 250\Delta\hat{t}$. (a) Fully resolved finite element solution $\hat{\sigma}_{hyd}^{FE}$ (b) reduced order solution $\hat{\sigma}_{hyd}^{ROM}$ and (c) the relative error with respect to their average $\frac{\hat{\sigma}_{hyd}^{FE} - \hat{\sigma}_{hyd}^{ROM}}{0.5(\hat{\sigma}_{hyd}^{FE} + \hat{\sigma}_{hyd}^{ROM})}$.

4.5.4 Effective Macroscopic Quantities

Next, we compare the macroscopic quantities $\bar{\mathbf{j}}$, $\dot{\bar{c}}$, $\bar{\boldsymbol{\sigma}}$ computed with the conventional transient homogenization and the developed reduced order homogenization. For conventional computational homogenization, the fully resolved finite element analysis of the coupled system of equations (4.56)–(4.57) is performed and then the macroscopic flux $\bar{\mathbf{j}}$ is computed using (4.96), the macroscopic concentration rate $\dot{\bar{c}}$ using (4.102) and the macroscopic stress $\bar{\boldsymbol{\sigma}}$ using (4.105), where the reaction fluxes $\underline{\mathbf{j}}_n^p$ and the reaction forces $\underline{\mathbf{t}}_n^p$ are post-processed using the expressions in (4.86) and (4.92), respectively. For the reduced model calculations, the eigenvalue problem (4.74) is solved in the offline stage and the coupling terms in (4.101), (4.104) and

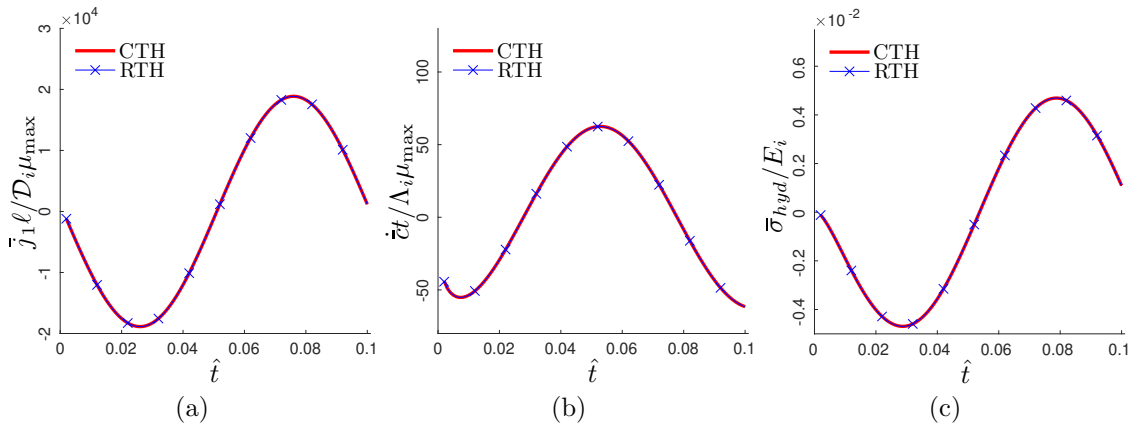


Figure 4.6: Comparison between the macroscopic quantities computed with the conventional computational homogenization (based on the fully resolved micro-scale RVE analysis), shown in red, and the reduced order homogenization, shown in blue. (a) Macroscopic mass flux \bar{j}_1 in \mathbf{x}_1 direction, (b) macroscopic concentration rate $\dot{\bar{c}}$ and (c) macroscopic hydrostatic stress $\bar{\sigma}_{hyd} = \frac{\bar{\sigma}_{11} + \bar{\sigma}_{22}}{3}$.

(4.108) are calculated and stored. During the online stage, the evolution equation (4.110) is solved for $\underline{\eta}$. Once $\underline{\eta}$ is known, the macroscopic quantities are calculated directly from the expressions (4.100), (4.103) and (4.107) for the macroscopic mass flux $\bar{\mathbf{j}}$, the macroscopic concentration rate $\dot{\bar{c}}$ and the macroscopic stress $\bar{\boldsymbol{\sigma}}$, respectively. Figure 4.6 shows the time evolution of the macroscopic quantities computed with the (expensive) conventional transient computational homogenization (CTH) method (shown in red) and the proposed inexpensive reduced computational homogenization (RTH) method (shown in blue). The reduced order homogenization method shows an excellent approximation without any noticeable discrepancies.

The computational gains achieved with the reduced model are substantial. Neglecting the off-line stage, motivated by the fact that for a specific microstructure and set of material parameters the off-line stage only needs to be performed once. Using Matlab 2018b on a computer with Core-i7 4.4GHz processor and 16Gb memory, for the conventional computational homogenization the coupled problem (4.56)–(4.57) takes approximately 5000 times more computational time than the solution of the uncoupled ordinary differential equations (4.110). Next, we assess the proposed reduced model with different value of coupling coefficient γ and the microscopic domain size ℓ .

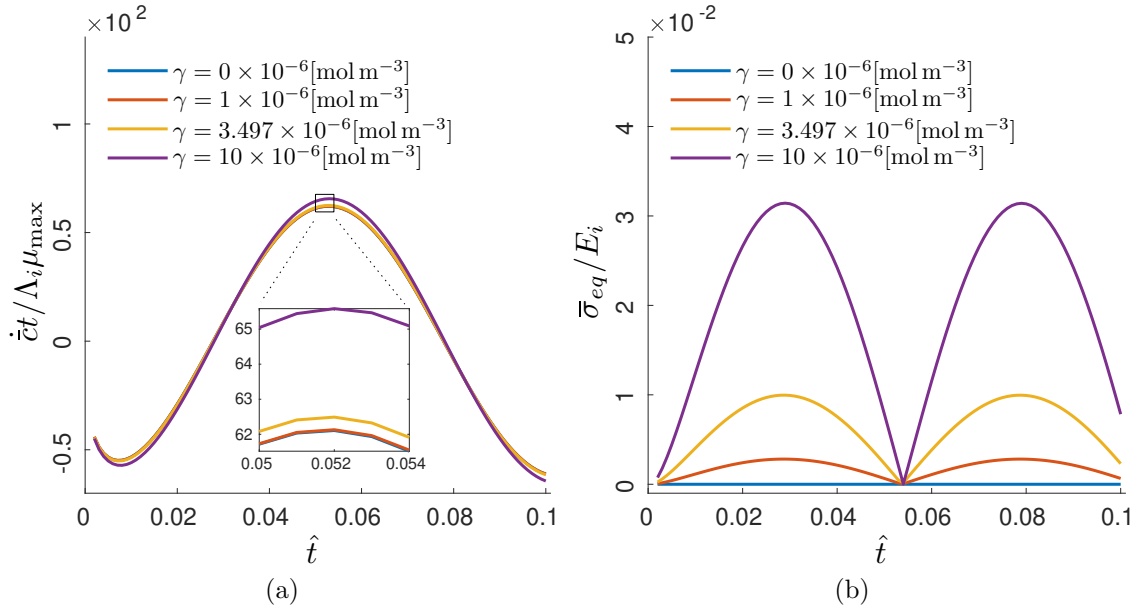


Figure 4.7: The effect of the coupling term γ on (a) the macroscopic rate term \dot{c} and (b) the macroscopic equivalent stress $\bar{\sigma}_{eq}$. The equivalent stress is calculated as $\bar{\sigma}_{eq} = \sqrt{\bar{\sigma}_{11}^2 + \bar{\sigma}_{22}^2 + 2\bar{\sigma}_{12}^2}$.

4.5.5 Diffusion-Mechanics Coupling Effect

In diffusion-mechanics, the coupling is governed by the partial molar volume parameter γ in equation (4.28). The higher the value of γ , the higher the coupling will be. The constitutive equation (4.23) has an upper limit of applicability since the effective elastic tensor $\mathbb{C}^* = (\mathbb{C} - \frac{\mathbf{S} \otimes \mathbf{S}}{\Lambda})$ can become non-positive definite, which will make the eigenvalues $\underline{\alpha}$ (4.76) equal to zero or even negative. However, for the realistic material properties of the cathode in lithium-ion batteries, this is not a problem since the upper limit for γ is $21 \times 10^{-6} [\text{mol m}^{-3}]$, which is much greater than the physical value of $\gamma = 3.497 \times 10^{-6} [\text{mol m}^{-3}]$. Figure 4.7 shows the effect of increasing the γ value. The macroscopic rate term \dot{c} and the macroscopic stress $\bar{\sigma}$ increase as γ increases in accordance with their microscopic counterparts (4.23) and (4.24), respectively. The proposed model reduction scheme captures the full finite element solution very well, and hence for clarity the finite element solution is not shown anymore. Next, we analyze the effect of the microscopic domain size on the macroscopic quantities.

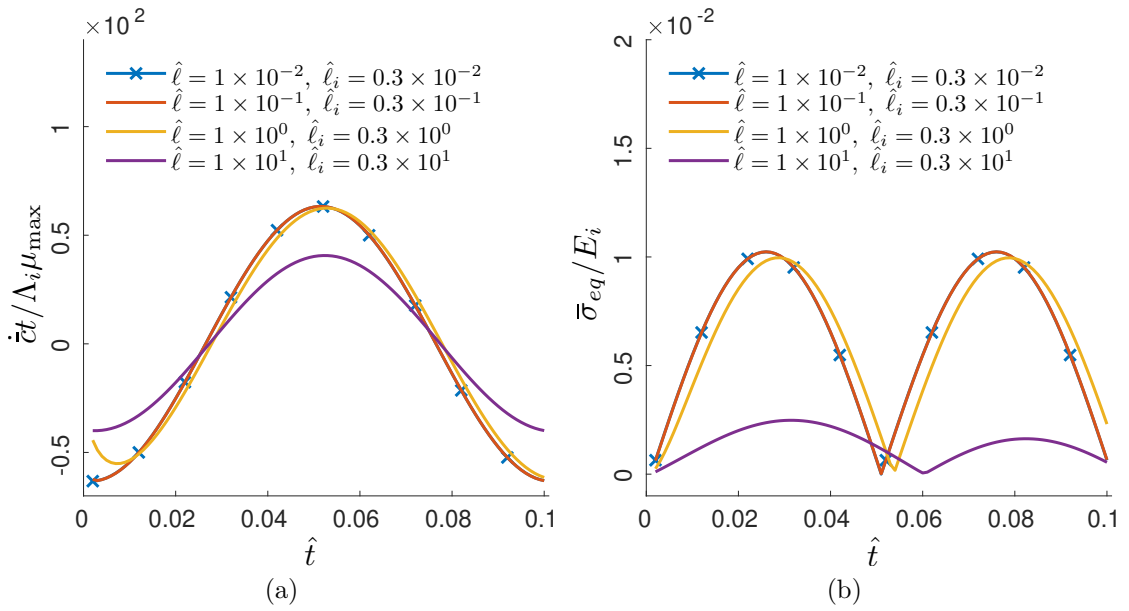


Figure 4.8: Influence of the microscopic characteristic length scale $\hat{\ell}$ on (a) the macroscopic concentration rate $\dot{\hat{c}}$ and (b) the equivalent macroscopic stress $\bar{\sigma}_{eq}$.

4.5.6 Size Effect

To measure microscopic size effect on the macroscopic quantities, the material parameters are kept the same and the characteristic size of the microscopic domain ℓ is changed while keeping the inclusions size d the same or scaling it along with the microscopic size. In the first case, the macroscopic quantities do not vary with the changing RVE size. However, if the inclusions size d is scaled along with the characteristic microscopic size ℓ the microscopic and the macroscopic quantities change. For the later case, the normalized characteristic length of the micro-scale is changed from $\hat{\ell} = 1 \times 10^{-2}$ to $\hat{\ell} = 1 \times 10^1$ and accordingly the inclusion characteristic length from $\hat{\ell}_i = 0.3 \times 10^{-2}$ to $\hat{\ell}_i = 0.3 \times 10^1$, respectively. As expected, for the smaller microstructures (up to $\hat{\ell} = 1 \times 10^{-1}$ with $\hat{\ell}_i = 0.3 \times 10^{-1}$), due to almost instantaneous mass diffusion in the inclusion at the micro-scale, the averaged macroscopic transient effects are negligible as compared to the transient effects computed with a larger unit-cell, as can be seen in Figure 4.8(a). For the larger microstructural sizes the response is clearly size dependent. In particular, the macroscopic stresses $\bar{\sigma}$ are much higher for small microstructures compared to the large ones. This is due to the coupling effect and the diffusion rate. For smaller sizes, the chemical potential (and the concentration of a species) increases in the inclusion domain, which causes the inclusions to swell and produce higher stresses on average. Conversely, when the micro-scale size is increased, within the

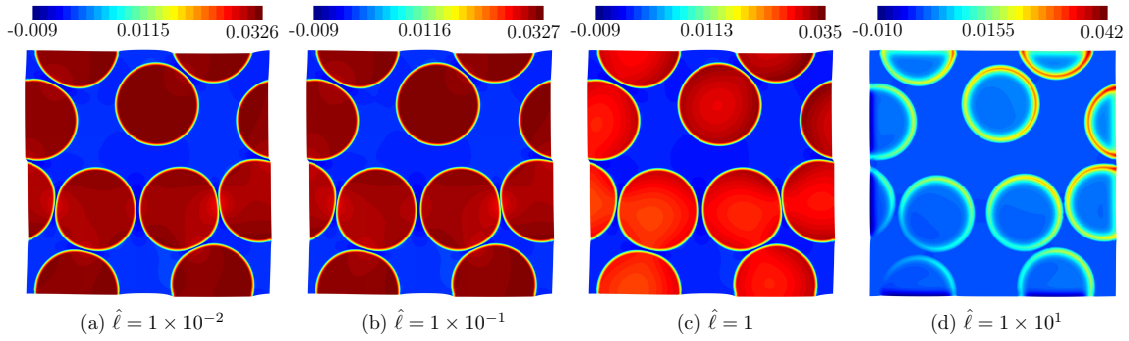


Figure 4.9: Hydrostatic stress field $\hat{\sigma}_{hyd} = \frac{\hat{\sigma}_{11} + \hat{\sigma}_{22}}{3}$ at the micro-scale with different microscopic sizes $\hat{\ell}$.

same time period, the mass diffusion happens to the outer layer of the inclusions, swelling only that part of the inclusions, which creates higher local stresses, as can be seen in Figure 4.9. However, due to overall increase in the volume of the microscopic domain and the small relative volume of high stress regions, the macroscopic volume average stresses decrease, as can be observed in Figure 4.8.

4.6 Conclusions

In this work, a model reduction based homogenization technique for coupled diffusion-mechanics problems has been presented. A formulation based on the chemical potential and linear strain field is derived, which eases the implementation since it only requires a C^0 -continuous discretization. This is in contrast with the conventional formulation used in diffusion-mechanics based on the concentration and strain fields, which requires a less convenient C^1 -continuous finite element formulation. For the homogenization of the coupled diffusion-mechanics, the equivalence of the virtual power for mass diffusion (extended Hill-Mandel condition), and the virtual work of internal forces (standard Hill-Mandel condition) are used for the diffusion and mechanical problems, respectively. A model reduction technique, inspired by the dynamic mode synthesis approach, is developed for the coupled system of equations relying on the linearity of the problem and the relaxed separation of scales. Accordingly, both the microscopic chemical potential and displacement fields are split into their steady-state and transient parts. Using static condensation, a reduced basis is first identified for the steady-state fields. Then for the transient part, a coupled eigenvalue problem is solved for the free part of the system. The expressions for the macroscopic effective quantities, i.e., macroscopic flux, rate of change of concentration field and the macroscopic stress, are

finally obtained. As an emergent result of the model reduction at the micro-scale, a coupled diffusion-mechanics enriched-continuum is obtained, in which the fully resolved microscopic coupled system of equations is replaced by a set of ordinary differential equations which are computationally inexpensive to solve. Numerical examples are presented, and a comparison is made between the fully resolved finite element calculations and the reduced order model for the cathode-electrolyte system of a lithium-ion battery. The proposed reduced order homogenization has been shown to capture the coupled behavior with an excellent accuracy and largely improved computational efficiency.

Possible extensions to the current work are:

- two-scale implementation of the coupled diffusion-mechanics enriched-continuum, which can be compared to direct numerical simulations;
- nonlinear regimes, both for elasticity and mass diffusion, can be analyzed, for example, by using model reduction technique with modal derivatives in combinations with a discrete empirical interpolation for the nonlinear forcing terms [102];
- inelastic regimes and large deformations can be performed by using appropriate model reduction methods, e.g. using proper generalized decomposition, at the micro-scale [10].

**Data-driven Reduced
Homogenization for Transient
Diffusion Problems with
Emergent History Effects**

Abstract

In this paper, we propose a data-driven reduced homogenization technique to capture diffusional phenomena in heterogeneous materials which reveal, on a macroscopic level, a history-dependent non-Fickian behavior. The adopted enriched-continuum formulation, in which the macroscopic history-dependent transient effects are due to the underlying heterogeneous microstructure is represented by enrichment-variables that are obtained by a model reduction at the micro-scale. The data-driven reduced homogenization minimizes the distance between points lying in a data-set and points associated with the macroscopic state of the material. The enrichment-variables are excellent pointers for the selection of the correct part of the data-set for problems with a time-dependent material state. Proof-of-principle simulations are carried out with a heterogeneous linear material exhibiting a relaxed separation of scales. Information obtained from simulations carried out at the micro-scale on a unit-cell is used to determine approximate values of metric coefficients in the distance function. The proposed data-driven reduced homogenization also performs adequately in the case of noisy data-sets. Finally, the possible extensions to non-linear history-dependent behavior are discussed.

5.1 Introduction

Transient mass diffusion phenomena in heterogeneous materials are prevalent in engineering applications, for example, Lithium-ion batteries [60], polycrystalline materials [5], diffusion in porous gels [59], etc. For their analysis, numerical methods like finite elements in conjunction with transient computational homogenization [8, 9] are used. Computational homogenization represents the heterogeneous domain by a homogeneous macro-scale and a heterogeneous micro-scale and solves the transient diffusion phenomena in a coupled two-scale setting. Despite the fact that the individual micro-scale constituents might reveal instantaneously linear behavior, the homogenization of transient mass diffusion phenomena in heterogeneous materials provides an emergent non-Fickian diffusion behavior [66, 103]. This lagging and history-dependent diffusion behavior obtained at the macro-scale is due to the transient nature of the mass diffusion occurring at the micro-scale. Diffusion in a heterogeneous material, consisting of inclusions embedded in a matrix material, can be characterized by a characteristic loading time T , a characteristic diffusion time for the inclusions $\tau_i = d^2/\mathcal{D}_i$ and a characteristic diffusion

time for the matrix $\tau_m = \ell^2/\mathcal{D}_m$, where d is the inclusion size (e.g. diameter), ℓ is the characteristic size of the representative microscopic domain (e.g. the unit-cell), \mathcal{D}_i and \mathcal{D}_m are the diffusivity constants for the inclusions and the matrix, respectively. In the regime of the relaxed separation of scales ($\tau_m \ll \tau_i \sim T$), the non-Fickian behavior at the macro-scale is due to the slow diffusion inside the inclusions. This gives rise to a lagging behavior at the macro-scale, which is more prominent in the macroscopic storage term than in the diffusion term.

The homogenization in transient regimes is generally computationally very expensive. In previous work [67], a model reduction technique, based on component mode synthesis [42, 43] was developed for transient diffusion phenomena in heterogeneous materials with linear material properties in the relaxed separation of scales regime. The microscopic primary field variable was decomposed into a steady-state and a transient part. Model reduction was achieved by solving an eigenvalue problem and selecting only a few eigenvectors in the reduced bases set. When projected onto the reduced bases subspace, the discretized mass balance equation at the micro-scale provides a set of ordinary differential equations in terms of the activity coefficients of the eigenvectors. At the macro-scale, the macroscopic initial boundary value problem, the ordinary differential equations of the activity coefficients, and the effective, homogenized, constitutive equations entail an enriched-continuum description, where the activity coefficients are the emerging enrichment-variables. These enrichment-variables can be treated as separate fields or as internal-variables, as used in the constitutive theories involving internal variables [104]. This method was later extended to coupled diffusion-mechanics phenomena [105], where diffusion induced stresses were correctly captured with the reduced method. The major limitation of the enriched-continuum formulation is the fact that it relies on the linear material models at the micro-scale to obtain the well-defined eigenvector reduced bases by solving an eigenvalue problem.

In this work, a further extension of the enriched-continuum formulation is proposed, which we call *data-driven reduced homogenization*. It combines of the model reduction at the micro-scale to obtain enrichment-variables playing the role of internal-variables, and the data-driven framework, which was first proposed in [106].

The data-driven computing [106] eliminates the need for a material model in computer simulations and instead directly uses raw data obtained from e.g. experiments or micro-scale simulations. In essence, the data-driven method tries to find a point in the data-set closest to the physical-state of the material obeying

compatibility and the balance laws (or vice-versa). It was further extended to noisy data-sets [107], dynamics [108] and inelastic material behavior [109]. Data-driven computational homogenization, was proposed in [110, 111], where the expensive micro-scale calculations were performed first to generate data containing homogenized quantities in an off-line stage, while in an on-line stage, the homogenized macro-scale problem was solved using the data-driven approach. It was also showed that the search through the data-set is much more efficient than solving micro-scale problems in a coupled manner.

The data-driven approach proposed in [106] is fundamentally different from other data-driven methods used in mechanics, where the data is typically used to learn the behavior of the material in terms of a stress-strain relationship or an energy potential. Classically, this learning process involves linear/non-linear regression through, experimentally collected, data points to build a model. The regression analysis has recently been replaced by techniques such as artificial neural networks, deep learning, etc., borrowed from the field of data science. For example, [112] employed a data-driven method that uses artificial neural networks to obtain a decoupled and efficient computational homogenization for non-linear elastic materials by approximating a density energy function. For a data-set with few points, a data-driven inverse problem was proposed in [113] to recover the entire constitutive manifold. Notably, [114] developed a multi-scale data-driven method using recurrent neural networks, which can capture the history-dependent behavior for plasticity and replaces the micro-scale calculations with a surrogate model. Detailed reviews for modern data-driven model building techniques can be found in [115–118].

The data-driven reduced homogenization, that will be proposed in this work, entails three stages, i.e. (1) model reduction, (2) data-generation, and (3) data-search.

1. The model reduction at the micro-scale, depending on the material models of the constituents, can be applied to the discrete mass balance equations. It can be categorized as a pre-processing stage. In the context of data-driven reduced homogenization, the central goals of performing model reduction at the micro-scale are to be able to (i) solve a large number of micro-scale problems in a computationally efficient manner during the data-generation stage and (ii) obtain internal-variables to represent the effect of the micro-scale transient behavior at the macro-scale. For the materials with memory, the internal-variables approach provides a computationally efficient way to

keep track of the history dependence [109], hence, easing the computational efforts later in the data-search stage.

2. The data-generation stage involves the solution of many micro-scale problems, post-processing, and storage of the results in the form of the macroscopic conjugate quantities. The data-generation stage is typically an off-line stage. To ensure that the data-set contains representative values of conjugate quantities involved in the problem, the micro-scale should be probed under different loading conditions with different frequencies.
3. Finally, the data-search is carried out to find an optimum point that reflects the minimal distance from the current physical-state of the material, satisfying balance equations.

In this work, following [106, 109, 119], a staggered distance-minimizing data-driven solver is adopted. It iteratively minimizes a quadratic distance function, defined on the material phase-space, while looking for a point in the data-set. The compatibility of the macroscopic primary field is enforced directly and the macroscopic balance law is enforced with the help of Lagrange multipliers. To find the physical-state of the material, the stationarity conditions are obtained and then solved by taking all possible variations of the Lagrangian function. Then, the search through the data-set is performed by an array indexing lookup operation. The data-search stage constitutes the on-line stage. The material models (linear) are known at the micro-scale and the data-driven approach is applied to the macro-scale only. Unlike usual finite element formulation, where the structure of the problem is highly dependent on the material model, the structure of the data-driven formulation is independent of the underlying material behavior (linear or non-linear). Hence, it can easily be extended to the non-linear history-dependent diffusion problems. In this preliminary work, the analysis is limited to the linear material behavior, and the results are compared with the reference enriched-continuum formulation [67], while the data-driven reduced homogenization approach for non-linear materials will be analyzed in future work. The novel contributions in this paper are:

- introduction of *data-driven reduced homogenization* for macroscopic history-dependent linear diffusion behavior;
- capturing the emergent macroscopic diffusion history dependence via enrichment-variables in the data-set;

- proposing a methodology to evaluate optimal numerical values of the coefficients in the distance function based on the information from micro-scale simulations.

5.1.1 Outline

The diffusion enriched-continuum formulation and model reduction for linear materials are briefly presented in Section 5.2. The data-driven reduced homogenization is derived in Section 5.3: first, the data-set and phase-space are defined; next the solution procedure and the algorithm is elaborated for a distance minimizing data-driven solver. All stages of the data-driven reduced homogenization are evaluated with numerical examples in Section 5.4, where after setting up the micro-scale and macro-scale problems, the data-generation is performed by micro-scale simulations. An important discussion is made on the selection of numerical values of the coefficients in the distance function and the performance and convergence of the proposed method is assessed with a noisy data-set. Future perspectives, along with an outlook to extend the proposed data-driven reduced homogenization method to non-linear history-dependent diffusion materials, are presented in Section 5.5 and finally the conclusions are given in Section 5.6.

5.1.2 Symbols and Notation

Macroscopic quantities are represented with a bar on top: for example scalar, vector and second-order tensor macroscopic quantities are written as \bar{a} , $\bar{\mathbf{a}}$, and $\bar{\mathbf{A}}$, respectively. Microscopic quantities are represented without a bar; microscopic scalar, vector and second-order tensorial quantities are written as a , \mathbf{a} and \mathbf{A} , respectively. The same Cartesian basis $\mathbf{e}_i, i = 1, 2, 3$ is adopted at the macro- and micro-scales. The dot products between two vectors, and between a second-order tensor and a vector are represented as $\mathbf{a} \cdot \mathbf{b} := a_i b_i$ and $\mathbf{A} \cdot \mathbf{a} := A_{ij} a_j \mathbf{e}_i$, respectively. A tensorial dyadic product is denoted as $\mathbf{a} \otimes \mathbf{b} := a_i b_j \mathbf{e}_i \otimes \mathbf{e}_j$ and $\mathbf{A} \otimes \mathbf{a} := A_{ij} a_k \mathbf{e}_i \otimes \mathbf{e}_j \otimes \mathbf{e}_k$. The gradient of a scalar and a vector is defined as $\nabla a := \frac{\partial a}{\partial x_i} \mathbf{e}_i$ and $\nabla \mathbf{a} := \frac{\partial a_i}{\partial x_j} \mathbf{e}_i \otimes \mathbf{e}_j$. Similarly, the divergence operates as $\nabla \cdot \mathbf{a} := \frac{\partial a_i}{\partial x_i}$ and $\nabla \cdot \mathbf{A} := \frac{\partial A_{ij}}{\partial x_i} \mathbf{e}_j$. For linear algebra operations, columns are represented with a tilde underneath a lowercase letter, e.g. \underline{a} , and matrices are represented with a bar underneath an uppercase letter e.g. \underline{A} .

5.2 Enriched Continuum for Diffusion Problems

Assuming that the micro-scale material properties and microstructural topology are known, the non-Fickian behavior at the macro-scale can be captured through a multi-scale approach such as transient computational homogenization [8, 9, 66]. For diffusion problems, the macroscopic behavior, in terms of the macroscopic chemical potential $\bar{\mu}$ as the primary unknown field, is obtained by solving a macroscopic transient mass balance equation

$$\begin{aligned} \bar{\nabla} \cdot \bar{\mathbf{j}} + \dot{\bar{c}} &= 0, & \text{in } & \bar{\Omega}, \\ \bar{\mu}(t=0) &= \bar{\mu}_0, & \text{in } & \bar{\Omega}, \\ \bar{\mu} &= \hat{\mu}, & \text{on } & \partial\bar{\Omega}_{\bar{\mu}}, \\ -\bar{\mathbf{j}} \cdot \bar{\mathbf{n}} &= \hat{j}, & \text{on } & \partial\bar{\Omega}_{\bar{j}}. \end{aligned} \quad (5.1)$$

where $\partial\bar{\Omega}_{\bar{\mu}}$ and $\partial\bar{\Omega}_{\bar{j}}$ are the Dirichlet and Neumann sub-parts of the macroscopic boundary $\partial\bar{\Omega}$, respectively, and $\bar{\mathbf{n}}$ is the outward unit-normal vector, \hat{j} is the prescribed mass influx and $\hat{\mu}$ is the prescribed macroscopic chemical potential. The explicit expressions for the macroscopic constitutive equations of the macroscopic mass flux $\bar{\mathbf{j}}$ and the rate of change of macroscopic concentration $\dot{\bar{c}}$ are not known and these are to be determined through homogenization, based on the micro-scale material behavior and morphological information.

The micro-scale problem is described by the balance equation

$$\nabla \cdot \mathbf{j} + \dot{c} = 0, \quad (5.2)$$

with the known constitutive equations given by

$$\mathbf{j} = -\mathbf{M} \cdot \mathbf{g}, \quad \text{where } \mathbf{g} = \nabla \mu \text{ and } \mu = \Lambda(c - c_0), \quad (5.3)$$

with \mathbf{M} the mobility tensor, Λ the chemical modulus and c_0 the reference concentration. The material properties are assumed to be known for each microstructural constituent. Transient computational homogenization involves down-scaling and up-scaling steps: the former consists in imposing the governing macroscopic quantities $(\bar{\mu}, \bar{\mathbf{g}})$, with $\bar{\mathbf{g}} = \bar{\nabla} \bar{\mu}$, on the micro-scale domain, and the latter involves the computation of the effective conjugate quantities $(\bar{\mathbf{j}}, \dot{\bar{c}})$, after solving the transient fully resolved micro-scale problem which can be computationally rather expensive.

In the relaxed separation of scales regime (requiring that the characteristic diffusion time of the matrix τ_m is much smaller than that of the inclusion τ_i which is of the same order of magnitude as the characteristic loading time T i.e., $\tau_m \ll \tau_i \sim T$), for micro-scale constituents with a linear material behavior, a reduced model has been proposed in [67]. Whereby the computationally expensive solution of the transient micro-scale problem is replaced by an inexpensive solution of a set of ordinary differential equations at the macro-scale by using computational homogenization along with component mode synthesis. A similar approach can be adopted for transient mass diffusion problems in heterogeneous materials. First, discretized (e.g. using FEM) the microscopic chemical potential field $\underline{\mu}$ can be decomposed into its steady-state $\underline{\mu}_{ss}$ and transient $\underline{\mu}_{tr}$ parts. Next, an Eigenvalue problem is solved at the micro-scale to obtain the reduced eigenmodes $\underline{\Phi}^{(q)}$, where $q = 1, 2, \dots, \mathcal{N}_q$, with \mathcal{N}_q are the reduced number of eigenvectors. Finally, the microscopic discretized problem is projected onto the subspace of the reduced eigenbasis yielding a decoupled system of first-order ordinary differential equations

$$\dot{\underline{\eta}} + \underline{\alpha} \underline{\eta} = -\underline{\bar{d}} \dot{\underline{\mu}} - \underline{\bar{a}} \cdot \dot{\underline{g}}. \quad (5.4)$$

where $\underline{\eta}$ is the column of the modal amplitudes, having the meaning of activity coefficients or reduced degrees of freedom $\eta^{(q)}$, $\underline{\alpha}$ is the diagonal matrix of eigenvalues $\alpha^{(q)}$, and $\underline{\bar{a}}^{(q)}$ and $\underline{\bar{d}}^{(q)}$ are the coefficients that couple the micro-scale to the macro-scale. Projection onto the reduced degrees of freedom, also provides the expression for the macroscopic constitutive equations of the macroscopic flux

$$\underline{\bar{j}} = -\underline{\bar{a}}^T \underline{\eta} - \underline{\bar{B}} \cdot \underline{g} - \underline{\bar{c}} \dot{\underline{\mu}} - \underline{\bar{C}} \cdot \dot{\underline{g}}, \quad (5.5)$$

and the rate of change of the macroscopic concentration

$$\dot{\underline{c}} = \underline{\bar{d}}^T \dot{\underline{\eta}} + \underline{\bar{e}} \cdot \underline{g} + \underline{\bar{f}} \dot{\underline{\mu}} + \underline{\bar{f}} \cdot \dot{\underline{g}}. \quad (5.6)$$

At the macro-scale, equations (5.1), (5.4), (5.5) and (5.6) present a diffusion enriched-continuum with $\underline{\eta}$ as the column of enrichment-variables. The effective coefficients $(\underline{\bar{a}}, \underline{\bar{B}}, \underline{\bar{c}}, \underline{\bar{C}})$ and $(\underline{\bar{d}}, \underline{\bar{e}}, \underline{\bar{f}}, \underline{\bar{f}})$ are the linear maps between the macroscopic quantities $(\underline{\eta}, \underline{g}, \dot{\underline{\mu}}, \dot{\underline{g}})$ and $(\underline{\bar{j}}, \dot{\underline{c}})$, respectively. Their magnitudes and directions depend on the microstructural material properties and microstructural morphology. The reader is referred to [67] for a detailed derivation of the enriched-continuum formulation in the context of transient heat conduction, and to the Appendix A.1

for the expressions of the effective coefficients used in equations (5.4)–(5.6) and the numerical implementation of the enriched-continuum for mass diffusion problems. The enriched-continuum formulation has also been extended to transient mass diffusion problems coupled to mechanics in [105].

The non-Fickian diffusion at the macro-scale, represented by $\bar{\mathbf{j}} = \bar{\mathbf{j}}(\underline{\eta}, \bar{\mathbf{g}}, \dot{\underline{\mu}}, \dot{\underline{\mathbf{g}}})$ in equation (5.5) and $\bar{c} = \bar{c}(\underline{\eta}, \bar{\mathbf{g}}, \dot{\underline{\mu}}, \dot{\underline{\mathbf{g}}})$ in equation (5.6), allows to capture the complex history dependence. The enrichment-variables $\underline{\eta}$ play similar role to the internal-variables used in the constitutive theory of inelastic materials [104]. However, here the macroscopic model is non-classical one since the storage terms \bar{c} also depend on the internal-variables, which is usually not the case for inelastic materials. In the data-driven approach, $\underline{\eta}$ can serve as an indicator in time for the selection of the conjugate quantities, hence capturing the history-dependent behavior efficiently. On the other hand, if instead of an enriched-continuum, the standard transient computational homogenization scheme [8] would be used for the data-driven approach, there would be no internal-variables $\underline{\eta}$ at the macro-scale. Instead, it would require the storage of the complete history of the discrete microscopic fields $\underline{\mu}(t)$, for the corresponding macroscopic quantities $(\bar{\underline{\mu}}, \bar{c}, \bar{\mathbf{g}}, \bar{\mathbf{j}})$ together with the data. The data-search stage would then consist of searching through the entire history of the discrete microscopic fields $\underline{\mu}$ up to a given time t . This would consume an enormous amount of computer resources for data-generation, data-storage, and data-search. Hence, the extraction of an enrichment-variable like quantity through the model reduction at the micro-scale is a crucial step towards an efficient data-driven solver for transient diffusion problems in heterogeneous materials. In the next section, the data-driven homogenization for transient diffusion problems with history effects is formally derived.

5.3 Data-Driven Reduced Homogenization

In this section, the data-driven reduced homogenization is derived for transient diffusion problems with history effects at the macro-scale. First, the notions of data-set and phase-space are presented. Then, a specific class of data-driven solver, i.e. a distance minimizing data-driven solver, is chosen for the current implementation, which results in a double minimization of the distance function. Next, the solution procedure using a staggered scheme is presented and finally, each step involved of the data-driven simulation algorithm.

For the sake of simplicity, a temporally and spatially discrete macroscopic problem is considered. The time is discretized by backward-Euler scheme, in which a rate term $\dot{\mathcal{F}}$ can be approximated by

$$\dot{\mathcal{F}} = \frac{\mathcal{F}^{n+1} - \mathcal{F}^n}{\Delta t}, \quad (5.7)$$

where $\Delta t = t^{n+1} - t^n$ is the time increment between the current t^{n+1} and previous t^n time instance. Spatial discretization of the domain $\bar{\Omega}$ is performed by finite elements containing $m = 1, 2, \dots, \mathcal{M}$ material (integration) points and $i = 1, 2, \dots, \mathcal{N}$ nodes. The notations and terminologies adopted here, follow from [109, 121].

5.3.1 Data-Set and Phase-Space

The data-driven reduced homogenization relies on a data-set generated by micro-scale reduced-order simulations. The choice of the macroscopic quantities to be stored in the data-set depends on the expressions of the constitutive equations (5.4)–(5.6) and the data extracted from the micro-scale simulations. Here, we choose to store all quantities and their rates (except for the flux rate). The local data-set

$$D_m = \left\{ \left(\bar{\mu}'_m, \dot{\mu}'_m, \bar{\mathbf{g}}'_m, \dot{\mathbf{g}}'_m, \underline{\eta}'_m, \dot{\eta}'_m, \bar{\mathbf{j}}'_m, \bar{c}'_m, \dot{c}'_m \right) \right\}_{I=1}^{n_{dp}}, \quad (5.8)$$

is available at each material point m of the macroscopic discrete model at each time instant t^{n+1} . In (5.8) the prime \bullet' differentiates between a quantity \bullet belonging to the physical-state of the macroscopic material or to the data-set D_m ; n_{dp} is the total number of data-points obtained from the micro-scale. However, it should be noted that after the data-generation stage the homogenization model is disregarded, and thereafter data-driven problems solely rely on the data at hand collected in (5.8). The local data-sets D_m , in general, can be different for each macroscopic material point m . Collectively, from all the material points, the total number of data-sets available in a discrete system represent a global data-set

$$D = D_1 \times D_2 \times \dots \times D_{\mathcal{M}}. \quad (5.9)$$

The physical-state of the material at the homogenized macro-scale can be characterized by a point in the local phase-space Z_m^{n+1}

$$z_m^{n+1} = \left(\bar{\mu}_m, \dot{\mu}_m, \bar{\mathbf{g}}_m, \dot{\mathbf{g}}_m, \underline{\eta}_m, \dot{\eta}_m, \bar{\mathbf{j}}_m, \bar{c}_m, \dot{c}_m \right)^{n+1} \in Z_m^{n+1}, \quad (5.10)$$

evolving in time, whereby the dimensions of the phase-space are $\dim(Z_m^{n+1}) = \mathbb{R}^1 \times \mathbb{R}^1 \times \mathbb{R}^{sd} \times \mathbb{R}^{sd} \times \mathbb{R}^{\mathcal{N}_q} \times \mathbb{R}^{\mathcal{N}_q} \times \mathbb{R}^{sd} \times \mathbb{R}^1 \times \mathbb{R}^1$, in which sd is the spatial dimension of the problem under consideration. Once combined, all the local states z_m^{n+1} make up the global physical-state

$$z^{n+1} = \left\{ \left(\bar{\mu}_m, \dot{\bar{\mu}}_m, \bar{\mathbf{g}}_m, \dot{\bar{\mathbf{g}}}_m, \bar{\boldsymbol{\eta}}_m, \dot{\bar{\boldsymbol{\eta}}}_m, \bar{\mathbf{j}}_m, \bar{c}_m, \dot{\bar{c}}_m \right)^{n+1} \right\}_{m=1}^{\mathcal{M}} \in Z^{n+1}, \quad (5.11)$$

in the global phase-space $Z^{n+1} = Z_1^{n+1} \times Z_2^{n+1} \times \dots \times Z_{\mathcal{M}}^{n+1}$. The physical-state of the material z^{n+1} at the macro-scale should obey the macroscopic compatibility and the discrete macroscopic mass balance laws at each time instance t^{n+1} .

For each material point, in an element of the discretized macroscopic domain, the compatibility is expressed in terms of the discretized macroscopic chemical potential, defined at the nodes $\bar{\mu}_i^{n+1}$ as

$$\bar{\mathbf{g}}_m^{n+1} = \sum_{i=1}^{\mathcal{N}} \nabla N_{mi} \bar{\mu}_i^{n+1}. \quad (5.12)$$

The macroscopic mass balance (5.1), once discretized in space and time and after applying the Dirichlet and the Neumann boundary conditions, reads at each node i and time instance t^{n+1} as

$$-\Delta t \sum_{m=1}^{\mathcal{M}} w_m \nabla N_{mi} \cdot \bar{\mathbf{j}}_m^{n+1} + \sum_{m=1}^{\mathcal{M}} w_m N_{mi} (\bar{c}_m^{n+1} - \bar{c}_m^n) = -\Delta t \hat{j}_i^{n+1}, \quad (5.13)$$

where $i = 1, 2, \dots, \mathcal{N}$. In equations (5.12) and (5.13), w_m contains information regarding quadrature weights and the volume of the elements, ∇N_{mi} is the gradient of finite element shape function N_{mi} evaluated at integration point m . Here, for the sake of simplicity of the notation, the finite element shape functions N and their gradients ∇N , are defined globally on the whole finite element mesh. Here, it should be noted that the macroscopic flux $\bar{\mathbf{j}}_m$ as well as the concentration \bar{c}_m , in equation (5.13), are the constitutive quantities which are evaluated at the material points. The primary unknown field is $\bar{\mu}_i$ defined on the nodes. This is different from the typical finite element discretization of the mass balance equation in which usually the concentration field are assumed primary unknown field. Note also that similar expressions could be obtained by alternative spatial discretization techniques. The compatibility (5.12) and the terms in the macroscopic mass balance law (5.13) are coupled through the data-set D_m . Through this coupling the discretized macroscopic chemical potential $\bar{\mu}_i^{n+1}$ is solved at the nodes. The

compatibility (5.12) and the balance law (5.13) pose restrictions on the state z^{n+1} of the material, hence constraining the phase-space Z^{n+1} as

$$E^{n+1} = \{z^{n+1} \in Z^{n+1} : \text{compatibility (5.12) and macroscopic mass balance (5.13)}\}. \quad (5.14)$$

5.3.2 Distance Minimizing Data-Driven Problem

A distance minimizing data-driven problem, as introduced in [106], seeks a compatible and equilibrated material physical-state $z^{n+1} \in E^{n+1}$ that has a minimum distance to a point in the global data-set D . To work with a distance, first the local phase-space Z_m^{n+1} is equipped with a local norm

$$|z_m^{n+1}| = \left[\frac{1}{2} {}^1\bar{\mathcal{C}}_m(\bar{\mu}_m^{n+1})^2 + \frac{1}{2} {}^2\bar{\mathcal{C}}_m(\dot{\bar{\mu}}_m^{n+1})^2 + \frac{1}{2} {}^3\bar{\mathcal{C}}_m(\bar{\mathbf{g}}_m^{n+1})^2 + \frac{1}{2} {}^4\bar{\mathcal{C}}_m(\dot{\bar{\mathbf{g}}}_m^{n+1})^2 + \frac{1}{2}(\bar{\eta}_m^{n+1})^T {}^5\underline{\mathcal{C}}_m(\bar{\eta}_m^{n+1}) + \frac{1}{2}(\dot{\bar{\eta}}_m^{n+1})^T {}^6\underline{\mathcal{C}}_m(\dot{\bar{\eta}}_m^{n+1}) + \frac{1}{2} {}^7\bar{\mathcal{C}}_m(\bar{\mathbf{j}}_m^{n+1})^2 + \frac{1}{2} {}^8\bar{\mathcal{C}}_m(\bar{c}_m^{n+1})^2 + \frac{1}{2} {}^9\bar{\mathcal{C}}_m(\dot{\bar{c}}_m^{n+1})^2 \right]^{\frac{1}{2}}, \quad (5.15)$$

where ${}^J\bar{\mathcal{C}}_m$ with $J = 1, 2, \dots, 9$ are the coefficients which non-dimensionalize the measure (5.15) and do not represent any material property. The coefficients ${}^5\underline{\mathcal{C}}_m$ and ${}^6\underline{\mathcal{C}}_m$ are diagonal matrices of size $\mathcal{N}_q \times \mathcal{N}_q$. The numerical values of these coefficients are important for the numerical convergence of the data-driven problem and will be discussed in Section 5.4.4. Each term in the measure (5.15) is quadratic, which, under the linear constraints of compatibility and equilibrium, leads to a convex optimization problem. Then, locally, at the material point level, the distance between two points $y_m^{n+1}, z_m^{n+1} \in Z_m^{n+1}$ can be measured as

$$d_m(z_m^{n+1}, y_m^{n+1}) = |z_m^{n+1} - y_m^{n+1}|. \quad (5.16)$$

The global norm can be obtained by taking squares and integrating the local norms over the entire domain

$$|z^{n+1}| = \left(\sum_{m=1}^{\mathcal{M}} w_m |z_m^{n+1}|^2 \right)^{\frac{1}{2}}, \quad (5.17)$$

which metrizes the global phase-space Z . Consequently the global distance from a point $y^{n+1} \in Z^{n+1}$ to $z^{n+1} \in Z^{n+1}$ is measured as

$$d(z^{n+1}, y^{n+1}) = |z^{n+1} - y^{n+1}|. \quad (5.18)$$

The distance minimizing data-driven problem is then written as a double minimization

$$\min_{y^{n+1} \in D} \min_{z^{n+1} \in E^{n+1}} d(z^{n+1}, y^{n+1}) = \min_{z^{n+1} \in E^{n+1}} \min_{y^{n+1} \in D} d(z^{n+1}, y^{n+1}). \quad (5.19)$$

It aims to find a point y^{n+1} in the global data-set D which is closest to a compatible and equilibrated material state E^{n+1} , or equivalently, find a compatible and equilibrated material state E^{n+1} which is closest to a point y^{n+1} in global data-set D while both minimizing the global distance function $d(z^{n+1}, y^{n+1})$.

The double minimization problem (5.19) is a combination of continuous and discrete optimization problems, the former over the continuous manifold E^{n+1} , the latter in the discrete data-set D . It has a combinatorial complexity, since for each material point m contributing to the global distance-function (5.18), n_{dp} points can be evaluated and the minimum should be chosen among those. To efficiently solve this computationally intensive combinatorial problem, following [119, 121], a staggered solution scheme is adopted here which freezes the continuous minimization problem while solving the discrete one and vice-versa. It assumes at an iteration k the optimum point in the data-set $y_k^{n+1} \in D$ to be known and finds a closest state $z_{k+1}^{n+1} \in E^{n+1}$ to that data-set point. This first step represents a projection operation $z_{k+1}^{n+1} = P_{E^{n+1}}^* y_k^{n+1}$, where $P_{E^{n+1}}$ denotes the closest point projection from D onto E^{n+1} .

Subsequently, in turn, the point z_{k+1}^{n+1} can be used to find the closest point in the data-set for the next iteration $y_{k+1}^{n+1} = P_D z_{k+1}^{n+1}$, where P_D denotes the closest point projection from Z^{n+1} onto D . The iterations are continued until there is no other optimum point in the data-set to choose i.e., $P_D z_{k+1}^{n+1} = P_D z_k^{n+1}$.

5.3.3 Solution Procedure

Assuming a known minimizing point $y_k^{n+1} \in D$, the projection $z_{k+1}^{n+1} = P_{E^{n+1}}^* y_k^{n+1}$ is followed after minimizing the quadratic distance function $d^2(\bullet, y_k^{n+1})$ subject to the constraints (5.12) and (5.13). The compatibility is imposed directly by introducing the chemical potential field as in equation (5.12) and the discrete mass balance is enforced by using Lagrange multipliers $\bar{\lambda}_i^{n+1}$ at the nodes. The Lagrangian can be

written as

$$\begin{aligned}
\bar{\mathcal{L}}^{n+1} = & \sum_{m=1}^{\mathcal{M}} w_m \left[\frac{1}{2} {}^1\bar{\mathcal{C}}_m \left(\sum_{i=1}^{\mathcal{N}} N_{mi} \bar{\mu}_i^{n+1} - {}^*\bar{\mu}_m^{n+1} \right)^2 + \frac{1}{2} {}^2\bar{\mathcal{C}}_m \left(\sum_{i=1}^{\mathcal{N}} N_{mi} \frac{\bar{\mu}_i^{n+1} - \bar{\mu}_i^n}{\Delta t} - {}^*\dot{\bar{\mu}}_m^{n+1} \right)^2 + \right. \\
& \frac{1}{2} {}^3\bar{\mathcal{C}}_m \left(\sum_{i=1}^{\mathcal{N}} \nabla N_{mi} \bar{\mu}_i^{n+1} - {}^*\bar{\mathbf{g}}_m^{n+1} \right)^2 + \frac{1}{2} {}^4\bar{\mathcal{C}}_m \left(\sum_{i=1}^{\mathcal{N}} \nabla N_{mi} \frac{\bar{\mu}_i^{n+1} - \bar{\mu}_i^n}{\Delta t} - {}^*\dot{\bar{\mathbf{g}}}_m^{n+1} \right)^2 + \\
& \frac{1}{2} {}^5\bar{\mathcal{C}}_m \left(\bar{\eta}_m^{n+1} - {}^*\bar{\eta}_m^{n+1} \right)^2 + \frac{1}{2} {}^6\bar{\mathcal{C}}_m \left(\frac{\bar{\eta}_m^{n+1} - \bar{\eta}_m^n}{\Delta t} - {}^*\dot{\bar{\eta}}_m^{n+1} \right)^2 + \\
& \left. \frac{1}{2} {}^7\bar{\mathcal{C}}_m \left(\bar{\mathbf{j}}_m^{n+1} - {}^*\bar{\mathbf{j}}_m^{n+1} \right)^2 + \frac{1}{2} {}^8\bar{\mathcal{C}}_m \left(\bar{c}_m^{n+1} - {}^*\bar{c}_m^{n+1} \right)^2 + \frac{1}{2} {}^9\bar{\mathcal{C}}_m \left(\frac{\bar{c}_m^{n+1} - \bar{c}_m^n}{\Delta t} - {}^*\dot{\bar{c}}_m^{n+1} \right)^2 \right] + \\
& \sum_{i=1}^{\mathcal{N}} \left[\left(-\Delta t \sum_{m=1}^{\mathcal{M}} w_m \nabla N_{mi} \cdot \bar{\mathbf{j}}_m^{n+1} + \sum_{m=1}^{\mathcal{M}} w_m N_{mi} (\bar{c}_m^{n+1} - \bar{c}_m^n) + \Delta t \hat{j}_i^{n+1} \right) \bar{\lambda}_i^{n+1} \right], \quad (5.20)
\end{aligned}$$

where the rate terms in the distance function are approximated using the backward-Euler time discretization introduced in (5.7).

Next, to find the stationarity conditions for all the variables appearing in the Lagrangian (5.20), it needs to be perturbed with respect to the admissible fields $\delta \bar{\mu}_i^{n+1}, \delta \bar{\eta}_m^{n+1}, \delta \bar{\mathbf{j}}_m^{n+1}, \delta \bar{c}_m^{n+1}, \delta \bar{\lambda}_i^{n+1}$. These stationarity conditions are discussed next, one-by-one. The perturbation with respect to the macroscopic chemical potential field $\bar{\mu}_i^{n+1}$, discretized at the nodes, provides,

$$\begin{aligned}
\delta \bar{\mu}_i^{n+1} : \frac{\partial \bar{\mathcal{L}}^{n+1}}{\partial \bar{\mu}_i^{n+1}} = 0 \implies \\
\sum_{m=1}^{\mathcal{M}} w_m \left[N_{mi} \left({}^1\bar{\mathcal{C}}_m + \frac{{}^2\bar{\mathcal{C}}_m}{\Delta t} \right) \sum_{j=1}^{\mathcal{N}} N_{mj} + \nabla N_{mi} \left({}^3\bar{\mathcal{C}}_m + \frac{{}^4\bar{\mathcal{C}}_m}{\Delta t} \right) \cdot \sum_{j=1}^{\mathcal{N}} \nabla N_{mj} \right] \bar{\mu}_j^{n+1} = \\
\sum_{m=1}^{\mathcal{M}} w_m \left[N_{mi} \frac{{}^2\bar{\mathcal{C}}_m}{\Delta t} \sum_{j=1}^{\mathcal{N}} N_{mj} + \nabla N_{mi} \frac{{}^4\bar{\mathcal{C}}_m}{\Delta t} \cdot \sum_{j=1}^{\mathcal{N}} \nabla N_{mj} \right] \bar{\mu}_j^n + \\
\sum_{m=1}^{\mathcal{M}} w_m \left[N_{mi} ({}^1\bar{\mathcal{C}}_m {}^*\bar{\mu}_m^{n+1} + {}^2\bar{\mathcal{C}}_m {}^*\dot{\bar{\mu}}_m^{n+1}) + \nabla N_{mi} \cdot ({}^3\bar{\mathcal{C}}_m {}^*\bar{\mathbf{g}}_m^{n+1} + {}^4\bar{\mathcal{C}}_m {}^*\dot{\bar{\mathbf{g}}}_m^{n+1}) \right], \quad (5.21)
\end{aligned}$$

which can be written in a matrix-column form as

$$\mathbb{K}^{\bar{\mu}} \bar{\mu}^{n+1} = \mathbb{M}^{\bar{\mu}} \bar{\mu}^n + \mathbb{F}^{\bar{\mu}}. \quad (5.22)$$

Equation (5.21) is a transient diffusion equation for $\bar{\mu}$ with corresponding bi-linear forms $(N_{mi} \bullet N_{mj})$ and $(\nabla N_{mi} \bullet \nabla N_{mj})$ as the capacity and diffusivity matrices, respectively. The macroscopic chemical potential field $\bar{\mu}^{n+1}$ calculated by (5.22),

with given $(\bar{\mu}_m^{*n+1}, \dot{\bar{\mu}}_m^{*n+1}, \bar{\mathbf{g}}_m^{*n+1}, \dot{\bar{\mathbf{g}}}_m^{*n+1})$ in the forcing term \mathbb{F}^* , is locally compatible with $(\bar{\mu}_m^{*n+1}, \bar{\mathbf{g}}_m^{*n+1})$ in a weak sense and also constrained by the corresponding rate terms $(\dot{\bar{\mu}}_m^{*n+1}, \dot{\bar{\mathbf{g}}}_m^{*n+1})$ in the data-set. The Dirichlet boundary conditions, appearing in equation (5.1), are enforced on the $\bar{\mu}$ field, while homogeneous Neumann conditions are considered on the complementary part of the boundary $\partial\bar{\Omega}_{\bar{j}}$.

The perturbation with respect to the enrichment-variables reads

$$\begin{aligned} \delta \underline{\eta}_m^{n+1} : \frac{\partial \bar{\mathcal{L}}^{n+1}}{\partial \underline{\eta}_m^{n+1}} &= 0 \\ \implies \underline{\eta}_m^{n+1} &= \frac{1}{(\Delta t \ ^5\underline{\mathcal{C}}_m + \ ^6\underline{\mathcal{C}}_m)} \left[\ ^6\underline{\mathcal{C}}_m \underline{\eta}_m^n + \Delta t \ ^5\underline{\mathcal{C}}_m \dot{\underline{\eta}}_m^{*n+1} + \Delta t \ ^6\underline{\mathcal{C}}_m \dot{\underline{\eta}}_m^{*n+1} \right], \end{aligned} \quad (5.23)$$

which means that locally $\underline{\eta}_m^{n+1}$ should be consistent with $\dot{\underline{\eta}}_m^{*n+1}$ and its rate $\dot{\underline{\eta}}_m^{*n+1}$, present in the data-set. Since $\underline{\eta}_m$ does not appear in the macroscopic balance equation (5.13) there are no Lagrange multipliers $\bar{\lambda}^{n+1}$ in (5.23); $\underline{\eta}_m$ is connected to the other physical-state variables via the data-set only.

The perturbation with respect to the macroscopic mass flux yields

$$\delta \bar{\mathbf{j}}_m^{n+1} : \frac{\partial \bar{\mathcal{L}}^{n+1}}{\partial \bar{\mathbf{j}}_m^{n+1}} = 0 \implies \bar{\mathbf{j}}_m^{n+1} = \dot{\bar{\mathbf{j}}}_m^{*n+1} + \Delta t \frac{1}{\ ^7\bar{\mathcal{C}}_m} \sum_{i=1}^{\mathcal{N}} \nabla N_{mi} \bar{\lambda}_i^{n+1}, \quad (5.24)$$

which states that the difference between the local macroscopic mass flux $\bar{\mathbf{j}}_m^{n+1}$ and its counterpart in the data-set $\dot{\bar{\mathbf{j}}}_m^{*n+1}$, at iteration k , should be balanced through the Lagrange multipliers field $\bar{\lambda}_i^{n+1}$. The perturbation with respect to the macroscopic concentration can be written as

$$\begin{aligned} \delta \bar{c}_m^{n+1} : \frac{\partial \bar{\mathcal{L}}^{n+1}}{\partial \bar{c}_m^{n+1}} &= 0 \implies \\ \bar{c}_m^{n+1} &= \frac{1}{(\Delta t \ ^8\bar{\mathcal{C}}_m + \ ^9\bar{\mathcal{C}}_m)} \left[\ ^9\bar{\mathcal{C}}_m \bar{c}_m^n + \Delta t \ ^8\bar{\mathcal{C}}_m \dot{\bar{c}}_m^{*n+1} + \Delta t \ ^9\bar{\mathcal{C}}_m \dot{\bar{c}}_m^{*n+1} - \Delta t \sum_{i=1}^{\mathcal{N}} N_{mi} \bar{\lambda}_i^{n+1} \right], \end{aligned} \quad (5.25)$$

which gives a local macroscopic concentration field \bar{c}_m^{n+1} consistent with $(\dot{\bar{c}}_m^{*n+1}, \dot{\bar{c}}_m^{*n+1})$ in the data-set, whereby the difference is rectified by the Lagrange multipliers field $\bar{\lambda}_i^{n+1}$.

Finally, taking the variation with respect to the Lagrange multiplier field $\bar{\lambda}_i^{n+1}$ amounts to

$$\begin{aligned} \delta \bar{\lambda}_i^{n+1} : \frac{\partial \bar{\mathcal{L}}^{n+1}}{\partial \bar{\lambda}_i} &= 0 \\ \implies -\Delta t \sum_{m=1}^M w_m \nabla N_{mi} \cdot \bar{\mathbf{j}}_m^{n+1} + \sum_{m=1}^M w_m N_{mi} (\bar{c}_m^{n+1} - \bar{c}_m^n) + \Delta t \hat{j}_i^{n+1} &= 0, \end{aligned} \quad (5.26)$$

which is the balance between the internal and the external macroscopic mass fluxes at the nodes. Substituting the expressions of $\bar{\mathbf{j}}_m^{n+1}$ and \bar{c}_m^{n+1} from equations (5.24) (5.25) into equation (5.26) and performing some straight forward manipulations provides the system of equations for the Lagrange multiplier field $\bar{\lambda}_i^{n+1}$ as follows

$$\begin{aligned} -\Delta t^2 \sum_{m=1}^M w_m \nabla N_{mi} \cdot \frac{1}{7\bar{c}_m} \sum_{j=1}^{\mathcal{N}} \nabla N_{mj} \bar{\lambda}_j^{n+1} - \\ \Delta t \sum_{m=1}^M w_m N_{mi} \frac{1}{\Delta t \ 8\bar{c}_m + 9\bar{c}_m} \sum_{j=1}^{\mathcal{N}} N_{mj} \bar{\lambda}_j^{n+1} = \Delta t \sum_{m=1}^M w_m \nabla N_{mi} \cdot \bar{\mathbf{j}}_m^* - \Delta t \hat{j}_i^{n+1} - \\ \sum_{m=1}^M w_m N_{mi} \left(\frac{1}{\Delta t \ 8\bar{c}_m + 9\bar{c}_m} \left[\Delta t \ 8\bar{c}_m \bar{c}_m^* + 9\bar{c}_m \bar{c}_m^n + \Delta t \ 9\bar{c}_m \dot{\bar{c}}_m^* \right] - \bar{c}_m^n \right), \end{aligned} \quad (5.27)$$

which in the matrix-column form can be written as

$$\mathbb{K} \bar{\lambda}^{n+1} = \mathbb{F}^{\lambda*}. \quad (5.28)$$

In equations (5.24)–(5.28), the Lagrange multiplier field can be interpreted as an equivalent macroscopic chemical potential which minimizes the difference between the physical-state $(\bar{\mathbf{j}}_m^{n+1}, \bar{c}_m^{n+1})$ and the point $(\bar{\mathbf{j}}_m^{*n+1}, \bar{c}_m^{*n+1}, \dot{\bar{c}}_m^{*n+1})$ in the data-set, which are present in $\mathbb{F}^{\lambda*}$. In equation (5.28), the Lagrange multiplier field is subject to $\bar{\lambda}_i^{n+1} = 0$ on $\partial\bar{\Omega}_{\bar{\mu}}$ and there is an influx of mass \hat{j} , which is zero, at the Neumann part of the boundary that naturally appears in the system of equations through the weak form (5.13). For a variational formulation and a detailed discussion on the boundary conditions on the fields appearing in the data-driven problems, the reader is directed to [119].

In a staggered approach, after solving for $\bar{\mu}^{n+1}$ and $\bar{\lambda}^{n+1}$ from equations (5.22) and (5.28), the projection $z_{k+1}^{n+1} = P_{E^{n+1}}^* \bar{y}_k^{n+1}$ can be obtained by evaluating $\eta_m^{n+1}, \bar{\mathbf{j}}_m^{n+1}$ and \bar{c}_m^{n+1} from (5.4), (5.24) and (5.25), respectively. The subsequent projection $\bar{y}_{k+1}^{n+1} = P_D z_{k+1}^{n+1}$ is achieved by a simple search through the data to find a point in the global data-set D which provides the minimum distance to z_{k+1}^{n+1} , as discussed in more detail in the next section.

5.3.4 Algorithm

The pseudo algorithm for distance minimizing data-driven reduced homogenization is shown in Algorithm 1. The data-driven solver initializes with setting the

Algorithm 1: Distance minimizing data-driven reduced homogenization.

```

▶ Initialize:  $maxIter = 100$ ,  $k = 0$ ,  $tol = 10^{-12}$ ,  $n = 1$  ;
▶ Assign:  $y_k^{n+1} = 0$  ;
▶ Assemble:  $\mathbb{K}^{\bar{\mu}}$ ,  $\mathbb{K}^{\bar{\lambda}}$ ,  $\underline{\mathbb{M}}^{\bar{\mu}}$ ,  $\underline{\mathbb{F}}_k^{\bar{\mu}}$  and  $\underline{\mathbb{F}}_k^{\bar{\lambda}}$  ;
for  $n = 0 \rightarrow T$  do
  while  $k < maxIter$  do
    ▶ Solve:  $\mathbb{K}^{\bar{\mu}} \bar{\mu}_{k+1}^{n+1} = \underline{\mathbb{M}}^{\bar{\mu}} \bar{\mu}_{k+1}^n + \underline{\mathbb{F}}_k^{\bar{\mu}}$  (5.22) and  $\mathbb{K}^{\bar{\lambda}} \bar{\lambda}_{k+1}^{n+1} = \underline{\mathbb{F}}_k^{\bar{\lambda}}$  (5.28) ;
    for  $m = 1 \rightarrow \mathcal{M}$  do
      ▶ Evaluate:  $z_{m,k+1}^{n+1} = P_{E^{n+1}} y_{m,k}^{n+1}$  ;
      ▶ Choose:  $y_{m,k+1}^{n+1} = P_D z_{m,k+1}^{n+1}$  such that
         $d_m(z_{m,k+1}^{n+1}, y_{m,k+1}^{n+1}) \leq d_m(z_{m,k+1}^{n+1}, D_m)$  ;
      ▶ Integrate:  $d(z_{k+1}^{n+1}, y_{k+1}^{n+1})$  from  $d_m(z_{m,k+1}^{n+1}, y_{m,k+1}^{n+1})$  ;
      ▶ Assemble:  $\underline{\mathbb{F}}_{k+1}^{\bar{\mu}}$  and  $\underline{\mathbb{F}}_{k+1}^{\bar{\lambda}}$  using  $y_{k+1}^{n+1}$  ;
    end
    if  $(P_D z_{k+1}^{n+1} - P_D z_k^{n+1}) \leq tol$  then
      ▶ Terminate ;
    else
      ▶  $k = k + 1$  ;
    end
  end
end
end

```

maximum number of allowed iterations $maxIter$, the data-driven iteration counter k , the allowed tolerance tol and the time stepping variable n . An initial guess for the optimum $y_k^{n+1} \in D$ is made. In the preliminary work [106], $y_{m,k}^{n+1}$ was initialized by assigning randomly a point in the D_m to each material point m . However, it was observed that an initial guess of $y_k^{n+1} = 0$ requires less number of iterations to converge to the desired tolerance, both for steady-state and transient problems.

Unlike material model based finite element solvers, independently of the existence of a potential non-linearity in the material behavior, the distance minimizing data-driven solver requires the assembly of the matrices $\mathbb{K}^{\bar{\mu}}$, $\mathbb{K}^{\bar{\lambda}}$ and $\underline{\mathbb{M}}^{\bar{\mu}}$ only once. For a specific physical phenomenon under consideration, for instance elasticity, diffusion, or history-dependent materials, the same solver can be used for different materials and different data-sets. Then, in the time stepping and data-driven

loops, first the pertinent $\underline{\bar{\mu}}^{n+1}$ and $\underline{\bar{\lambda}}^{n+1}$ problems are solved. In the current formulation these two problems, (5.22) and (5.28), are algebraically independent, the only coupling is through the data-set D . However, in some other data-driven problems, as can be seen in the case of dynamics [107] and transient Fickian diffusion [119] (formulated in concentrations), a coupled system of equations emerges after taking variations of the Lagrangian.

Next, at the material point level, the projection $z_{m,k+1}^{n+1} = P_{E^{n+1}}^* y_{m,k}^{n+1}$ is performed. It involves evaluating the physical-state of the material $z_{m,k+1}^{n+1}$, from the previously calculated y_k^{n+1} , $\underline{\bar{\mu}}_{k+1}^{n+1}$ and $\underline{\bar{\lambda}}_{k+1}^{n+1}$. The local values of $\underline{\bar{\mu}}_{m,k+1}^{n+1}$ are evaluated by interpolating $\underline{\bar{\mu}}_{i,k+1}^{n+1}$ using the finite element shape functions N_{mi} , $\underline{\bar{g}}_{m,k+1}^{n+1}$ is computed by using compatibility (5.12), while $\underline{\eta}_{m,k+1}^{n+1}$, $\underline{\bar{j}}_{m,k+1}^{n+1}$ and $\underline{\bar{c}}_{m,k+1}^{n+1}$ are calculated by (5.23), (5.24) and (5.25), respectively and their rates $(\dot{\underline{\mu}}_m, \dot{\underline{g}}_m, \dot{\underline{\eta}}_m, \dot{\underline{c}}_m)_{k+1}^{n+1}$ using the approximation in (5.7).

The global distance function (5.18) is minimized by finding the minima of the local distance function (5.16), using all the points in the local data-set D_m , at each material point m , and then integrating it using numerical quadrature. The minimum for the local distance function (5.16) is found through a simple lookup array search algorithm, which amounts to performing the projection $y_{m,k+1}^{n+1} = P_D z_{m,k+1}^{n+1}$. Searching through the data-set D_m is the computationally expensive part of data-driven algorithm. If the data-set is large enough, a smart search algorithm, for instance, based on a tree search algorithm [122], should be used to accelerate this step. Then, using the newly found values of $y_{m,k+1}^{n+1}$, the flux columns $\underline{\mathbb{F}}_{k+1}^{\underline{\bar{\mu}}}$ and $\underline{\mathbb{F}}_{k+1}^{\underline{\bar{\lambda}}}$ are assembled. Finally, the convergence is checked and the iterations are terminated if there is no change in the optimum data point. For a noisy data-set, convergence criteria based on the stagnation of the global distance function can be used to terminate the data-driven iterations.

5.4 Numerical Examples

In this section, the proposed framework for data-driven reduced homogenization for transient diffusion problems with history effects is illustrated through numerical examples. First, the problem settings are presented for the micro-scale and the macro-scale. Next, the data-generation step is performed by loading the micro-scale, post-processing, and storing the relevant quantities. After that, the data-driven simulations are carried out, whereby the homogenized chemical potential fields obtained by the data-driven approach are compared with the ones obtained

by the regular enriched-continuum formulation. Information from the reduced micro-scale model is used to select the coefficients in the distance function. The micro-scale chemical potential fields are post-processed and also compared. The performance of the data-driven approach using noisy and different data-sets is also analyzed. Finally, a convergence analysis, with respect to the number of points in the data-set, is carried out.

5.4.1 Problem Settings: Micro-scale and Macro-scale

5.4.1.1 Micro-scale

The micro-scale consists of a two-dimensional square unit-cell with side length ℓ and a single circular inclusion of diameter d embedded in a matrix. The material properties and linear constitutive material models for the inclusion and the matrix are assumed to be known and complying with the relaxed separation of scales regime ($\tau_m \ll \tau_i \sim T$). The unit-cell is discretized with nearly 4400 linear triangular elements and 2200 nodes. The material properties and other parameters used in the simulations are listed in Table 5.1. After the assembly of the finite element system and application of the periodic boundary conditions, at the micro-scale, an eigenvalue problem is solved for the smallest 100 eigenvalues $\underline{\alpha}$ and eigenvectors $\underline{\Phi}$. Next, a criterion based on either the energy consistency or coupling terms, as proposed in [67, 105], is used to select a limited number (\mathcal{N}_q) eigenmodes that contribute most, in terms of transient effects, to the macro-scale response. For the unit-cell with a single inclusion, as shown in Figure 5.1, and the material properties given in Table 5.1, the selection criteria based on the coupling terms provides 6 important eigenvectors as a reduced basis set, see [120] for more details and the contour plots of the selected eigenvectors. Finally, the homogenized coefficients ($\bar{\underline{a}}, \bar{\underline{a}}^*, \bar{\underline{B}}, \bar{\underline{c}}, \bar{\underline{C}}, \bar{\underline{d}}, \bar{\underline{d}}^*, \bar{\underline{e}}, \bar{\underline{f}}, \bar{\underline{f}}$) are determined and stored [67]. The values for the first components of these coefficients can be found in Table 5.2. Note that, even though the macro-scale considered here is a one-dimensional domain, a two-dimensional micro-scale problem has to be solved to obtain the required values of the homogenized coefficients, since in a one-dimensional micro-scale domain the diffusion around the inclusion can not be represented at the macro-scale through homogenization. The reduced order model (5.4)–(5.6) is now ready for the data-generation stage.

Table 5.1: Default parameters used in the simulations.

Parameter	Symbol	Value	Units
Micro-scale			
Characteristic unit-cell length	ℓ	1×10^{-2}	[m]
Inclusion diameter	d	0.6×10^{-2}	[m]
Mobility in matrix	M_m	1.1×10^{-4}	[mol ² J ⁻¹ m ⁻¹ s ⁻¹]
Mobility in inclusion	M_i	1.85×10^{-9}	[mol ² J ⁻¹ m ⁻¹ s ⁻¹]
Reference temperature	θ_0	298	[K]
Boltzman's constant	k_b	8.314	[J K ⁻¹ mol ⁻¹]
Maximum concentration	c_{\max}	24161	[mol m ⁻³]
Minimum concentration	c_0	$0.0547c_{\max}$	[mol m ⁻³]
Chemical modulus	$\Lambda = k_b\theta_0/c_0$	1.83	[J m ³ mol ⁻²]
Characteristic diffusion time of inclusion	τ_i	$d^2/M_i\Lambda = 36000$	[s]
Characteristic diffusion time of matrix	τ_m	$\ell^2/M_m\Lambda = 1.69$	[s]
Number of nodes in unit-cell mesh		$\sim 2.2 \times 10^3$	
Macro-scale			
Macroscopic domain length	L	100×10^{-2}	[m]
Total simulation time T	T	$0.1\tau_i$	[s]
Number of elements (reference)		50	
Number of nodes (reference)	\mathcal{N}	51	
Time step size	Δt	$T \times 10^{-3}$	[s]
Data-Driven Solver			
Number of data points	n_{dp}	1000	
Maximum number iterations	$maxIter$	100	
Tolerance for the termination criteria	tol	10^{-12}	

Table 5.2: The values of the coefficients appearing in equations (5.5) and (5.6), for the unit-cell shown in Figure 5.1 with geometrical and material parameters given in Table 5.1, $\mathbf{A}_{(\bullet)}$ indicates the (\bullet) component of the tensor \mathbf{A} .

Coefficient	$\bar{\mathbf{a}}_{(1)}^{(1)}$	$\bar{\mathbf{B}}_{(11)}$	$\bar{\mathbf{c}}_{(1)}$	$\bar{\mathbf{C}}_{(11)}$
Units	$[\text{mol m}^{-2} \text{s}^{-1}]$	$[\text{J}^{-1} \text{mol}^2 \text{m}^{-1} \text{s}^{-1}]$	$[\text{J}^{-1} \text{mol}^2 \text{m}^{-2}]$	$[\text{J}^{-1} \text{mol}^2 \text{m}^{-1}]$
Value	1.3×10^{-7}	0.6×10^{-4}	1.3×10^{-8}	0.6×10^{-5}
Coefficient	$\bar{\mathbf{d}}^{(1)}$	$\bar{\mathbf{e}}_{(1)}$	$\bar{\mathbf{f}}$	$\bar{\mathbf{f}}_{(1)}$
Units	$[\text{mol m}^{-3} \text{s}^{-1}]$	$[\text{J}^{-1} \text{mol}^2 \text{m}^{-2} \text{s}^{-1}]$	$[\text{J}^{-1} \text{mol}^2 \text{m}^{-3}]$	$[\text{J}^{-1} \text{mol}^2 \text{m}^{-2}]$
Value	-33.46	-0.6×10^{-16}	0.534	-0.13×10^{-7}

5.4.1.2 Macro-scale

The homogenized macroscopic domain $\bar{\Omega}$, both for the enriched-continuum and the data-driven simulations, is a one-dimensional bar of length L with a Dirichlet boundary condition on $\partial\Omega_{\bar{\mu}}$ on the left side of the domain and Neumann no-flux boundary condition on the right side of the domain. It is discretized with 50 linear one-dimensional finite elements, unless stated otherwise, which are integrated using a two-point Gauss quadrature rule. For consistency, in the following the vectorial/tensorial quantities in one-dimension are still shown with a tensorial notation. Total loading time is chosen to be $T = 0.1\tau_i[\text{s}]$ and both the enriched-continuum and the data-driven problems are discretized in time using the backward-Euler time integration scheme. The reference time step size Δt is taken to be $\Delta t = T \times 10^{-3}[\text{s}]$. For the macro-scale simulations, the ramp loading conditions

$$\bar{\mu}_p^{n+1}(t) = \begin{cases} \frac{t}{T_R} \bar{\mu}_{\max}, & \text{if } t \leq T_R \text{ (loading)} \\ \bar{\mu}_{\max}, & T_R < t \leq T \text{ (relaxation)} \end{cases} \quad \text{on } \partial\Omega_{\bar{\mu}}, \quad (5.29)$$

are used on the Dirichlet part of the macroscopic boundary $\partial\bar{\Omega}_{\bar{\mu}}$, where $\bar{\mu}_{\max} = \Lambda(c_{\max} - c_0)$ is the maximum attainable chemical potential during mass diffusion and $T_R = T/2$. The first part of the ramp till T_R represents a loading path and the second part from T_R to T represents a relaxation path. The data-driven reduced homogenization solver is initialized with an initial guess $\bar{y}_k^{*n+1} = 0$ and the stagnation criteria $|d(z_{k+1}^{n+1}, \bar{y}_{k+1}^{*n+1}) - d(z_{k+1}^{n+1}, \bar{y}_k^{*n+1})| \leq \text{tol}$ is used to terminate the iterations of the staggered scheme. The numerical solution of the enriched-continuum formulation at the macro-scale is used as a reference solution.

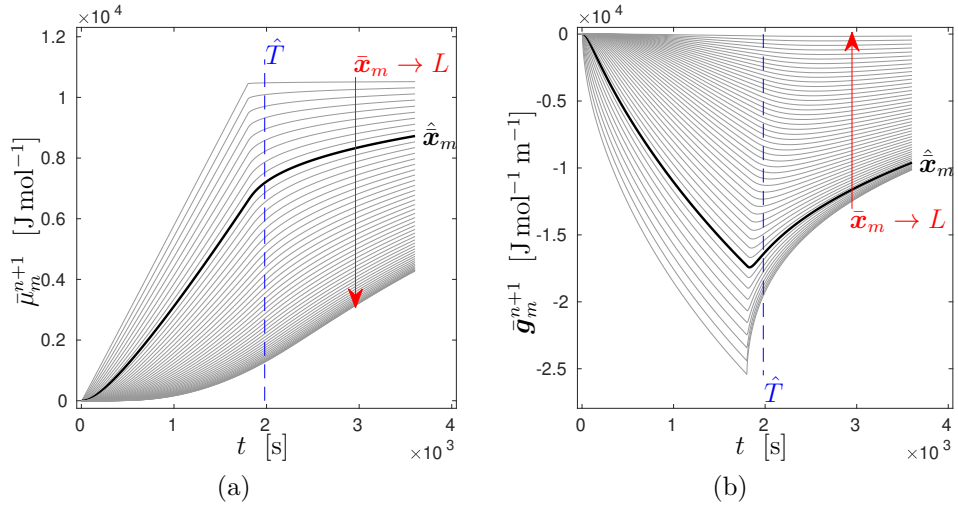


Figure 5.2: (a) Local macroscopic chemical potential field $\bar{\mu}_m^{n+1}$ and (b) local gradient of macroscopic chemical potential field $\bar{\mathbf{g}}_m^{n+1}(t)$ to be used as the input for the micro-scale data-generation step. These are post-processed, from the solution of the enriched-continuum problem, at the first Gauss quadrature point of every element in the macroscopic domain loaded with the ramp condition (5.31). The dark black line represents $\bar{\mu}_m^{n+1}$ and $\bar{\mathbf{g}}_m^{n+1}$ at a reference macroscopic point $\hat{\mathbf{x}}_m$ which will be used to compare the local elemental quantities. The dashed blue line is at a reference time $\hat{T} = 0.55T$ at which the global quantities, at the nodes, will be compared.

$\bar{\mu}_i^{n+1}$ at the nodes will be compared at a time instance $\hat{T} = 0.55T$ as shown with a dashed blue line in Figure 5.2.

5.4.2.2 Data-Generation

The data-generation is performed by solving the reduced model (5.4)–(5.6), for $\bar{\mu}_m^{n+1}(t)$ and $\bar{\mathbf{g}}_m^{n+1}(t)$ computed in the previous section, with the time discretization performed using the approximation in equation (5.7). The data is stored in a local data-set

$$D_m = \{(\bar{\mu}'_m, \dot{\bar{\mu}}'_m, \bar{\mathbf{g}}'_m, \dot{\bar{\mathbf{g}}}'_m, \underline{\eta}'_m, \underline{\eta}'_{m'}, \bar{\mathbf{j}}'_m, \bar{\mathbf{c}}'_m, \dot{\bar{\mathbf{c}}}'_m)\}_{I=1}^{n_{dp}} \quad (5.30)$$

In current work, for the data-driven simulations the same local data-set D_m is available to all the material points i.e., $D_1 = D_2 = \dots = D_M$; in general, a different data-set can be available for each material point.

As stated before, the selection criteria for the dominant eigenvectors, as proposed in [67, 105], provide $\mathcal{N}_q = 6$ for the considered unit-cell. It turns out, however, that out of these six, only one eigenvalue has the largest contribution

to the lagging behavior at the macro-scale. This can be verified from the time evolution of $\eta_m^{(q),n+1}$ and $\dot{\eta}_m^{(q),n+1}$ at $\hat{\mathbf{x}}_m$, as shown in Figure 5.3. Therefore, it has been chosen to use only $\eta_m^{(1),n+1}$ and $\dot{\eta}_m^{(1),n+1}$ in the data-driven calculations to capture the history-dependent response. The different loading conditions (Table

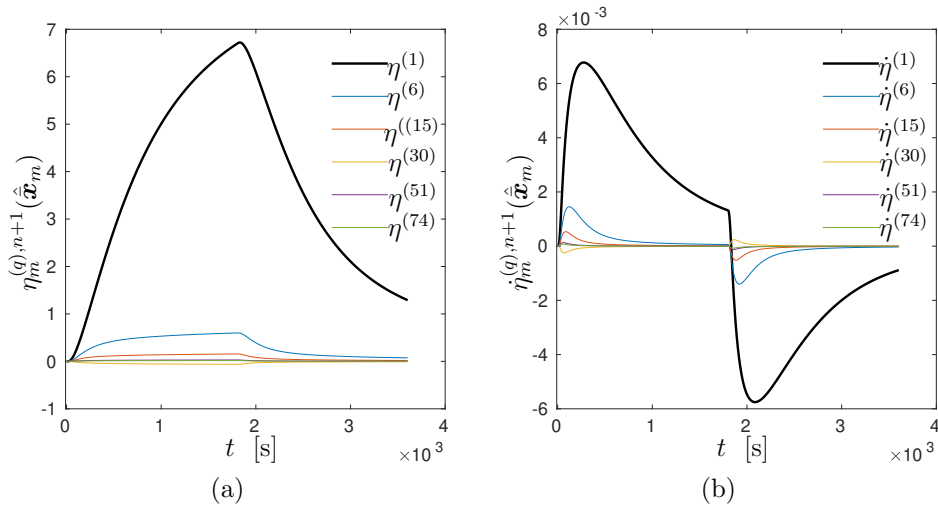
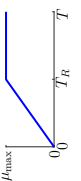
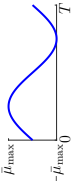
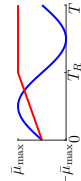
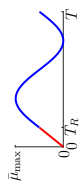


Figure 5.3: (a) Time evolution of the enrichment-variables $\eta_m^{(q),n+1}(t)$ and (b) their rates $\dot{\eta}_m^{(q),n+1}$ at the reference macroscopic point $\hat{\mathbf{x}}_m$. For the unit-cell shown in Figure 5.1, the eigenvalue and the corresponding eigenvector corresponding to $\eta_m^{(1),n+1}$ are dominant one.

5.3) have provided different data-sets which are indexed as listed in Table 5.3. The number of data-points $n_{dp} = T/\Delta t + 1$ are also given in the table. After the data-generation stage, the information about the micro-scale must be discarded, as the data-driven solver should only rely on the raw data.

Pairs $(\bar{\mathbf{g}}_m^{n+1}, \bar{\mathbf{j}}_m^{n+1})$, $(\dot{\bar{\mu}}_m^{n+1}, \dot{\bar{c}}_m^{n+1})$ and $(\dot{\bar{\mu}}_m^{n+1}, \dot{\eta}_m^{(1),n+1}, \dot{\bar{c}}_m^{n+1})$ in D_R are visualized in Figure 5.4 (a), (b) and (c), respectively. The pairs $(\bar{\mathbf{g}}_m^{n+1}, \bar{\mathbf{j}}_m^{n+1})$ show a negative linear behavior that is independent of the loading path, which indicates that the history effects are not prominent in the diffusion contribution at the macro-scale and can also be sufficiently accurately calculated by the standard volume averaging of the Fickian diffusion behavior at the micro-scale. However, a prominent history dependence and non-Fickian behavior can be observed in the graphs of $(\dot{\bar{\mu}}_m^{n+1}, \dot{\bar{c}}_m^{n+1})$, where there is neither a linear nor logarithmic relation between $\dot{\bar{\mu}}_m^{n+1}$ and $\dot{\bar{c}}_m^{n+1}$ at the macro-scale. This can also be observed in $(\dot{\bar{\mu}}_m^{n+1}, \dot{\eta}_m^{(1),n+1}, \dot{\bar{c}}_m^{n+1})$ graph, which clearly indicates that the history effect emerges from the storage/-capacitance term at the macro-scale and can be tracked by the internal-variable $\dot{\eta}_m^{(1),n+1}$. A correct value of $\dot{\eta}_m^{(1),n+1}$, at a spatial point $\bar{\mathbf{x}}_m$ and time t^{n+1} , selected

Table 5.3: Names, expressions and graphs of the macroscopic loading conditions and symbol and the number of data-points n_{dp} for different data-sets used in present study.

Name	Loading condition expression	$\bar{\mu}_p^{n+1}(t)$ Graph	Data-Set	n_{dp}
Ramp	$\bar{\mu}_p^{n+1}(t) = \begin{cases} \frac{tT}{T_R} \bar{\mu}_{\max}, & \text{if } t \leq T_R \\ \bar{\mu}_{\max}, & \text{otherwise} \end{cases}$ <p>where $T_R = T/2$</p>		D_R	1000
Sine	$\bar{\mu}_p^{n+1}(t) = \bar{\mu}_{\max} \sin(\omega t)$ <p>where $\omega = 2\pi/T$</p>		D_S	1000
Ramp + Sine	(5.31) and (5.32)		$D_{(R+S)}$	2000
Ramp & Sine	$\bar{\mu}_p^{n+1}(t) = \begin{cases} \frac{tT}{2T_R} \bar{\mu}_{\max}, & \text{if } t \leq T_R \\ \frac{\bar{\mu}_{\max}}{2} \sin(\omega t) + \frac{\bar{\mu}_{\max}}{2}, & \text{otherwise} \end{cases}$ <p>where $T_R = T/7$ and $\omega = 2\pi/(T - T_R)$</p>		$D_{(RS)}$	1000

by the projection $y_{m,k+1}^{*n+1} = P_D z_{m,k+1}^{n+1}$, will direct the other quantities, in the data-set D_m , to be either in the loading or the relaxation path, hence keeping track of the history effects. Next, the macroscopic chemical potential field $\bar{\mu}$ and the

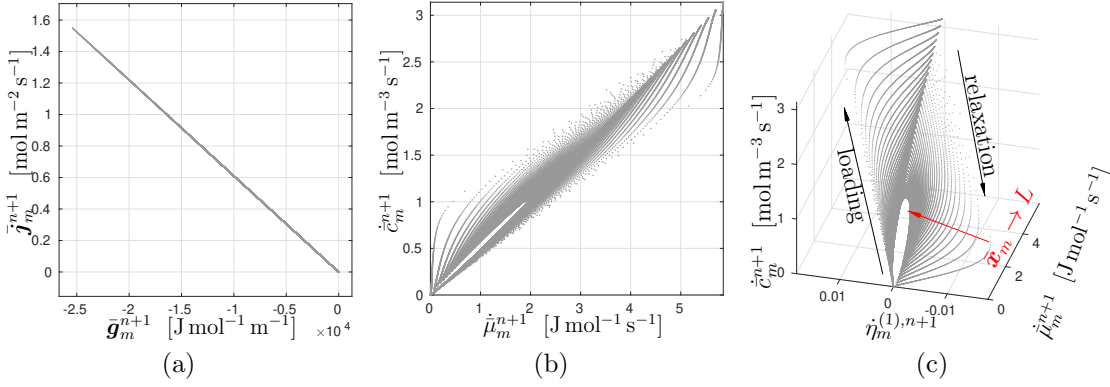


Figure 5.4: From the data-set D_R , the pairs (a) $(\bar{g}_m^{n+1}, \bar{J}_m^{n+1})$, (b) $(\dot{\mu}_m^{n+1}, \dot{c}_m^{n+1})$ and (c) $(\dot{\mu}_m^{n+1}, \dot{\eta}_m^{(1),n+1}, \dot{c}_m^{n+1})$ are visualized.

microscopic chemical potential fields μ obtained from the data-driven reduced homogenization and the enriched-continuum formulation will be compared to provide an indication of the performance of the data-driven approach.

5.4.3 Homogenized and Microscopic Fields

In this section, the developed data-driven reduced homogenization is verified using the data-set D_R generated from the enriched-continuum problem, with the same loading condition (5.31) as it is used for the data-driven boundary value problem. In this scenario, the data-set can be assumed to be ideal and if the data-driven problem is formulated correctly, both, the enriched-continuum and the data-driven solutions must match very accurately. In Figure 5.5, the macroscopic chemical potential field at time \hat{T} obtained by the enriched-continuum formulation $\bar{\mu}_E^{n+1}$ (reference) is shown with the gray line, while the one obtained by the proposed data-driven reduced homogenization method $\bar{\mu}_D$ using the data-set D_R is shown with the blue line. It can be observed that $\bar{\mu}_E^{n+1}$ and $\bar{\mu}_D^{n+1}$ lie on top of each other. The micro-scale chemical potential fields $\underline{\mu}_E^{n+1}$ and $\underline{\mu}_D^{n+1}$, shown in Figure 5.6, are post-processed at $\bar{x}_1 = 0.6842[\text{m}]$ using

$$\underline{\mu}_m^{n+1} = \underline{S}(\underline{I}\bar{\mu}_m^{n+1} + \bar{g}_m^{n+1} \cdot \Delta \underline{x}_m) + \underline{\Phi}^{(1)}\eta_m^{(1),n+1}, \quad (5.34)$$

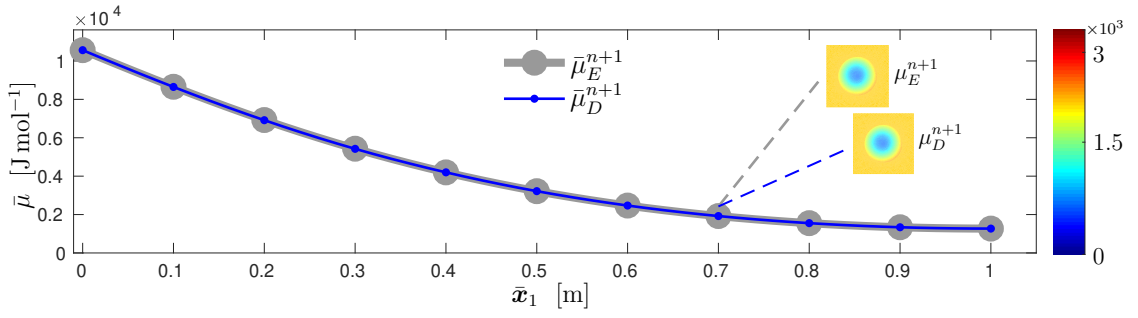


Figure 5.5: Comparison between the macroscopic chemical potential fields obtained via enriched continuum formulation $\bar{\mu}_E^{n+1}$ (reference), shown with the gray line, and the data-driven reduced homogenization $\bar{\mu}_D^{n+1}$ using D_R , shown with the blue line, at time step \hat{T} . The microscopic chemical potential fields μ_E^{n+1} and μ_D^{n+1} are post-processed $\bar{x}_1 = 0.6842[\text{m}]$. The marker is plotted at every tenth node of the finite element mesh.

where \underline{S} is the Schur-complement of the microscopic finite element matrices, \underline{I} is a column of ones and $\Delta \underline{x}_m$ is the microscopic position vector connecting the spatial coordinates to the center of the unit-cell. For more details on the post-processing of the microscopic field μ_m by using (5.34) the reader is referred to [67]. The post-processed microscopic fields also reveal an excellent agreement with the reference simulation where the maximum of the absolute error is of the order of 10^{-11} . To

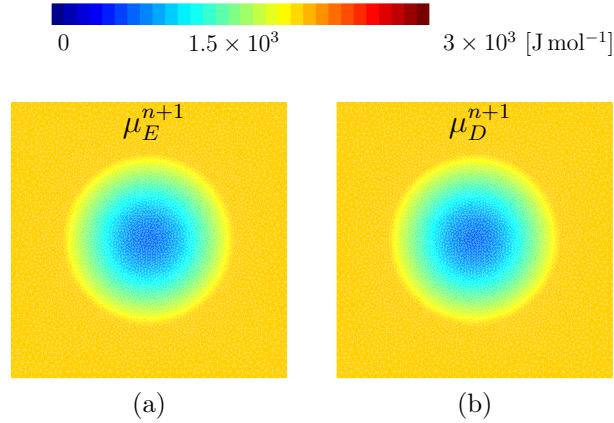


Figure 5.6: Microscopic chemical potential fields μ_E^{n+1} and μ_D^{n+1} using D_R data-set post-processed at time \hat{T} and $\bar{x}_1 = 0.6842[\text{m}]$ using equation (5.34).

obtain these results, the values of the coefficients ${}^J\bar{\mathcal{C}}_m$ were chosen based on the information available from the micro-scale, as will be detailed next.

5.4.4 Numerical Values of the Coefficients ${}^J\bar{\mathcal{C}}_m$

In the data-driven simulations, the coefficients ${}^J\bar{\mathcal{C}}_m$ in the norm (5.15) used in the distance function (5.18) serve two purposes, one is to non-dimensionalize the distance function and second is to give different weights to the parts of the distance function. In a data-set with a large number of data points n_{dp} , the influence of the coefficients ${}^J\bar{\mathcal{C}}_m$ is insignificant [123]. However, these coefficients play a crucial role when the data-set has a finite number of data points and if there are inconsistencies in the data-set such as presence of noise or missing points. In a one dimensional problem i.e., $sd = 1$, the solution of the data-driven reduced homogenization exists on a manifold in a $7 + 2\mathcal{N}_q$ dimensional space, which is computationally intractable to fill in completely. Instead, in data-driven simulations, sparse data-sets are used and the coefficients in the distance function should be selected carefully to achieve minimum error with a limited number of iterations.

The total number of coefficients can be reduced by grouping them according to their “classical” thermodynamic conjugacy. In the norm (5.15) $(\dot{\bar{\mu}}_m, \dot{\bar{c}}_m)$ and $(\bar{\mathbf{g}}_m, \bar{\mathbf{j}}_m)$ are the conjugate quantities. The coefficient which goes along with one of the conjugate quantities should be equal to the inverse of the other. Some entries of the diagonal matrices ${}^5\bar{\mathcal{C}}_m$ and ${}^6\bar{\mathcal{C}}_m$ can be neglected if the activity of a particular enrichment-variable $\eta_m^{(q),n+1}$ and its rate $\dot{\eta}_m^{(q),n+1}$ is smaller than that of the other enrichment variables.

The values for these coefficients can be selected by using the information, if available, from the micro-scale calculations. The coefficients which go along with the macroscopic variables appearing in the distance function, are selected to be equal to the corresponding coupling terms for the respective macroscopic variable in the macroscopic constitutive equations (5.5) and (5.6). The coefficients whose corresponding macroscopic variables do not appear in equations (5.5) and (5.6) and the ones with an insignificant value, as compared to the other coefficients, are chosen to be zero. The values for these coefficients used in the simulations are given in Table 5.4. To test the selected values of the coefficients, the data-driven simulations were conducted with the data-sets $D_{(R+S)}$ and $\tilde{D}_{(R+S)}$. The relative L_2 -error norm, between the chemical potential fields $\bar{\mu}_D^{n+1}$ and $\bar{\mu}_E^{n+1}$, is compared. Both, the data-driven problem and the enriched-continuum problem are actuated by the default boundary condition (5.29). The results are shown in Figures A.1, A.2, A.3 and A.4 in Appendices A.2 and A.3. It can be observed, that the values of the coefficients selected as proposed above (the black lines in the Figures), for most of the cases, yield the smallest values of the relative L_2 -error norms. Also,

Table 5.4: The values of the coefficients appearing in the norm (5.15) distance function (5.18).

Coefficient	Value	Units
${}^1\bar{\mathcal{C}}_m$	0	[J ⁻¹ mol m ⁻³ s ⁻¹]
${}^2\bar{\mathcal{C}}_m$	0.534	[J ⁻¹ mol m ⁻³ s]
${}^3\bar{\mathcal{C}}_m$	0.6×10^{-4}	[J ⁻¹ mol m ⁻¹ s ⁻¹]
${}^4\bar{\mathcal{C}}_m$	0	[J ⁻¹ mol m ⁻¹ s]
${}^5\bar{\mathcal{C}}_m^{(1)}$	0	[J mol ⁻¹ m ⁻³ s ⁻¹]
${}^6\bar{\mathcal{C}}_m^{(1)}$	33.46	[J mol ⁻¹ m ⁻³ s]
${}^7\bar{\mathcal{C}}_m$	1666	[J mol ⁻³ m s]
${}^8\bar{\mathcal{C}}_m$	0	[J mol ⁻³ m ³ s ⁻¹]
${}^9\bar{\mathcal{C}}_m$	1.872	[J mol ⁻³ m ³ s]

less iterations k are required for the convergence of the staggered scheme. Similar trends have been seen using different data-sets with different number of data points n_{dp} (not shown here for brevity).

5.4.5 Noisy Data-Set

Uncertainties during the data-generation steps may result in a noisy data-set, which can affect the final result and the convergence of a data-driven solver. To analyze how the proposed data-driven solver behaves in the presence of the noise in the data, a white Gaussian noise, with a signal-to-noise ratio of 30, is added to each element of the original data-sets D_m which results in a data-sets with noise $\tilde{D}_m = \{(\tilde{\mu}_m', \tilde{\mu}_m', \tilde{\mathbf{g}}_m', \tilde{\mathbf{g}}_m', \tilde{\eta}_m', \tilde{\eta}_m', \tilde{\mathbf{j}}_m', \tilde{c}_m', \tilde{c}_m')\}_{I=1}^{n_{dp}}$. For the pairs $(\tilde{\mathbf{g}}_m^{n+1}, \tilde{\mathbf{j}}_m^{n+1})$ and $(\tilde{\mu}_m^{n+1}, \tilde{\eta}_m^{(1),n+1}, \tilde{c}_m^{n+1})$ in the data-set \tilde{D}_R the noise in the data is shown in Figure 5.7.

As can be seen in Figure 5.8, the relative L_2 -error between the macroscopic chemical potential fields $\bar{\mu}_E^{n+1}$ and $\bar{\mu}_D^{n+1}$ increases with the addition of noise in the data-set. However, with the amount of added noise, this error is still reasonably small, see Figure 5.8 (a). The data-driven reduced homogenization also captures the local quantities adequately in the presence of noise as can be seen in Figure 5.8(b) and (c), where the time evolutions of the macroscopic mass flux $\bar{\mathbf{j}}_m^{n+1}$ and the macroscopic concentration \bar{c}_m^{n+1} are evaluated at the macroscopic reference point $\hat{\mathbf{x}}_m$ computed with the noisy and original data-sets. Different values of the coefficient ${}^J\bar{\mathcal{C}}_m$ in the distance function were also checked with the noisy data-set

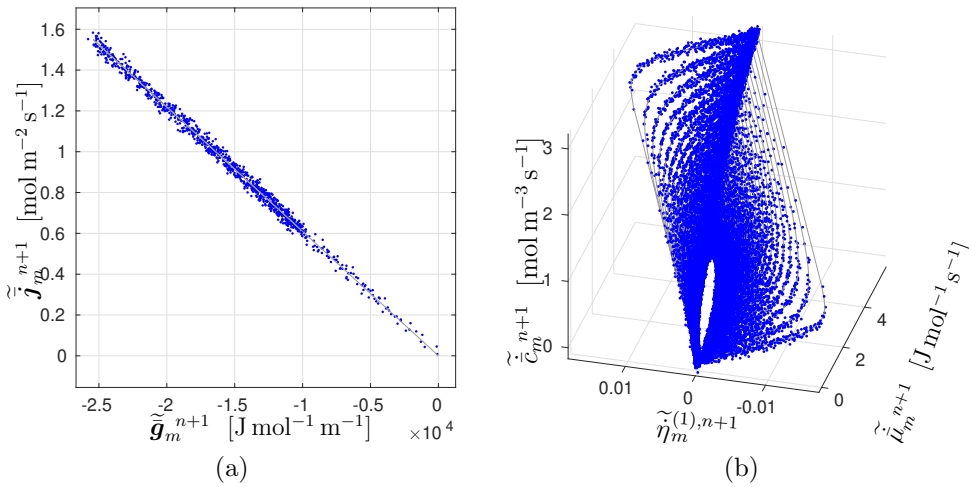


Figure 5.7: The white Gaussian noise, with the signal-to-noise ratio of 30, was added to the original data-set. From the noisy data-set \tilde{D}_R , (a) the pair $(\tilde{\mathbf{g}}_m^{n+1}, \tilde{\mathbf{j}}_m^{n+1})$ and (b) the pair $(\tilde{\mu}_m^{n+1}, \tilde{\eta}_m^{(1),n+1}, \tilde{\mathbf{c}}_m^{n+1})$ are shown with blue circular markers on top of the corresponding points in the original data-set D_R , shown with light gray lines.

$\tilde{D}_{(R+S)}$, see Figure A.3 and Figure A.4 in Appendix A.3. In that case, the relative L_2 -error increases but there are less differences in the relative L_2 -error for different values of the coefficients, which indicates that in the presence of noise the influence of the value of the coefficient is less significant. However, the coefficients ${}^J\bar{\mathbf{C}}_m$ still play an essential role in terms of the convergence towards the expected solution.

To reduce the effect of noise in a data-set and obtain smoother fields, a regression can be performed on neighboring data-points [124]. Noisy data-sets with significant outliers may create a larger problem. In that case, clustering techniques can be used, as proposed in [107]. In the presence of noise, and considering the way in which the data-set is generated, there is a chance that the first and second laws of thermodynamics are not strictly obeyed. To circumvent this problem, [125] formulated the problem in GENERIC framework to guarantee the thermodynamic consistency in data-driven computations.

5.4.6 Different Data-Sets

For convergence of the data-driven procedure towards a true solution, data-sets used in the simulations should include the states (and their histories) representative for the problem under consideration. To achieve this, a general data-set can be generated by loading the stand-alone micro-scale problem with a complete range of inputs and different loading conditions with different rates. In the following,

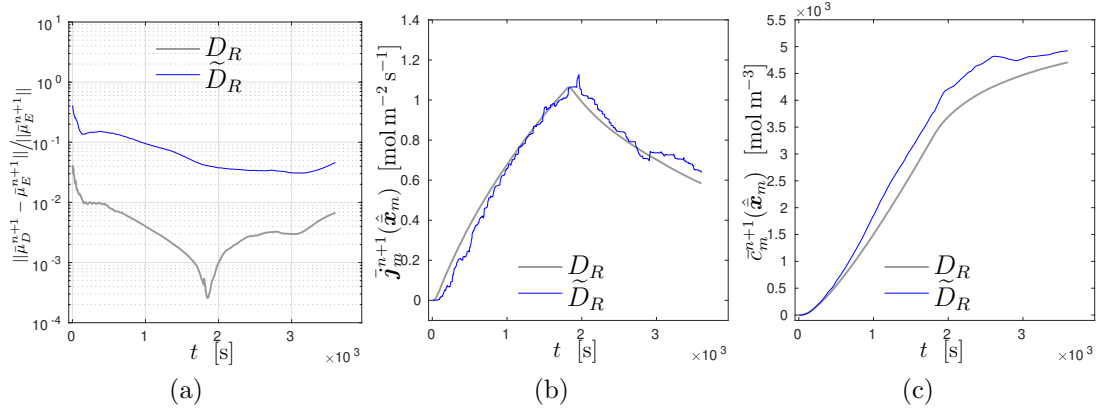


Figure 5.8: Comparison between the results for the original data-set D_R (gray) and the noisy data-set \tilde{D}_R (blue) (a) Time evolution of the relative L_2 -error for the macroscopic chemical potential $\bar{\mu}^{n+1}$, (b) macroscopic mass flux \bar{j}_m^{n+1} and (c) macroscopic concentration \bar{c}_m^{n+1} .

the performance of the proposed data-driven reduced homogenization is studied on an example where the data-set is obtained under another loading than the final data-driven problem is solved for. To this end the data-set D_S that is obtained by post-processing the enriched-continuum results with a sine loading, as given in Table 5.3, is used to solve the problem under the ramp loading (5.29). This

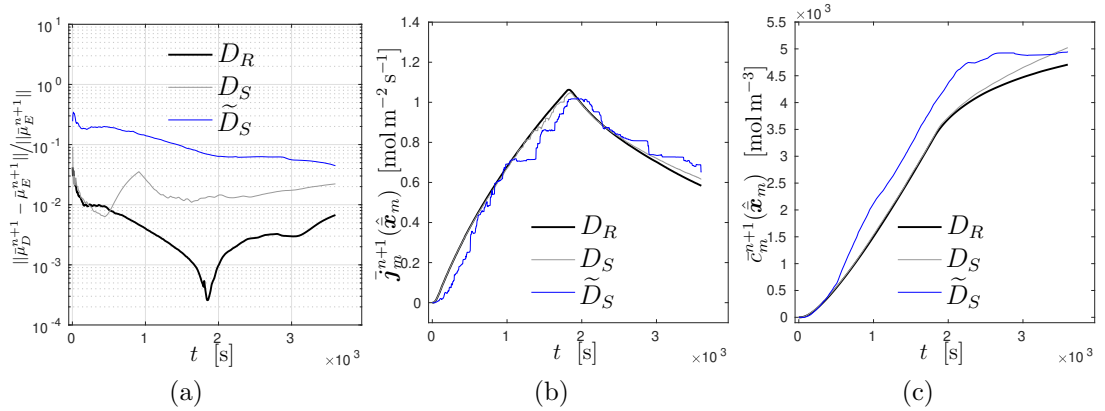


Figure 5.9: The comparison of the solutions of the data-driven initial boundary value problem with the ramp loading condition (5.29) using data-sets D_R shown in black, D_S shown in gray and \tilde{D}_S shown in blue. The time evolution of (a) the relative L_2 -error norm, (b) macroscopic mass flux \bar{j}_m^{n+1} at $\hat{\mathbf{x}}_m$ and (c) the macroscopic concentration \bar{c}_m^{n+1} at $\hat{\mathbf{x}}_m$.

provides a challenging test case, because there are (non-physical) negative values of $\bar{\mu}$ present in the data-set, which do not appear in the solution of the problem

with ramp loading. Also the time evolution of the state variables is different from the one present in the data. The results of this analysis are shown in Figure 5.9.

In this case, the data-driven algorithm is still able to select the representative state z_m^{n+1} , for which the macroscopic mass flux $\bar{\mathbf{j}}_m^{n+1}$ and the macroscopic concentration \bar{c}_m^{n+1} , evaluated at the reference macroscopic point $\hat{\mathbf{x}}_m$, are shown in Figure 5.9 (b) and (c), respectively. There is an increase in the relative L_2 -error, as shown in Figure 5.9(a), when D_S is used instead of D_R and an even larger increase in the case of the noisy data-set \tilde{D}_S . Here, \tilde{D}_S is obtained by adding white Gaussian noise, with signal-to-noise ratio of 30, to the data-set D_S . Reversely, the data-sets D_R and \tilde{D}_R cannot be used for the macroscopic initial boundary value problem under sine loading conditions at all, since the negative values are not present in these data-sets. Therefore this analysis is not presented here.

5.4.7 Convergence Analysis

The convergence of the proposed data-driven reduced homogenization method with respect to the increase in the number of data-points $n_{dp} = T/\Delta t + 1$ is analyzed here. The data-sets $D_{(RS)}$, generated by the loading condition (5.33), and $\tilde{D}_{(RS)}$, with added noise to $D_{(RS)}$, were used in this regard to solve the macroscopic problem with the ramp loading conditions (5.29). As observed in Figure 5.10, the increase in the number of data points n_{dp} in the data-set decreases the time averaged relative L_2 -error for both the noisy and noiseless data-sets, where, the noisy data-set $\tilde{D}_{(RS)}$ reveals higher errors than the noiseless data-set $D_{(RS)}$. After a certain data-set coverage, in this case $n_{dp} = 10^3$, the error first reaches a plateau and then slightly increases. This behavior suggests, that, for the problem at hand, the data-set $D_{(RS)}$ has reached its saturation at $n_{dp} = 10^3$ and that it is incomplete by construction, since it does not contain the data-points from all the possible loading conditions with different frequencies. Even with a data-set containing the reference solution, the staggered scheme, adopted for the solution of the double-minimization problem (5.19), may converge to a local minimum. For an algorithm able to seek the global minimum, see [124].

As the number of data-points n_{dp} increases, the data-driven problem becomes computationally more expensive because the lookup search through an array of distance functions in a large data-set is required at each iteration. Similar to the observation in [106], the number of iterations also increases with an increase in the number of data-points. In a large dimensional spaces such as here, computationally

efficient search schemes thus rapidly become necessary. However, these algorithmic aspects were not explored here.

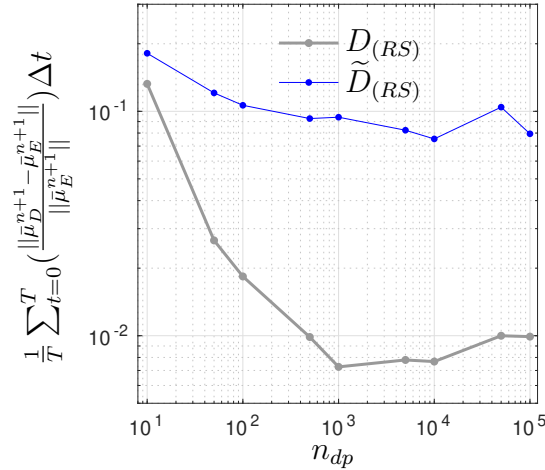


Figure 5.10: The convergence analysis of the proposed data-driven reduced homogenization upon increasing in the data-set size $D_{(RS)}$ (gray line) and $\tilde{D}_{(RS)}$ (blue line). $\bar{\mu}_D^{n+1}$ is calculated with data-driven approach and $\bar{\mu}_E^{n+1}$ is calculated with the enriched-continuum approach.

5.5 Future Perspectives

The current work establishes a firm foundation, based on data-driven mechanics, for a computationally efficient homogenization methodology for *non-linear history-dependent diffusion* behavior. The model reduction preserves a prominent two-fold advantage of cheap micro-scale calculations and provides the effective history tracking through the enrichment-variables. The challenge for the non-linear case lies in the extraction of a reduced bases set, since an eigenvalue problem is not at hand, complicating the identification of the enrichment-variables. Possible extensions of the proposed data-driven reduced homogenization methodology to the non-linear regime may be inspired by the literature. An example is the nonuniform transformation analysis (NTFA), as proposed in [126], where it is possible to decompose the time-dependent non-linear micro-scale response into a linear and a non-linear part. Then, the micro-scale is divided into several subdomains based on, for example, the material distribution of the constituents. An analytical reduced bases set is found for the non-linear part of the response in each subdomain of the micro-scale unit-cell, while the linear response can be obtained through a simple linear micro-scale calculation. It should be possible to upscale the activity coefficients of the non-linear reduced bases to the macro-scale.

The downside of NTFA is the construction of the analytical reduced bases set. In this context, a more general model reduction method, which relies on reduced bases set by the proper orthogonal decomposition (POD) [127, 128] of the primary micro-scale field, can be used instead. It entails performing micro-scale simulations and collecting the snapshots collected from time responses of the given micro-structure under various loading scenarios. The responses of these micro-scale simulations, i.e. snapshots of the primary field variable, are collected in a matrix format and the reduced bases set is obtained via a proper orthogonal decomposition. Then, the Galerkin projection onto the reduced bases set can be performed for the micro-scale discrete system of equations providing the evolution equations of the activity coefficients of the reduced bases set, which serve as internal-variables that efficiently capture the history-dependent macroscopic behavior in a data-set. A different approach using proper generalized decomposition (PGD) [129] can also be considered. It parameterizes the micro-scale solution in spatial directions, time, constituents and nonlinear behavior. The reduced bases are then constructed iteratively with an alternating direction algorithm.

The structure of the data-driven problems depends on the type of problem under consideration, the terms considered in the distance function, and the form of the evolution equations emerging as a result of the model reduction. The general expressions obtained in (5.4), (5.5) and (5.6) remain valid when the modes are obtained from a different approach, e.g. NTFA, POD, PGD. In non-linear data-driven reduced homogenization, the coefficients ${}^J\vec{\mathcal{C}}_m$ in the distance function might also be approximated by the eigenvalue analysis on the linearized micro-scale material response as presented in section 5.4.4 or some analytical averaging maybe used technique instead. If on top of the data-set also the micro-scale model is known, there is not a sufficiently close point in the data-set, then an on-the-fly micro-scale calculation can be performed to generate the desired point in the data-set.

The current framework can also be extended to other physical phenomena, where the emergent macro-scale behavior is caused by the underlying microstructure. For example, the homogenized response of locally resonant acoustic metamaterials in the linear regimes was proposed in [43] in which an enrichment-variable emerges at the macro-scale by performing model reduction at the micro-scale. The evolution equation of these enrichment-variables is a second-order ordinary differential equation. To solve this problem by data-driven formulation, a combination

of a data-driven approach for dynamics problems, as presented in [108], and history dependent materials using internal-variables, as proposed in [109], can be used. Similar extensions apply to other multi-physics phenomena, as considered in [105], where an enriched-continuum formulation for mass diffusion was coupled to mechanics. There, taking the advantage of the linear material properties and the relaxed separation of scales, a coupled eigenvalue problem was solved to obtain the enrichment-variables representing the history-dependent coupled chemo-mechanical behavior at the macro-scale. Obviously, the present work can be extended to an-isotropic macroscopic and two/three-dimensional behavior.

5.6 Conclusions

In this work, a *data-driven reduced homogenization* method is proposed for capturing the non-Fickian and history-dependent transient diffusion behavior in heterogeneous materials. It is built on the enriched-continuum formulation, developed earlier in [67] for linear material behavior exhibiting a relaxed separation of scales, and the data-driven mechanics, proposed in [106]. An enriched-continuum is a macroscopically homogenized description of a heterogeneous material in which the transient effects emerging from the micro-scale, through a model reduction, are captured by enrichment-variables at the macro-scale. For linear material properties and the relaxed separation of scales, the model reduction at the micro-scale can be performed by using the eigenvectors, obtained via the solution of an eigenvalue problem at the micro-scale, as the reduced bases. The data-driven method seeks a physical-state of the material closest to a point in the data-set, which can be obtained by experiments (in this work micro-scale simulations). Following [109], instead of using the whole history of the microscopic primary field variables, the enrichment-variables are used to efficiently keep track of the history-dependent state of the macroscopic behavior. The data-driven reduced homogenization uses a staggered solution scheme [121] to tackle the combinatorial complexity of a mixed, continuous and discrete, double-minimization problem, in which the state and the closest point in the data-set, which minimizes a global distance function, are found iteratively. The macroscopic compatibility is imposed directly and the macroscopic mass balance law is imposed through Lagrange multipliers.

Numerical examples are conducted for a macroscopically isotropic response in a one-dimensional domain, showing an adequate performance and robustness of

the proposed methodology. A two-dimensional micro-scale problem, under one-dimensional loading conditions, is considered to obtain the macroscopic quantities and to provide the input for generating the data-sets. The enriched-continuum problem is used as a reference solution, and to generate the data-sets by post-processing the primary field and its gradient, as well. The actual generation of the data-set is done using stand-alone micro-scale simulations with different loading conditions having different frequencies. The obtained point in the data-set can then be added to the already existing data-set. The large number of coefficients in the distance function make the current data-driven problem more prone to numerical errors and instabilities, so a methodology is presented to carefully select the numerical values of these coefficients, based on the information available from the micro-scale simulations. By doing so, a substantial decrease in the number of iterations and numerical error was obtained. Data-driven reduced homogenization captures the homogenized enriched-continuum response very well and also the post-processed micro-scale fields are in close agreement with each other. The proposed data-driven approach performs adequately in the presence of noise in the data-set and also in the case when a different data-set is used. Finally, by increasing the number of points in the data-set the error is reduced substantially, however at the expense of an increased number of iterations and computational effort.

Conclusions and Recommendations

This PhD thesis was aimed at the modeling of transient heat and mass diffusion problems in heterogeneous materials through the development of computationally efficient homogenization methods. When the full separation of scales is violated, a steady-state assumption at the micro-scale does not work. Instead, a transient diffusion problem should be considered at the micro-scale and consequently the homogenization methods require a computationally expensive solution of a FEM problem at the micro-scale fully coupled to the macro-scale. In this thesis, a model reduction was performed at the micro-scale in a two-scale computational homogenization setting, through which an enriched macroscopic description was obtained. It adequately captures the results obtained from conventional homogenization methods and also direct numerical simulations at significantly lower computational costs. The model reduction is performed by extracting reduced bases from an eigenvalue problem, and projecting the solution of the discrete micro-scale governing equations onto a lower-dimensional subspace. This methodology was also extended to multi-physics problems. The expressions for the macroscopic constitutive equations contain additional field variables, hence yielding a more general micromorphic description at the macro-scale. More importantly, in the developed homogenization method the micro-scale transient effects can also be represented by internal-variables appearing in the effective constitutive equations. These internal-variables are the coefficients of the reduced bases and their acquisition via the model reduction procedure at the micro-scale is the crux of the current development. The role of the internal-variables at the macro-scale bears a resemblance to those in viscoelastic material models, however, unlike in viscoelasticity, these are here not postulated but follow from the model reduction of a well-established micro-scale RVE model. At the homogeneous macro-scale, due to

the underlying microstructure, the transient diffusion reveals a history-dependent behavior with internal-variables keeping track of the history. This concept enables to extend it to nonlinear and more complicated material behavior, for example, by using the data-driven homogenization approach.

In the following, the main concepts and results obtained in this dissertation are summarized and followed by recommendations for future research.

6.1 Summary and Results

Model reduction at the micro-scale

Computational homogenization splits the heterogeneous problem into a micro-scale and a macro-scale. Both scales are solved by finite element methods, because of the transient nature of the problem; usually, the micro-scale is computationally more expensive. Therefore, a model reduction can be performed at the micro-scale to reduce computational cost. The reduced information is then used in the homogenization procedure to obtain the macroscopic constitutive equations. The homogenization in transient regimes entails the equivalence of virtual powers (extended Hill-Mandel conditions) between the micro- and macro-scales. The proposed reduced order homogenization methods rely on the assumption of relaxed scale separation regime; i.e., short diffusion time in the matrix and long diffusion times in the inclusions and linear material behavior. In relaxed separation of scales, the micro-scale primary fields are always steady-state in the matrix which facilitates the use of a model reduction technique based on component mode synthesis. The micro-scale primary field was divided into its steady-state and transient parts and the global reduced bases was found using the Schur-complement and eigenvalue problem, respectively.

A few eigenvectors were selected for projecting the micro-scale discretized governing equations onto a lower-dimensional subspace. For this purpose, a criterion based on the coupling terms is used and then verified by checking the convergence in the error for the micro-scale field as well as the energy consistency. The activity coefficients of the reduced bases, at the macro-scale, behave like internal-variables and in this work are referred to as enrichment-variables. The macroscopic balance laws, constitutive equations and the evolution equations for the enrichment-variables are combined together to form an enriched-continuum description. The expensive solution of the micro-scale problem is, hence, replaced in the “on-line”

stage with the solution of ordinary differential equations obtained through model reduction in the “off-line” stage.

The developed reduced order homogenization procedure captures the micro-scale fields accurately. The macroscopic quantities, which are averaged properly, do not show substantial deviation compared to the quantities computed with conventional transient homogenization. Size effects and the transient (inertial) behavior are also captured. However, if the size of the micro-scale RVE, material properties, or loading conditions change such that the relaxed separation of scales assumption gets violated, then results obtained with the proposed reduced order homogenization method deviate from the true (reference) diffusion behavior. The developed procedure is equally well applicable to both heat and mass diffusion problems.

For the coupled mass diffusion-mechanics problems, at the micro-scale, the Legendre transformation is used to obtain the constitutive equations and balance laws in terms of the chemical potential field and strain field instead of the more conventional concentration field and strain formulation. This allows to use, comparatively simpler, C^0 finite element formulation. Next, the micro-scale fields were decomposed into a steady-state and transient parts and, likewise, the global reduced bases were found by the Schur-complement and the solution of a coupled eigenvalue problem. The mode selection was performed according to the coupling terms. For the cathode-electrolyte system of a lithium-ion battery material the transient effects, size-dependent macroscopic behavior, and the coupling effects are captured very accurately. In the case of coupled micro-scale problems, the computational time gains are substantial, since, the solution of the expensive coupled chemo-mechanics balance laws is replaced by the solution of ordinary differential equations.

Macro-scale Enriched-Continuum

Depending on the location of the evaluation of the enrichment-variables, either at the nodes or the quadrature points of the finite element mesh, different numerical methods can be used to solve the enriched-continuum at the macro-scale. When enrichment-variables are evaluated at the quadrature points, these are treated as internal-variables, hence, giving rise to an internal-variable solution method. The placement of the enrichment-variables at the nodes yields a multi-field solution problem. The internal-variable method has the advantage that it allows for the use of higher-order time integration schemes for capturing the micro-scale transient effect more accurately. For the number of enrichment-variables used in the current

work, the multi-field method is computationally more efficient than the internal-variable method, because it does not involve the calculation of the internal flux vector and its assembly at each time step. As compared to conventional transient homogenization and direct numerical simulations, the enriched-continuum based homogenization has excellent accuracy and is $\mathcal{O}(10^3)$ faster for the examples tested here.

Data-driven mechanics can be used to homogenize the diffusion phenomena in heterogeneous materials and poses a great potential to be extended to the nonlinear regime. Transient effects at the micro-scale, represented by the enrichment-variables at the macro-scale, make the diffusion phenomena at an enriched-continuum level history-dependent. The enrichment-variables provide an efficient way to keep track of history by eliminating the need to know the microscopic fields at all time instances. Data-driven mechanics relies entirely on the data rather than a model. The data-set can be efficiently generated by the reduced-order homogenization presented in this work. Then, the data-driven reduced homogenization involves minimizing the distance between the balanced state of the material and a data point in the data-set. It poses a double minimization problem which is solved by a staggered scheme. Different data-sets are generated by different loading conditions at the micro-scale RVE. The values of the coefficients in the distance function play an essential role in the rate of convergence and accuracy of the solution, so, these are selected carefully by looking into the available information from the micro-scale. The data-driven reduced homogenization scheme is capable of capturing the enriched-continuum response accurately. However, with noisy and different data-sets the error increases. Increasing the number of points in the data-set increases the accuracy but on the downside, the computational cost to search a close point in the data-set increases.

To conclude, it has been demonstrated that it is possible to capture the transient diffusion phenomena in heterogeneous materials efficiently by using numerical techniques such as computational homogenization combined with model reduction. The homogenized macro-scale is enriched by the coefficients of the micro-scale reduced bases. Different spatial and temporal discretizations can be chosen for the solution of the enriched-continuum. The extension towards multi-physics problems is also at reach. However, the developed methodology is limited to the relaxed scale separation regimes and the material linearity. Ideas can be borrowed from the field of data-science to obtain efficient homogenization methods for the nonlinear regimes. Next, recommendations for the future research are made, different

than those already mentioned in the chapters.

6.2 Recommendations for Future Research

Realistic Micro-Scale Morphologies

In this work, simple morphologies were used to validate the developed homogenization method. In reality, materials reveal more complex microstructural features, e.g. they can contain poly-dispersed, randomly distributed, non-periodic inclusions in a matrix, or randomly shaped grains with separating grain boundaries, or more than two constituent materials, etc. Therefore, RVE containing a single or mono-dispersed inclusions, as used in this work, is a crude approximation of real materials. However, simulation of realistic microstructures with the proposed reduced homogenization can lead to several complications. The micro-scale RVE may not be very well defined due to the random and non-periodic material distribution. In that case, the periodic boundary conditions might not be a proper choice, while the fully prescribed or flux boundary conditions would be leading to, respectively, an over or underestimation of the actual response.

To address this concern, ensemble averaging of the macroscopic quantities can be utilized [130, 131]. It entails calculating macroscopic quantities and averaging their values for different microstructural realizations. It is, however, unclear which eigenmodes should be used to build the macroscopic quantities in the case of ensemble averaging. Similar discussion holds for materials with defects, e.g. when cracks and voids are present at the micro-scale. It can also be tested if the proposed reduced homogenization is capable of dealing with a macroscopically anisotropic medium. The macroscopic anisotropy can arise either as a result of anisotropy present in one or multiple micro-scale constituents or a directional distribution of isotropic constituents.

Separation of Scales

This work is primarily based on the relaxed separation of scales assumption, which states that the characteristic diffusion time of the matrix is much smaller than the characteristic diffusion time of the inclusion. It does extends over the material properties for which only the steady-state homogenization is applicable. However, it is still limited to the heterogeneous materials obeying relaxed separation of scales. It would be interesting to analyze how the proposed framework can be extended, at least to the vicinity where the relaxed separation of scales is not obeyed

very strictly. If the characteristic diffusion time of the matrix is not small enough, as compared to the characteristic diffusion of the inclusion and the characteristic loading time, there may be transient effects present in the matrix. One consequence of that can be that the application of boundary conditions by prescribing a point in the microscopic domain to be equal to the macroscopic field, to satisfy the extended Hill-Mandel conditions, yields a stiffer response. In this regard, Lagrange multipliers can be used to enforce the boundary conditions in a weak sense at the micro-scale [132, 133]. Also, the size of the reduced basis might increase due to the presence of transient effects in the matrix. The reduced bases selection criterion which relies on the coupling terms might not be sufficient, so the alternative (but computationally expensive) energy consistency criterion can be used in an off-line stage to build the reduced basis set. In the macroscopic model, some terms which are negligible due the relaxed separation of scales will have a significant contribution to the homogenized behavior at the macro-scale. Their effect on the enriched-continuum description will need to be analyzed properly.

Nonlinear Physical Properties

A general transient nonlinear system can be written as $\dot{u} = \mathbf{L}(u)u$, where u is the primary field variable and $\mathbf{L}(u)$ is the nonlinear transformation operator which depends on the primary field variable u . The nonlinearity is assumed to be weak when it can be sufficiently represented by a linear and a nonlinear operator $\dot{u} = \mathbf{L}u + \epsilon\mathbf{N}(u)$ where ϵ is a small number and $\mathbf{N}(u)$ is a nonlinear operator. Strong nonlinearity appears when the split is of the form $\dot{u} = \mathbf{L}u + \mathbf{N}(u)$. When the nonlinearity is weak, based on Taylor's expansion, the eigenvectors can be expanded and approximated around the solution of the linear eigenvalue problem [102]. The derivatives in the higher-order expansion terms can be calculated by the finite difference method or by solving the sensitivity of the linearized eigenvalue problem with respect to the activity coefficient (enrichment-variable). The eigenvector expansion technique is inadequate if the nonlinearity is strong or, for the coupled diffusion-mechanics problem, if inelastic/large deformations are present.

In this case, more general model reduction methods such as a-posteriori proper orthogonal decomposition (POD) or a-priori proper generalized decomposition (PGD) [10] can be used. POD takes the discrete solution vectors, so-called snapshots, of a parameterized problem in a correlation matrix and determines the reduced bases by solving an singular value decomposition problem. The reduced system and the internal-variables are obtained by Galerkin projection. In PGD,

first, the problem is parameterized in spatial directions, time, constituents, and nonlinearity, then, the problem-specific reduced bases are constructed iteratively with an alternating directions algorithm.

In nonlinear problems, at the micro-scale the discrete internal flux vector, which is used to evaluate the macroscopic quantities, still depends on all degrees of freedoms preserving the full computational complexity. To this end, hyper-reduction techniques such as discrete empirical interpolation method (DEIM) along with POD [134] or modal derivatives [102] can be used to efficiently reduce the complexity of the problem.

When different model reduction techniques are used, different number of internal-variables will appear at the macro-scale. For instance, Taylor's expansion method will introduce one extra type of internal-variables, at the macro-scale, which represent the activity coefficient of the eigenvector derivatives. PGD will introduce internal-variables which are equal to the number of parameters for the micro-scale problem. POD will introduce internal variables which are the activity coefficients of the global shape functions obtained from SVD analysis. With different model reduction methodologies, adopted at the micro-scale, the enriched-continuum representation will be different and will require different solution techniques at the macro-scale.

Source Term and Multi-Physics

In diffusion problems, the source term describes the addition of species or heat generation due to e.g. a chemical reaction taking place inside the material. It is possible to perform model reduction, similar to the one proposed in this work when the source term belongs to the inclusions only, and instantaneous diffusion in the matrix still holds. Otherwise, DEIM can be used to approximate the source term contribution in the micro-scale internal flux vector.

The multi-physics problems tackled in this work consisted of only two fields. For instance, lithium-ion batteries have a nonlinear and complex multi-physics nature in which electro-magneto-chemo-thermo-mechanical fields are coupled. It would be interesting to identify the fields that violate the steady-state assumption at the micro-scale during charging/discharging cycles and how the model reduction can be performed for such a complex system.

Microstructural Optimization

Microstructures can be optimized using topology optimization [135], in which microstructures can be reverse engineered for specific values of the macroscopic material properties [136]. It can be extended to a two-scale setting for time dependent problems as well [137]. Multi-scale topology optimization entails definition of macroscopic objective functions in terms of micro-scale design variables and constraints on the design space [138]. In continuum mechanics applications, optimization is typically performed by a gradient based method, which requires sensitivities of the objective function and the constraints with respect to the design variables. It becomes an expensive task in a two-scale and temporal settings [133, 139]. The proposed reduced order homogenization can provide an efficient way to perform optimization in these cases.

Modern day material design for engineering applications requires robust and fast analysis methods. This is a multi-disciplinary subject and involves in-depth understanding of mechanics, numerical methods and computer science. At the moment, when Moore's law has reached its physical limits, the development of efficient numerical methods for computer simulations bears an utmost importance. This thesis was a small step towards that goal.

Appendix

A.1 Coupling Terms for Mass Diffusion Problem

The derivation of the coefficients appearing in the expressions for the macroscopic mass flux $\bar{\mathbf{j}}$ in equation (3.11) and the macroscopic rate of change of concentration field $\dot{\bar{c}}$ in equation (3.12) briefly summarized here, for the detailed derivation in the context of transient heat diffusion, see [67]. The mass balance equation at the micro-scale (3.8), after using the constitutive forms for the microscopic mass flux \mathbf{j} and concentration c and applying the necessary boundary conditions, which satisfy the extended Hill-Mandel energy criteria, can be written in its semi-discrete form as,

$$\underline{\underline{K}}^* \underline{\underline{\mu}} + \underline{\underline{M}}^* \dot{\underline{\underline{\mu}}} = -\underline{\underline{j}}_n, \quad (\text{A.1})$$

where $\underline{\underline{K}}^*$ and $\underline{\underline{M}}^*$ are the so-called stiffness and mass matrices respectively, $\underline{\underline{\mu}}$ and $\underline{\underline{j}}_n$ are the columns of microscopic chemical potential field and the input mass flux at the micro-scale. This microscopic system of equations is then partitioned into prescribed ‘ p ’ and free ‘ f ’ parts. The reduced basis is determined using the static condensation and the solution of the corresponding eigenvalue problem. The discrete system of equations (A.1), when projected onto the steady state and transient basis, can be written as,

$$\underline{\underline{K}}_{ss} \underline{\underline{\mu}}^p + \underline{\underline{M}}_{ss} \dot{\underline{\underline{\mu}}}^p + \underline{\underline{\varrho}} \dot{\underline{\underline{\eta}}} = -\underline{\underline{j}}_n^p, \quad (\text{A.2})$$

$$\underline{\underline{\alpha}} \underline{\underline{\eta}} + \dot{\underline{\underline{\eta}}} + \frac{1}{V} \underline{\underline{\varrho}}^T \dot{\underline{\underline{\mu}}}^p = \underline{\underline{0}}, \quad (\text{A.3})$$

where,

$$\underline{\underline{K}}_{ss} = \underline{\underline{K}}^{*pp} + \underline{\underline{K}}^{*pf} \underline{\underline{S}}, \quad (\text{A.4})$$

$$\underline{\underline{M}}_{ss} = \underline{\underline{M}}^{*pp} + 2\underline{\underline{M}}^{*pf} \underline{\underline{S}} + \underline{\underline{S}}^T \underline{\underline{M}}^{*ff} \underline{\underline{S}}, \quad (\text{A.5})$$

$$\underline{\varrho} = \underline{S}^T \underline{M}^{*ff} \underline{\Phi} + \underline{M}^{*pf} \underline{\Phi}. \quad (\text{A.6})$$

$\underline{S} = (\underline{K}^{*ff})^{-1} \underline{K}^{*fp}$ is the Schur complement of the stiffness matrix and $\underline{\Phi}^*$ are the enrichment functions obtained by solving the eigenvalue problem

$$(\underline{K}^{*ff} - \underline{\alpha} \underline{M}^{*ff}) \underline{\Phi} = \underline{0}, \quad (\text{A.7})$$

with $\underline{\alpha}$ is the diagonal matrix of the eigenvalues arranged in the ascending order. The model reduction is performed by selecting a limited set of enrichment functions $\underline{\Phi}^*$ from a full set of eigenvectors $\underline{\Phi}$. The expressions for the macroscopic mass flux and concentration rate term in equation (3.9) can be converted to boundary integrals by using the divergence theorem, which in their discrete form can be written as

$$\bar{\mathbf{j}} = \frac{1}{V} (\Delta \underline{\mathbf{x}}^p)^T \underline{j}_n^p, \quad \text{and} \quad \dot{\bar{c}} = -\frac{1}{V} (\underline{I}^p)^T \underline{j}_n^p, \quad (\text{A.8})$$

where $\Delta \underline{\mathbf{x}}^p = (\underline{\mathbf{x}}^p - \bar{\mathbf{x}})$ and \underline{I}^p is the column of ones of length $(p \times 1)$. By substituting the expression for \underline{j}_n^p from (A.2) into (A.8) and rearranging the terms, the macroscopic constitutive form in equations (3.11) and (3.12) are obtained. The coefficients in these equations are given as follows,

$$\begin{aligned} \bar{\mathbf{a}} &= \frac{1}{V} (\Delta \underline{\mathbf{x}}^p)^T \underline{\varrho}, && \text{(Column of } \mathcal{N}_q \text{ 1st-order tensors)} \\ \bar{\mathbf{a}}^* &= V \underline{\mathbf{a}} \\ \bar{\mathbf{B}} &= \frac{1}{V} [(\Delta \underline{\mathbf{x}}^p)^T \underline{K}_{ss}] \otimes \Delta \underline{\mathbf{x}}^p, && \text{(2nd-order tensor)} \\ \bar{\mathbf{c}} &= \frac{1}{V} (\Delta \underline{\mathbf{x}}^p)^T [\underline{M}_{ss} \underline{I}^p], && \text{(1st-order tensor)} \\ \bar{\mathbf{C}} &= \frac{1}{V} [(\Delta \underline{\mathbf{x}}^p)^T \underline{M}_{ss}] \otimes \Delta \underline{\mathbf{x}}^p. && \text{(2nd-order tensor)} \\ \bar{\underline{d}} &= \frac{1}{V} (\underline{I}^p)^T \underline{\varrho}, && \text{(Column of } \mathcal{N}_q \text{ scalars)} \\ \bar{\underline{d}}^* &= V \bar{\underline{d}} \\ \bar{\mathbf{e}} &= \frac{1}{V} (\underline{I}^p)^T [(\Delta \underline{\mathbf{x}}^p)^T \underline{K}_{ss}], && \text{(1st-order tensor)} \\ \bar{f} &= \frac{1}{V} (\underline{I}^p)^T [\underline{M}_{ss} \underline{I}^p], && \text{(Scalar)} \\ \bar{\mathbf{f}} &= \frac{1}{V} (\underline{I}^p)^T [(\Delta \underline{\mathbf{x}}^p)^T \underline{M}_{ss}]. && \text{(1st-order tensor)} \end{aligned} \quad (\text{A.9})$$

where V is the volume of the microscopic domain Ω_{\square} as shown in Figure 3.2(b).

A.2 Relative L_2 -Error for Different Coefficient Values Using Data-Set $D_{(R+S)}$

The performance of the data-driven reduced homogenization is checked with different values of coefficients ${}^J\bar{\mathcal{C}}_m$, appearing in the definition of the norm (5.15) for the distance function (5.18), with the data-set $D_{(R+S)}$. The results are presented in Figure A.1 and A.2.

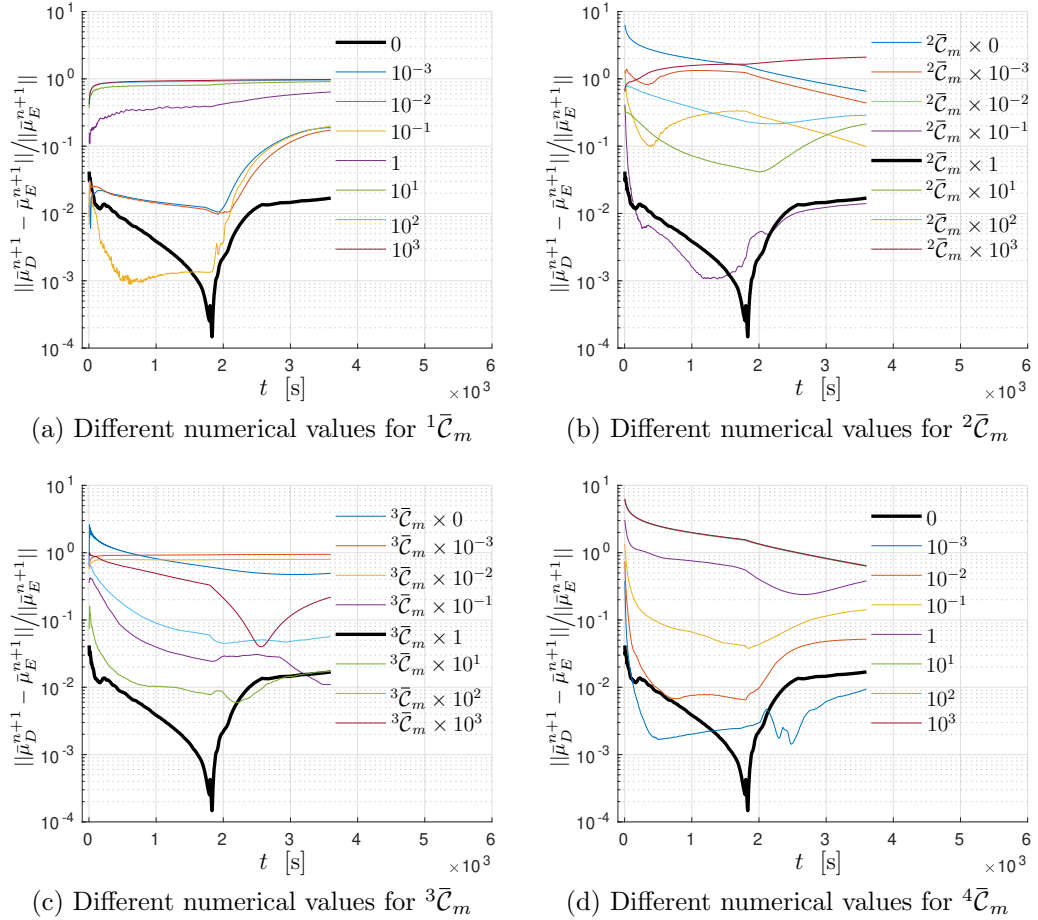


Figure A.1: For the coefficients ${}^1\bar{\mathcal{C}}_m$, ${}^2\bar{\mathcal{C}}_m$, ${}^3\bar{\mathcal{C}}_m$ and ${}^4\bar{\mathcal{C}}_m$ the time evolution of the relative L_2 -error norm, calculated as $\|\bar{\mu}_D^{n+1} - \bar{\mu}_E^{n+1}\| / \|\bar{\mu}_E^{n+1}\|$, where $\bar{\mu}_D^{n+1}$ is the chemical potential field obtained by the data-driven reduced homogenization (proposed) using the data-set $D_{(R+S)}^{n+1}$ and $\bar{\mu}_E^{n+1}$ is the chemical potential field obtained by the enriched-continuum formulation (reference) under boundary conditions (5.29). The default values and the units of the coefficients are given in Table 5.4. The relative L_2 -error computed with the proposed default value for the coefficients ${}^J\bar{\mathcal{C}}_m$ is marked with the black lines.

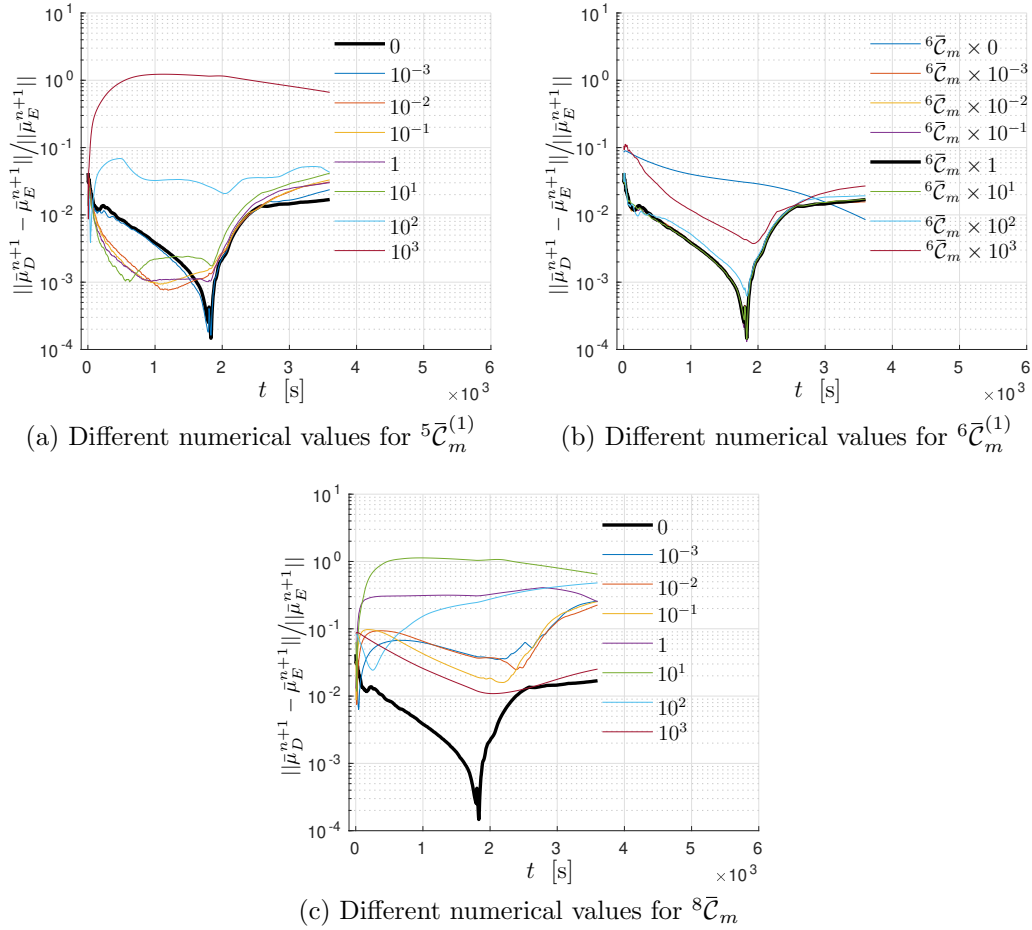


Figure A.2: For the coefficients ${}^5\bar{\mathcal{C}}_m^{(1)}$, ${}^6\bar{\mathcal{C}}_m^{(1)}$ and ${}^8\bar{\mathcal{C}}_m$ the time evolution of the relative L_2 -error norm, calculated as $\|\bar{\mu}_D^{n+1} - \bar{\mu}_E^{n+1}\|/\|\bar{\mu}_E^{n+1}\|$, where $\bar{\mu}_D^{n+1}$ is the chemical potential field obtained by the data-driven reduced homogenization (proposed) using the data-set $D_{(R+S)}^{n+1}$ and $\bar{\mu}_E^{n+1}$ is the chemical potential field obtained by the enriched-continuum formulation (reference) under boundary conditions (5.29). The default values and the units of the coefficients are given in Table 5.4. The relative L_2 -error computed with the proposed default value for the coefficients ${}^J\bar{\mathcal{C}}_m$ is marked with the black lines.

A.3 Relative L_2 -Error for Different Coefficient Values Using Data-Set with Noise $\tilde{D}_{(R+S)}$

The performance of the data-driven reduced homogenization is checked with different values of coefficients ${}^J\bar{\mathcal{C}}_m$, appearing in the definition of the norm (5.15) for the distance function (5.18), with a noisy data-set $\tilde{D}_{(R+S)}$, the result is shown in Figure A.3 and A.4. An increase in the relative L_2 -error is observed as compared to the data without noise $D_{(R+S)}$. With the introduction of the noise, the error is

comparatively less influenced by the numerical values of the coefficients and more by the noisiness of the data.

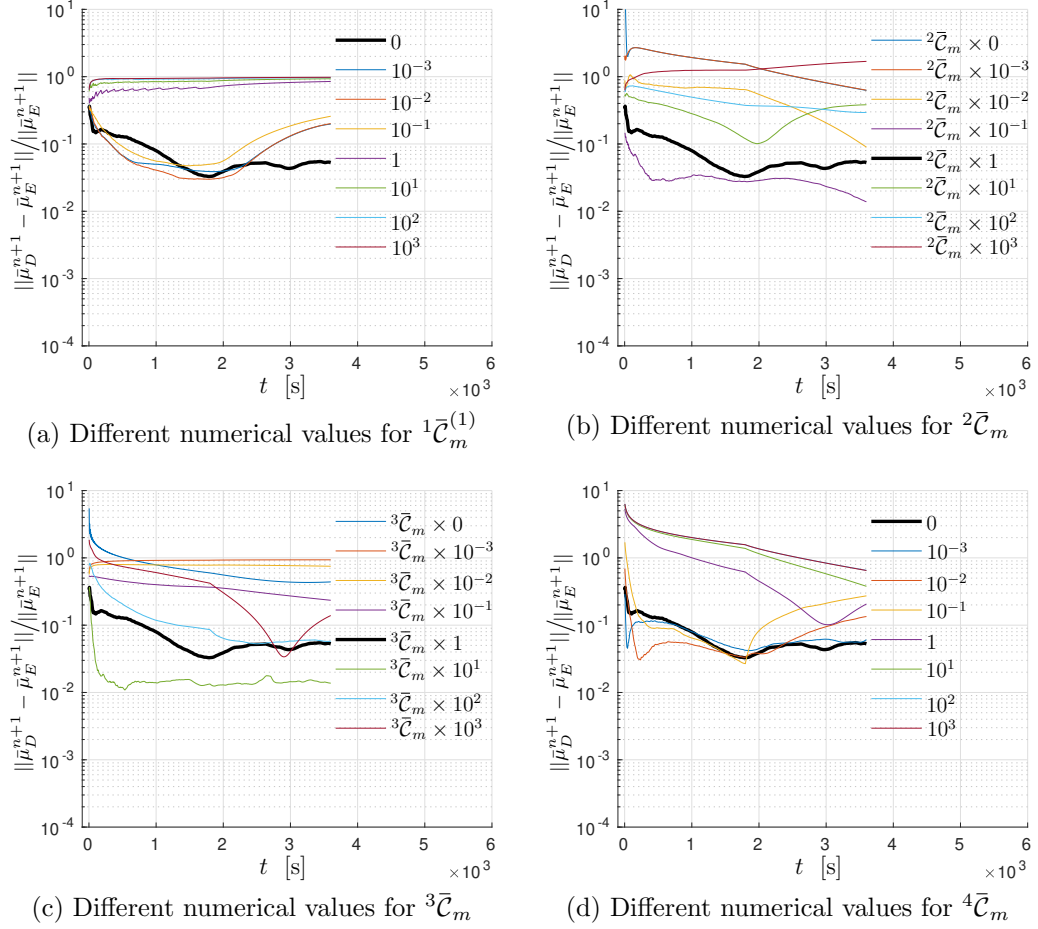


Figure A.3: For the coefficients ${}^1\bar{\mathcal{C}}_m$, ${}^2\bar{\mathcal{C}}_m$, ${}^3\bar{\mathcal{C}}_m$ and ${}^4\bar{\mathcal{C}}_m$ the time evolution of the relative L_2 -error norm, calculated as $\|\bar{\mu}_D^{n+1} - \bar{\mu}_E^{n+1}\| / \|\bar{\mu}_E^{n+1}\|$, where $\bar{\mu}_D^{n+1}$ is the chemical potential field obtained by the data-driven reduced homogenization (proposed) using the data-set $\tilde{D}_{(R+S)}^{n+1}$ and $\bar{\mu}_E^{n+1}$ is the chemical potential field obtained by the enriched-continuum formulation (reference) under boundary conditions (5.29). The default values and the units of the coefficients are given in Table 5.4. The relative L_2 -error computed with the proposed default value for the coefficients ${}^J\bar{\mathcal{C}}_m$ is marked with the black lines.

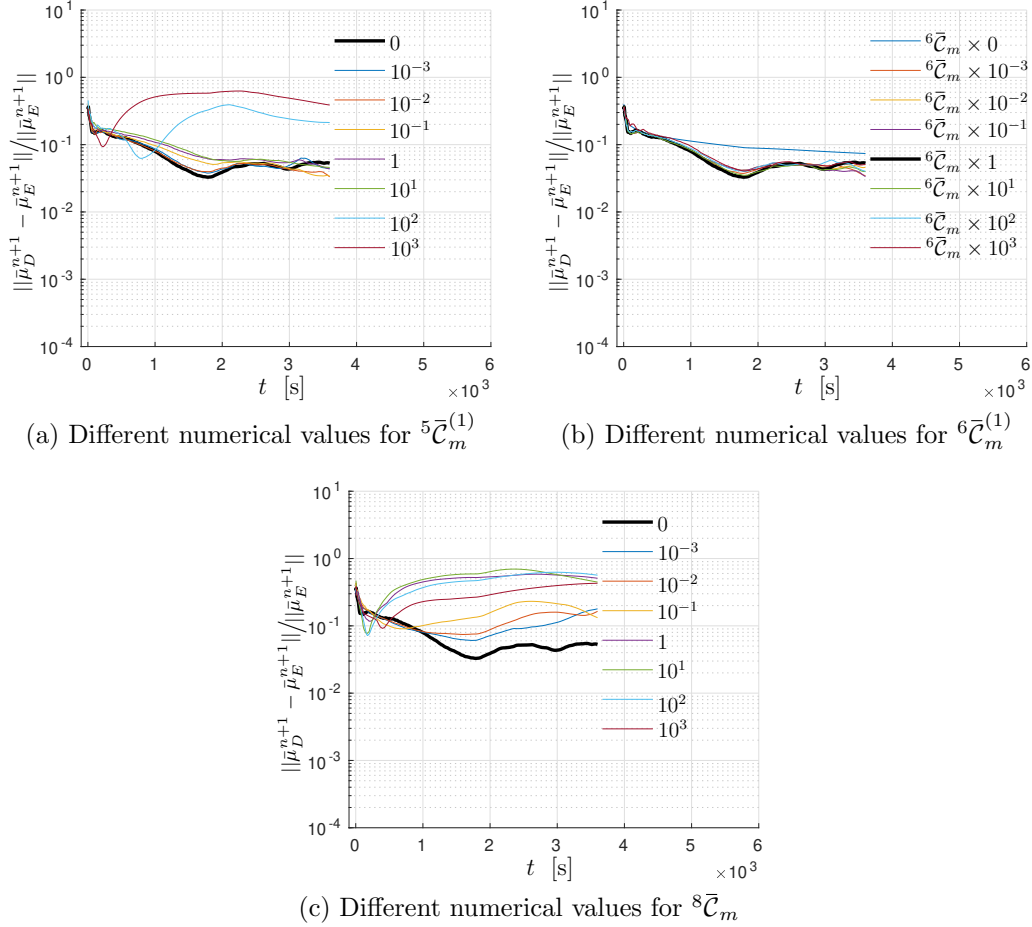


Figure A.4: For the coefficients ${}^5\bar{\mathcal{C}}_m^{(1)}$, ${}^6\bar{\mathcal{C}}_m^{(1)}$ and ${}^8\bar{\mathcal{C}}_m$ the time evolution of the relative L_2 -error norm, calculated as $\|\bar{\mu}_D^{n+1} - \bar{\mu}_E^{n+1}\| / \|\bar{\mu}_E^{n+1}\|$, where $\bar{\mu}_D^{n+1}$ is the chemical potential field obtained by the data-driven reduced homogenization (proposed) using the data-set $\tilde{D}_{(R+S)}^{n+1}$ and $\bar{\mu}_E^{n+1}$ is the chemical potential field obtained by the enriched-continuum formulation (reference) under boundary conditions (5.29). The default values and the units of the coefficients are given in Table 5.4. The relative L_2 -error computed with the proposed default value for the coefficients ${}^J\bar{\mathcal{C}}_m$ is marked with the black lines.

Bibliography

- [1] X. C. Tong. *Advanced materials for thermal management of electronic packaging*, volume 30. Springer Science & Business Media, 2011.
- [2] John L. J. Metal injection molding of heat sinks. URL <https://tinyurl.com/yb953xob>.
- [3] tanmay. Li-ion battery for mobile market industry analysis 2020 overview by top players : Sony, boston-power, sunwoda electronics, tianjin lishen battery. URL <https://tinyurl.com/y8wtn6eg>.
- [4] D. Grazioli, M. Magri, and A. Salvadori. Computational modeling of Li-ion batteries. *Computational Mechanics*, 58(6):889–909, 2016.
- [5] R. W. Balluffi, S. Allen, and W. C. Carter. *Kinetics of materials*. John Wiley & Sons, 2005.
- [6] J. M. Bergheau and R. Fortunier. *Finite element simulation of heat transfer*. John Wiley & Sons, 2013.
- [7] V. G. Kouznetsova, M. G. D. Geers, and W. A. M. Brekelmans. Multi-scale constitutive modeling of heterogeneous materials with a gradient-enhanced computational homogenization scheme. *International Journal for Numerical Methods in Engineering*, 54(8):1235–1260, 2002.
- [8] F. Larsson, K. Runesson, and F. Su. Variationally consistent computational homogenization of transient heat flow. *International Journal for Numerical Methods in Engineering*, 81(13):1659–1686, 2010.
- [9] G. R. Ramos, T. dos Santos, and R. Rossi. An extension of the Hill–Mandel principle for transient heat conduction in heterogeneous media with heat generation incorporating finite RVE thermal inertia effects. *International Journal for Numerical Methods in Engineering*, 111(6):553–580, 2017.
- [10] F. Chinesta and E. Cueto. *PGD-based Modeling of Materials, Structures and Processes*. Springer, 2014.

- [11] M. J. Jackson. *Micro-and Nanomanufacturing*. Springer, 2007.
- [12] J. Lau. *Thermal stress and strain in microelectronics packaging*. Springer Science & Business Media, 2012.
- [13] A. D. Kraus and A. Bar-Cohen. Thermal analysis and control of electronic equipment. *Washington, DC, Hemisphere Publishing Corp.*, 1983.
- [14] M. Kadic, T. Bückmann, R. Schittny, and M. Wegener. Metamaterials beyond electromagnetism. *Reports on Progress in Physics*, 76(12):126501, 2013.
- [15] C. T. Roman. Investigation of thermal management and metamaterials. Technical report, Airforce Institute of Technology Wright-Patterson AFB Ohio School of Engineering and Management., 2010.
- [16] Z. Chen, B. Guo, Y. Yang, and C. Cheng. Metamaterials-based enhanced energy harvesting: A review. *Physica B: Condensed Matter*, 438:1–8, 2014.
- [17] P. R. Bandaru, K. P. Vemuri, FM Canbazoglu, and RS Kapadia. Layered thermal metamaterials for the directing and harvesting of conductive heat. *AIP Advances*, 5(5):053403, 2015.
- [18] S. Narayana and Y. Sato. Heat flux manipulation with engineered thermal materials. *Physical Review Letters*, 108(21):214303, 2012.
- [19] S. Guenneau and C. Amra. Anisotropic conductivity rotates heat fluxes in transient regimes. *Optics Express*, 21(5):6578–6583, 2013.
- [20] H. Xu, X. Shi, F. Gao, H. Sun, and B. Zhang. Ultrathin three-dimensional thermal cloak. *Physical Review Letters*, 112(5):054301, 2014.
- [21] T. Z. Yang, Y. Su, W. Xu, and X. D. Yang. Transient thermal camouflage and heat signature control. *Applied Physics Letters*, 109(12):121905, 2016.
- [22] T. Yang, W. Xu, L. Huang, X. Yang, and F. Chen. Experimental realization of a carpet cloak for temperature field and heat flux. *arXiv preprint arXiv:1403.4799*, 2014.
- [23] S. Torquato. *Random heterogeneous materials: microstructure and macroscopic properties*, volume 16. Springer Science & Business Media, 2013.
- [24] G. Pavliotis and A. Stuart. *Multiscale methods: averaging and homogenization*. Springer Science & Business Media, 2008.

- [25] S. Nemat-Nasser and M. Hori. *Micromechanics: overall properties of heterogeneous materials*, volume 37. Elsevier, 2013.
- [26] T. I. Zohdi and P. Wriggers. *An introduction to computational micromechanics*. Springer Science & Business Media, 2008.
- [27] J. Fish. *Practical multiscale modeling*. John Wiley & Sons, 2013.
- [28] J. L. Auriault, C. Boutin, and C. Geindreau. *Homogenization of coupled phenomena in heterogeneous media*, volume 149. John Wiley & Sons, 2010.
- [29] C. Miehe, J. Schröder, and J. Schotte. Computational homogenization analysis in finite plasticity simulation of texture development in polycrystalline materials. *Computer Methods in Applied Mechanics and Engineering*, 171(3-4):387–418, 1999.
- [30] S. M. Giusti, A. A. Novotny, R. A. Feijóo, and E. A. de Souza Neto. Variational formulation for multi-scale constitutive models in steady-state heat conduction problem on rigid solids. In *19th International Congress of Mechanical Engineering, COBEM Proceedings, Brasilia, Brasil*, 2007.
- [31] J. L. Auriault. Effective macroscopic description for heat conduction in periodic composites. *International Journal of Heat and Mass Transfer*, 26(6):861–869, 1983.
- [32] İ. Özdemir, W. A. M. Brekelmans, and M. G. D. Geers. Computational homogenization for heat conduction in heterogeneous solids. *International Journal for Numerical Methods in Engineering*, 73(2):185–204, 2008.
- [33] İ. Özdemir, W. A. M. Brekelmans, and M. G. D. Geers. Fe2 computational homogenization for the thermo-mechanical analysis of heterogeneous solids. *Computer Methods in Applied Mechanics and Engineering*, 198(3-4):602–613, 2008.
- [34] İ. Temizer and P. Wriggers. Homogenization in finite thermoelasticity. *Journal of the Mechanics and Physics of Solids*, 59(2):344–372, 2011.
- [35] İ. Temizer. On the asymptotic expansion treatment of two-scale finite thermoelasticity. *International Journal of Engineering Science*, 53:74–84, 2012.

- [36] K. Runesson, F. Su, and F. Larsson. Assessment of homogenization errors in transient problems. In *Recent Developments and Innovative Applications in Computational Mechanics*, pages 207–214. Springer, 2011.
- [37] S. Kaessmair and P. Steinmann. On the computational homogenization of transient diffusion problems. *PAMM*, 16(1):529–530, 2016.
- [38] K. Pham, V. G. Kouznetsova, and M. G. D. Geers. Transient computational homogenization for heterogeneous materials under dynamic excitation. *Journal of the Mechanics and Physics of Solids*, 61(11):2125–2146, 2013.
- [39] P. J. Blanco, P. J. Sánchez, E. A. de Souza Neto, and R. A. Feijóo. Variational foundations and generalized unified theory of rve-based multiscale models. *Archives of Computational Methods in Engineering*, 23(2):191–253, 2016.
- [40] E. A. de Souza Neto, P. J. Blanco, P. J. Sánchez, and R. A. Feijóo. An RVE-based multiscale theory of solids with micro-scale inertia and body force effects. *Mechanics of Materials*, 80:136–144, 2015.
- [41] P. J. Blanco, P. J. Sánchez, E. A. de Souza Neto, and R. A. Feijóo. The method of multiscale virtual power for the derivation of a second order mechanical model. *Mechanics of Materials*, 99:53–67, 2016.
- [42] R. Craig and M. Bampton. Coupling of substructures for dynamic analyses. *AIAA journal*, 6(7):1313–1319, 1968.
- [43] A. Sridhar, V. G. Kouznetsova, and M. G. D. Geers. Homogenization of locally resonant acoustic metamaterials towards an emergent enriched continuum. *Computational Mechanics*, 57(3):423–435, 2016.
- [44] E. Aggestam, F. Larsson, K. Runesson, and F. Ekre. Numerical model reduction with error control in computational homogenization of transient heat flow. *Computer Methods in Applied Mechanics and Engineering*, 326:193–222, 2017.
- [45] F. L. Rivarola, G. Etse, and P. Folino. On thermodynamic consistency of homogenization-based multiscale theories. *Journal of Engineering Materials and Technology*, 139(3):031011, 2017.

- [46] D. S. Schicchi, A. Caggiano, M. Hunkel, and E. A. B. Koenders. Thermodynamically consistent multiscale formulation of a thermo-mechanical problem with phase transformations. *Continuum Mechanics and Thermodynamics*, 31(1):273–299, 2019.
- [47] Q. S. Nguyen. Gradient thermodynamics and heat equations. *Comptes Rendus Mécanique*, 338(6):321–326, 2010.
- [48] W. Liu, K. Saanouni, S. Forest, and P. Hu. The micromorphic approach to generalized heat equations. *Journal of Non-Equilibrium Thermodynamics*, 42(4):327–357, 2017.
- [49] O. C. Zienkiewicz, R. L. Taylor, and J. Z. Zhu. *The finite element method: its basis and fundamentals*. Elsevier, 2005.
- [50] Christan T. Experimental identification of thermal modes. *Master’s Thesis, Delft University of Technology*, 2013.
- [51] T. J. R. Hughes. *The finite element method: linear static and dynamic finite element analysis*. Courier Corporation, 2012.
- [52] B. Sonon, B. Francois, and T. J. Massart. A unified level set based methodology for fast generation of complex microstructural multi-phase rves. *Computer methods in applied mechanics and engineering*, 223:103–122, 2012.
- [53] R.F. Gibson. *Principles of composite material mechanics*. CRC press, 2011.
- [54] G. W. Milton. *The theory of composites*. Cambridge University Press, 2002.
- [55] Z. Hashin and S. Shtrikman. A variational approach to the theory of the elastic behaviour of multiphase materials. *Journal of the Mechanics and Physics of Solids*, 11(2):127–140, 1963.
- [56] Y. Benveniste. On the effective thermal conductivity of multiphase composites. *Zeitschrift für angewandte Mathematik und Physik*, 37(5):696–713, 1986.
- [57] R. Hill. A self-consistent mechanics of composite materials. *Journal of the Mechanics and Physics of Solids*, 13(4):213–222, 1965.
- [58] P. Moldrup, T. Olesen, P. Schjønning, T. Yamaguchi, and D. E. Rolston. Predicting the gas diffusion coefficient in undisturbed soil from soil water characteristics. *Soil Science Society of America Journal*, 64(1):94–100, 2000.

- [59] E. M. Johnson, D. A. Berk, R. K. Jain, and W. M. Deen. Hindered diffusion in agarose gels: test of effective medium model. *Biophysical Journal*, 70(2):1017–1023, 1996.
- [60] S. I. Nishimura, G. Kobayashi, K. Ohoyama, R. Kanno, M. Yashima, and A. Yamada. Experimental visualization of lithium diffusion in Li_xFePO_4 . *Nature Materials*, 7(9):707, 2008.
- [61] C. Miehe, J. Schotte, and J. Schröder. Computational micro–macro transitions and overall moduli in the analysis of polycrystals at large strains. *Computational Materials Science*, 16(1-4):372–382, 1999.
- [62] M. G. D. Geers, V. G. Kouznetsova, and W. A. M. Brekelmans. Multi-scale computational homogenization: Trends and challenges. *Journal of Computational and Applied Mathematics*, 234(7):2175–2182, 2010.
- [63] S. Saeb, P. Steinmann, and A. Javili. Aspects of computational homogenization at finite deformations: a unifying review from Reuss’ to Voigt’s bound. *Applied Mechanics Reviews*, 68(5):050801, 2016.
- [64] K. Matouš, M. G. D Geers, V. G. Kouznetsova, and A. Gillman. A review of predictive nonlinear theories for multiscale modeling of heterogeneous materials. *Journal of Computational Physics*, 330:192–220, 2017.
- [65] L. Brassart and L. Stainier. Effective transient behaviour of inclusions in diffusion problems. *ZAMM-Journal of Applied Mathematics and Mechanics/Zeitschrift für Angewandte Mathematik und Mechanik*, 98(6):981–998, 2018.
- [66] L. Brassart and L. Stainier. Effective transient behaviour of heterogeneous media in diffusion problems with a large contrast in the phase diffusivities. *Journal of the Mechanics and Physics of Solids*, 124:366–391, 2019.
- [67] A. Waseem, T. Heuzé, L. Stainier, M. G. D. Geers, and V. G. Kouznetsova. Model reduction in computational homogenization for transient heat conduction. *Computational Mechanics*, 65(1):249–266, 2020.
- [68] J. C. Simo and T. J. R. Hughes. *Computational inelasticity*, volume 7. Springer Science & Business Media, 2006.

- [69] E. Cuthill and J. McKee. Reducing the bandwidth of sparse symmetric matrices. In *Proceedings of the 1969 24th National Conference*, pages 157–172. ACM, 1969.
- [70] J. L. Chu and S. Lee. The effect of chemical stresses on diffusion. *Journal of Applied Physics*, 75(6):2823–2829, 1994.
- [71] F. Yang. Interaction between diffusion and chemical stresses. *Materials Science and Engineering: A*, 409(1-2):153–159, 2005.
- [72] A. Marmarou. A review of progress in understanding the pathophysiology and treatment of brain edema. *Neurosurgical Focus*, 22(5):1–10, 2007.
- [73] D. Gupta and P. S. Ho. Diffusion phenomena in thin films and microelectronic materials. *Noyes Data Corporation, Mill Rd. at Grand Ave, Park Ridge, New Jersey 07656, USA, 1989. 588*, 1989.
- [74] Z. Cui, F. Gao, and J. Qu. A finite deformation stress-dependent chemical potential and its applications to lithium ion batteries. *Journal of the Mechanics and Physics of Solids*, 60(7):1280–1295, 2012.
- [75] M. J. Aziz. Thermodynamics of diffusion under pressure and stress: Relation to point defect mechanisms. *Applied Physics Letters*, 70(21):2810–2812, 1997.
- [76] V. S. Eremeev, V. N. Mikhailov, and E. B. Boiko. Analysis of the level of concentration stresses and their effect on the mass transport process under diffusion saturation. *Mat. Met. Fiz.-Mekh. Polya*, 17:43–48, 1983.
- [77] G. Frohberg. Diffusion and atomic transport. In *Materials Sciences in Space*, pages 93–128. Springer, 1986.
- [78] M. E. Gurtin, E. Fried, and L. Anand. *The Mechanics and Thermodynamics of Continua*. Cambridge University Press, 2010.
- [79] C. Herring. Diffusional viscosity of a polycrystalline solid. *Journal of Applied Physics*, 21(5):437–445, 1950.
- [80] C. Zener. *Elasticity and anelasticity of metals*. University of Chicago press, 1948.
- [81] E. C. Aifantis. On the problem of diffusion in solids. *Acta Mechanica*, 37(3-4):265–296, 1980.

- [82] W. S. Gorsky. Theorie der elastischen nachwirkung in ungeordneten mischkristallen (elastische nachwirkung zweiter art). *Physikalische Zeitschrift der Sowjetunion*, 8:457–471, 1935.
- [83] S. Golmon, K. Maute, and M. L. Dunn. Numerical modeling of electrochemical–mechanical interactions in lithium polymer batteries. *Computers & Structures*, 87(23-24):1567–1579, 2009.
- [84] J. G. Swallow, W. H. Woodford, Y. Chen, Q. Lu, J. J. Kim, D. Chen, Y. M. Chiang, W. C. Carter, B. Yildiz, H. L. Tuller, and K. J. Van Vliet. Chemo-mechanics of ionically conductive ceramics for electrical energy conversion and storage. *Journal of Electroceramics*, 32(1):3–27, 2014.
- [85] X. Zhang, W. Shyy, and A. M. Sastry. Numerical simulation of intercalation-induced stress in Li-ion battery electrode particles. *Journal of the Electrochemical Society*, 154(10):A910–A916, 2007.
- [86] K. Zhao, M. Pharr, J. J. Vlassak, and Z. Suo. Fracture of electrodes in lithium-ion batteries caused by fast charging. *Journal of Applied Physics*, 108(7):073517, 2010.
- [87] S. Golmon, K. Maute, and M. L. Dunn. Multiscale design optimization of lithium ion batteries using adjoint sensitivity analysis. *International Journal for Numerical Methods in Engineering*, 92(5):475–494, 2012.
- [88] Y. M. Chiang and B. Hellweg. Reticulated and controlled porosity battery structures, June 30 2009. US Patent 7,553,584.
- [89] F. Larché and J. W. Cahn. A linear theory of thermochemical equilibrium of solids under stress. *Acta Metallurgica*, 21(8):1051–1063, 1973.
- [90] S. C. Ko, S. Lee, and Y. T. Chou. Chemical stresses in a square sandwich composite. *Materials Science and Engineering: A*, 409(1-2):145–152, 2005.
- [91] M. Ebner, F. Geldmacher, F. Marone, M. Stampanoni, and V. Wood. X-ray tomography of porous, transition metal oxide based lithium ion battery electrodes. *Advanced Energy Materials*, 3(7):845–850, 2013.
- [92] S. Kaessmair and P. Steinmann. Computational first-order homogenization in chemo-mechanics. *Archive of Applied Mechanics*, 88(1-2):271–286, 2018.

- [93] M. G. D. Geers, V. G. Kouznetsova, and W. A. M. Brekelmans. Multi-scale computational homogenization: Trends and challenges. *Journal of Computational and Applied Mathematics*, 234(7):2175–2182, 2010.
- [94] C. Miehe and A. Koch. Computational micro-to-macro transitions of discretized microstructures undergoing small strains. *Archive of Applied Mechanics*, 72(4-5):300–317, 2002.
- [95] M. Ender, J. Joos, T. Carraro, and E. Ivers-Tiffée. Three-dimensional reconstruction of a composite cathode for lithium-ion cells. *Electrochemistry Communications*, 13(2):166–168, 2011.
- [96] A. Salvadori, E. Bosco, and D. Grazioli. A computational homogenization approach for Li-ion battery cells: Part 1–formulation. *Journal of the Mechanics and Physics of Solids*, 65:114–137, 2014.
- [97] A. Salvadori, D. Grazioli, and M. G. D. Geers. Governing equations for a two-scale analysis of Li-ion battery cells. *International Journal of Solids and Structures*, 59:90–109, 2015.
- [98] Davide G. *Multiscale and Multiphysics Modeling of Li-Ion Battery Cells*. PhD thesis, Università Degli Studi di Brescia, 2015.
- [99] S. Kaessmair and P. Steinmann. Comparative computational analysis of the Cahn–Hilliard equation with emphasis on c1-continuous methods. *Journal of Computational Physics*, 322:783–803, 2016.
- [100] L. Ji and Z. Guo. Analytical modeling and simulation of porous electrodes: Li-ion distribution and diffusion-induced stress. *Acta Mechanica Sinica*, 34(1):187–198, 2018.
- [101] B. Wu and W. Lu. A battery model that fully couples mechanics and electrochemistry at both particle and electrode levels by incorporation of particle interaction. *Journal of Power Sources*, 360:360–372, 2017.
- [102] O. Weeger, U. Wever, and B. Simeon. Nonlinear frequency response analysis of structural vibrations. *Computational Mechanics*, 54(6):1477–1495, 2014.
- [103] J. L. Auriault, C. Boutin, and C. Geindreau. *Homogenization of coupled phenomena in heterogeneous media*, volume 149. John Wiley & Sons, 2010.

- [104] B. D. Coleman and M. E. Gurtin. Thermodynamics with internal state variables. *The Journal of Chemical Physics*, 47(2):597–613, 1967.
- [105] A. Waseem, T. Heuzé, L. Stainier, M. G. D. Geers, and V. G. Kouznetsova. Enriched continuum for multi-scale transient diffusion coupled to mechanics. *Advanced Modeling and Simulation in Engineering Sciences*, 7(1):1–32, 2020.
- [106] T. Kirchdoerfer and M. Ortiz. Data-driven computational mechanics. *Computer Methods in Applied Mechanics and Engineering*, 304:81–101, 2016.
- [107] T. Kirchdoerfer and M. Ortiz. Data driven computing with noisy material data sets. *Computer Methods in Applied Mechanics and Engineering*, 326:622–641, 2017.
- [108] T. Kirchdoerfer and M. Ortiz. Data-driven computing in dynamics. *International Journal for Numerical Methods in Engineering*, 113(11):1697–1710, 2018.
- [109] R. Eggersmann, T. Kirchdoerfer, S. Reese, L. Stainier, and M. Ortiz. Model-free data-driven inelasticity. *Computer Methods in Applied Mechanics and Engineering*, 350:81–99, 2019.
- [110] R. Xu, J. Yang, W. Yan, Q. Huang, G. Giunta, S. Belouettar, H. Zahrouni, T. B. Zineb, and H. Hu. Data-driven multiscale finite element method: From concurrence to separation. *Computer Methods in Applied Mechanics and Engineering*, 363:112893, 2020.
- [111] J. Yang, R. Xu, H. Hu, Q. Huang, and W. Huang. Structural-genome-driven computing for composite structures. *Composite Structures*, 215:446–453, 2019.
- [112] J. Yvonnet, D. Gonzalez, and Q. C. He. Numerically explicit potentials for the homogenization of nonlinear elastic heterogeneous materials. *Computer Methods in Applied Mechanics and Engineering*, 198(33-36):2723–2737, 2009.
- [113] R. Ibañez, D. Borzacchiello, J. V. Aguado, E. Abisset-Chavanne, E. Cueto, P. Ladevèze, and F. Chinesta. Data-driven non-linear elasticity: constitutive manifold construction and problem discretization. *Computational Mechanics*, 60(5):813–826, 2017.

- [114] F. Ghavamian and A. Simone. Accelerating multiscale finite element simulations of history-dependent materials using a recurrent neural network. *Computer Methods in Applied Mechanics and Engineering*, 357:112594, 2019.
- [115] F. E. Bock, R. C. Aydin, C. J. Cyron, N. Huber, S. R. Kalidindi, and B. Klusemann. A review of the application of machine learning and data mining approaches in continuum materials mechanics. *Frontiers in Materials*, 6:110, 2019.
- [116] F. J. Montáns, F. Chinesta, R. Gómez-Bombarelli, and J. N. Kutz. Data-driven modeling and learning in science and engineering. *Comptes Rendus Mécanique*, 347(11):845–855, 2019.
- [117] D. Huang, J. N. Fuhg, C. Weißenfels, and P. Wriggers. A machine learning based plasticity model using proper orthogonal decomposition. *arXiv preprint arXiv:2001.03438*, 2020.
- [118] F. Chinesta, E. Cueto, E. Abisset-Chavanne, J. L. Duval, and F. El Khaldi. Virtual, digital and hybrid twins: a new paradigm in data-based engineering and engineered data. *Archives of Computational Methods in Engineering*, pages 1–30, 2018.
- [119] L. T.K. Nguyen, M. Rambausek, and M. A. Keip. Variational framework for distance-minimizing method in data-driven computational mechanics. *Computer Methods in Applied Mechanics and Engineering*, 365:112898, 2020.
- [120] A. Waseem, T. Heuzé, M. G. D. Geers, and V. G. Kouznetsova. Two-scale analysis of transient diffusion problems through a homogenized enriched continuum. *European Journal of Mechanics – A/Solids*, pages –, 2020.
- [121] L. Stainier, A. Leygue, and M. Ortiz. Model-free data-driven methods in mechanics: material data identification and solvers. *Computational Mechanics*, 64(2):381–393, 2019.
- [122] T. H. Cormen, C. E. Leiserson, R. L. Rivest, and C. Stein. *Introduction to algorithms*. MIT press, 2009.
- [123] S. Conti, S. Müller, and M. Ortiz. Data-driven problems in elasticity. *Archive for Rational Mechanics and Analysis*, 229(1):79–123, 2018.

- [124] Y. Kanno. Simple heuristic for data-driven computational elasticity with material data involving noise and outliers: a local robust regression approach. *Japan Journal of Industrial and Applied Mathematics*, 35(3):1085–1101, 2018.
- [125] D. González, F. Chinesta, and E. Cueto. Thermodynamically consistent data-driven computational mechanics. *Continuum Mechanics and Thermodynamics*, 31(1):239–253, 2019.
- [126] V. Sepe, S. Marfia, and E. Sacco. A nonuniform TFA homogenization technique based on piecewise interpolation functions of the inelastic field. *International Journal of Solids and Structures*, 50(5):725–742, 2013.
- [127] E Monteiro, Julien Yvonnet, and Qi-Chang He. Computational homogenization for nonlinear conduction in heterogeneous materials using model reduction. *Computational Materials Science*, 42(4):704–712, 2008.
- [128] F. Fritzen and M. Leuschner. Reduced basis hybrid computational homogenization based on a mixed incremental formulation. *Computer Methods in Applied Mechanics and Engineering*, 260:143–154, 2013.
- [129] Hajer Lamari, Amine Ammar, Patrice Cartraud, Grégory Legrain, Francisco Chinesta, and Frédéric Jacquemin. Routes for efficient computational homogenization of nonlinear materials using the proper generalized decompositions. *Archives of Computational methods in Engineering*, 17(4):373–391, 2010.
- [130] A. Waseem, J. Guilleminot, and İ. Temizer. Stochastic multiscale analysis in hydrodynamic lubrication. *International Journal for Numerical Methods in Engineering*, 112(8):1070–1093, 2017.
- [131] O. Rokoš, M. M. Ameen, R. H. J. Peerlings, and M. G. D. Geers. Micro-morphic computational homogenization for mechanical metamaterials with patterning fluctuation fields. *Journal of the Mechanics and Physics of Solids*, 123:119–137, 2019.
- [132] D Roca, Oriol Lloberas-Valls, Juan Cante, and Javier Oliver. A computational multiscale homogenization framework accounting for inertial effects: Application to acoustic metamaterials modelling. *Computer methods in applied mechanics and engineering*, 330:415–446, 2018.

- [133] D. Roca, D. Yago, J. Cante, O. Lloberas-Valls, and J. Oliver. Computational design of locally resonant acoustic metamaterials. *Computer Methods in Applied Mechanics and Engineering*, 345:161–182, 2019.
- [134] S. Chaturantabut and D. C. Sorensen. Nonlinear model reduction via discrete empirical interpolation. *SIAM Journal on Scientific Computing*, 32(5):2737–2764, 2010.
- [135] O. Sigmund and M. P. Bondsgc. Topology optimization. *State-of-the-Art and Future Perspectives, Copenhagen: Technical University of Denmark (DTU)*, 2003.
- [136] A. Waseem, Í. Temizer, J. Kato, and K. Terada. Homogenization-based design of surface textures in hydrodynamic lubrication. *International Journal for Numerical Methods in Engineering*, 108(12):1427–1450, 2016.
- [137] A. Waseem, Í. Temizer, J. Kato, and K. Terada. Micro-texture design and optimization in hydrodynamic lubrication via two-scale analysis. *Structural and Multidisciplinary Optimization*, 56(2):227–248, 2017.
- [138] J. Kato, D. Yachi, K. Terada, and T. Kyoya. Topology optimization of micro-structure for composites applying a decoupling multi-scale analysis. *Structural and Multidisciplinary Optimization*, 49(4):595–608, 2014.
- [139] C. Gustavo Méndez, J. M. Podestá, O. Lloberas-Valls, S. Toro, A. E. Huespe, and J. Oliver. Computational material design for acoustic cloaking. *International journal for numerical methods in engineering*, 112(10):1353–1380, 2017.

Publications

Below is a list of publications related to the thesis

1. A. Waseem, T. Heuzé, L. Stainier, M. G. D. Geers and V. G. Kouznetsova. Model reduction in computational homogenization for transient heat conduction. *Computational Mechanics*, 65(1):249-266, 2020.
2. A. Waseem, T. Heuzé, L. Stainier, M. G. D. Geers and V. G. Kouznetsova. Two-scale analysis of transient diffusion problems through a homogenized enriched continuum. *European Journal of Mechanics A/Solids*, – (revised) 2020.
3. A. Waseem, T. Heuzé, L. Stainier, M. G. D. Geers and V. G. Kouznetsova. Enriched continuum for multi-scale transient diffusion coupled to mechanics *Advanced Modeling and Simulation in Engineering Sciences*, 7:1-32, 2020.
4. A. Waseem, T. Heuzé, M. G. D. Geers, V. G. Kouznetsova and L. Stainier. Data-driven reduced homogenization for transient diffusion problems with emergent history effects. *Computer Methods in Applied Mechanics and Engineering*, – (submitted) 2020.

Acknowledgments

First of all, I would like to sincerely thank my supervisors at Ecole Centrale de Nantes (ECN) and Eindhoven University of Technology (TUE). Prof. Laurent Stainier (ECN), for trusting in my learning abilities and providing with the necessary freedom and time to develop the technical skills during the first two years of the project. Dr. Thomas Heuzé (ECN), for providing scientifically rigorous remarks on the research work and always being critical about the content of the papers. Dr. Varvara Kouznetsova (TUE), I highly appreciate your guidance during the last two years. Your pragmatic approach substantially accelerated the research work and helped finishing the project in time. Prof. Marc Geers (TUE), for being a super manager and providing scientific critique on papers.

I acknowledge friends, whom I met, during the first two years of the Ph.D. in Nantes. Especially, Zoltan Csati for your company to CROUS cafeteria everyday, for organizing trips in Barcelona and Pavia during SEED summer schools, for long walks along Edre river and for detailed discussions on scientific topics. Xiaodong Liu for introducing me to Chinese cuisine, for your help in the official paperwork and for the biking trip La Loire à Vélo. Victor Gomez, for being an elder brother, for all the Mexican recipes, musculation tips and for always being there during ups-and-downs. Haris Malik, for helping me, in the beginning, with the official documentation, opening a bank account, CAF, etc. Saman Lessani and George Jagite for running, biking, and going to Île de Nantes at the weekends. I was lucky to be in the company of brilliant office mates at ECN Adrian Renaud, Rohit Pethe, Baptiste Reyne, Erwan Grelier, Quentin Ayoul-Guilmard, Pierre Robard, and Tauno Tiirats. They cultivated a learning environment through long whiteboard discussions and via an online forum, providing constructive critiques on the ideas and sharing sincere thoughts on the topic. I would also like to thank Cynthia NOZAY, secretary in GeM - Institut de Recherche en Génie Civil et Mécanique for helping with all the documentation regarding ECN, SEED, and conferences. Two organizations, I must mention, which are important for any foreigner to integrate quickly into the French culture and student life Maison des Chercheurs Étrangers Nantes and Erasmus Student Network. They organized cultural and food events,

trips to nearby cities and provided opportunities to meet people.

I would like to mention wonderful friends I made in Eindhoven. Especially, Aslan for all the engaging philosophical and scientific discussions, for long walks, and short trips to nearby cities. Priyam Samantray, I highly appreciate all the effort you put in for helping me to prepare for the presentations and the interviews. Varun Raj, for long discussions on viscoelastoplastic constitutive modeling and their finite element formulations, and I owe you big times for all the delicious food that you shared. Ondrej Rokos, for accompanying me to the bouldering wall at SSCE and later on in the Monk. Martin Doskar, for sharing your code to generate micro-textures used in second and fourth chapter of this dissertation. I would like to thank friends outside of TUE who also contributed to my well being. Especially, Bianca Carague for introducing me to the concept of Social Design and for the weekly errands to the Saturday market. Dirk van Mierlo for teaching me how to climb properly. Among others Karine Cochetel, Yawei Wang, Jayanthi van Kampen, Tingting Wu, and Adrian Stefan Vramulet.

Finally, I would like to mention my mentors. Dr. İlker Temizer, who supervised me during the master studies at Bilkent University. He instilled in me the passion for hard work, taught me how to be organized and strive for knowledge. Finally, my virtual mentor prof. Jordan B. Peterson, who, through his video lectures and books, has a positive impact on how I conduct life.

The financial support for this research by Erasmus Mundus Joint Doctorate SEED project (Ref. 2013-0043) for the first three years and TUE for last year is also highly appreciated.

Curriculum Vitae

Abdullah Waseem was born on the 6th of December 1988 in Jhelum, Pakistan. He obtained the Bachelor of Science in Industrial and Manufacturing Engineering from the University of Engineering and Technology, Lahore, Pakistan, in 2011. He enrolled in Bilkent University, in 2013, for pursuing the Master of Science in Mechanical Engineering and carried out research under the supervision of dr. İlker Temizer. He completed the master thesis titled: “Homogenization-based microscopic texture design and optimization in hydrodynamic lubrication” in 2016. Right after completing the masters, he accepted a joint doctorate project between Ecole Centrale de Nantes (ECN), France and Eindhoven University of Technology (TUE), the Netherlands. He worked at ECN for two years (2016–2018), where he conducted research under the supervision of prof. Laurent Stainier and dr. Thomas Heuzé in the laboratory of GeM–Institut de Recherche en Génie Civil et Mécanique. At TU/e, the research work, which was carried out in the Mechanics of Material research group during 2018–2020, was supervised by prof. dr. ir. Marc Geers and dr.ir. Varvara Kouznetsova. The results of the project are presented in this thesis.

Titre : Homogénéisation numérique et réduction de modèle pour les problèmes de transfert de chaleur transitoire, de diffusion et de mécanique couplée

Mots clés : homogénéisation numérique, réduction de modèles, diffusion non-Fickienne, mécanique data-driven

Résumé : Dans cette thèse, des techniques d'homogénéisation numérique efficaces en termes de calcul sont présentées pour les phénomènes de diffusion dans des matériaux hétérogènes. Comme étape préliminaire, une réduction de modèle pour l'équation de diffusion de chaleur transitoire est effectuée à la micro-échelle en utilisant la synthèse en mode composants, qui fournit une description émergente enrichie-continuum à l'échelle macroscopique.

Sur la base de la localisation des variables d'enrichissement, soit sur les nœuds d'éléments finis, soit sur les points de quadrature, deux schémas de discrétisation spatiale sont analysés pour le déplacement milieu continu.

La formulation du potentiel chimique et des champs de déformation est utilisée, ce qui permet

l'utilisation d'éléments finis continus en C0 standard. Le problème de la micro-échelle, qui implique généralement une solution coûteuse du problème de la mécanique de diffusion de masse couplée est maintenant remplacée par un ensemble d'équations différentielles ordinaires grâce à la réduction du modèle.

Enfin, une approche alternative de réduction de modèle utilisant la mécanique basée sur les données est explorée. Il repose sur une recherche directe et une interpolation à partir d'une base de données au lieu de la solution d'un problème microscopique. La base de données est construite et stockée en utilisant les calculs microscopiques dans une étape hors ligne. Il fournit également une voie pour étendre la méthode de réduction du modèle proposée au régime non linéaire.

Title : Numerical Homogenization and Model Reduction for Transient Heat, Diffusion and Coupled Mechanics Problems

Keywords : computational homogenization, model order reduction, non-Fickian diffusion, data-driven mechanics

Abstract : In this thesis computationally efficient numerical homogenization techniques are presented for diffusion phenomena in heterogeneous materials. As a preliminary step, a model reduction for the transient heat diffusion equation is performed at the micro-scale using component mode synthesis, which provides an emergent enriched-continuum description at the macro-scale.

Based on the location of the enrichment-variables, either on the finite element nodes or the quadrature points, two spatial discretization schemes are analyzed for the enriched-continuum.

The proposed model reduction is also extended to the transient mass diffusion coupled to the mechanics with application to lithium-ion

batteries. Chemical potential and strain fields formulation is used which allows the use of standard C0-continuous finite elements. The micro-scale problem, which usually involves an expensive solution of the coupled mass diffusion-mechanics problem is now replaced by a set of ordinary differential equations through model reduction.

Finally, an alternative model reduction approach using data-driven mechanics is explored. It relies on a direct search and interpolation from a database instead of the solution of a microscopic problem. The database is constructed and stored using the microscopic calculations in an offline stage. It also provides a route to extend the proposed model reduction method to the non-linear regime.